

**Diffraction Modelling of Mobile
Radio Wave Propagation in
Built-up Areas**

A Thesis submitted for the degree of Doctor of Philosophy

by

Simon Reza Saunders

Department of Electrical Engineering and Electronics, Brunel University

October 1991

Abstract

Diffraction Modelling of Mobile Radio Wave Propagation in Built-Up Areas

S.R. Saunders, Department of Electrical and Electronic Engineering, Brunel
University, Uxbridge.

Doctor of Philosophy, October 1991.

This thesis examines theoretical methods of modelling radio wave propagation in built-up areas, with particular application to mobile radio systems. Theoretical approaches allow precise quantitative description of the environment in terms of parameters such as mean building heights and densities, in contrast to the ambiguous nature of more conventional empirical models.

The models are constructed using both scalar and vector field analysis techniques. The vector analysis is accomplished using the Geometrical Theory of Diffraction to describe the detailed effects of building shape and positioning, particularly for short-range situations. Over longer ranges propagation can often be described in terms of multiple edge diffraction over building rooftops using a scalar field representation. This mechanism accounts well for measured field strength variations, but is time consuming to calculate accurately using standard methods. A rapid algorithm for calculating scalar diffraction over multiple building edges with arbitrary positioning is constructed. This model can be used for deterministic prediction of sector median field strengths including slow fading variations when appropriate building data exists. It is also applicable to terrain diffraction problems. For the case when only average building parameters are available a closed form solution to the problem of multiple diffraction over buildings of equal heights and spacings is derived. The solution is applicable to any antenna heights and so provides a rapid and efficient way to predict gross propagation characteristics. Both models are tested against measurements made in the UHF band and are found to yield good prediction accuracy.

Acknowledgements

This work has been supported by the Science and Engineering Research Council under award number 889088999 and by Philips Radio Communication Systems Ltd. of Cambridge under an industrial studentship.

My most sincere thanks are due to my supervisor, Frank Bonar, for his unending patience and uncanny ability to condense the solution to any problem onto a single sheet of paper. Thanks also to all those at Philips that helped, especially to Bob Stevens, David Warford and Tumi Kafaru.

This work is dedicated to my Father and to Gráinne for never giving up on me.

Table of Contents

Chapter One - Introduction	1
1.0 Overview.....	1
1.1 Chapter Summary.....	5
Chapter Two - The Mobile Radio Signal	7
2.1 Mobile Radio Systems: Past, Present and Future.....	7
2.2 Factors Affecting Mobile Radio Propagation.....	11
2.2.1 Path Loss	11
2.2.3 Plane Earth Loss	13
2.2.4 Real Situations	14
2.3 Signal Variation : Parameters of Interest.....	16
2.3.1 Fast Fading.....	16
2.3.2 Slow Fading.....	18
2.3.3 Path Loss Characteristic.....	20
2.4 Summary.....	20
Chapter Three - Existing Prediction Models	21
3.0 Introduction.....	21
3.1 Definition of Terms.....	21
3.1.1 Great Circle Path.....	21
3.1.2 Terrain.....	22
3.1.3 Clutter	22
3.1.4 System Parameters.....	23
3.2 Description of Existing Models	24
3.2.1 The Egli Model.....	24
3.2.2 The Okumura Model.....	26
3.2.3 The Ibrahim and Parsons Model	29
3.2.4 The Allsebrook and Parsons Model.....	31
3.2.5 The Ikegami Model	32
3.2.6 The Walfisch Model	34
3.3 Comparison of Models.....	36
3.3.1 Range Variation	37
3.3.2 Base Station Antenna Heights.....	39
3.3.3 Mobile Antenna Heights	40
3.3.4 Frequency.....	41
3.3.5 Overall Prediction Level.....	43
3.4 Conclusions	44

Chapter Four - Modelling Concepts	46
4.0 Introduction.....	46
4.1 Measurements of Scattered Field structure from Buildings.....	46
4.2 Main Ray / Weak Ray model.....	49
4.3 Previous Modelling Work.....	54
4.4 Scalar Diffraction.....	55
4.4.0 Introduction.....	55
4.4.1 Scalar Waves.....	55
4.4.2 Fresnel-Kirchhoff Diffraction Theory.....	56
4.4.3 Modelling Assumptions - The half plane.....	59
4.4.4 Fresnel Integrals.....	60
4.4.6 Fresnel Zones.....	65
4.5 Analysis of Direct and Reflected Ray Diffraction.....	66
4.6 Summary.....	70
Chapter Five - Ray Methods	71
5.1 Geometrical Optics.....	71
5.2 The Geometrical Theory of Diffraction.....	74
5.2.1 Introduction.....	74
5.2.2 Wedge Diffraction.....	76
5.3 Rooftop Diffraction.....	83
5.3.1 Conducting Half Plane.....	83
5.3.2 Conducting wedge.....	86
5.3.3 Rough Lossy Wedge.....	88
5.4 Street Orientation Model.....	94
5.4.1 Introduction.....	94
5.4.2 Ray Path Analysis.....	95
5.4.3 Results.....	98
5.5 Conclusions.....	105
Chapter Six - Multiple Knife Edge Diffraction	106
6.0 Introduction.....	106
6.1 Approximate Methods.....	106
6.1.0 Discussion.....	106
6.1.1 The Giovanelli Method.....	107
6.1.2 The Near Field Method.....	112
6.1.3 Double Knife Edge Diffraction.....	118
6.2 The Multiple Edge Diffraction Integral.....	121
6.2.1 Development of the Integral.....	121
6.2.2 The Multiple Edge Integral.....	121

6.2.3 Characteristics of The Integral.....	123
6.3 Closed Form Solutions of Multiple Edge Diffraction.....	129
6.4 Methods of Evaluating the Multiple Edge Integral	132
6.4.0 Introduction.....	132
6.4.1 The Vogler Evaluation.....	132
6.4.2 Quadrature Methods	136
6.4.3 Monte Carlo Evaluation	141
6.4.4 Comparison of Methods	144
6.5 Summary	145
Chapter Seven - New Propagation Models.....	146
7.0 Introduction.....	146
7.1 The Flat Edge Model	146
7.1.0 Introduction.....	146
7.1.2 Example Calculations.....	150
7.1.3 Normalising Properties.....	151
7.1.4 Grazing Incidence.....	152
7.1.5 Inclusion of Final Building Diffraction.....	153
7.1.6 Characteristics of the Flat Edge Model	155
7.1.7 Frequency Variation	158
7.1.8 Remote Base Station Model	159
7.1.9 Conclusions	161
7.2 Edge Reduction Technique	162
7.3 Hybrid Prediction Model.....	166
7.3.0 Introduction.....	166
7.3.1 Description of Model	166
7.4 Location Variability.....	169
7.4.0 Introduction.....	169
7.4.1 Fundamentals.....	169
7.4.2 Previous Work.....	170
7.4.3 Building Height Distributions	171
7.4.4 Single Building Height Variation	172
7.4.5 Multiple Building Height Variations.....	174
7.4.6 Summary.....	176
7.5 Conclusions.....	176
Chapter Eight - Measurement Programmes	177
8.0 Introduction.....	177
8.1 Description of First Programme.....	177
8.2 Measurement System	182
8.3 Link Budget	183
8.4 Collection of Building Data.....	184

8.5 Construction of Building Profiles.....	185
8.6 Results	189
8.7 Predictions.....	191
8.7.1 933MHz Comparisons	192
8.7.2 1890 MHz Comparisons.....	194
8.8 Second Measurement Programme	199
8.8.1 Description.....	199
8.8.2 Results	201
8.8.3 Discussion	208
8.9 Conclusion	208
Chapter Nine - Conclusions and Further Work	209
9.1 Summary of Achievements	209
9.2 Further Work.....	211
9.2.1 Collection of Building Data.....	211
9.2.2 Modelling	212
9.2.3 Measurements	213
9.2.4 Overall.....	214
9.3 Conclusions	214
Appendix A	215
References.....	218

Chapter One

Introduction

1.0 : Overview

The performance of any communications system must be considered as the result of the performance of all of its component parts acting together. In the particular case of a mobile radio system the radio channel is usually the most variable system component, yet its behaviour is usually dominant in determining system quality (see figure 1.1). If the channel's performance is poorly understood, then either the system has to be needlessly over-engineered to provide an adequate safety margin, or else degraded system reliability has to be tolerated. Thus considerable motivation exists for understanding and predicting the behaviour of the radio channel.

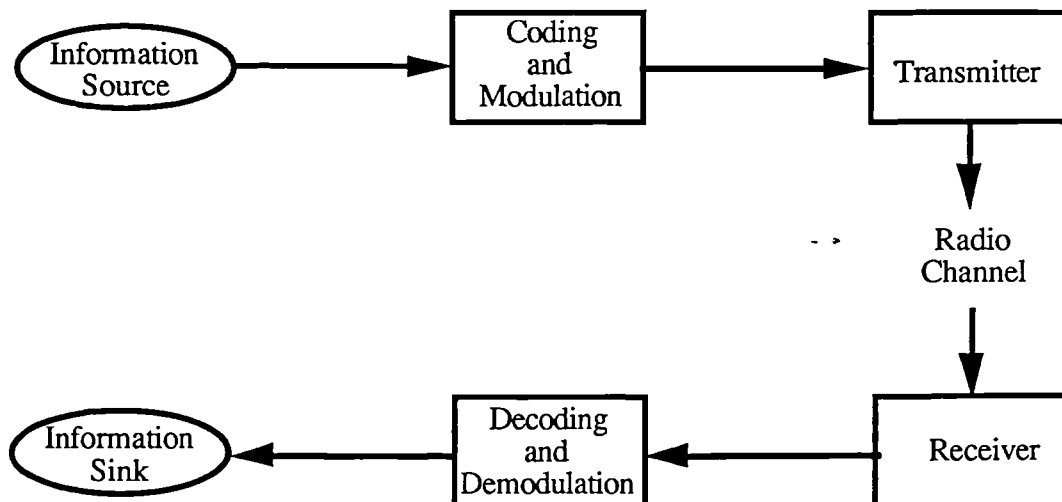


Figure 1.1: A generalised radio communication system.

This work describes one approach to improving methods of predicting the process of radio wave propagation, usually taking place between a fixed base station and a mobile terminal

such as a car or a pedestrian. The usual method of doing this is represented pictorially in figure 1.2. The area within which the mobile may be travelling is divided into a number of regions, each of which is considered by the engineer to be an example of a fixed class of environment. Using the results of measurements which have previously been made in other areas of the same class, together with some elementary physical laws, a prediction of the propagation characteristics across the area can be made. This leads to an assessment of projected service quality in the area, which is the ultimate measure of success for the system under design. This is an **empirical** approach, since the methods used are based principally upon the results of measurements. The characteristics of the whole of an area within a given class are considered identical and usually no account is taken of the differing classes through which the signal has had to propagate before reaching the mobile. More importantly, the classification process relies upon the designer's judgement of the the area, based upon little or no physical data. All of these factors can result in ambiguities and inaccuracies, leading to a poorly designed system.

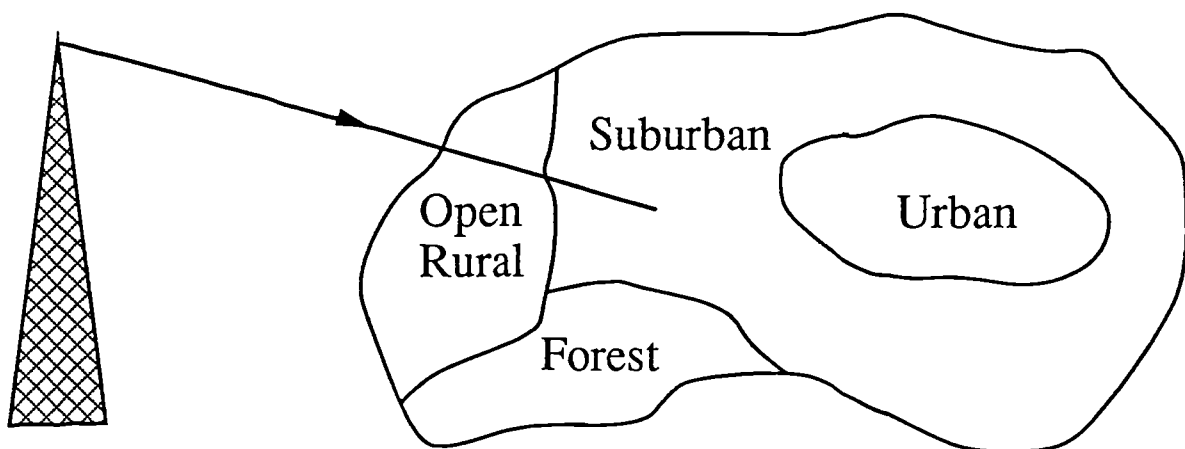


Figure 1.2: *Qualitative classification of the environment.*

In this report another approach to propagation prediction will be considered. If the propagation process is sufficiently well understood then it may be described in terms of a **theoretical model**. Such a model would have as its input a **physical description** of the environment. This description would be quantitative and hence, as far as possible, unambiguous. It may consist of a deterministic description of the positions and

characteristics of environmental features in a given region, or it may comprise a set of statistical parameters which have been selected to give enough information to allow predictions to be made. This approach is pictured in figure 1.3.

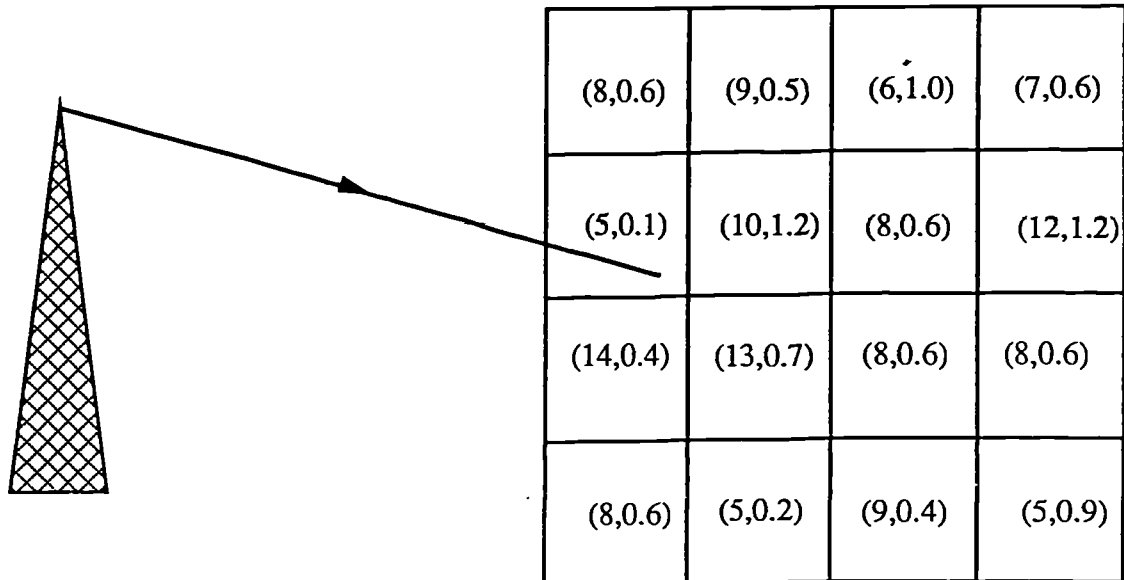


Figure 1.3: *Quantitative environmental description.*

The next step in a prediction is to perform an **analysis**, the characteristics of which will depend upon both the physical description available and the purpose for which the prediction will be used. If the physical description and the analysis technique were exact, then the resulting prediction would be essentially identical to the results of measurements. In practice, the quantity of data available is limited and analysis techniques have to rely upon approximations in order to be tractable. As a result, the theoretical model may need to be modified by corrections found by measurement. The success of the model may thus be measured by how little correction is required.

The prediction process is summarised in figure 1.4. The input for the model consists of the physical description and a limited quantity of measurement data, both of which may require some initial processing before being passed to some combination of the available analysis tools. This report will concentrate on developing the analysis tools, although some consideration of the input data and the output requirements is necessary. The work will mainly be concerned with developing tools for analysis of the effects of buildings, both in

isolation and in built-up areas. This topic is important for two reasons: firstly, the mobile radio signal is subject to greatest variation (and hence most uncertainty) in these areas [Okumura,1968] and secondly because this is where 90% of mobile radio usage takes place.

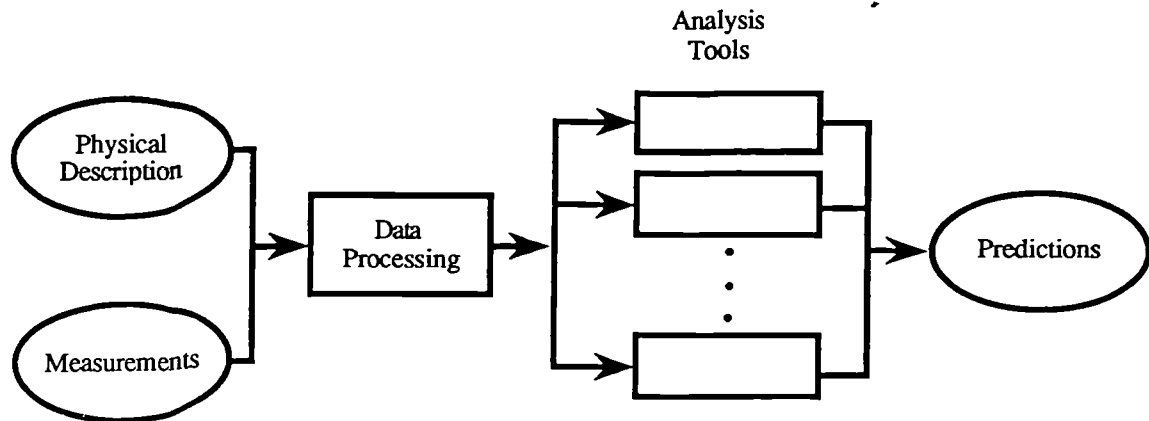


Figure 1.4: *The prediction process.*

In built-up areas the principal mechanism of propagation over a large range (when there is no direct line between the antennas) is diffraction, while reflection and scattering play an increased role over shorter distances. For this reason and because analysis of reflection and scattering processes is relatively well established, the analysis of diffraction effects will be central to this work. The main contribution presented is in the selection and critical examination of analysis techniques for mobile radio applications. Additionally these techniques are used to analyse some particular situations, resulting in some new results which should be of value in the future.

Although the work has been motivated by the study of mobile radio systems, it has many other applications: these include multiple terrain diffraction effects for fixed link radio systems, as well as less obvious wave propagation problems in acoustics and other fields.

1.1 : Chapter Summary

Chapter Two gives some history, examines common systems and then describes the factors which affect the mobile radio signal in a built-up area, giving pointers to the processes which need to be modelled. The resulting characteristics of the signal are examined, including the causes to which others have attributed each of the observed effects. Any successful model must be capable of predicting these variations.

Chapter Three describes a selected group of existing prediction methods, pointing out their strengths and weaknesses. The methods examined include both traditional empirical methods and newer theoretical models. Predictions from the methods are compared using system parameters appropriate to modern systems in order to ascertain their areas of agreement and disagreement. It is found that the theoretical models offer considerable scope for development: these ideas are developed in subsequent chapters.

Chapter Four examines the likely success of theoretical models which are driven by the physical data which is likely to be available in practice. Measurements of the physical structure of the radio wave field encountered in urban situations are surveyed to determine whether enough structure exists to be amenable to analysis. The necessary assumptions about the environment are explained, as are the approximations used in practical analysis techniques. Previous attempts to model the effects of buildings are also examined.

In Chapter Five, diffraction modelling techniques based on ray theory are examined and it is found that these offer considerable scope and flexibility, particularly for modelling the effects of the detailed structure of buildings immediately adjacent to the mobile. The geometrical theory of diffraction is used to model the effects of various building shapes and multiple building configurations. The same theory is also used to develop a model of the effect of street orientation on slow fading. It is concluded that these techniques are useful in these situations provided that care is taken in situations such as multiple buildings at close to grazing incidence.

Chapter Six examines techniques for predicting diffraction over multiple buildings, an important situation for wide area coverage predictions. Efficient techniques for calculating these fields are described, for use when sufficient information about the locations and heights of buildings is available.

In Chapter Seven a technique for predicting diffraction over multiple buildings of the same height and spacing is constructed. This is used as the basis of two new models of propagation in built-up areas. The first of these is stochastic, relying only on average building parameters to characterise an area. The second is deterministic, using a detailed description of the buildings between two locations to provide a prediction of median field strength at a particular location. The models are then used in simulations of the effects of buildings on signal variability.

Chapter Eight describes two sets of measurements conducted in built-up areas. Data describing the building positions and heights in the area were gathered and used with the prediction methods developed in the previous chapters, so as to provide some verification of the approaches used. Good agreement between the theory and the measurements is found.

Finally, Chapter Nine examines the success of the various methods introduced, and examines their applicability in other situations than those for which they were originally developed. The work concludes by setting directions for future extension of this work.

Four conference papers and one journal paper have been published describing various aspects of this work. The first of the conference papers [Saunders,1990a] described general aspects of the feasibility of theoretical modelling, while the others examined location variability due to building height variations as in Chapter Seven [Saunders,1990b,1991,1991b]. The journal paper [Saunders,1991c] presented the Flat Edge model derived in Chapter Seven. This model has also been presented to the COST-231 programme together with a comparison with measurements in the form of [Saunders,1991d].

Chapter Two

The Mobile Radio Signal

2.1 : Mobile Radio Systems : Past, Present and Future

A mobile radio system is any radio-linked communication system in which the position of at least one of the terminals is not fixed, thereby creating flexibility for the user but uncertainty for the designer. The range of possible mobile terminals includes boats and planes, as well as the more familiar situations in cars and as personal portables. Indeed, the first demonstration of a mobile system was in 1897 when Marconi successfully communicated with a tugboat over an 18 mile radio path [Lee,1982]. The first regular mobile service was provided in 1921 for the Detroit police department, followed in 1932 by the New York police department. Both systems were operated at around 2MHz and constituted the first services in the group known as private mobile radio or PMR. This group continues to be of major importance today and includes all of the emergency services (police, fire, ambulance, coastguard and mountain rescue) as well as taxi operators, haulage companies and other users requiring good service over a defined area.

In 1938 the United States Federal Communications Commission licensed regular services in the range 30-40MHz, establishing an upward trend in frequencies which is now resulting in the development of equipment for use in the microwave bands. The use of VHF/UHF frequencies (above 30MHz) is important for the system designer since propagation characteristics are better defined than at HF, with fewer and less frequently occurring anomalous modes of propagation.

In 1947 the first private radio licences in the UK were issued for use on tugs on the Tyne and Wear rivers and by a fleet of taxis in Cambridge [Parsons,1989]. By 1977 there were 200,000 licensed PMR transceivers in use in the UK alone. In 1964 and 1969 mobile radio telephone systems at 150MHz and 450MHz were established, providing the first commercial services for the private individual. Although private users were then an elite group, the concept of personal communications for all is rapidly becoming entrenched, as evinced by the current level of interest in personal communications networks (PCNs).

This massive growth in the number of users to be accommodated within the finite radio spectrum has made frequency re-use techniques essential, requiring ever increasing care and accuracy in propagation design. The primarily line of sight propagation modes at high frequencies allow hills and other obstacles to be used in clearly defining coverage areas, but re-use distances for PMR have previously been as high as 150km [Pye,1979].

Today mobile radio services are well-established and still growing, creating an ever greater demand on finite spectrum resources, together with a need for higher service quality as greater quantities of information are passed by each service. Since 90% of mobile radio usage takes place in built-up areas, the need for good propagation predictions in such areas is intense. However, the combined uncertainties of the mobile position and the nature of the way buildings affect propagation make this task very difficult.

Currently most interest in the mobile radio world is being generated by so-called second generation mobile systems. In 1983 the UK government decided to opt for a system known as TACS - the total access communication system. This system was based upon the North American Advanced Mobile Phone System, and is now the fastest growing network in Europe, supporting some 3/4 million users [Groves,1990]. The system is better known as simply the cellular telephone network, having been the first systematic use of the cellular concept to improve frequency re-use. This concept is now briefly explained.

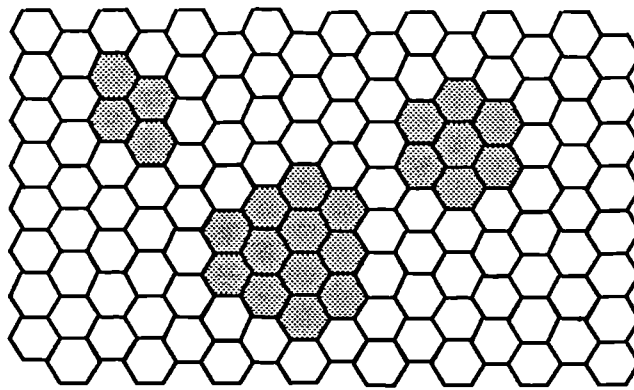


Figure 2.1: *The cellular structure of modern radio systems*

A group of cells is illustrated in figure 2.1. The coverage area is divided into cells, which are taken to be hexagonal for easy conceptualisation. Within each cell a group of frequencies is in use, although coverage may be provided by several base stations in some cases. The cells are then grouped into clusters, where every cell within a cluster occupies a distinct frequency group. Examples of four cell, seven cell and twelve cell clusters are shown. If the field strength decreases sufficiently rapidly away from the cells, frequency groups may be re-used at intervals equal to the distances between the centres of clusters. A seven cell cluster is ordinarily taken to be the smallest useful cluster size, so, according to this simple model, an arbitrarily large area may be covered using just seven frequency groups.

In practice, of course, the safe re-use distance is not constant across an area, but is strongly dependent upon the environment in which the mobile travels. Additionally real cells are neither hexagonal nor even symmetrical, but vary rapidly in shape according to local terrain and clutter variations. Typically the TACS system uses cell radii of from 1km in Central London to some 20km in rural areas. Cells of this magnitude are generally termed **macrocells**. Good propagation predictions are crucial in this situation, in two particular respects. Firstly it is essential that coverage within a given cell is adequate, to ensure that the user receives an acceptable quality of service. Secondly interference must be kept to low levels to permit as much frequency re-use as possible.

In 1991/2 the GSM (*Groupe Spéciale Mobile*) pan-European digital cellular telephone system will be deployed. This is another telephone system operating on macro-cellular

principles in the 890-960MHz region, using a common standard to allow operation right across Europe. The new DCS 1800 system is the first use of PCNs and is likely to be operational by 1992/3. This system will operate between 1710 and 1880 MHz and will use considerably smaller cells than GSM, the first of the projected **microcell** based systems. The CT2 or telepoint series of systems are already operational at 864-868 MHz. These allow a small handset to access the public telephone network from one of a large number of fixed locations spread across the country. For such systems interference planning is eased since there is no requirement to provide seamless coverage across any large area. Similar systems are likely to emerge shortly in the US, again around the 1.7-2.3GHz bands [Taylor,1991].

The clear trend for future systems is towards systems designed for the ordinary person, operating around 1.5-4GHz. Cell sizes are likely to get smaller, creating a greater need for prediction methods which take careful account of building characteristics, since these may be the dominant influence on microcellular propagation. This work will thus be concerned with predicting propagation at high frequencies (above 100MHz) over relatively short paths.

2.2 : Factors Affecting Mobile Radio Propagation

Firstly the major mechanisms which need to be considered when modelling mobile radio propagation are examined. The resulting signal characteristics are then described. A fundamental definition is first required:

2.2.1: Path Loss

In any radio channel only a small proportion of the power transmitted will be received by the intended receiving antenna. This phenomenon is commonly described by the **path loss**, a quantity which is most convenient when expressed relative to two **isotropic radiators**, hypothetical antennas which radiate and receive equally in all directions with no power loss. If the power transmitted and received by these antennas is P_T and P_R respectively, then the total path loss L_T is normally expressed in decibels as :

$$L_T = 10 \log_{10} \left(\frac{P_T}{P_R} \right)$$

Equivalently L_T may be expressed as:

$$L_T = 20 \log_{10} \left(\frac{1}{A} \right)$$

where A is the attenuation function, expressing the ratio between received and transmitted field strengths.

2.2.2: Free Space Loss

At a distance d from an isotropic radiation source the total power has to pass through the surface of a sphere of area $(4 \pi d^2)$ (see figure 2.2).

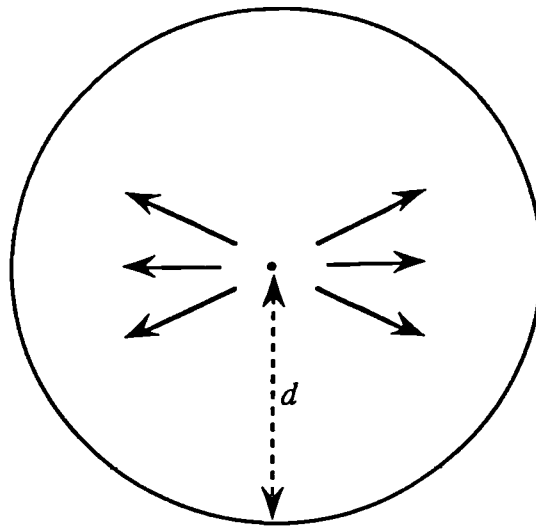


Figure 2.2: *Isotropic radiation causing free space loss*

The power density on this surface is therefore $F = P_T / (4 \pi d^2)$. The effective receiving aperture of an isotrope can be expressed as $A_e = \lambda^2 / 4 \pi$. The power received is therefore:

$$P_R = F \cdot A_e = P_T \left(\frac{1}{4\pi d} \right)^2$$

$$\text{So } \frac{P_T}{P_R} = \left(\frac{4\pi d}{\lambda} \right)^2$$

When expressed in decibels this is the **free space loss**, L_F . Since, in the far field, the wavefronts from any antenna can be regarded as spherical, this loss will effectively always apply. Only under anomalous atmospheric conditions can the received field exceed the free space field strength. This field is therefore taken as a basic reference in propagation calculations. Calculations are usually concerned with predicting the **excess loss**, $L_E = L_T - L_F$. Note that L_F increases at a rate of 20dB per decade of distance or of frequency. In the real atmosphere, loss may be increased beyond the free space value at microwave frequencies due to absorption by oxygen or water vapour [CCIR,370-1] or by rain [CCIR,721-2].

2.2.3: Plane Earth Loss

Another fundamental propagation situation is illustrated in figure 2.3:

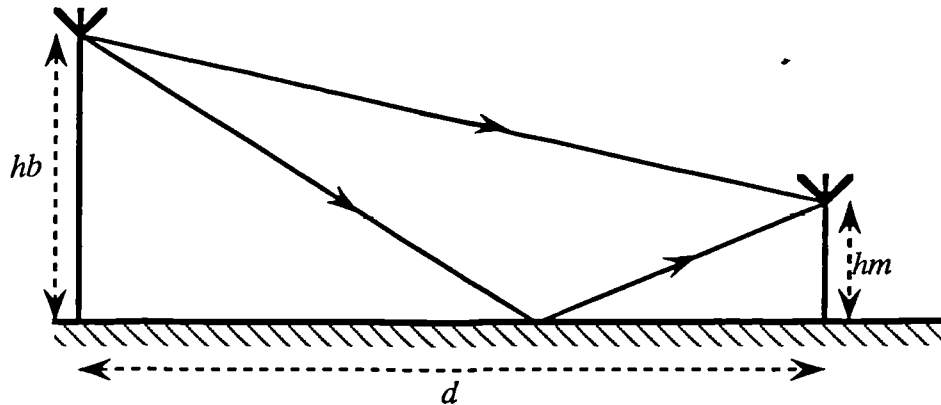


Figure 2.3: Propagation over a plane

When propagation takes place over a slightly lossy plane, power is received as the sum of two discrete waves. If it is assumed that the antenna heights h_b and h_m above the plane are small compared with the horizontal distance, d between them then, to a good approximation, the ground has a reflection coefficient of (-1) for vertical or horizontal polarisation. If the power received in the absence of the plane is P_O then the attenuation function is given by [Shearman,1989]p.36 as:

$$A = 2 \sin \frac{2\pi h_m h_b}{d\lambda}$$

The assumption commonly made for propagation calculations is that the argument of the sine term is very small. Under these conditions it follows that:

$$\frac{P_O}{P_R} = \left(\frac{d\lambda}{4\pi h_m h_b} \right)^2$$

When expressed in decibels this is the excess **plane earth loss**, L_P . Taken together with the free space loss the total loss increases by 40dB per decade of distance and is independent of frequency. The plane earth loss is often used as the basis of models of propagation in built-up areas as will be seen in Chapter Three.

2.2.4: Real Situations

Except in unusually barren areas, real-world propagation will be affected by obstacles such as hills, trees and buildings. These will obstruct the direct (line-of-sight) path between the base station and the mobile, increasing the excess path loss. It is assumed first that atmospheric and other conditions are sufficiently stable that there is no appreciable time variation of signal strength [Saunders,1989]. There are then three main mechanisms by which these obstructions can affect propagation:

i) Specular Reflection:

This is reflection from a large flat surface, such as that treated in the plane earth calculation. If the electrical characteristics of the surface are known then the reflected field strength may be calculated using the Fresnel reflection coefficients (see, for example, [Born,1980], p40). Such a situation may occur at the faces of a large building.

ii) Scattering:

More commonly, the surface of an obstacle is rough, so the field is scattered over a range of angles, with the scattered beam becoming wider as the roughness is increased. The range of surface variation over which reflection may be considered specular is predicted by the Rayleigh criterion [Reudink,1974]. Beyond this it is usual to assume that the surface heights are statistically distributed, and then scattered fields can be predicted by modifying the Fresnel coefficients appropriately. This technique has successfully been applied to predicting scattering from rough terrain [Luebbbers,1984].

iii) Diffraction:

If waves propagated only according to the laws of classical geometrical optics, then the field in the shadow of any building would be zero (see figure 2.4). In practice some field is present in this region due to the complex interaction of the electromagnetic field with the obstacle, especially at the top edge of the building. This phenomenon is **diffraction**, and the resulting field diminishes only slowly as the mobile moves further into the shadow

region, and an interference pattern is observed along the shadow boundary. Whenever the building density in an area is moderate and propagation is taking place over a reasonable distance, line-of-sight paths will rarely exist. Diffraction is then the major mode of propagation and will be crucial to this study.

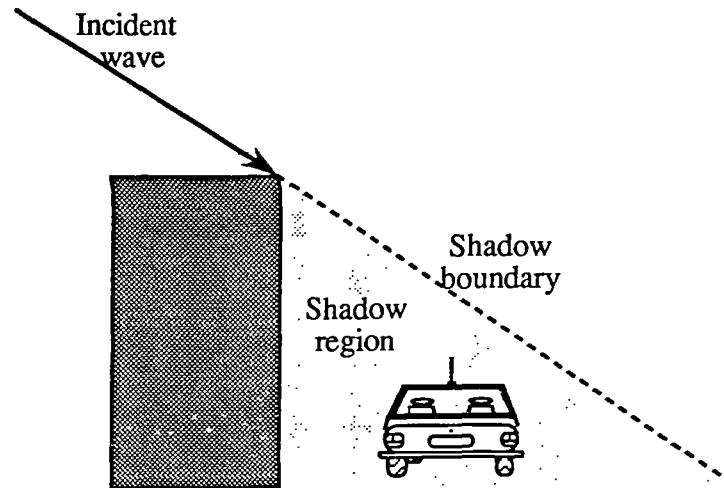


Figure 2.4: Diffraction into the shadow region

All three of the mechanisms described act together to produce considerable variations in field strength as the mobile moves around within its designated service area. The resulting fluctuations can themselves be conveniently separated into three classes: **fast fading**, **slow fading** and **path loss**, each of which is examined in the next section.

2.3 : Signal Variation : Parameters of Interest

An example of a typical mobile radio signal, measured in an urban area, is shown in figure 2.5. As the mobile moves the signal is subject to some very deep fades and small enhancements occurring at intervals comparable to half a wavelength. This is known as **fast fading**. If the median value of the signal is calculated over sliding intervals of around 10 wavelengths another level of variation is apparent : this is **slow fading**. Finally, if the distance between the mobile and the base station is significantly altered then the overall level of the signal will change. This represents the overall **path loss characteristic**. Each of these variations is now examined in more detail.

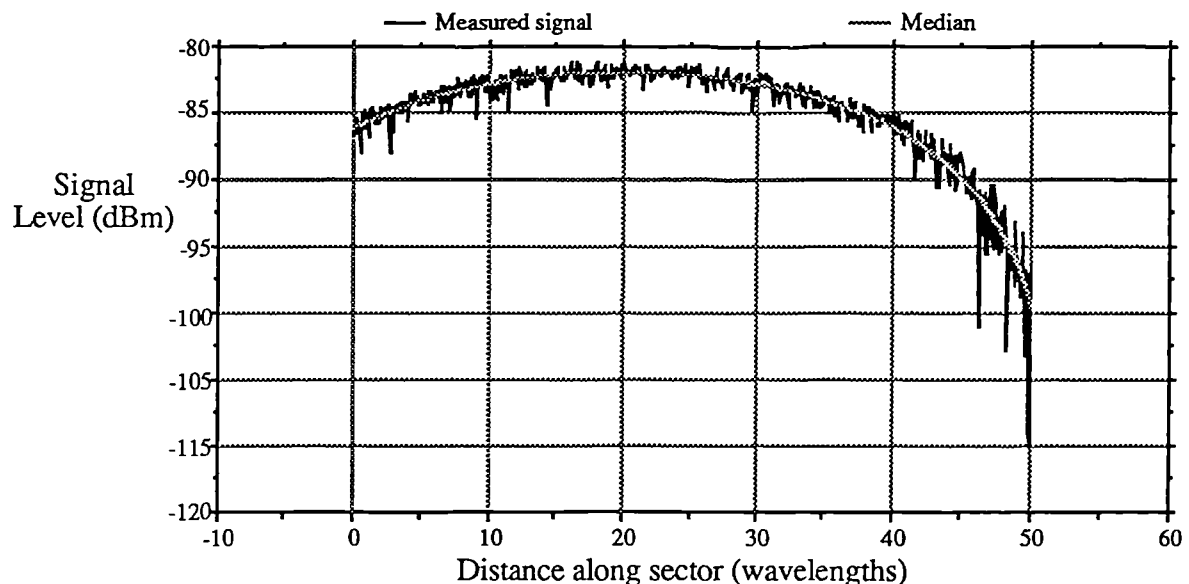


Figure 2.5: A typical mobile radio signal

2.3.1: Fast Fading

It is useful to first divide the area being examined into **sectors**, defined as a region over which the median level is essentially constant so that slow fading may be neglected. Sectors have dimensions which are typically of the order of tens of wavelengths, comparable with the size of major features such as buildings which may affect propagation.

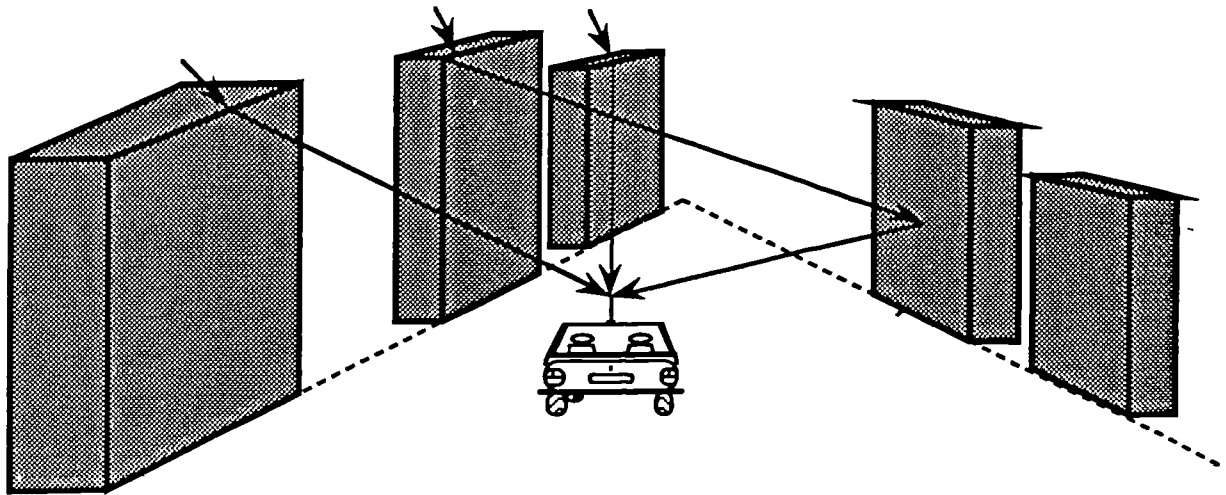


Figure 2.6: *The multipath nature of the mobile radio signal*

Figure 2.6 shows that in a typical built up area the field may arrive at the mobile via a large number of ray paths, with each ray having its own magnitude and associated phase which will depend upon the precise characteristics of the scatterers adjacent to the mobile. The addition of such rays produces fast fading as the position of the mobile varies over distances comparable with a half wavelength. This fast fading, also known as multipath fading, is therefore usually described statistically. The most usual distribution suggested is a Rayleigh distribution of amplitudes, which is the result of adding a large number of sinusoids of equal amplitude and uniformly distributed phase. A number of different distributions have been proposed to cater for a wider range of situations than the simple Rayleigh case, such as the Rice distribution which is appropriate when one wave dominates, usually at short distances where a line-of-sight path exists. Other distributions such as the Weibull, Nakagami and Suzuki distributions have also been proposed [Parsons,1983]. In the time domain fast fading appears as a smearing of the channel's impulse response or **delay spread**. This effect has important implications for the operation of digital modulation schemes, so considerable work has gone into attempting to correlate measured delay spreads with types of environment, such as [COST207,1989].

The median value of the signal within a sector, by definition, is constant: this median value is known as the **sector median** or **local median**. (Note that it is sensible to use the median

rather than some other measure of central tendency such as the mean because the mean tends to be very sensitive to changes in extreme data points when a distribution is asymmetric. The median is also independent of whether the field is expressed in amplitude terms or in decibels) This median level arises from the gross propagation characteristics of the whole sector, although the instantaneous signal level may fluctuate widely.

2.3.2: Slow Fading

Consider a ring of sectors, all a distance R from the base station and within a similar environment (figure 2.7).

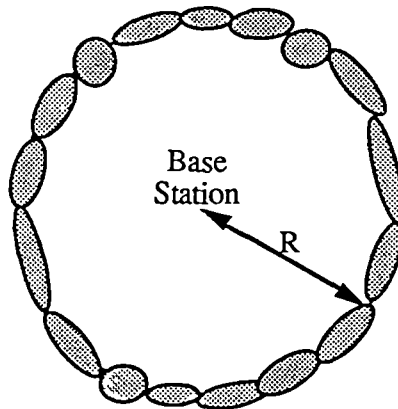


Figure 2.7: *Distribution of sectors at a range R .*

If the local median values for all of the sectors around the ring are measured in decibels and grouped into equally sized (dB) bins, the resulting relative frequencies are found to exhibit an approximately normal distribution, or, equivalently, the underlying amplitudes are distributed lognormally [Lee,1982]. This is the **slow fading**, or **shadowing** component of signal variability. An example is shown in figure 2.8, where the data was collected in New Jersey [Jakes,1974],p119. Despite the fact that the terrain and clutter features along the propagation path to each sector are of similar types and sizes, the precise arrangement will be different for each sector. It has been argued [Chrysanthou,1991] that, since each factor causes a multiplicative loss (a consequence of the linearity of the propagation channel), a lognormal distribution is to be expected from central limit theory. Confirmation of this idea, however, requires detailed modelling of propagation processes.

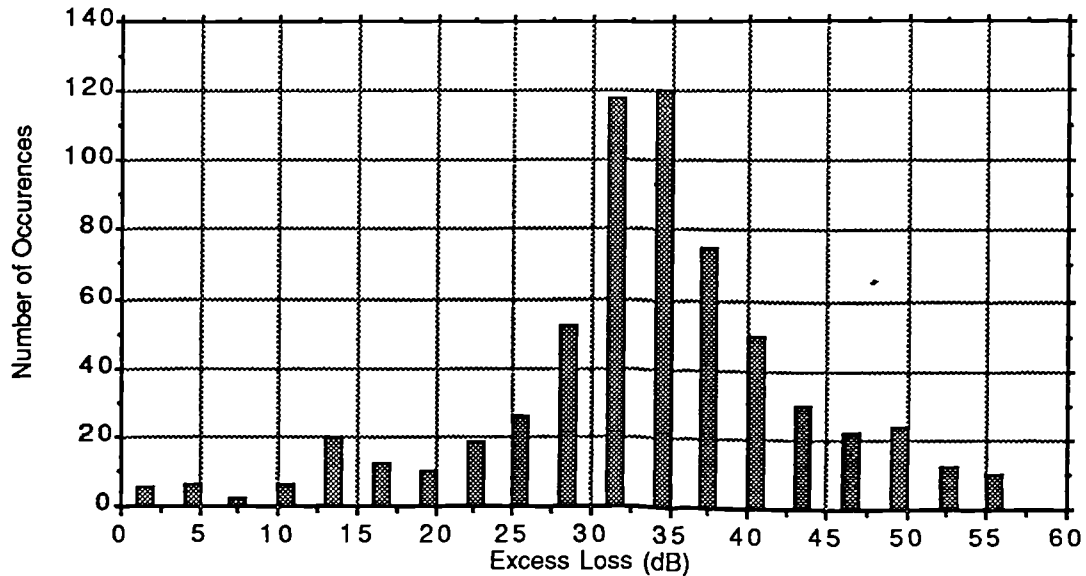


Figure 2.8: Typical slow fading distribution

The standard deviation of this distribution, the **location variability**, depends upon just how irregular the scatterers are. Note that the term 'location' is being used here to denote a **sector's** local median and not just an arbitrary position. The location variability (denoted henceforth by σ_L) varies between around 4dB and 8dB [Holbeche,1985] p.36, and is usually highest in suburban areas. Within a built-up area σ_L appears to increase with the proportion of high buildings and with frequency, but is essentially independent of range [Ibrahim,1983]. Longley [Longley 1978] has produced an empirical formula to predict location variability, but more accurate prediction methods remain to be found. Certainly the value is likely to increase with the range of terrain heights and will be larger in built up areas than in open ones. Standard prediction techniques do not account explicitly for this variation, and the system designer has to assign an estimated value across a given area, with no precise knowledge of where the propagation 'black spots' might be. Deterministic propagation methods capable of predicting these variations are the ultimate aim of this study.

2.3.3 Path Loss Characteristic

Finally, the mean of the lognormal distribution (ie the value of local median not exceeded for 50% of sectors at constant R) is called simply the **median field strength**, arising from the **median transmission loss**. This is the parameter predicted by most existing prediction models. It is conventionally assumed that field strength is proportional to R^{-n} . In built-up areas many reported measurements eg[Ibrahim,1983] have found that n is between 1.5 and 2 (30 to 40dB per decade of range). There is some evidence to suggest that n is still smaller at very short distances [Steele,1991]. Establishing physical reasons why this should be the case is part of the aim of this work.

2.4 : Summary

This chapter has described the history of some the uses to which the radio channel may be put, as well as some of the reasons for variations in its characteristics. This study aims to produce quantitative predictions of the relationships between some of the physical characteristics of the environment and the measured characteristics of the mobile signal. The path loss characteristic and the slow fading behaviour will be of particular interest, since fast fading effects require very detailed modelling for accurate prediction and can usually be considered in terms of simple statistical descriptions.

Specifically the study will concentrate on predicting the effects of buildings on determining the value of the sector median of the signal by taking both average and specific data regarding the positions and types of buildings and analysing their effects using theoretical models. These models will be found to have certain advantages over existing models, a selection of which is described in the next chapter.

Chapter Three

Existing Prediction Methods

3.0 : Introduction

This chapter describes in depth a set of standard models for predicting path loss characteristics, which has been the main aim of prediction models in the past. Theoretical models are capable of giving information in more detail than this, but it is important to examine their performance in this respect first. Common terms will first be discussed and defined.

3.1: Definition of Terms

3.1.1: Great Circle Path

Propagation predictions are usually made between two points close to the surface of the earth. The propagation characteristics between the two points are mainly determined by points which lie along the **great circle path**, which is the geodesic or shortest path between the points. This does not, in general, correspond to the straight line path which would be drawn between the two points on a conventional map, but for short paths (less than, say, 50km) the error is considered negligible. The **path profile** is a two dimensional slice along the path which shows the terrain and other features affecting propagation. Features well off the main path may occasionally affect propagation, but such cases are unusual and are not often considered. See, however [Lebherz,1991] for some discussion of this effect.

3.1.2: Terrain

Terrain heights are the heights of the bare ground along the propagation path relative to some fixed datum. In the past this datum was the sea level, so heights were specified above this (eg 200' asl). More recently, to avoid ambiguity, the datum has been fixed to a level which corresponds approximately to median ocean levels, but is internationally agreed. Heights are therefore now specified above the ordnance datum (eg 180m aod).

In the past, terrain data has been collected using conventional land based surveying techniques. Now methods involving aerial photography and satellite imaging are common (resolutions of around 10m are available from commercial satellites). Interpolation techniques are used to reconstruct a continuous path profile from a finite set of data points between the terminals of the path. For the long distances involved in fixed links (both terminals stationary), terrain is usually dominant in determining whether a given path will be viable.

3.1.3: Clutter

The term clutter is used to describe all features found on the path besides terrain. Trees, buildings and other man-made structures are all examples. Clutter heights are usually specified above local ground (terrain) level (eg 10m agl). There is currently some debate as to how clutter databases should be collected and used for propagation prediction purposes [Mehler,1991]. Clutter has previously been collected into a number of categories in a given area (eg [Okumura,1969]). However, considerable overlap between categories often exists since they are only specified in descriptive terms. There is thus considerable potential for ambiguity and inaccuracy. Usually only two classifications of built-up areas (urban and suburban) are available to describe the regions having the greatest location variability. This work will concentrate on describing clutter in built-up areas in a consistent and reliable manner.

3.1.4: System Parameters

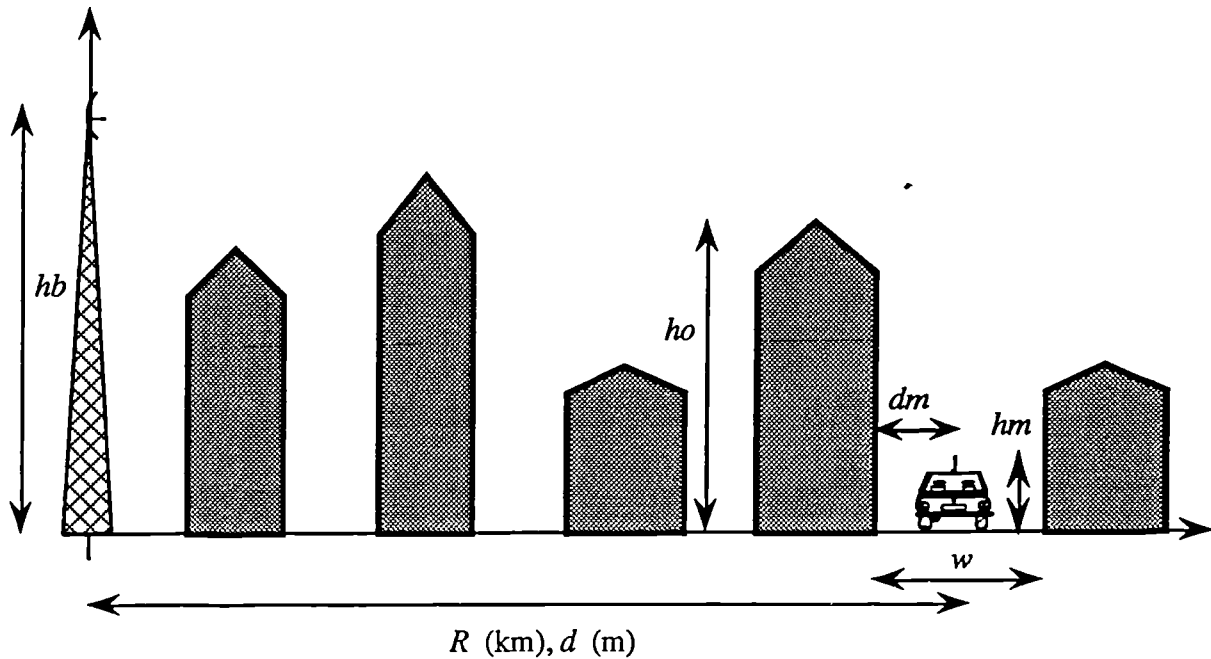


Figure 3.1 : Definitions of physical dimensions in a path profile.

Figure 3.1 shows a path profile in a situation where there is essentially no terrain variation along the great circle path, and defines many of the geometrical parameters which will be used in this text. Other system parameters are defined as follows:

f_c	Frequency (MHz)
f	$f = f_c \cdot 10^6$; Frequency (Hz).
λ	Wavelength (m)
h_b, h_m	Base station / mobile antenna heights, measured from the local ground level to the effective radiation centres of the antennas.
R	Range of mobile from base station. (km)
d	$d = R \cdot 10^3$; Range (m)
w	Street width (m)
d_m	Distance between mobile and nearest building in the direction of the base station.
h_o	Height of last building before mobile.

If terrain variation is moderate, the same definitions are used by simply increasing or

decreasing effective building heights appropriately. Isolated terrain obstacles (hills) have to be treated more carefully.

3.2 : Description of Existing Models

A selection of path loss prediction models is described here. Although they comprise only a small subset of all the models published, it is believed that they are representative in that they describe a wide spread of types, including fully empirical and fully theoretical models. All of those described are frequently quoted in the literature and applied in practice.

3.2.1: The Egli Model

The method due to Egli [Egli,1957] is semi-empirical, being based upon a large number of measurements taken around American cities. Field strength is calculated as the plane earth value decreased by an empirical correction factor to account for clutter and terrain effects. This approach was adopted because Egli's data showed a better fit to plane earth loss than to free space loss, rather than from any theoretical argument.

Egli's overall results were originally presented in nomograph form, but [Delisle,1985] has given an approximation to these results for easier computation:

$$L_T = 20 \log_{10} f_c + 40 \log_{10} R - 20 \log_{10} h_b + \left\{ \begin{array}{l} 76.3 - 10 \log_{10} h_m ; \text{ if } h_m < 10 \\ 85.9 - 20 \log_{10} h_m ; \text{ if } h_m > 10 \end{array} \right\}$$

Note that this approximation involves a small discontinuity at $h_m = 10\text{m}$ (30').

Although plane earth loss is frequency independent, the results show that, with irregular terrain consisting of hills with a height of around 500 feet, an additional f_c^{-1} field strength dependence is introduced down to around 40 MHz. Thus the sector median field strength is inversely proportional to frequency measured with respect to 40 MHz.

The distribution of local median field strength is stated to be lognormal, with a frequency dependent location variability (σ_L). Egli gives $\sigma_L = 8.3$ dB at 127.5 MHz and $\sigma_L = 11.6$ dB at 510 MHz. For very large antenna heights the predicted field strength may exceed the

free-space value, in which case the free-space value is used.

The base station antenna height gain characteristic is found similar to the plane earth calculation so long as the 50 percentile (median) locations are considered. The receiving antenna characteristic is found linear with height (as with plane earth) for antennas which clear the surrounding terrain features. Elsewhere there is a square root variation for heights in the range 6-30 feet, linear above 30 feet. The transition value (30') presumably corresponds to the mean obstruction height, although no correction is made for other heights. The average effect of polarisation is considered negligible.

3.2.2: The Okumura Model:

This is a fully empirical prediction method [Okumura,1968], based entirely upon an extensive series of measurements made in and around Tokyo city between 200MHz and 2GHz. Predictions are made via a series of graphs, the most important of which have since been approximated in a set of formulae by Hata [Hata,1980]. The thoroughness of these two works taken together has made them the most widely quoted prediction model, often regarded as a standard against which to judge new approaches.

The method involves dividing the prediction area into a series of clutter and terrain categories, summarised as follows:

Clutter definitions

Open Area:

Open space, no tall trees or buildings in path, plot of land cleared for 300-400m ahead, e.g. farm land, rice fields, open fields etc.

Suburban Area:

Village or highway scattered with trees and houses, some obstacles near the mobile but not very congested.

Urban Area:

Built up city / large town with large buildings and two or more storied houses, or larger villages with close houses and tall, thickly grown trees.

These definitions rely heavily upon subjective judgement and the method has often been criticised on these grounds. Additionally, it is clear that the categories are quite specific to the Tokyo area.

Okumura takes urban areas as a reference and applies correction factors for conversion to the other classifications. This is a sensible choice since such areas avoid the large location variability in suburban areas and yet include the effects of obstructions better than could be done with open areas. A series of terrain types is also defined, but is not particularly relevant to the current discussion. Quasi-smooth terrain is taken as the reference and correction factors are added for the other types.

Okumura's predictions of median path loss are usually calculated using Hata's approximations [Hata,1980] as follows:

Urban:

$$L_T = 69.55 + 26.16 \log f_c - 13.82 \log h_b - a(h_m) + (44.9 - 6.55 \log h_b) \log R$$

$$a(h_m) = \left\{ \begin{array}{l} (1.1 \log f_c - 0.7) h_m - (1.56 \log f_c - 0.8); \text{ Medium / small city} \\ 8.29 (\log 1.54 h_m)^2 - 1.1; \text{ Large city, } f_c \leq 200\text{MHz} \\ 3.2 (\log 11.75 h_m)^2 - 4.97; \text{ Large city, } f_c \geq 400\text{MHz} \end{array} \right\}$$

The behaviour of $a(h_m)$ in between 200 and 400 MHz does not appear to be specified by either Okumura or Hata. To avoid the small discontinuity which would result from taking $a(h_m) = 0$, a transition frequency of 300MHz has been adopted in the comparisons which follow.

Suburban:

$$L_T = L_T (\text{urban area}) - 2 \left\{ \log \left(\frac{f_c}{28} \right)^2 \right\} - 5.4$$

Another formulation exists for open areas, but is not relevant here. It should be noted that the above equations represent only best fit approximations to Okumura's graphs and should not be considered indicative of underlying propagation mechanisms.

Base station antenna height, h_b , is defined as the height above the average ground level in the range 3-15km from the base station; h_b may therefore vary slightly with the bearing of the mobile from the base. The height gain factor varies between 6dB/octave ($E \propto h_b$) and 9dB/octave ($E \propto h_b^{3/2}$) as the height is increased from 30m to 1km. Measurements also suggested that this factor depends upon range. The value of n in the regime $E \propto R^{-n}$ was found to decrease as h_b increases for $R < 15\text{km}$. For $40\text{km} < R < 100\text{km}$, n reaches a maximum of 3.3 when $h_b = 200\text{m}$, and decreases from this value when $h_b \leq 70\text{m}$.

Mobile antenna height gain was found to vary between 3dB/octave up to $h_m = 3\text{m}$ agl and 8dB/octave for greater antenna heights. It depends partially upon urban density, apparently

as a result of the effect of building heights on the angle-of-arrival of wave energy at the mobile and the consequent shadow loss variation (location variability). Urban areas are therefore subdivided into large cities and medium/small cities, where an area having an average building height in excess of 15m is defined as a large city.

Other correction factors are included for the effects of street orientation (if an area has a large proportion of streets which are either radial or tangential to the propagation direction) and a fine correction for rolling hilly terrain (used if a large proportion of streets are placed at either the peaks or valleys of the terrain undulations). Application of the method involves first finding the basic median field strength in concentric circles around the base station, then amending these according to the terrain and clutter correction graphs.

Okumura's predictions have been found useful in many cases [COST207,1989], particularly in suburban areas. However, other measurements have been in disagreement with these predictions, with the reasons for error often being cited as the difference in the characteristics of the area under test with Tokyo [Eggers,1990]. Other authors such as [Kozono,1977] have attempted to modify Okumura's method to include a measure of building density, but such approaches have not found common acceptance.

3.2.3: The Ibrahim and Parsons Model:

This method [Ibrahim,1983] is based upon a series of field trials around London. The method is not intended as a fully general prediction model, but as a first step towards quantifying urban propagation loss. It integrates well with a previous method [Edwards,1969] for predicting terrain diffraction effects since the same 0.5km square database is also used. Each square is assigned three parameters, H , U and L , defined as follows:

Terrain height, H :

Overall terrain height in each square is defined in the same way as in the [Edwards,1969] model, as follows:

- a) the actual height of a peak, basin, plateau or valley found in each square, or
- b) the arithmetic mean of the minimum and maximum heights found in the square if it does not contain any of the features listed under (a).

Degree of urbanisation factor, U :

The percentage of building site area within the square which is occupied by buildings having four or more floors. For the 24 test squares in inner London which were analysed, U varied between 2% and 95%, suggesting that this parameter is sensitive enough for the purpose.

Land usage factor, L :

The percentage of the test area actually occupied by any buildings. This parameter would perhaps be better termed land coverage factor, since land usage is conventionally used by cartographers to denote the crop types grown in an area.

These parameters were selected empirically as having good correlation with the data. Two models were proposed. The fully empirical method shows marginally lower prediction errors, but relies on a complex formulation which bears no direct relationship to propagation

principles.

The semi-empirical method, as with the Egli method, is based upon the plane earth loss together with a clutter factor β , expressed as a function of f_c , L , H and U . The latter method will be examined here since it has been quoted in later work by the same author [Parsons,1989b], and since it forms a better basis for future development. The model is given as:

$$L_T = 40 \log d - 20 \log (h_m h_b) + \beta$$

$$\text{where } \beta = 20 + \left(\frac{f_c}{40} \right) + 0.18 L - 0.34 H + K$$

$$\text{and } K = 0.094 U - 5.9$$

Data is extracted from the data bases compiled by local authorities in the UK. Since information on U is only available in highly urbanised city centres, K is set to zero elsewhere. Considerably lower accuracy may be expected in such areas since $K = 0$ would correspond to $U = 63\%$. RMS errors calculated from the original data on which the model is based vary from 2.0 to 5.8 dB as frequency is increased from 168 to 900 MHz. A comparison is also shown for some independent data, but error statistics are not given.

A companion paper [Parsons,1983] discusses signal variability. It concludes that the data is Rayleigh distributed within areas of the order of a few tens of wavelengths and lognormally distributed over areas within which the Rayleigh process cannot be regarded as stationary, with a standard deviation of approximately 4dB. The Suzuki distribution is examined as a means of providing global statistics, by combining both fast fading and shadowing. It is proposed that this should be used in conjunction with the median prediction when a given system's area coverage is required to be predicted. It is suggested that location variability increases with U and with the spread of H within the considered area but unfortunately the data is insufficient to establish a reliable relationship. The model is of limited use in suburban areas since U will normally be zero, giving no measure of building height distribution.

3.2.4: The Allsebrook and Parsons Model:

Although this model [Allsebrook,1977] is based upon a series of measurements, it may be regarded as an early attempt to provide a theoretical basis for urban prediction models.

Measurements are made in three British cities (Bradford, Bath and Birmingham) at 86, 167 and 441MHz. These cities cover a wide range of terrain and building classifications. A 40dB/decade range dependence is again forced, as would be expected for plane earth loss. This results in an Egli type model with a maximum RMS error of 8.3dB at 441MHz. (Note that a least-squares approximation at this frequency results in a range dependence of only 24dB/decade). A clutter factor β is introduced to account for excess loss relative to the plane earth calculation.

The frequency dependence of the measured clutter factor is compared with an approximation to the excess loss which would be expected from a 10m absorbing knife edge, placed 30m away from a 2m high mobile antenna. The predictions compare reasonably well with the mean values of β at 86 and 167 MHz, but considerably underestimate it at 441MHz. The knife edge calculation is used as a generalised means of calculating building diffraction adjacent to the mobile, with a UHF correction factor γ included to force agreement with the measured values above 200MHz. It is suggested that this deviation is the result of building width being more significant at the higher frequencies, but this is not confirmed by any analysis. Also, the same small sector size (250m) has been used at all frequencies. This may be expected to cause greater variability (and prediction error) at UHF.

Allsebrook and Parsons' "flat city " model can be expressed as :

$$L_T = L_P + L_B + \gamma$$

$$\text{where } L_B = 20 \log_{10} \left\{ \frac{h_o - h_m}{548 \sqrt{\frac{d_m \times 10^{-3}}{f_c}}} \right\}$$

For ease of computation in the comparisons which follow, the prediction curve for γ has been replaced by the following quadratic approximation:

$$\gamma = -2.03 - 6.67f + 8.1 \times 10^{-5} f^2$$

Note that in the calculation of L_p here the effective antenna heights are those of the base station and the *building*, resulting in a physical model which may be represented by figure 3.2:

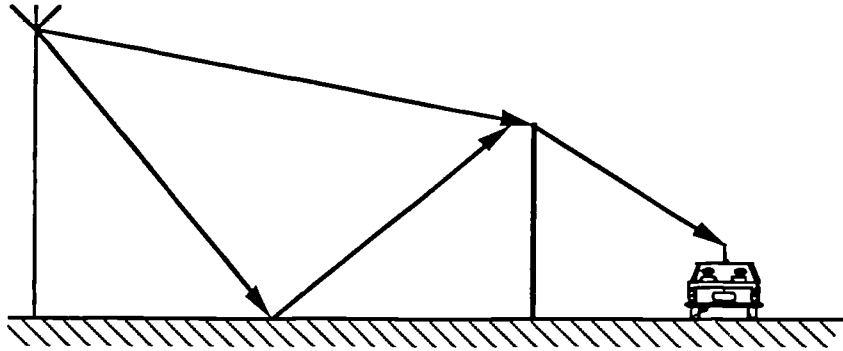


Figure 3.2: *Physical interpretation of Allsebrook model*

A discussion of this model by Delisle [Delisle,1985] finds that the correction factor γ is necessary in open areas as well as in (sub)urban areas, although the physical cause suggested for γ cannot apply in line-of-sight situations. Additionally, the quoted value of γ is found to be too large in all situations, casting doubt upon the model's generality. The model is only physically valid in terms of the final building diffraction; the use of the plane earth calculation suggests the existence of a specular ground reflection, which is highly unlikely in a built-up area. Despite this, the model may be considered an improvement over empirical methods since it is the first that attempts to allow for the geometry of the specific path being considered.

3.2.5: The Ikegami Model

This model attempts to produce an entirely deterministic prediction of field strengths at specified points [Ikegami,1983],[Ikegami,1984],[Ikegami,1991]. Using a detailed map of building heights, shapes and positions, ray paths between the transmitter and receiver are traced, with the restriction that only single reflections from walls are accounted for.

Diffraction is calculated using a single edge approximation at the building nearest the mobile, and reflection loss is assumed to be fixed at a constant value (6dB). The model itself relies on an approximation to single knife edge diffraction: the two rays (reflected and diffracted) are power summed, resulting in the following model:

$$L_E = 10 \log_{10} f_c + 10 \log_{10} (\sin \phi) + 20 \log_{10} (h_o - h_m) - 10 \log_{10} w - 10 \log_{10} \left(1 + \frac{3}{L_r^2} \right) - 5.8$$

This assumes that the mobile is in the centre of the street and that ϕ is the angle between the street and the direct line from base to mobile. It further assumes that the elevation angle of the base station from the top of the knife edge is negligible in comparison to the diffraction angle down to the mobile level.

A comparison of the results of this model with measurements at 200, 400 and 600MHz shows that the general trend of variations along a street is accounted for successfully. The predictions suggest that field strength is broadly independent of a mobile's position across the street. This is confirmed by the mean values of a large number of measurements, although the spread of values is rather high. Acceptable agreement is also obtained for variations with street angle and width.

Although it accounts reasonably well for 'close-in' variations in field strength, the assumption that base station antenna height does not affect propagation is flawed. The same assumption means that the free space variation with range is assumed, so the model tends to underestimate loss at large distances. Similarly, the variation with frequency is underestimated compared with measurements.

3.2.6: The Walfisch Model

This model of urban propagation [Walfisch,1988] examines the case when propagation takes place over the rooftops of a large number of buildings of equal height and spacing (see figure 3.3). The propagation process is split into two independent parts: multiple forward diffraction over the rooftops, followed by a single edge diffraction down to the mobile at ground level. The buildings are modelled as absorbing knife edges with a plane wave incident upon them at a given elevation angle, α . Using a numerical evaluation of the Kirchhoff-Huygens integral the field at the n -th edge is calculated for various values of α and of the edge spacing, w , and it is found that the excess field settles to a constant value if n is taken large enough. Since the calculations are extremely time consuming to perform, a simple power-law formula is fitted to the results for the settled field, which, in combination with a simple approximation to single edge diffraction at the building nearest the mobile, forms a complete theoretical model of propagation over buildings.

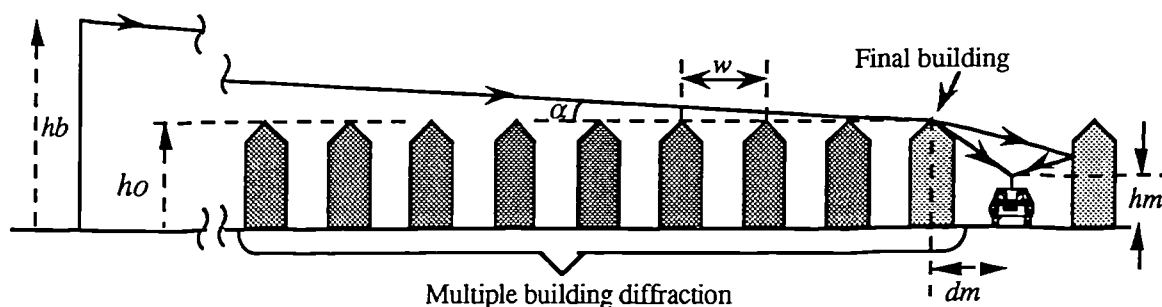


Figure 3.3: Geometry for Walfisch model

The settled field approximation is as follows:

$$A_{settled} \approx 0.1 \left(\frac{\alpha \sqrt{\frac{w}{\lambda}}}{0.03} \right)^{0.9}$$

This is only valid over a limited range of the parameter $\{\alpha \sqrt{(w/\lambda)}\}$ (between 0.03 and 0.4). The 0.9 power suggests that the field will decrease by around 38dB per decade of range, which is usefully close to expectations from measurements.

Overall the median field strength relative to the free-space value is given by:

$$\frac{u}{u_o} = A_{\text{settled}} D_{\text{down}} \sqrt{2}$$

D_{down} is the single knife edge approximation, while the $\sqrt{2}$ factor is intended to account for the ray reflected from the opposite side of the street. It is argued that, since multipath fading is observed to cause very deep fading of the total signal, the two rays must be of comparable amplitude. The sector median field strength is then the power sum of two equal waves. The complete model is expressed as:

$$L_e = 57.1 + A + \log_{10} f_c + 18 \log_{10} R - 18 \log_{10} (h_b - h_d) - 18 \log_{10} \left[1 - \frac{R^2}{17 (h_b - h_d)} \right]$$

$$\text{where } A = 5 \log_{10} \left[\left(\frac{w}{2} \right)^2 + (h_o - h_m)^2 \right] - 9 \log_{10} w + 20 \log_{10} \left\{ \tan^{-1} \left[\frac{2(h_o - h_m)}{w} \right] \right\}$$

Since it is assumed that all of the buildings are of equal height and spacing, significant inaccuracies may be expected when these assumptions are violated. Additionally, the concept of the settled field requires that large numbers of buildings are present, particularly when α is small. Despite these limitations, the Walfisch model is the first to have accounted for observed path loss variation using realistic physical assumptions rather than relying upon forcing agreement using propagation models of entirely different situations.

3.3 : Comparison of Models

In this section the path loss predictions of all of the models are compared in two environmental classes, urban and suburban. Additionally the plane earth calculation is included as a reference assuming antenna heights to be very much greater than their horizontal spacing (see §2.2.3). It is used in this form because this is the basis used for some of the models, but a real calculation over a plane earth would have to include the possibility of signal level nulls.

Variations with all of the significant system parameters are examined: range, frequency, and base station and mobile antenna heights. In the suburban case a building height of 8m and a street width of 40m are assumed. Moderate urban parameters are used, with a building height of 15m and a street width of 30m. In both situations $f_c = 933.5\text{MHz}$, $R = 1\text{km}$, $hb = 25\text{m}$ and $hm = 1.5\text{m}$. For the Ibrahim model the parameters used are $\{L, H, U\} = \{58, 12.7, 54\}$ in the urban case and $\{30, 50, 0\}$ for suburban areas.

First examine the table shown in figure 3.4. It shows the exponents of field strength variation predicted by each model. Thus a '-2' in the range column means that the model predicts that field strength is inversely proportional to the square of range. In some cases (particularly the Hata h_m variation) it is difficult to express the variation in this form, but otherwise it is very useful as a means of comparison.

Model	Range	hb	hm	fc
Free Space	-1	0	0	-1
Plane Earth	-2	1	1	0
Egli	-2	1	0.5 (hm < 10), 1 (hm > 10)	-1
Okumura / Hata	-2.25 + 0.33 log hb	0.69 + 0.33 log R	(see note)	-1.3 (-0.055hm if med/small city) (-0.2 extra if suburban)
Ibrahim	-2	1	1	Field $\propto 10^{(-fc/800)}$
Allsebrook	-2	1	$E \propto 1 / (h_o - h_m)$	-0.5 plus γ variation
Ikegami	-1	0	$E \propto 1 / (h_o - h_m)$	-1.5
Walfisch	-1.9	0.9	$E \propto \left[\left(\frac{w}{2} \right)^2 + (h_o - h_m)^2 \right]^{0.25}$	-1.05

Figure 3.4: Predictions of field strength by various models

Each of the system parameters will now be examined individually:

3.3.1: Range Variation

An accurate prediction of the variation of field strength with range is initially the most important to the system designer, since it determines the coverage area or interference levels for a given system.

It is clear that most of the models predict an inverse range squared variation, since they take the plane earth calculation as a starting point (see figures 3.5 and 3.6). However, the Hata expressions show that, with practical base station antenna heights, the measured path loss exponent is usually rather smaller than this (-1.8 with $h_b = 20\text{m}$, -1.6 for $h_b = 100\text{m}$). Other examples abound : for instance, Black [Black,1972] reports an exponent of -1.5 at 836MHz with $h_b = 152\text{m}$ in Philadelphia, and Ibrahim [Ibrahim,1983] with $h_b = 46\text{m}$ calculates -1.8 at 168MHz. The Ikegami model fails to properly account for range variation due to its reliance on the free-space field. The Walfisch model, however, predicts an exponent of -1.9. Although this value is independent of h_b , its approximate agreement with measurements suggests that the multiple edge diffraction mechanism proposed may be correct. The increase of loss at large ranges is due to a correction for the effect of earth

curvature built in to the model.

Note that the large loss in the Allsebrook case is due to an extrapolation of the model's frequency correction factor outside of its intended range of application.

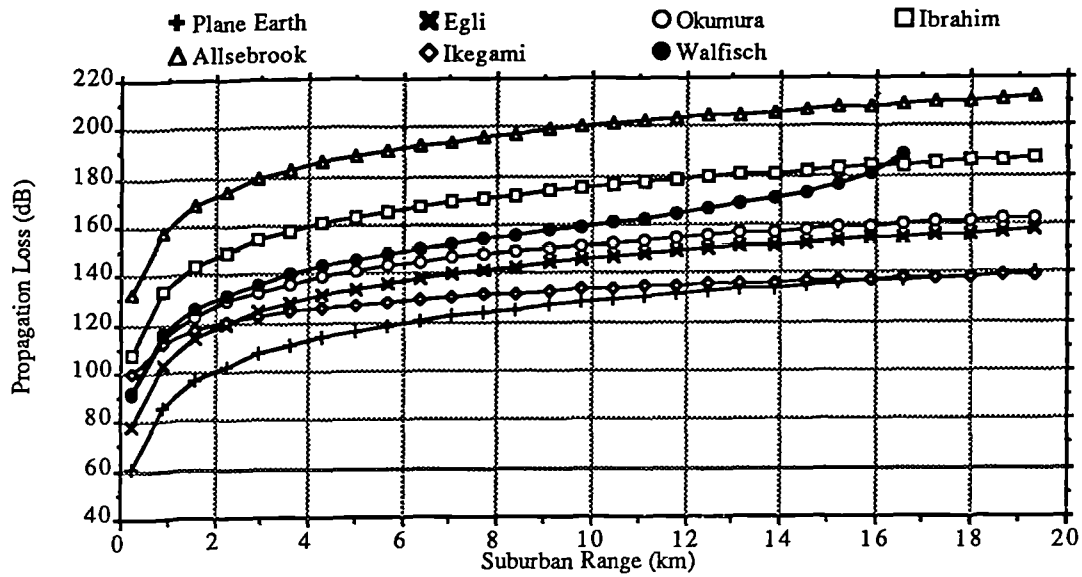


Figure 3.5: Range variation; suburban areas

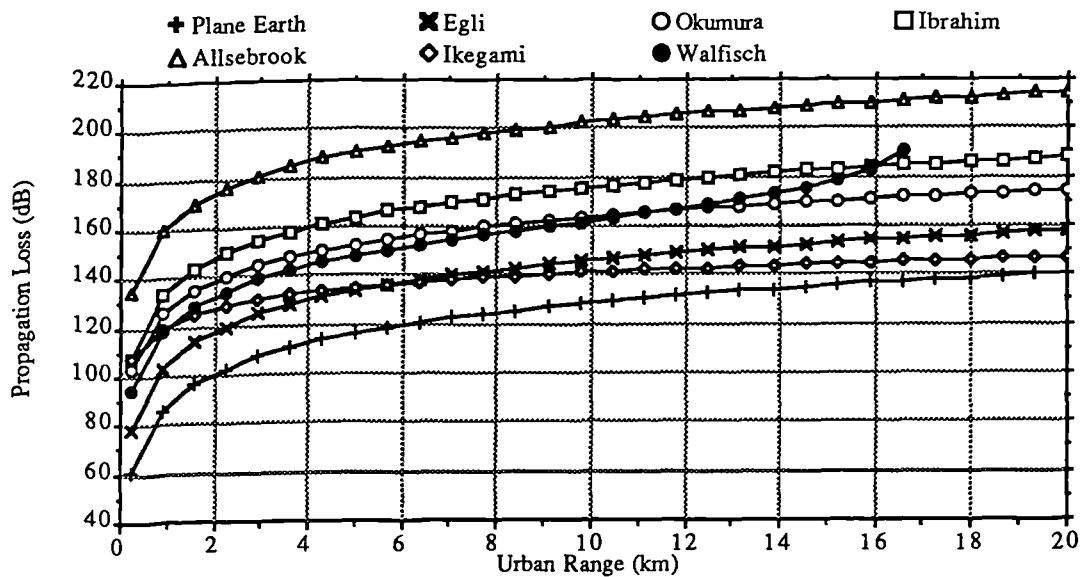


Figure 3.6: Range variation; urban areas

3.3.2: Base Station Antenna Heights

The base station antenna height, together with the transmitter power, is the system parameter which is easiest for the designer to alter. It is important to have an accurate knowledge of the antenna height gain, since additional antenna height is very expensive. Similar conclusions obtain for the base station antenna height gain as for range, suggesting that the two parameters are closely linked. The plane earth calculation predicts simple proportionality between field strength and antenna height, so this law is adopted by most models (see figures 3.7 and 3.8). Empirically, however, the exponent is rather smaller (between 0.69 for $R = 1\text{km}$ and 0.99 for $R = 10\text{km}$ according to the Hata expressions). Again the Ikegami free space approach is misleading, while Walfisch usefully predicts 0.9. It is interesting to note that Walfisch predicts that loss will increase rapidly when the antenna is close to rooftop height. This is an effect which may occur in practice but has not been measured by most studies.

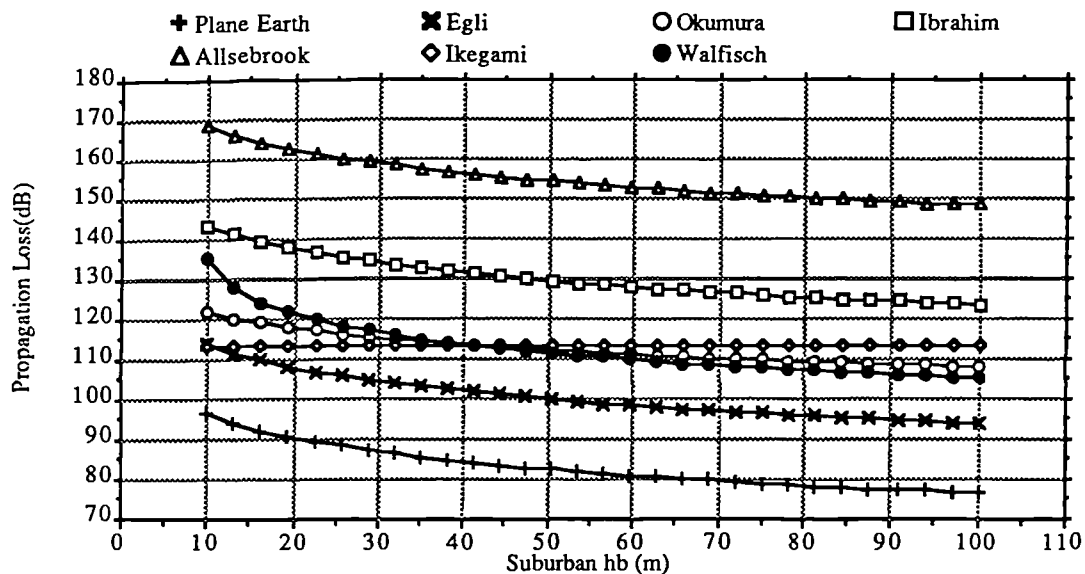


Figure 3.7: Base station antenna height variation ; suburban

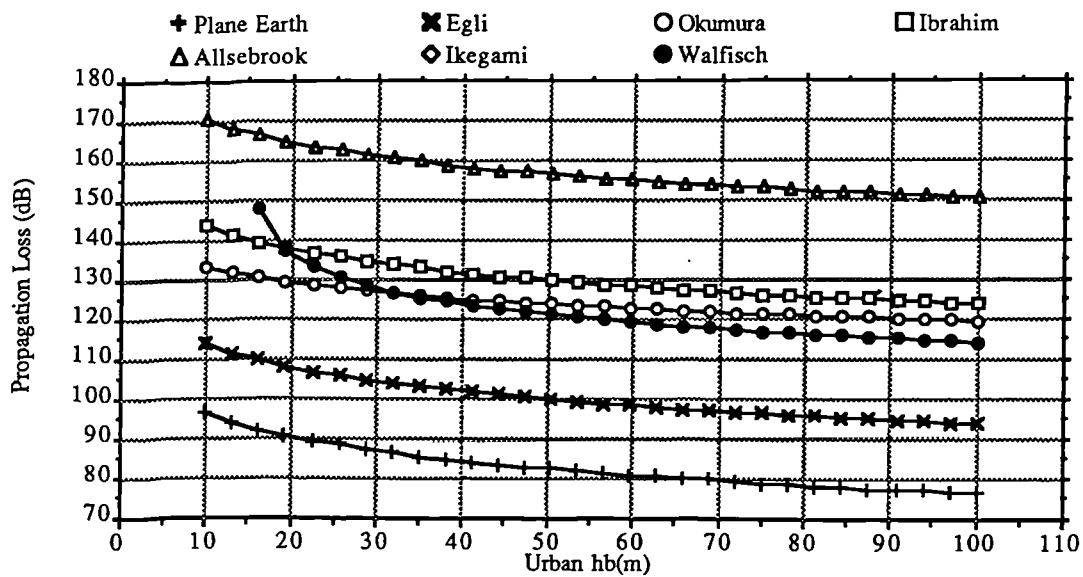


Figure 3.8: Base station antenna height variation : urban

3.3.3: Mobile Antenna Heights

The mobile antenna height is rarely under the designer's control, but is likely to be fixed by the type of system under design. As a result, few studies actually measure this information, with the exception of Okumura. The non-theoretical methods (Egli, Ibrahim) therefore assume the plane earth variation, which figure 3.9 suggests is rather too gradual. The remaining methods (Allsebrook, Walfisch and Ikegami) all use approximate knife edge diffraction at the final building to predict this effect. The result is a sensible variation for moderate antenna heights, but a very abrupt change when h_m approaches the building height. Use of a more complete diffraction calculation is likely to account for this change.

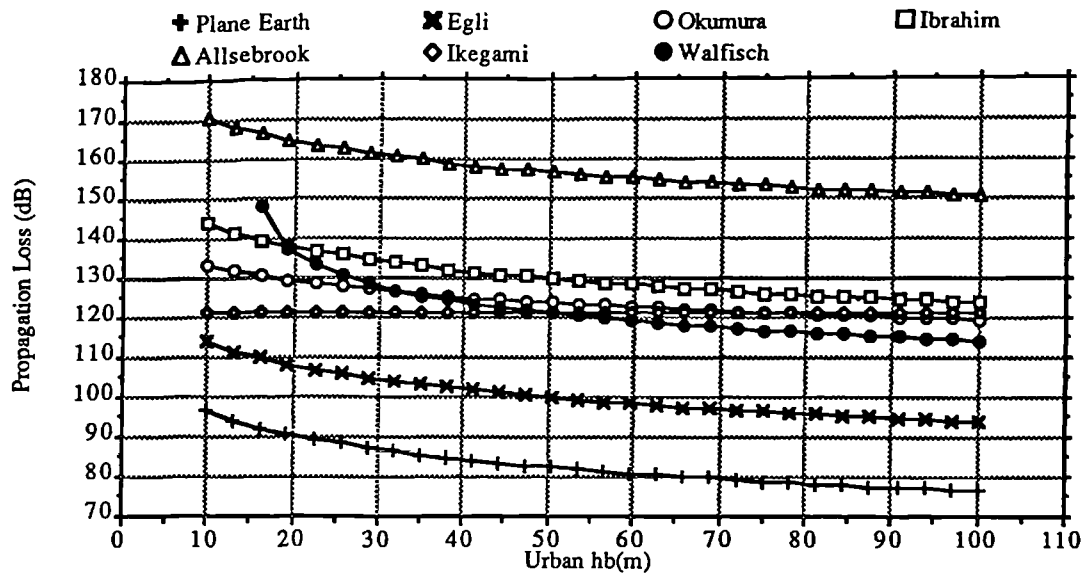


Figure 3.9: Mobile antenna height variation; suburban

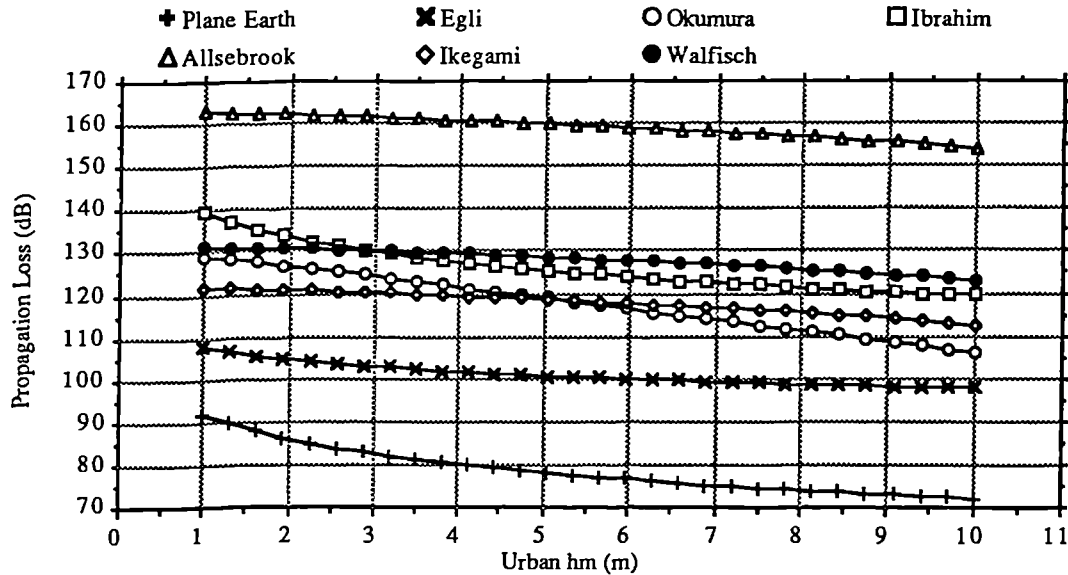


Figure 3.10: Mobile antenna height variation ; urban

3.3.4: Frequency

Empirically, field strength is proportional to frequency raised to a power between -1.5 and -1.3 depending upon the density of buildings. This is considerably greater than the free space value of -1 which is adopted by Egli and appears to be accounted for by the extra -0.5 exponent introduced by single knife edge diffraction in the Ikegami model. This advantage is lost in the Allsebrook calculation due to the use of plane earth field strength as a basis. The result is that the extra function γ has to be introduced, whose extrapolation produces a

major overestimation of loss above 450MHz. Ibrahim also overestimates loss at the higher frequencies due to the empirical correction factor. Note that the Hata expressions are only based upon the Okumura measurements up to 1GHz. More recent work [Eggers,1990] has extended the applicable range up to 2GHz.

Finally, the Walfisch model produces a frequency variation which is only slightly more rapid than free space, rather smaller than the measured effect. This results from a prediction of rooftop field which actually increases with the square root of frequency, tending to reduce the variation overall. It will be seen in Chapter Six that this is a consequence of assuming that the number of significant buildings is always very large. It does not affect the absolute values of the loss predictions unduly, but it would be useful for the model to correctly predict this since it would help to confirm that the correct mechanism is being modelled.

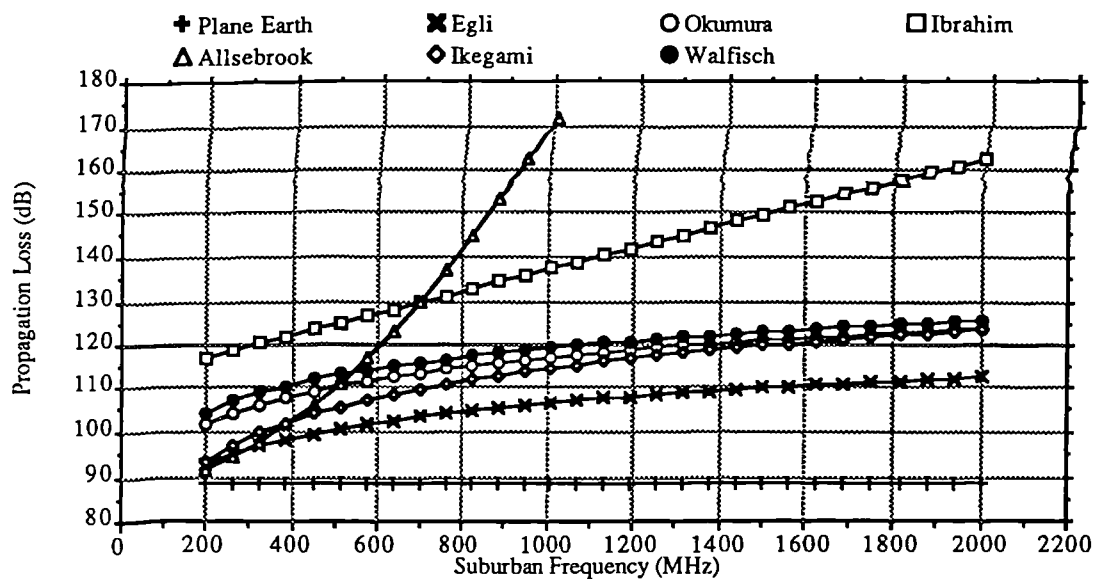


Figure 3.11: Frequency variation ; suburban areas

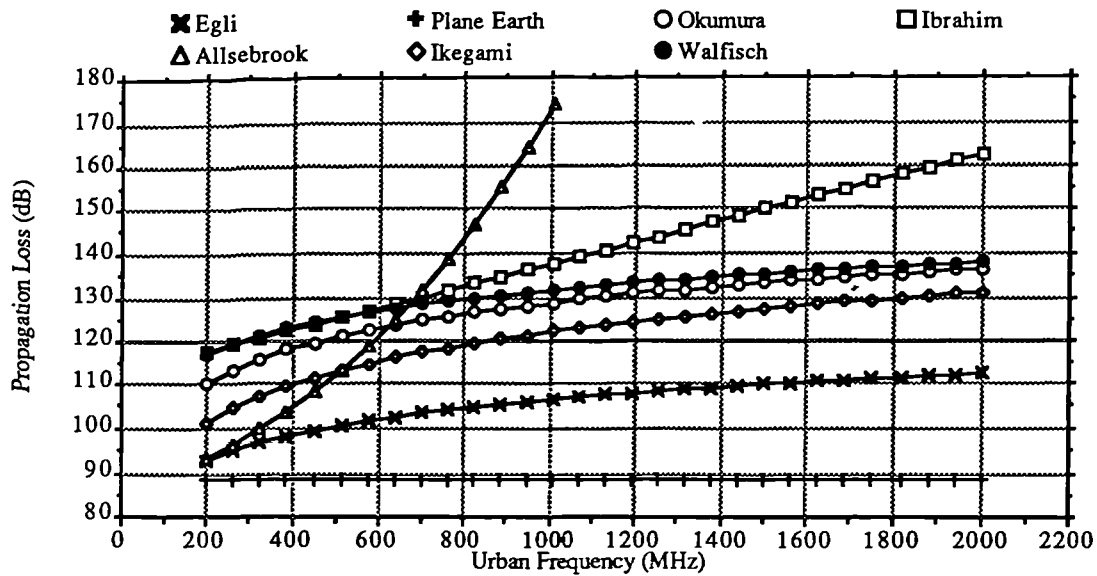


Figure 3.12: Frequency variation; urban

3.3.5: Overall Prediction Level

Apart from the variations due to each parameter, it is of course important to consider the absolute level of the loss predictions. In this case the differences between the models are large, due mainly to the different characteristics of the cities in which the measurements were made. This emphasises the need for a clear method of quantifying the environment. The Allsebrook predictions are consistently higher than the others, due to the extrapolation of the frequency correction factor outside of its intended range of application. It does have the virtue of having at least some variation according to building density. The Ibrahim model also has a tendency to overestimate loss, particularly in the suburban case. This shows that it is really only useful in the environment in which the measurements were originally made: dense urban.

Although it is convenient to account for range variations using the plane earth model, it is clear that the cause of the measured variation in built-up areas is not the same. The multiple edge diffraction mechanism appears far more likely since it accounts for all the other major variations with good accuracy with the exception of frequency variation. The new model proposed in Chapter Seven overcomes this difficulty also.

3.4 : Conclusions

A selection of models having different approaches to the problem of making propagation predictions have been described and compared. The results of the comparisons suggest that the best way to proceed with the development of new models in future is to consider models that have a clear physical and theoretical foundation, although such methods still require further development. It is useful to explicitly state the merits of theoretical models:

- A quantitative description of the environment via building heights, street widths etc. is embodied in theoretical models, avoiding ambiguous subjective classification techniques. If this information is not directly available, then an intelligent estimate is a more consistent approach than simple classification.
- Greater resolution is possible, since the description parameters can vary continuously over a region. The only limitations here are the accuracy required from the predictions and the availability of physical data.
- Potentially greater range of application: It is clear from the foregoing discussion that all models will be valid over only a limited range of parameters. In the case of empirical models this corresponds only to the original range of measurements, since no accuracy in describing the physics of the process is implied. For theoretical models, however, the range of validity depends only upon the reliability of the basic assumptions made in constructing the model. The same is true for applying them in environments different from those originally surveyed.
- Accuracy at least comparable with empirical methods. In the comparisons above it is clear that there is little to choose between the methods in the parameter ranges they are intended for, while the theoretical models are probably more consistent across the whole range considered.
- Although the ultimate test of any model must of course be how well it agrees with real

measurements, it is vital to account for the measurements via physical theories to avoid the need to repeat measurements for every new system combination.

- Point to point predictions: Empirical models give only average characteristics, while theoretical ones can do just this when required, or can additionally predict on a point-by-point basis when physical data is available. It may be anticipated that, when theoretical methods are used to make predictions for individual sectors, errors may be considerably smaller than would be the case using a mean prediction for the whole area.
- Theoretical models relate the physical processes involved in propagation to loss predictions in a form which allows the designer to make useful modifications of the system to vary performance.

These merits have to be weighed against the greater computational expense of theoretical models as compared with their simpler empirical counterparts. *This is an important consideration, especially when it is required to make calculations for many sectors in an area coverage prediction.* However, with the use of modern computing devices and rapid numerical algorithms, very many calculations may be made within acceptable processing times.

The other important consideration is the increased quantity of physical data which must be collected and stored to drive the models. Some important unknowns remain in this subject, so this work will identify those parameters which are actually significant in determining propagation characteristics so as to minimise the data needed.

The rest of this work will be concerned with constructing and testing theoretical models of propagation around and over buildings, which may be of genuine use in making better predictions.

Chapter Four

Modelling Concepts

4.0: Introduction

The aim of this chapter is to introduce and examine the fundamental concepts of theoretical modelling for built-up areas. Measurements of the structure of field variation in such areas are surveyed to determine whether sufficient regularity exists to be amenable to prediction. Using a simple model of multiple ray arrival at the mobile, the effect of neglecting low-level field components is determined and found to cause acceptably small errors. A paradigm for modelling sector median field strengths is thus established, which will be applied throughout the rest of this work. Scalar diffraction theory is introduced and then used in conjunction with the modelling paradigm to predict the effect of varying mobile antenna position and height.

4.1 : Measurements of Scattered Field structure from Buildings

Here previous measurements of the 3D structure of the scattered field in built-up environments are considered in order to establish whether any coherent physical structure is discernible.

Bramley and Cherry [Bramley,1973] made measurements of the scattering coefficients of some tall buildings at 9.4GHz using a helicopter-borne bistatic radar. They found that, although energy was scattered in all directions, the predominant component was always in the specular direction, with a reflection loss some 20-30dB lower than in other directions. The specular component was measured at between 3.5dB and 7dB below the incident field for buildings of mixed glass, concrete and metal construction. Direct measurements of the Fresnel reflection coefficient produced values in the range -2 to 8 dB, with reflection loss

being greatest for rough surfaces such as pebble dash, and smallest for smooth surfaces such as glass. The horizontally polarised field component was generally around 2dB lower than the vertically polarised signal. Overall the authors suggest that the level and angular dependence of the field can be explained in terms of reflections from visible features of the buildings. In general the buildings did not act as a single scattering element but as a collection of imperfectly aligned smaller elements which give rise to the non-specular components.

These findings were supported by [Ranade,1987]. Using geometrical optics and the geometrical theory of diffraction radiation patterns from the face of a large building were simulated. The building surface was modelled as a large number of small panels with random deviations from flat. The resulting patterns show that the directions of strong reflection correspond to the specular components, with non-specular components some 30-40dB lower.

More detailed measurements of received signal structure in an urban environment have been made by [Ikegami,1980]. A directional receiving antenna was used to receive a pulsed signal from a base station at around 200MHz to allow measurements of wave angular distribution and path length. The conclusions suggested that the signal could be decomposed into two classes of components. The first - main rays - were strong in amplitude and varied only slowly in direction of arrival as the measurement position was varied. They were reasonably independent of frequency and their path lengths showed good correspondance with those that would be predicted from a simple geometrical model. There were generally no more than four such rays at a given location. The second class of components-weak rays - were diffuse in character and varied very rapidly along the measurement route, showing no clear relationship to the buildings around them and being at a much lower level than the principal rays.

A third class of components was also identified by [Ikegami,1991]. These are waves which are channeled down a long straight street oriented almost radially from the base station.

These occur relatively infrequently (around 3% of the time- see Chapter Five) and are therefore not considered further in this work. It is likely that they may be modelled in terms of propagation along an open waveguide, or by using a multiple ray model such as that proposed in [Rustako,1991].

A more detailed set of direction of arrival measurements was performed by [Matthews,1991] using a phased array antenna system. This showed that the multipath signal often consists of relatively few strong components whose directions of arrival could be identified with the physical positions of large buildings around the measurement position and having elevation angles which often correspond to diffraction over the tops of adjacent buildings.

In summary, it would appear that the stronger components of the signal received at a typical urban location are produced by simple specular reflections and diffractions from building surfaces and edges; they would probably be amenable to reasonably accurate predictions using tractable theory. The remainder of the signal, resulting from small surface irregularities of the buildings would be very much harder to predict accurately given reasonable quantities of physical building data, but it is at a much lower level and has negligible effect over most of the service area.

4.2: Main Ray / Weak Ray model

Here a simple model of ray arrival within a sector is constructed and considered, with the aim of examining the effect of 'weak' rays on a prediction method which considers main rays only. Main rays are those which may be predicted using straightforward geometrical theories, while weak rays account for all other field contributions.

It is assumed that the parameter of interest is the sector median field strength. This is measured by recording field strength at a large number of positions equally spaced along a straight track, represented in fig 4.1.

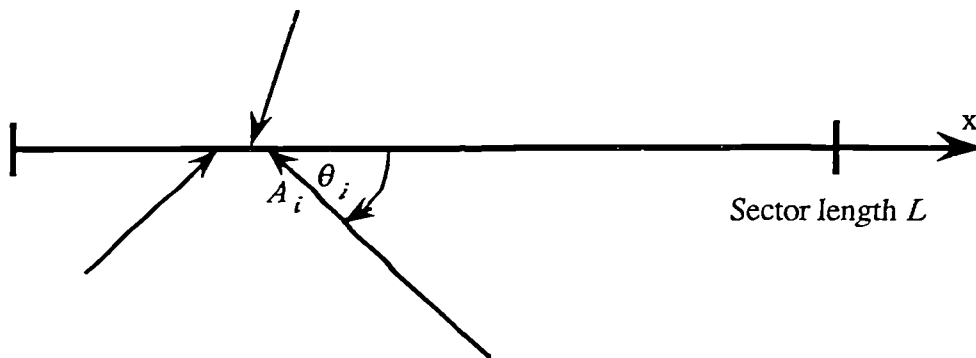


Figure 4.1: Model of ray arrival within a sector

Assume that N main rays arrive at the sector. Using the definition of a sector (§2.3.1) the amplitudes of all of these may be assumed constant along the length of the sector, L . It is further assumed that the azimuthal angle of arrival of each main ray can be assumed constant along the sector since the source for the ray is very distant by comparison with L . The effect of the vertical angle of arrival of the rays is not modelled.

Weak rays differ from the strong rays in having no coherent phase structure. They are modelled in overall effect by two components in quadrature, $p(x)$ and $q(x)$, where x is distance measured along the sector. Both of these are assumed to be normally distributed with zero mean and equal variance, σ^2 . The resultant distribution is therefore Rayleigh

when no main ray component is present, and Rician-like when $N = 1$.

Total instantaneous field strength, $v(x)$, can therefore be expressed as :

$$v(x) = \sum_{i=1}^N A_i e^{j(\phi_i - kx \cos \theta_i)} + p(x) + j q(x)$$

where:

k is the wavenumber

A_i is the amplitude of the i th main ray

ϕ_i is the reference phase of the i th main ray at $x = 0$ relative to $p(x)$. In practice the values would depend on the arbitrarily chosen initial position of the measuring antenna. Here they are all set to zero since they will not materially affect the results.

θ_i is the azimuthal angle of the i th main ray to the x direction in the sense shown in figure 4.1.

All quantities are assumed to be time-invariant.

The sector median m , is defined by :

$$Pr(|v(x)| \leq m) = 1/2$$

An experimental estimate m_m of the median is produced from measurements of the field strength at a large number of points within the sector range. In this work, various propagation models will be used to produce estimates m_e of the median as follows:

$$m_e = \sqrt{\left\{ \sum_{i=1}^N A_i^2 \right\}}$$

This estimate is exact if the phase variation of all the rays is uniformly distributed and independent. If the modelling process is to be successful then the estimation error, (m_m / m_e) , should be acceptably close to unity.

First consider the case when weak rays are absent ($\sigma^2 = 0$). Under certain extreme conditions it is possible that no phase variation in the arriving rays is encountered at all and a

very misleading estimation of the median would be made. This is a possible limitation of the measuring process but is usually prevented in practice by small irregularities in building reflection and diffraction characteristics; a better measurement procedure would sample the field over an area, but this is usually impractical. The difficulty is avoided here by considering only oblique incidence to ensure that there is some phase variation along x . The greater this variation, the smaller the estimation error.

As a representative example, take $N = 2$ and $\theta_1 = 80^\circ$, $\theta_2 = 260^\circ$. Then with $L = 50\lambda$ and unit ray amplitudes, $m_e = \sqrt{2}$ and the following results would be obtained experimentally:

Number of sampling points	Measured median m_m	Estimation error (m_m/m_e) dB
10	1.078	-2.36
25	1.402	-0.078
50	1.426	0.069
100	1.427	0.080
1000	1.423	0.05

Figure 4.2 shows the way in which the measured value of $|v(x)|$ varies in this case:

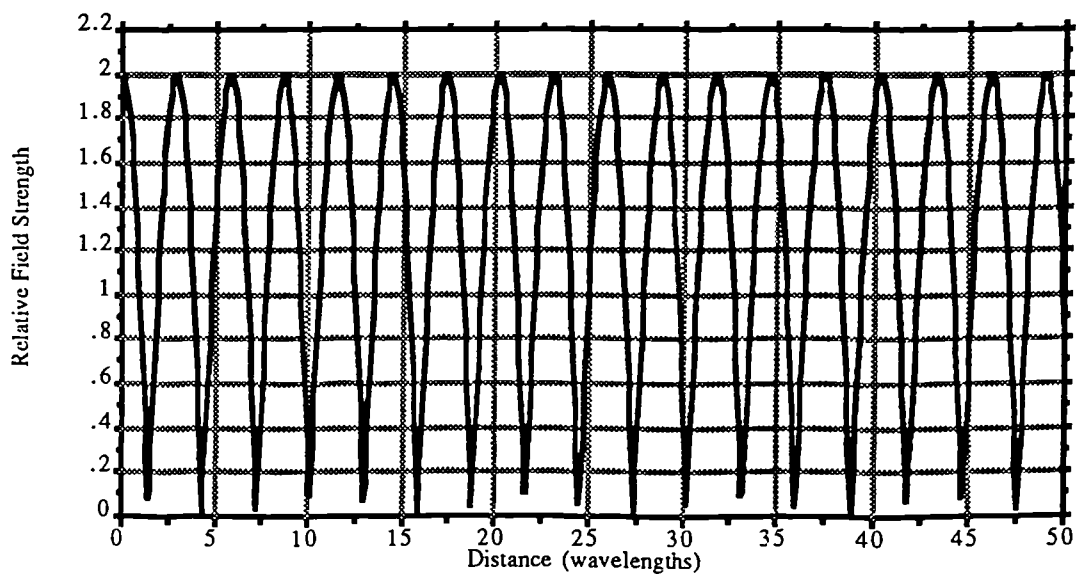


Figure 4.2: Field strength variation : two strong rays

Notice that in this case the error is actually an artifact of the measurement process rather than the estimation, since $\sqrt{2}$ is the true median. It is clear from these results that the error reduces rapidly as the number of sample points per wavelength is increased; best results are obtained with several points per wavelength. In the results that follow $L = 50\lambda$ throughout, and 4 points per wavelength are used.

Recall first from §4.1 that measurements suggested that weak rays may be typically 30dB below main rays in a representative situation. The total power in p and q combined is $(2\sigma^2)$. If this were 30dB below a main ray of unit amplitude then $\sigma = \sqrt{(10^{-3}/2)}$. Using this value an appropriate set of realisations of p and q was produced at each of the sample points and the estimation error was calculated. This procedure was then repeated for varying σ , with the same main rays as above, yielding the following results:

Power in one strong ray : overall weak power (dB)	Estimation error (<i>rm/me</i>) dB
30	0.03
20	0.32
10	0.41
5	0.40
0	1.196

Figures 4.3 and 4.4 show the variation of $|v(x)|$ with 0dB and 10dB ratio between one main ray and the total weak contribution. In the latter case little field structure is visible, yet an acceptably low estimation error is obtained. Overall the results show that even quite large weak components can be tolerated with low estimation errors provided the assumptions of the model are valid. The effect of larger numbers of main rays is to reduce the estimation error still further since greater phase variation occurs within the sector.

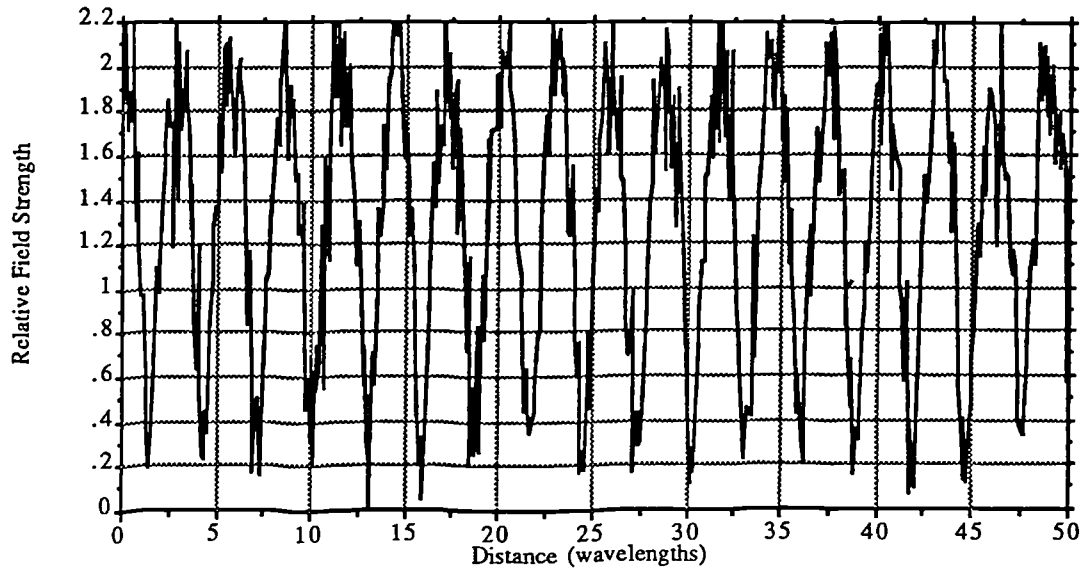


Figure 4.3: Variation of field strength with 10dB main : weak ray

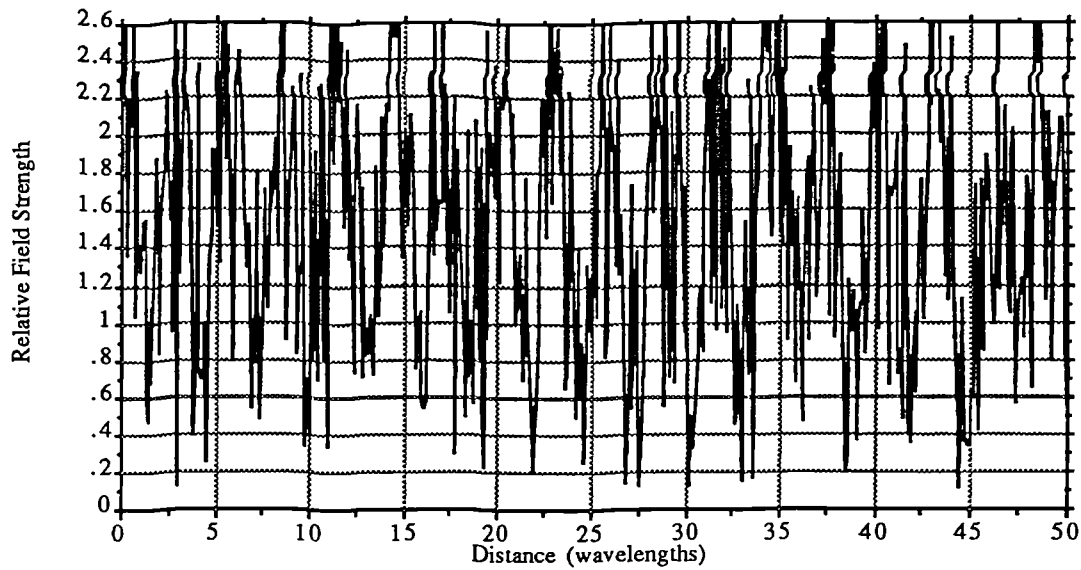


Figure 4.4: Variation of field strength with 0dB main : weak ray

A paradigm for prediction of sector median field strengths has now been established : by power summing main ray contributions, sector medians may be predicted without significant error caused by weak rays except in very extreme cases.

4.3: Previous Modelling Work

This section surveys some previous attempts to model propagation in built-up areas, excluding the Walfisch and Ikegami models which were covered in Chapter Three. Little work in this area has previously been published, but two particular studies are worthy of mention.

The first, by Kafaru [Kafaru,1989], uses a physical model of the building scattering process to predict path delay profiles. Significant scatterers close to the mobile are identified from a database of buildings. The amplitude of their contribution to the received energy is predicted by knowledge of their physical dimensions and assumed reflection properties. The resulting predictions correlate well with measurements, in terms of both the delay times and the amplitudes of individual signal components. This confirms that the mechanisms of propagation in built-up areas are sufficiently well understood to be amenable to prediction and that the field structure is simple enough to allow field components from individual buildings to be correctly modelled. Note however that no diffraction effects were modelled.

The other work of interest here is by Thomas *et al.* [Thomas,1990]. Measurements were made of field variation in the presence of some simple building arrangements, simulated by placement of stackable shipping containers in a disused airfield, as well as some direct measurements on single buildings. This enabled the mechanisms of propagation around individual buildings to be isolated and predicted. A model based on the Geometrical Theory of Diffraction (see Chapter Five) was used to predict the field in a large number of cases. Excellent agreement was found, except in cases where the original modelling assumptions are contravened. This study confirms that theoretical models can account for diffraction around buildings.

4.4: Scalar Diffraction

4.4.0: Introduction

This section produces a simple model of diffraction over the rooftop of the single building closest to the mobile in the direction of the base station (the **final building**) using some approximate theory. This is useful as a task in itself and also serves to introduce the concepts of modelling which will be employed in more depth later. In this chapter only scalar waves will be considered, since such waves provide a sufficiently accurate approach for many simple problems and are amenable to more straightforward analysis. Chapter Six will show that scalar waves are also useful in cases where complete vector field analysis becomes intractable.

4.4.1: Scalar Waves

Electromagnetic waves in free space are **polarised**. Electric and magnetic field components exist in a direction transverse to the direction of propagation, so that a complete description of the field's properties requires a vector formulation. If, however, the main parameter of interest is the variation in the power transmitted by the wave, then a purely **scalar** description will usually suffice. This is so in propagation predictions whenever overall path loss alone is to be calculated. The wave can then be considered as simply carrying power in a manner analogous to the propagation of an acoustic wave through a gas.

In a region where the medium is homogeneous and contains no charges or currents, Maxwell's equations lead to:

$$\nabla^2 E - \frac{\epsilon\mu}{c^2} \frac{\partial^2 E}{\partial t^2} = 0$$

$$\nabla^2 H - \frac{\epsilon\mu}{c^2} \frac{\partial^2 H}{\partial t^2} = 0$$

These are the equations of wave motion with a propagating velocity of $v = c / \sqrt{\mu\epsilon}$. Thus each of the field components, V , satisfies the homogeneous scalar wave equation :

$$\nabla^2 V - \frac{1}{v^2} \frac{\partial^2 V}{\partial t^2} = 0$$

The Kirchhoff integral theorem introduced in §4.4.2 relies on this equation and is therefore

valid in current and charge free regions. In principle the theorem should be applied separately to each of the Cartesian components of the field, but can usually be applied to a single complex scalar wave function with good accuracy, when the main parameter of interest is the relative power contained in the wave rather than the field components themselves. As a consequence, a purely scalar model can express no polarisation dependence.

In such a case the quantity of interest is the time average power flow per unit area at a given point, the **intensity** in optical terminology, or, more commonly, the **average Poynting vector**:

$$I = |E \times H^*|$$

This will be assumed to be represented by a single complex scalar wave, V , as : $I = |V|^2$. Such a representation will be sufficient in most cases dealt with here, except when the effect of polarisation is considered. A more rigorous approach is used in Chapter Five for considering such effects.

4.4.2: Fresnel-Kirchhoff Diffraction Theory

This theory arises from the original supposition by Huygens that the field at a given point arising from any source can be considered as the superposition of contributions from a series of virtual secondary sources located on the wavefronts of the original source. Fresnel subsequently made calculations using the theory, which was then made mathematically more rigorous by Kirchhoff [Born,1980],p.370.

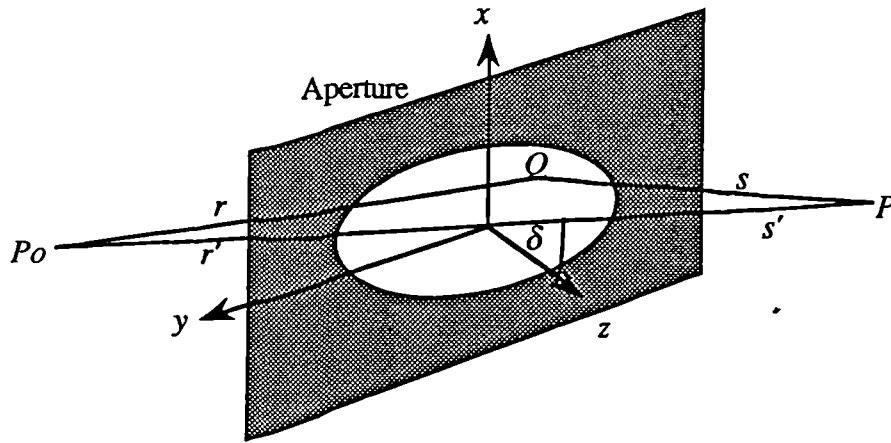


Figure 4.5 : *Huygens-Fresnel diffraction*

The field at a point P in figure 4.5 arises from the superposition of a number of secondary sources located across a surface, known as the **aperture**, located between P and the source at P_0 . These secondary sources are determined from the incident field at the aperture. The theory is embodied mathematically in the following **Fresnel-Kirchhoff** diffraction integral [Born,1980],p382 :

$$U(P) = -\frac{Aj}{\lambda} \frac{\cos \delta}{r' s'} \iint_{Ap} \cdot \exp(jk(r+s)) dS$$

where the quantities are defined in figure 4.5 and the incident field is that of a point source at P_0 , so :

$$U^{(i)} = \frac{A \exp(jkr)}{r}$$

This formulation assumes that the distances of P_0 and P from the aperture are large compared to the linear dimensions of the aperture. The integration is over the aperture Ap and may be regarded as an infinite sum of point sources located on Ap at points such as Q . It may be derived from the scalar wave equation using Green's theorem.

The aperture is chosen as the xy -plane, with the x direction being the projection of $P_0 P$ onto the aperture. The integral can then be rewritten as $U(P) = B \cdot (C + j S)$, where :

$$C = \int dx \int dy_{Ap} \cos \left\{ \frac{\pi}{\lambda} \left(\frac{1}{r'} + \frac{1}{s'} \right) (x^2 \cos^2 \delta + y^2) \right\}$$

$$S = \int dx \int dy_{Ap} \sin \left\{ \frac{\pi}{\lambda} \left(\frac{1}{r'} + \frac{1}{s'} \right) (x^2 \cos^2 \delta + y^2) \right\}$$

$$B = -A \frac{j}{\lambda} \cos \delta \frac{\exp \{jk(r' + s')\}}{r' s'}$$

Now a change of variable from (x, y) to (u, v) is introduced:

$$\frac{\pi}{\lambda} \left(\frac{1}{r'} + \frac{1}{s'} \right) x^2 \cos^2 \delta = \frac{\pi}{2} u^2$$

$$\frac{\pi}{\lambda} \left(\frac{1}{r'} + \frac{1}{s'} \right) y^2 = \frac{\pi}{2} v^2$$

Then:

$$C = b \int_{Ap} du \int dv \cdot \cos \left\{ \frac{\pi}{2} (u^2 + v^2) \right\}$$

$$S = b \int_{Ap} du \int dv \cdot \sin \left\{ \frac{\pi}{2} (u^2 + v^2) \right\}$$

$$\text{where } b = \frac{\lambda}{2 \left(\frac{1}{r'} + \frac{1}{s'} \right) \cos \delta}$$

The domain of integration is now Ap' , the transformation of Ap from the xy -plane into the uv -plane. The above expressions can, in principle, now be applied to any aperture shape.

4.4.3: Modelling Assumptions - The half plane

It is now necessary to choose an appropriate aperture shape for the building diffraction problem. In effect, the building will be represented by a **canonical scatterer**. This is an idealised shape for which the corresponding diffraction problem has been solved : The set of such problems includes single scattering by conducting and dielectric wedges and cylinders, together with a small class of multiple scattering problems involving these scatterers. In the single building case a very simple shape will be used, the absorbing **half-plane**, more often called a **knife-edge** in propagation applications. Both terms will be used interchangeably throughout this report. This is a screen of negligible thickness, with an edge of infinite lateral extent. Above the edge energy may propagate freely, while below it no energy at all propagates through the screen. Using such a representation implies certain assumptions about the characteristics of the building being modelled and these should be examined here:

Assumptions:

- The building rooftop may be represented by a single diffracting edge. Although this assumption is more exactly valid for a pointed rooftop than for a flat one, appropriate choice of the edge position makes the error small.
- The edge width is infinite and transverse to the direction of propagation, implying that no energy can propagate around the sides of the building. At high frequencies diffraction is a localised phenomenon, so extending the edge width beyond the diameter of the first few Fresnel zones (see §4.4.6) will have little effect. In the case of terraced houses the infinite width assumption is well justified. Over reasonable path lengths even detached buildings will act in a similar way since previous buildings will block energy arrival at a vertical edge. Work has been performed by [Gong,1991] on solutions for a truncated edge, but the extra complexity of a solution is unlikely to be justified by improved prediction accuracy.
- No energy propagates through the building. This will depend to some extent upon building materials and construction, but for most buildings the assumption is likely to be

justified even at relatively low VHF frequencies. In any case, the energy propagated through the building will be far smaller than the diffracted field.

- Forward diffraction only is calculated. This assumption is valid on the grounds of the diffraction angles involved, since backward diffraction from subsequent buildings along the path will produce a far smaller field. The only exception to this would be in the unusual case of multiple diffraction between very closely spaced buildings, but this possibility is discounted here.

- Diffraction at the final building may be separated from any effects of the buildings nearer to the base station. Later chapters will discuss this point further, but the assumption is valid provided the height of the buildings is reasonably uniform. Non-uniform building heights will also be considered.

The ultimate justification for any of these assumptions is whether the resulting theory successfully predicts measured effects, which will be found true in this case.

4.4.4: Fresnel Integrals

Here the Fresnel integrals are defined, since they are needed for the half-plane analysis and will be used frequently in later results. Many definitions have been used by various authors, but here the most common and widely used definitions from [Abramowitz,1970],p.300 are adopted:

$$\text{The Fresnel cosine integral : } C(w) = \int_0^w \cos\left(\frac{\pi}{2} \tau^2\right) d\tau$$

$$\text{The Fresnel sine integral : } S(w) = \int_0^w \sin\left(\frac{\pi}{2} \tau^2\right) d\tau$$

The integrals are usually evaluated using a series expansion [Abramowitz,1970],p.301 or, as here, via a standard library algorithm, [NAG,S20ACF] which uses Tchebychev polynomials. The forms of $C(w)$ and $S(w)$ are plotted in figure 4.6 for positive values of w .

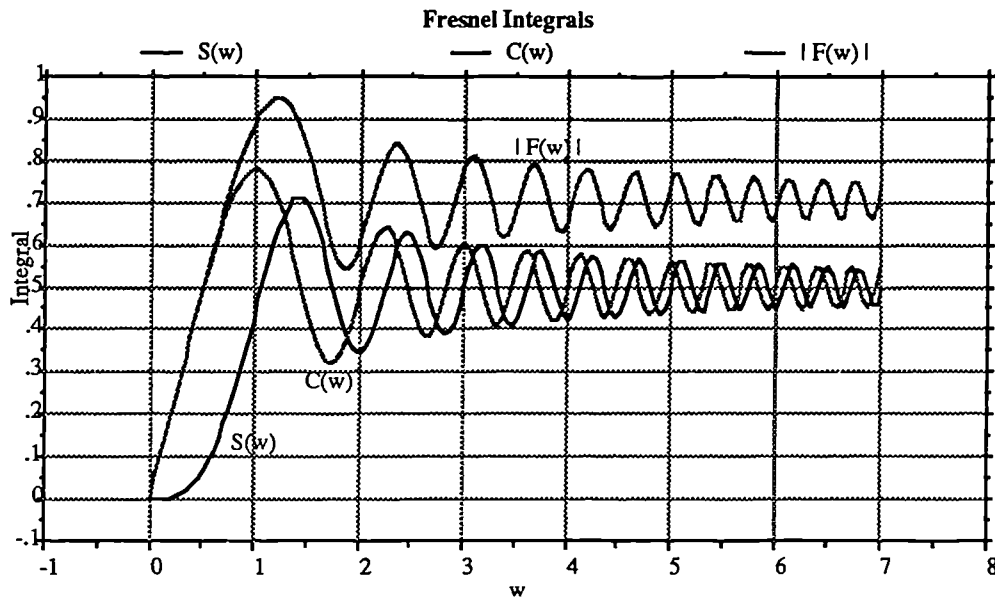


Figure 4.6: The Fresnel Integrals

Note that both integrals settle to a constant value for large w :

$$C(\infty) = S(\infty) = \frac{1}{2}$$

It is convenient to also define a complex Fresnel integral :

$$F(w) = C(w) + jS(w) = \int_0^w \exp\left(j \frac{\pi}{2} \tau^2\right) d\tau$$

$$F(\infty) = \frac{1+j}{2}$$

The path of integration here is along the real axis, but may be deformed to any oblique half-line through the origin. The magnitude of $F(w)$ is also plotted in figure 4.6.

To calculate the integrals for negative values of w , the following symmetry relations are used:

$$C(-w) = -C(w); S(-w) = -S(w)$$

Using integration by parts the following asymptotic representations for $F(w)$ may be derived and will be used later:

$$\text{If } w \text{ is positive, } F(w) = \sqrt{\frac{j}{2}} - \frac{j \exp\left(\frac{j\pi w^2}{2}\right)}{w\pi} + O\left(\frac{1}{w^3}\right)$$

$$\text{If } w \text{ is negative, } F(w) = -\sqrt{\frac{j}{2}} - \frac{j \exp\left(\frac{j\pi w^2}{2}\right)}{w\pi} + O\left(\frac{1}{w^3}\right)$$

4.4.5: Single Half-Plane Diffraction

The geometry of the half-plane is shown in figure 4.7.

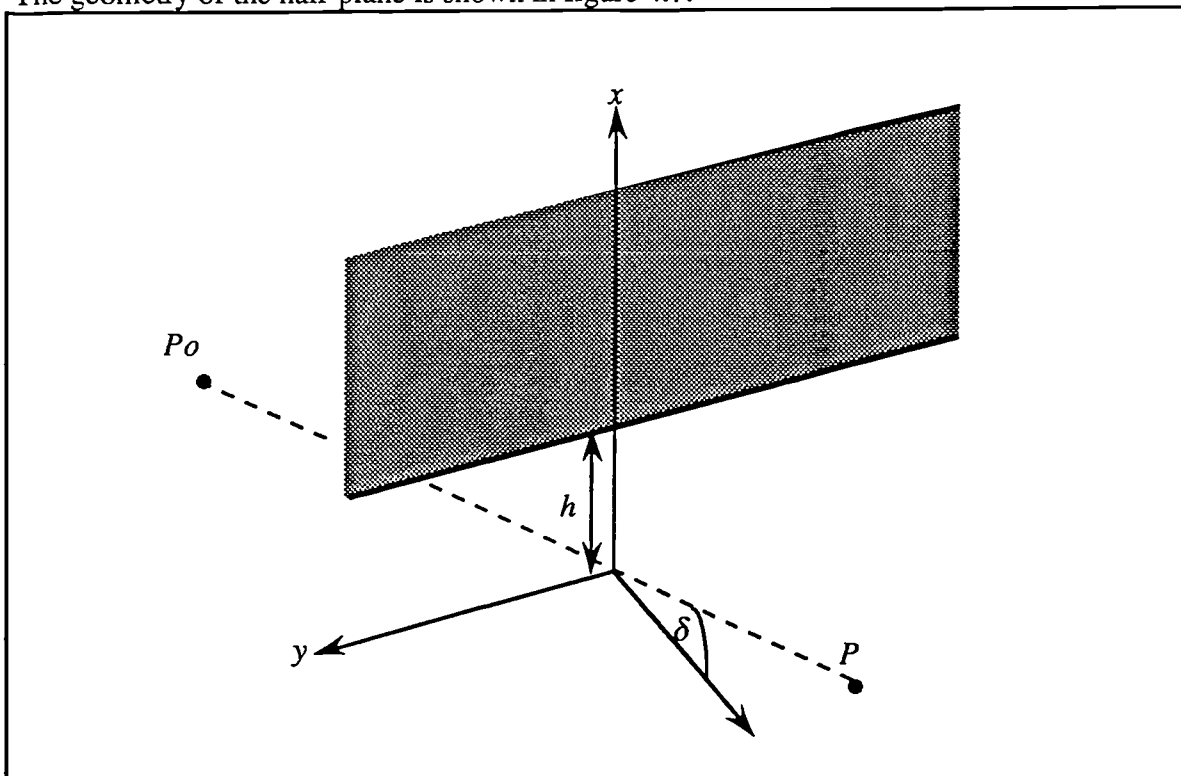


Figure 4.7: Half plane geometry

In this case, the aperture is the whole of the xy -plane not occupied by the half-plane, so A_p is defined by: $-\infty < x < h, -\infty < y < \infty$. Note that h is negative when P is in the shadow

region and that the line PoP is perpendicular to the edge. As before, δ is the angle between PoP and the normal to the half-plane.

This transforms into Ap' : $-\infty < u < w$, $-\infty < v < \infty$, where:

$$w = h \cos \delta \sqrt{\frac{2}{\lambda} \left(\frac{1}{r'} + \frac{1}{s'} \right)}$$

Hence:

$$C = b \int_{-\infty}^w du \int_{-\infty}^{\infty} dv \left\{ \cos \left(\frac{\pi}{2} u^2 \right) \cos \left(\frac{\pi}{2} v^2 \right) - \sin \left(\frac{\pi}{2} u^2 \right) \sin \left(\frac{\pi}{2} v^2 \right) \right\}$$

$$S = b \int_{-\infty}^w du \int_{-\infty}^{\infty} dv \left\{ \sin \left(\frac{\pi}{2} u^2 \right) \cos \left(\frac{\pi}{2} v^2 \right) + \cos \left(\frac{\pi}{2} u^2 \right) \sin \left(\frac{\pi}{2} v^2 \right) \right\}$$

Using the definitions given previously for the Fresnel integrals these results may be expressed as:

$$C = b \left\{ \left[\frac{1}{2} + C(w) \right] - \left[\frac{1}{2} + S(w) \right] \right\}$$

$$S = b \left\{ \left[\frac{1}{2} + C(w) \right] + \left[\frac{1}{2} + S(w) \right] \right\}$$

The field may now be expressed relative to the incident field at P (the field at P in the absence of the edge):

$$\frac{U(P)}{U^{(i)}(P)} = \frac{B(C + jS)}{\left\{ \frac{A \exp(jk(r' + s'))}{(r' + s')} \right\}}$$

$$= \frac{\exp\left(-j \frac{\pi}{4}\right)}{\sqrt{2}} (C(w) + jS(w)) + \frac{1}{2}$$

$$= \frac{F(w) \exp\left(-j \frac{\pi}{4}\right)}{\sqrt{2}} + \frac{1}{2} = A_{hp}$$

where A_{hp} is the half-plane attenuation function and will be used extensively later on.

In propagation prediction applications, the geometry of the situation is likely to resemble figure 4.8, where the half-plane represents the peak of a hill or, in this case, a building rooftop.

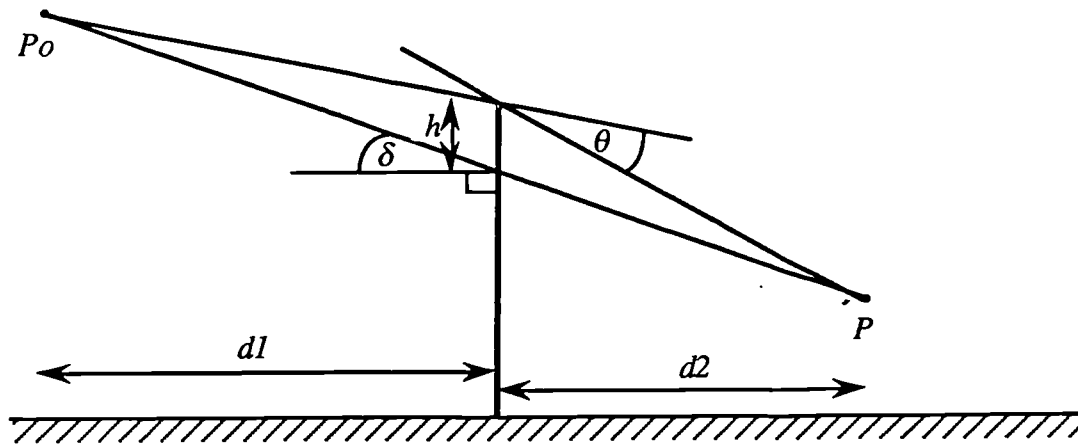


Figure 4.8: Practical half plane diffraction

It is then desirable to express the parameter w in terms of the diffraction angle θ (negative as illustrated) and the distances d_1 and d_2 . If these distances are assumed large compared with the vertical heights, then $\delta \approx 0^\circ$ and

$$w \approx \theta \sqrt{\frac{2}{\lambda \left(\frac{1}{d_1} + \frac{1}{d_2} \right)}}$$

Figure 4.9 illustrates the result of plotting the diffracted field as the height of P is varied. Here $d_1 \rightarrow \infty$ and $d_2 = 10\lambda$.

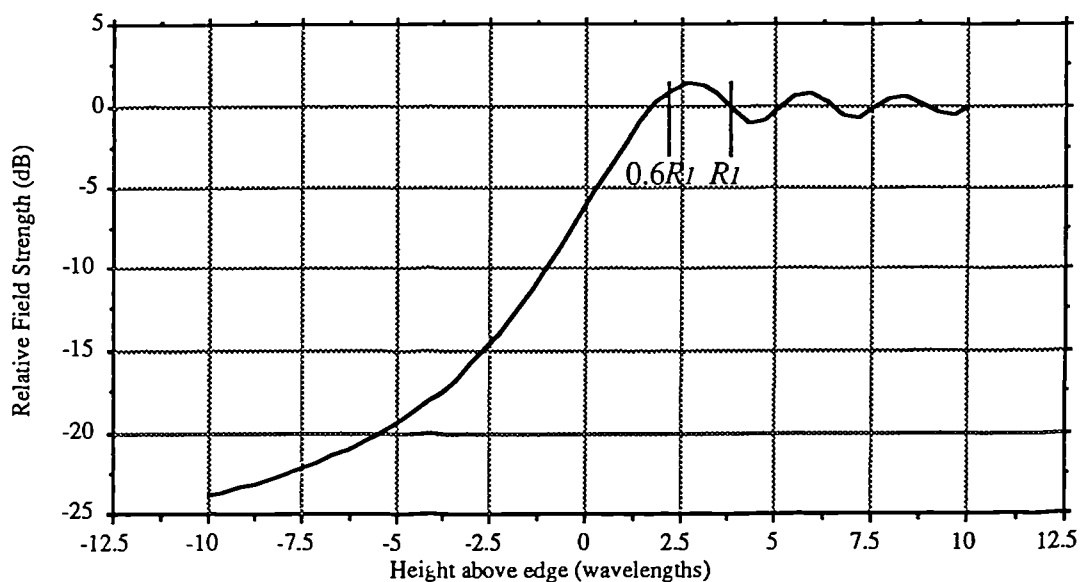


Figure 4.9: Half plane diffraction pattern

The field diminishes monotonically as P is moved below the edge ($h < 0$): when P is just above the edge there is the possibility of an **obstacle gain**, or enhancement of the field relative to the free space level. In terrain diffraction applications this possibility is usually

discounted, since the large radii of curvature usually encountered at hilltops tend to mask this effect. In building diffraction cases, however, such effects may be significant, particularly when the analysis is extended to multiple buildings as in Chapter Six.

4.4.6: Fresnel Zones

A normalisation of the diffraction parameter, w , produces the concept of **Fresnel Zones**, which is also useful for visualising the properties of the field. These are zones bounded by ellipsoids with foci at the source and field points P_o and P , defined such that a point F on the Fresnel ellipsoids satisfies the relation:

$$P_o F + F P = P_o P + \frac{n \lambda}{2}; n = 1, 2, \dots$$

where n denotes the order of the zone. An example is shown in figure 4.10. Under the usual assumption that vertical heights are much smaller than horizontal distances it can be shown that:

$$R_n \approx \sqrt{\frac{n \lambda d_1 d_2}{d_1 + d_2}}$$

using the same notation as in figure 4.8. Later on an expression for the Fresnel zone in the case of a very distant source will be needed. In such a case, $d_1 \rightarrow \infty$ and :

$$R_n = \sqrt{n \lambda d_2}$$

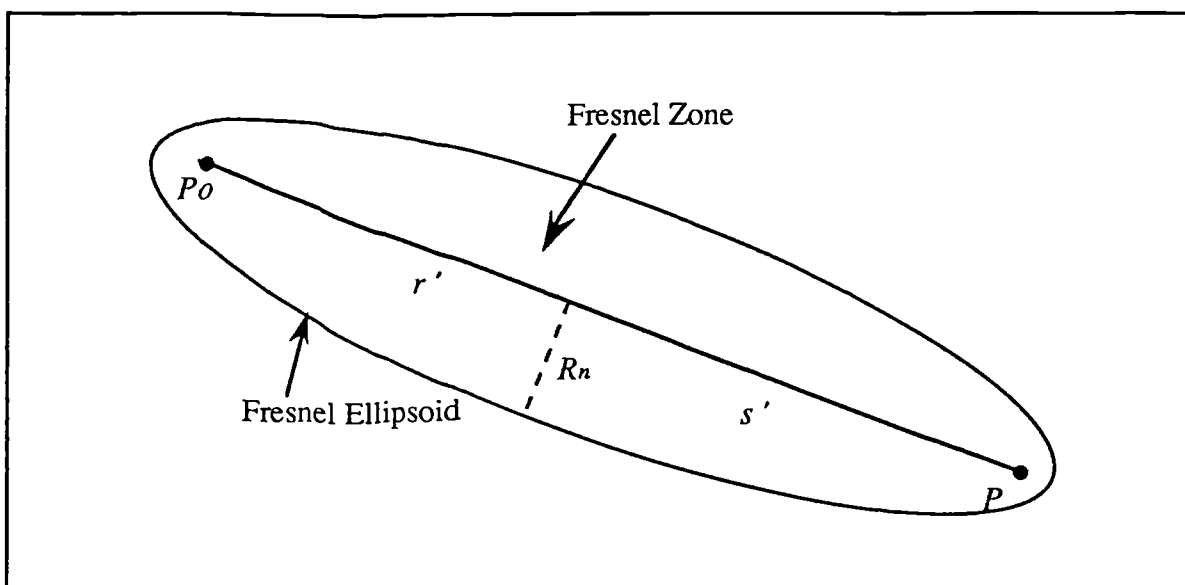


Figure 4.10: Fresnel zones

The diffraction parameter w can then be expressed in terms of the Fresnel zone radius:

$$w = \frac{\theta \sqrt{2} R_1}{\lambda} = \frac{\theta R_2}{\lambda}$$

$$\text{or } w = \frac{x \sqrt{2}}{R_1} = \frac{2x}{R_2}$$

The diffraction parameter is therefore a measure of the fractional obstruction of the Fresnel Zone, positive values representing edges which do not obstruct the line-of-sight ($P_0 P$). A common criterion for an 'unobstructed' propagation path is that 0.6 of the first Fresnel zone radius be clear. Figure 4.9 shows the field strengths corresponding to R_1 and $0.6 R_1$.

4.5: Analysis of Direct and Reflected Ray Diffraction

Using the tool for half-plane diffraction developed above, a simple but important analysis of building diffraction will now be attempted. It is assumed that close to the mobile terminal, propagation may be represented by two *main* rays. The first of these is diffracted from the rooftop of the building nearest the mobile in the direction of the base station (the direct-diffracted or d-d ray), while the second is reflected from the face of the building across the street (the diffracted-reflected or d-r ray). This process is illustrated in figure 4.11.

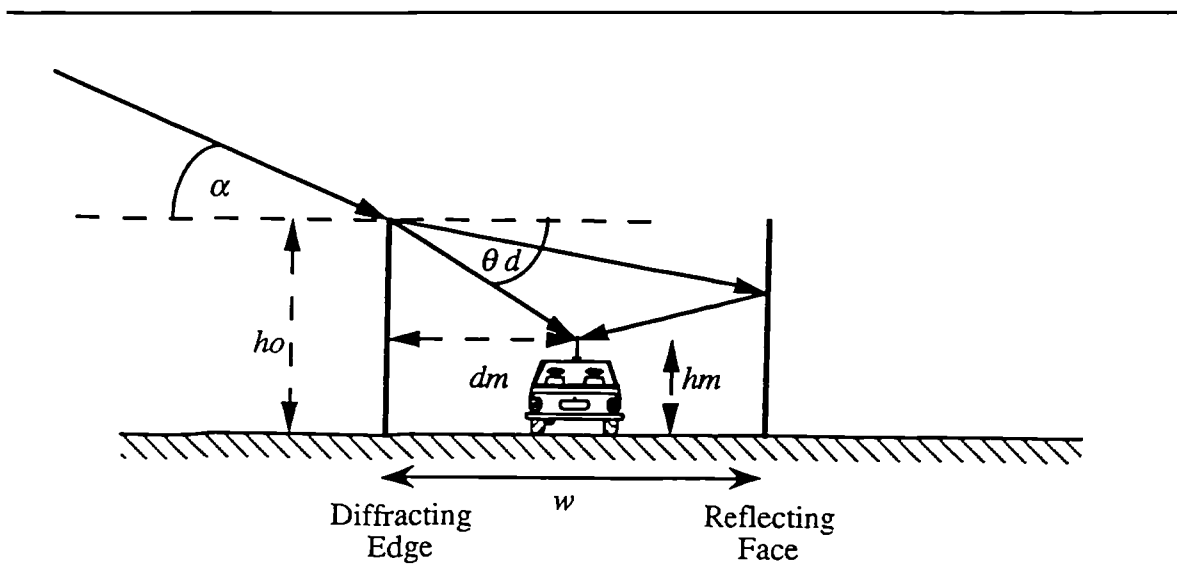


Figure 4.11: Ray arrival at the mobile

The result used is therefore :

$$A_{d,r} = \frac{F(w_{d,r}) \exp\left(-\frac{j\pi}{4}\right)}{\sqrt{2}} + \frac{1}{2}$$

where $A_{d,r}$ represents the amplitudes of the d-d and d-r rays respectively.

In the case of the d-d ray the Fresnel diffraction parameter is given by :

$$w_d = -\theta_d \sqrt{\frac{2}{\lambda \left(\frac{1}{d_1} + \frac{1}{d_m}\right)}}$$

with $\theta_d = \frac{\pi}{2} - \tan^{-1}\left(\frac{d_m}{h_o - h_m}\right) - \alpha$

Here d_1 represents the distance of the effective source from the building rooftop. For plane wave incidence, $d_1 \rightarrow \infty$. If it is further assumed that $\alpha \ll \theta_d$ then :

$$\text{Direct ray: } w_d = -\left[\frac{\pi}{2} - \tan^{-1}\left(\frac{d_m}{h_o - h_m}\right)\right] \sqrt{\frac{2d_m}{\lambda}}$$

In exactly the same manner the diffraction parameter for the d-r ray is found to be:

$$\text{Reflected ray: } w_r = -\left[\frac{\pi}{2} - \tan^{-1}\left(\frac{2w - d_m}{h_o - h_m}\right)\right] \sqrt{\frac{2(2w - d_m)}{\lambda}}$$

The direct-diffracted ray is diffracted through the larger angle and is therefore subject to greater attenuation than the other ray. However, the diffracted-reflected ray is also attenuated by the reflection coefficient of the building face, so it has been suggested [Walfisch, 1988] that it is appropriate to consider both rays as being of equal magnitude. The total median field strength would then be simply the field strength of the direct ray multiplied by $\sqrt{2}$. This suggestion is now examined and compared with the use of the more complete paradigm discussed in §4.2. In the latter case the median field strength is given by:

$$|U| = \sqrt{A_d^2 + (\rho A_r)^2}$$

The aim next is to investigate, on the basis of this model, how field strength may be expected to vary across the street and as the relative height of the buildings and the mobile antenna is varied. The reflection coefficient of the building face (ρ) is assumed to be 0.5, independent of the angle of incidence. This has been found representative for concrete walls by [Mitobe,1974]. Comparisons are made here at 900MHz.

In figure 4.12 the variation of the field with the mobile antenna height is examined, with the mobile at the centre of the street. The significant parameter here is $(h_o - h_m)$, so the same variation may be expected if building height is varied. System parameters are $h_o = 10\text{m}$, $d_m = 20\text{m}$, $w = 40\text{m}$ and $f_c = 900\text{MHz}$. The field strength increases smoothly as h_m increases and both representations predict a similar variation. However a small, approximately constant error of slightly more than 1dB exists, however, with the single ray approximation suggesting a higher field. This may be an acceptable error in some cases.

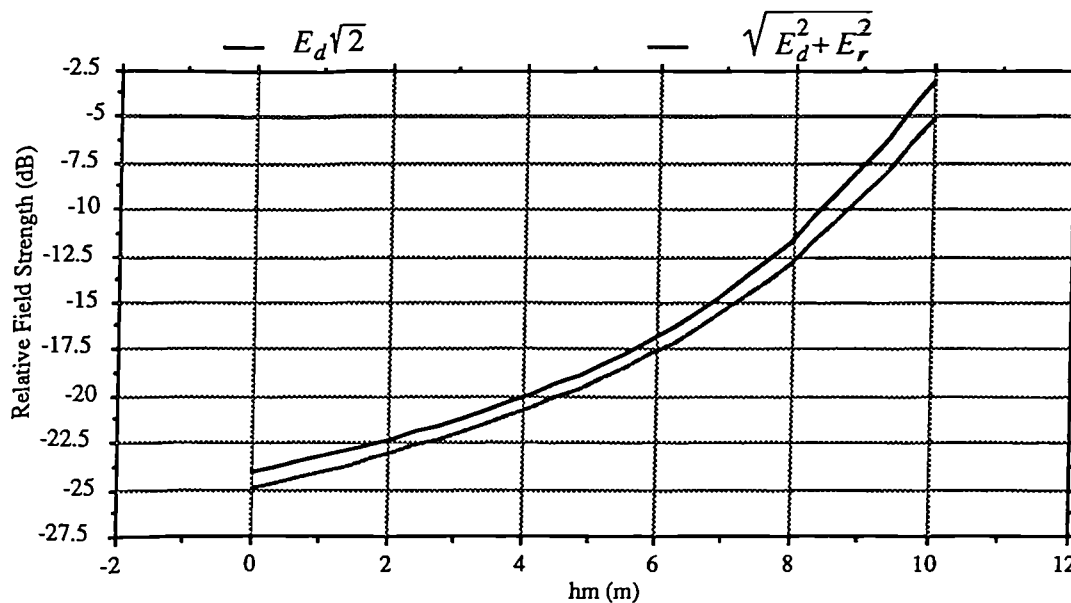


Figure 4.12: Knife edge model of mobile antenna height gain

Figure 4.13 shows the corresponding variation as the mobile is moved across the street, with $h_m = 1.5\text{m}$. Both curves predict a field minimum near to the diffracting building, but the two-ray representation predicts a rather shallower variation, and significant differences in predicted field strength are evident at some places.

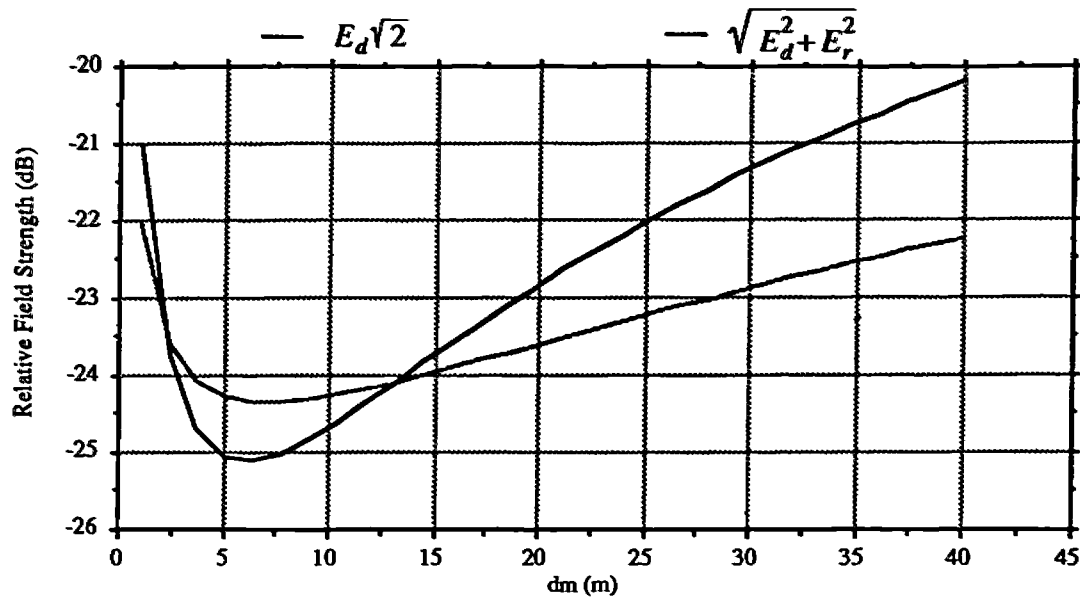


Figure 4.13: Knife edge model of mobile positioning on street

Measurements [Ikegami,1984] have suggested that field strength varies relatively little across a street, so the two ray model is to be preferred on these grounds as well as for analytic completeness. It is likely that the predicted minimum would not be noticed in most measurements, since these would only probe the field across the road width rather than across the entire space between adjacent buildings.

It is concluded that both rays should be included in modelling whenever the extra computation required is not prohibitive, although the single ray approach may be acceptable in some cases.

For a more practical comparison, figure 4.14 compares the two-ray knife edge model with the measured mobile antenna height gain factor, $a(h_m)$ for suburban areas from [Okumura,1968]. The parameters used in the comparison, considered typical for a suburban environment, were: $h_o = 8\text{m}$, $d_m = 20\text{m}$, $w = 40\text{m}$ and $f_c = 900\text{MHz}$. Good agreement between the two curves is evident. The empirical curve does not reveal the full structure of the field variation since it results from averaging measurements over a large number of locations, at each of which the building height, mobile positioning and other factors will vary.

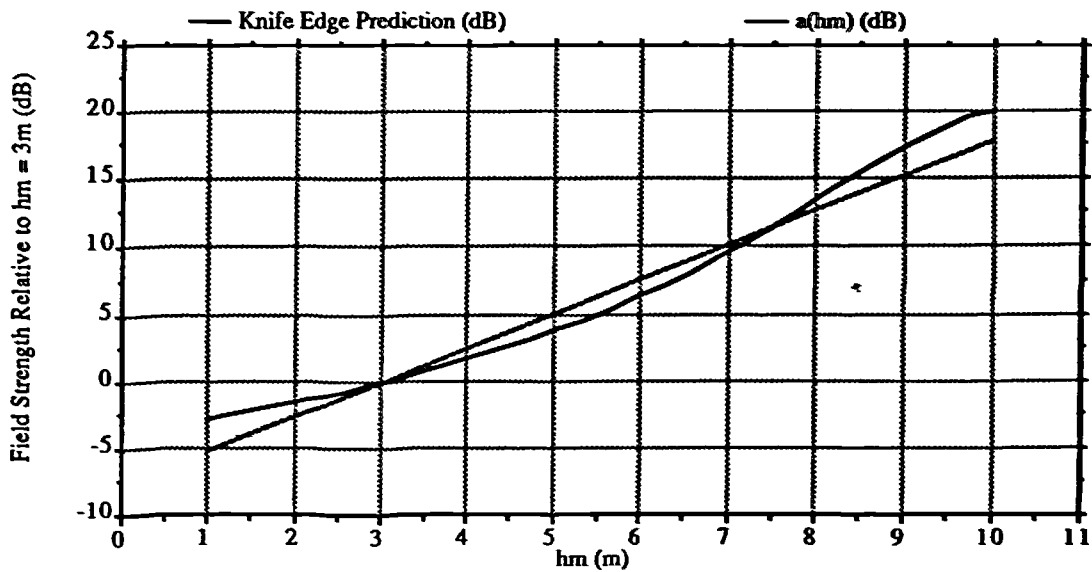


Figure 4.14: Comparison of knife edge model with empirical data.

It is reasonable to conclude that the two-ray knife edge model accounts for observed variations in signal at the mobile terminal with good accuracy.

4.6: Summary

In this chapter the feasibility of theoretical modelling of propagation in built-up areas was asserted by reference to measurements and calculations, while the assumptions necessary for the use of such theory were justified. The principles of modelling have been introduced and shown to produce useful results, even using only simple theory. Subsequent chapters will use these principles to produce models of more realistic situations.

Chapter Five

Ray Methods

5.1: Geometrical Optics

Here the concepts of geometrical optics are briefly explained as background to the geometrical theory of diffraction, which will be found well suited to analysing building diffraction in many cases.

Geometrical optics is an approximate method of analysis of electromagnetic fields, having its roots in classical theories of light propagation. Energy is assumed to propagate along narrow beams or rays which are easy to determine and which have considerable appeal in helping to visualise the mechanisms of propagation.

When a ray impinges on a smooth surface, it is reflected at a point of reflection which is such as to make the total path length APB a minimum (see figure 5.1).

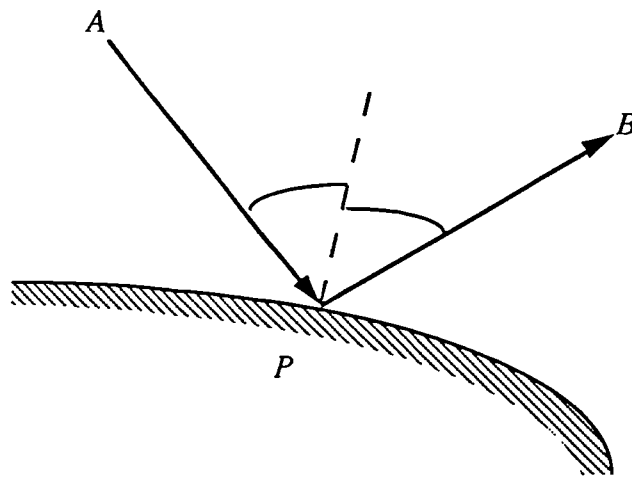


Figure 5.1: Reflection according to Fermat's principle

This is an example of Fermat's principle (the principle of least time), which states that the

total optical path length $S(C)$ of a ray path C is stationary with respect to small variations in C . The path length is defined as:

$$S(C) = \int_C n \, d\sigma$$

where the refractive index, n , is a function of position, σ . If n is constant, then rays travel in straight lines. This is a reasonable assumption for tropospheric radio wave propagation over small paths, but for longer ranges the vertical lapse rate of temperature causes n to decrease with height, so that rays tend to curve towards the earth's surface when launched horizontally. This effect is usually accounted for by drawing path profiles with an effective earth radius rather larger than its true value, allowing straight line ray tracing to be carried out.

Classically, the theory of geometrical optics neglects the wave nature and the polarisation of the field, but these may be included by treating ray theory as an asymptotic (high-frequency) solution to Maxwell's equations (see, for example, [Kouyoumjian, 1975] p.166). If the electric field is represented as a Luneberg-Kline expansion in decreasing powers of frequency, then Maxwell's equations result in the following asymptotic representation, assuming that the frequency is high enough to justify retaining only the first term of the expansion:

$$E(s) = E_o(0) \exp(-jk\psi(0)) \sqrt{\frac{\rho_1 \rho_2}{(\rho_1 + s)(\rho_2 + s)}} \exp(-jks) \quad (5.1)$$

Here s is the distance measured along the ray path from a reference point and ρ_1 and ρ_2 are the principal radii of curvature of the wavefront at $s=0$. $\psi(s)$ is the phase function which describes the ray trajectory in accordance with the eikonal equation, which is essentially an expression of Fermat's principle :

$$|\nabla\psi|^2 = n^2$$

and $E_o(0)$ is the reference field strength at $s=0$. The quantity under the square root in equation (5.1) is the divergence factor, which can be interpreted as expressing the principle of conservation of energy within a narrow tube of rays, as illustrated in figure 5.2.

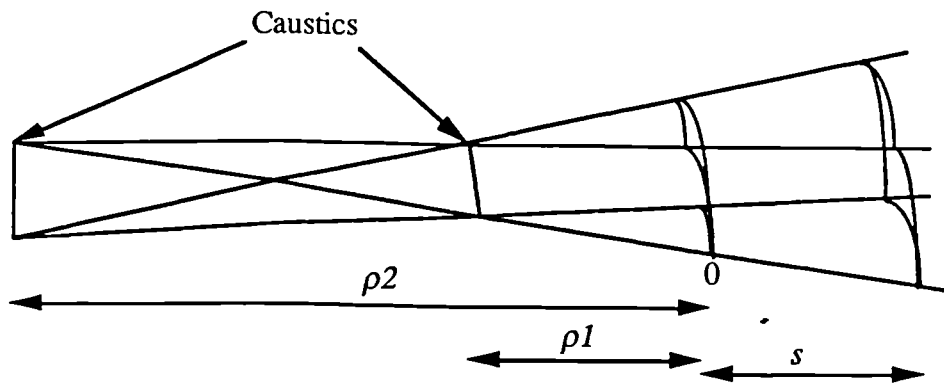


Figure 5.2: Astigmatic ray pencil

This allows a very general representation of a ray as an **astigmatic ray pencil** which has caustics at $s = -\rho_1$ and $s = -\rho_2$. The divergence factor allows the intensity of the ray to be determined at all values of s except at the caustics, where ray theory breaks down since the asymptotic assumptions are violated.

Finally, the Maxwell curl equation allows the corresponding representation of the magnetic field to be determined:

$$\mathbf{H} = \frac{\hat{\mathbf{s}} \times \mathbf{E}}{Z_c}$$

where $\hat{\mathbf{s}}$ is a unit vector along the ray in the direction of propagation and Z_c

is the characteristic impedance of the medium. This expression shows that the geometric optics field can be regarded as behaving locally as a plane wave. This enables plane wave analysis to be used to determine ray reflection and refraction properties, which has been used classically in the design of optical systems. Only more recently, however, has such an approach been possible in the case of diffracted fields, which is our main interest.

5.2: The Geometrical Theory of Diffraction

5.2.1: Introduction

The geometrical theory of diffraction, or GTD was first devised by Joseph Keller in the 1950s [Keller,1962]. In the past, GTD has been applied mainly to the analysis of small shapes such as antennas, or for calculating the radar cross sections of complex objects. More recently it has been successfully applied to terrain modelling [Luebbers,1984]. In this chapter GTD will be used for predicting the effects of building shape and orientation. Some previous work has been carried out in this field by [Lebherz,1991b].

The central idea of GTD is that an extended version of Fermat's principle may be used to predict the existence of diffracted rays, which may then be treated with the ease of any other ray in geometrical optics. Figure 5.3 shows a ray obliquely incident upon the edge of an obstacle at an angle θ_o to the edge. Fermat's principle for edge diffraction predicts that a cone of diffracted rays will be produced, where the cone has semi-angle θ_o . In the simpler case of normal incidence $\theta_o = \pi/2$ and the cone reduces to a disc.

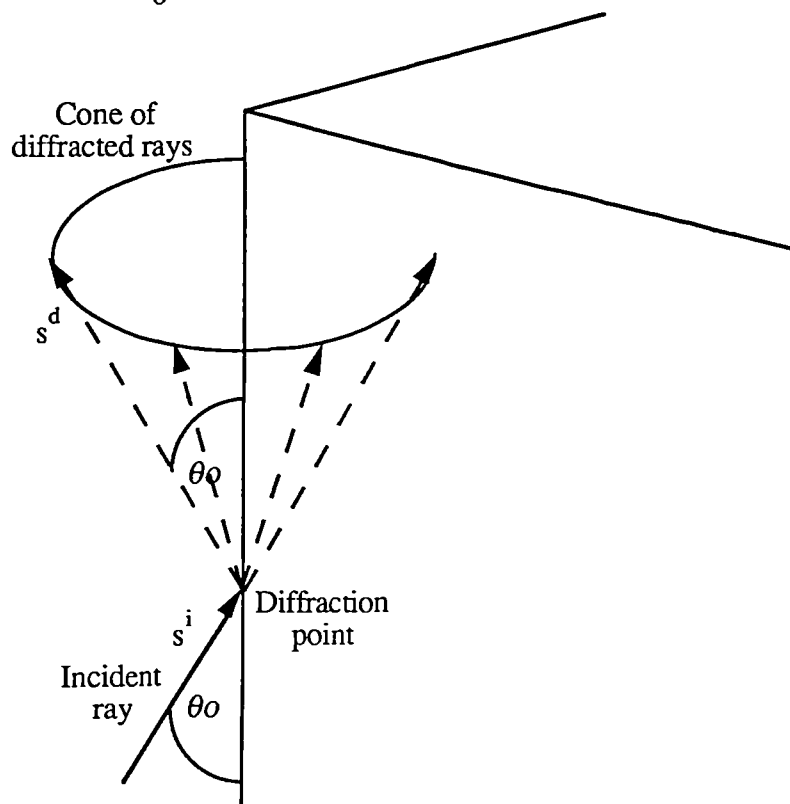


Figure 5.3: The generation of edge diffracted rays

Once the diffracting point is determined, the diffracted field is given by:

$$\begin{pmatrix} E_z^d \\ H_z^d \end{pmatrix} = \begin{pmatrix} E_z^i D^e \\ H_z^i D^m \end{pmatrix} \sqrt{\frac{\rho}{s(\rho+s)}} \exp(-jks)$$

which is of the same form as (5.1). In this expression ρ is the distance between the caustics of the diffracted field. In the two-dimensional problems considered here $\rho = \infty$, so :

$$\begin{pmatrix} E_z^d \\ H_z^d \end{pmatrix} = \begin{pmatrix} E_z^i D^e \\ H_z^i D^m \end{pmatrix} \frac{\exp(-jks)}{\sqrt{s}}$$

and the field appears to emanate from a line source situated along the edge with polar diagram modified by D^e and D^m . These are the **diffraction coefficients** describing the diffraction characteristics of the scatterer at the point of diffraction, assuming that the frequency is high enough that the diffraction characteristics can be determined with regard to local characteristics only, rather than by those of the entire scatterer. Thus, in the case of building rooftop diffraction, once the diffraction point has been determined, only the characteristics of the building at that point are significant rather than across its entire geometry, greatly easing the data requirement and the complexity of the calculation.

An analysis of a given structure using GTD therefore takes place in three stages:

- i) Ray Tracing : Fermat's principle is used to calculate the trajectories of direct, reflected and diffracted rays between the source and field points. Although this is simple in principle, this stage is usually the most time consuming.
- ii) From the calculated ray paths appropriate diffraction and reflection parameters are calculated. These parameters include distances and diffraction/reflection angles.
- iii) Finally the amplitude of each of the ray fields is calculated using using the appropriate diffraction or reflection coefficients and the individual ray contributions are summed to produce a total prediction of the field strength at a given point.

In GTD, the diffraction coefficients are determined from one of a number of **canonical problems**. These are diffraction problems for simple scattering objects such as a half-plane, a wedge or a cone which have been solved using exact methods. The resulting solutions are reduced via asymptotic assumptions to the terms which correspond to a ray theoretical

description of the field. Such assumptions are only valid if the obstacle dimensions are large compared to a wavelength and if the spatial variation of the scattered field is not too rapid. Despite these restrictions, GTD has been applied with reasonable accuracy to scatterers having dimensions comparable with a single wavelength [James,1980].

5.2.2: Wedge Diffraction

The canonical problem of particular interest here is the **wedge**, of which the half-plane is a special case. Figure 5.4 shows a perfectly conducting wedge with a ray incident upon it. The field component in the z - direction (E for *soft*, *Dirichlet* or *transverse electric* polarisation, H for *hard*, *Neumann*, or *transverse magnetic* polarisation) produces a diffracted ray in the same plane as the incident ray if oblique incidence ($\theta_o = \pi/2$) is assumed.

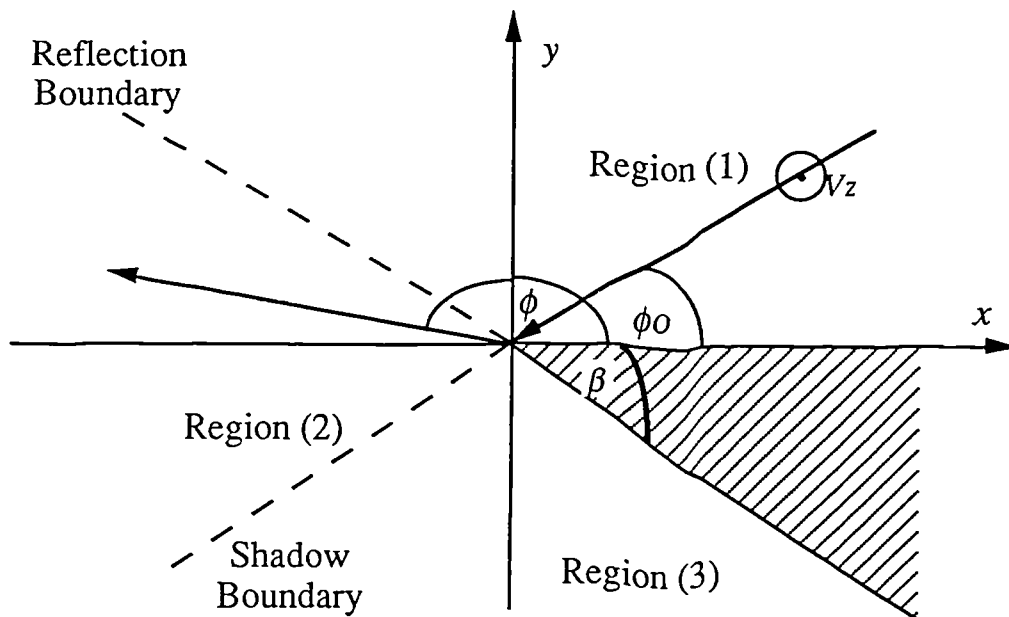


Figure 5.4: *Geometry for wedge diffraction*

There are three distinct regions to consider: in region (1) the field is composed of a direct component, an edge diffracted component and a component reflected from the upper face of the wedge. The total field is calculated as the superposition of these three rays. In region (2) the image of the source in the upper wedge face is no longer visible, so the reflected ray no

longer contributes. In region (3), the **shadow region**, the direct ray is blocked by the wedge, so only the diffracted ray can contribute. This is the most important region for mobile radio applications due to the absence of a line-of-sight path in most cases. Diffraction increases with diminishing frequency, accounting for the principally line-of-sight propagation modes encountered at microwave frequencies. The precise level of the diffracted ray will, however, depend upon the particular shape of the scatterer.

In the case of a perfectly conducting wedge, the GTD diffraction coefficients are given by [James,1980] as:

$$D_c^{e,m} = \frac{1}{N \sin \theta_o \sqrt{8\pi jk}} \left[\begin{array}{c} \left\{ \cot \left(\frac{\pi + \Phi^i}{2N} \right) + \cot \left(\frac{\pi - \Phi^i}{2N} \right) \right\} \\ \pm \left\{ \cot \left(\frac{\pi + \Phi^r}{2N} \right) + \cot \left(\frac{\pi - \Phi^r}{2N} \right) \right\} \end{array} \right]$$

with $\Phi^{i,r} = \phi \pm \phi_o$; $0 \leq \phi, \phi_o \leq 2\pi$; $N = \frac{2\pi - \beta}{\pi}$

where the quantities are defined in figure 5.4.

An algorithm was devised and constructed to enable arbitrary two dimensional building profiles to be entered, with the buildings represented by a series of wedges and/or half-planes. The algorithm traces direct and diffracted rays for single and double diffraction which reach the specified mobile position. Polarisation and source types can be varied as required. The algorithm was implemented in PASCAL for a SUN workstation. From this ray tracing the necessary diffraction parameters are calculated and field strengths can then be calculated as necessary.

5.2.3: Limitations of GTD - Uniform Theories

A limitation of the GTD approach is quickly manifest when plotting fields on or close to either of the geometrical boundaries shown in figure 5.4. The derivation of the GTD diffraction coefficient involves an asymptotic approximation to a modified Fresnel integral whose argument is $s = |a^{i,r}| \sqrt{k\rho}$ where:

$$a^{r,i} = \sqrt{2} \cos \frac{1}{2}(\phi \pm \phi_o)$$

and it is assumed that $s \rightarrow \infty$. This is invalid on each of the boundaries where one of the a terms becomes zero. Moreover, one of the cotangent terms in D_c becomes singular on each boundary. The regions within which s is too small for the asymptotic assumption to be valid (usually taken as $s \leq 2\sqrt{\pi}$) are the **transition regions** and are parabolic with the edge as their focus. On the optical boundaries themselves the field has plane wave characteristics, but elsewhere in the transition regions the field is in an intermediate state between plane and cylindrical behaviour. The general shape of the transition regions is shown in figure 5.5.

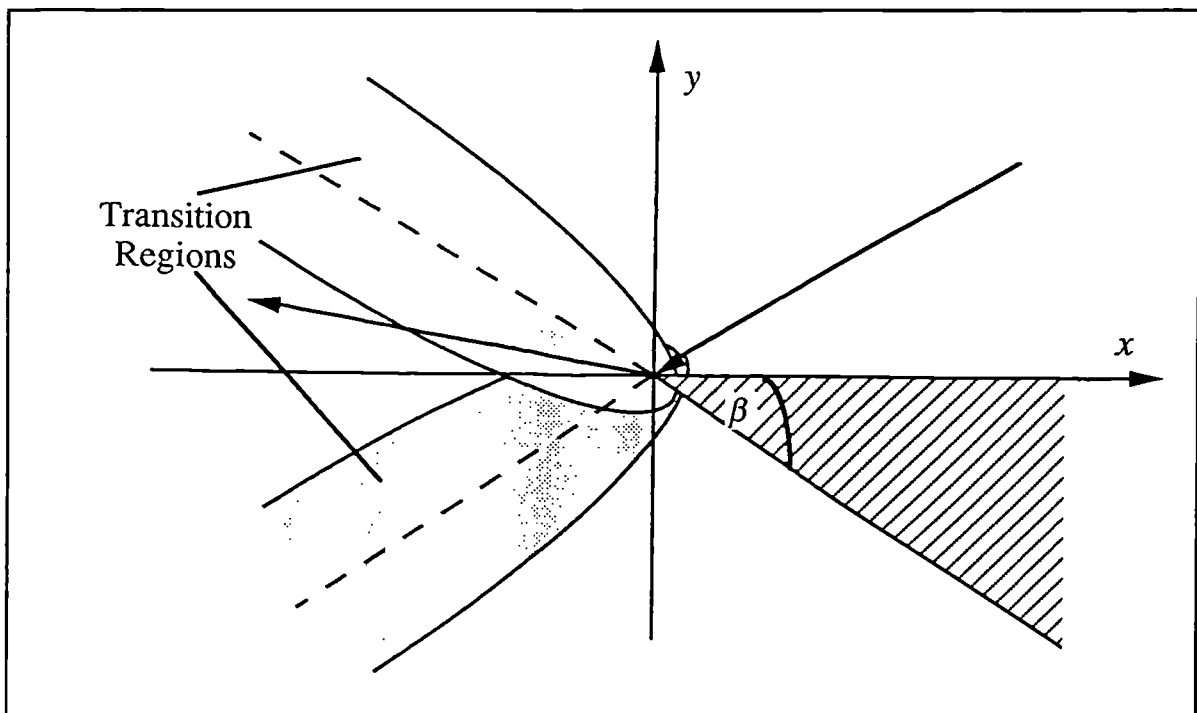


Figure 5.5: Transition regions

The difficulty is avoided by introducing the transition functions $F(X)$ to each of the GTD terms. These provide for the proper behaviour of the field inside the transition regions and cancel the singularities on each optical boundary ensuring that the field remains always finite.

This approach is the uniform geometrical theory of diffraction or **UTD** and was first suggested by [Kouyoumjian,1974]. The UTD wedge coefficient is given by:

$$D_u^{e,m} = \frac{1}{N \sin \theta_o \sqrt{8\pi j k}} \left[\begin{array}{c} \left\{ \cot \left(\frac{\pi + \Phi^i}{2N} \right) F \left[kLa^{\dagger}(\Phi^i) \right] + \cot \left(\frac{\pi - \Phi^i}{2N} \right) F \left[kLa^{\dagger}(\Phi^i) \right] \right\} \\ \pm \left\{ \cot \left(\frac{\pi + \Phi^r}{2N} \right) F \left[kLa^{\dagger}(\Phi^r) \right] + \cot \left(\frac{\pi - \Phi^r}{2N} \right) F \left[kLa^{\dagger}(\Phi^r) \right] \right\} \end{array} \right]$$

$$\text{where } F(X) = 2j\sqrt{X} \exp(jX) \int_{\sqrt{X}}^{\infty} \exp(-j\tau^2) d\tau$$

$$a^{\pm}(\Phi) = 2 \cos^2 \left(\frac{2n\pi I^{\pm} - \Phi}{2} \right)$$

and I^{\pm} are the integers which most nearly satisfy:

$$2\pi n I^{\pm} - \Phi = \pm\pi$$

$$L = s \sin^2 \theta_o \text{ for plane wave incidence}$$

Outside the transition regions, $F(X) \rightarrow 1$ and the diffraction coefficient is identical to the GTD case.

As an example of the use of UTD, the ray tracing algorithm previously mentioned is used to predict field strength contours for the two edge diffraction problem illustrated in figure 5.6, with results shown in figure 5.7. The units are wavelengths and the first edge, as in all of the examples which follow, is arbitrarily situated 10km away from the origin. Vertical polarisation is assumed, which is magnetic polarisation with respect to both of the edges in this situation.

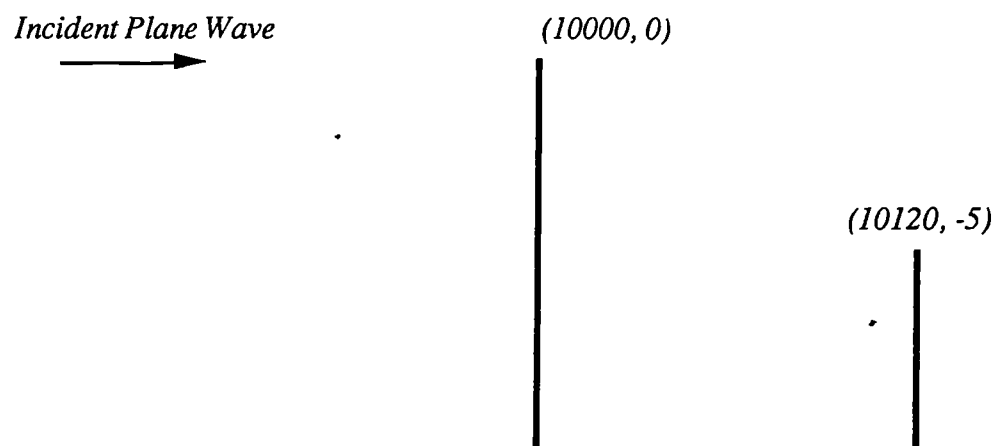
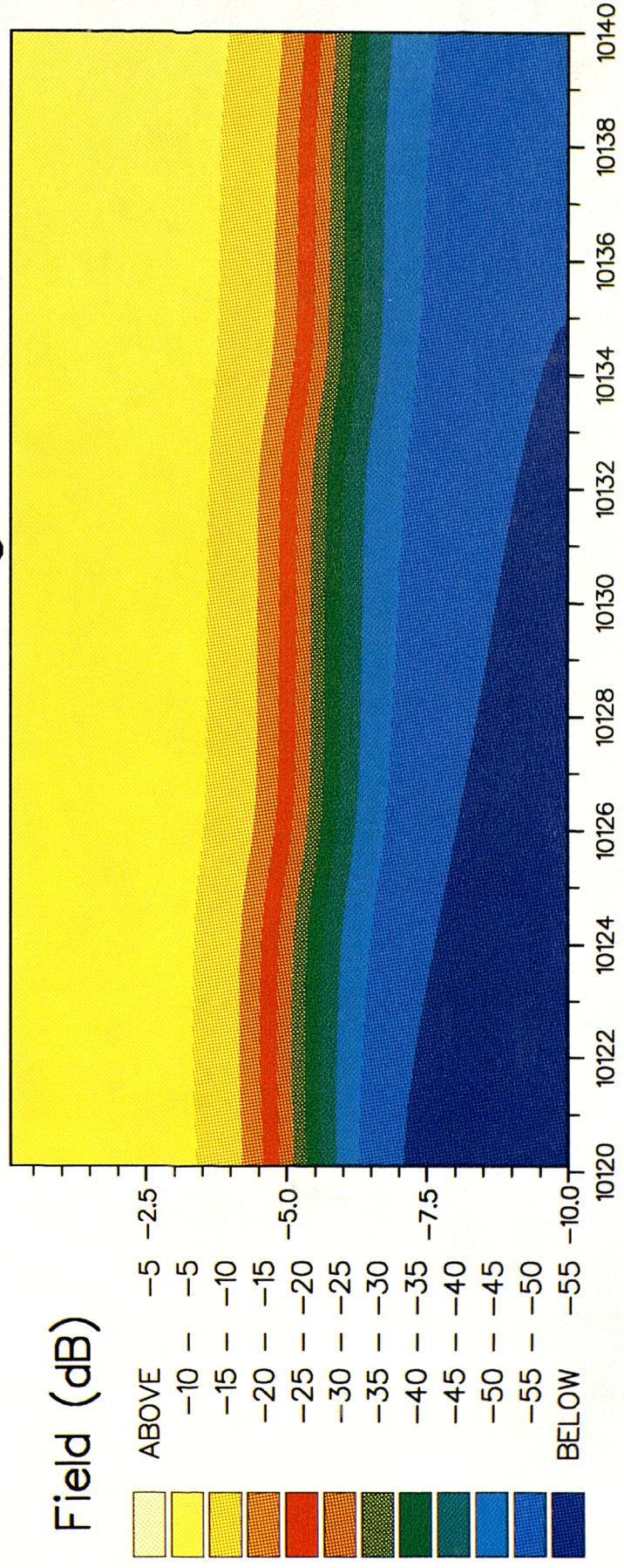


Figure 5.6: Example building diffraction geometry

Well above both edges a direct path exists so the field is close to its free-space value. At heights below the first edge but above the second, the field changes only slowly as a result of the slowly varying diffraction angle in the singly diffracted ray from the first edge. Lower down, however, this singly diffracted component is blocked and the total field arises only from a doubly diffracted ray emanating from the second edge. In the shadow of this edge the field strength diminishes rapidly. This illustrates the ease with which UTD may be applied in relatively complex diffraction problems, but also shows how rapid spatial field variation may be for multiply diffracted fields, especially in the vicinity of shadow boundaries.

UTD Field Strength Prediction



Rapid spatial field variation does result in complications when an edge is illuminated by the transition region field of a previous edge. In this case the spatial field variation is too rapid to permit use of the asymptotic assumptions of UTD so special methods must be applied. In these cases higher order terms in the series expansion of the field must be considered, resulting in the use of **slope diffraction coefficients** (see [Kouyoumjian,1975],p.180). This severely limits the usefulness of ray methods for multiple building diffraction problems when adjacent buildings are of similar heights. Authors such as [Tiberio,1984] have developed UTD methods for the case of two wedges illuminated at grazing incidence, but the methods are complex, losing the intuitive appeal of ray methods and are unlikely to be of use for more than two wedges.

Ray methods are therefore most useful for predicting the effects of the shape of a particular building, or the field around a complex arrangement of buildings of simple shapes rather than for predictions of propagation across large numbers of buildings. Notwithstanding these limitations, the diffraction algorithm constructed has been found particularly useful for rapid visualisation of the effect of varying building profiles.

5.3: Rooftop Diffraction

This section examines the application of ray theories to rooftop diffraction over buildings of various shapes. The main region of interest is the deep shadow region, since the mobile is located in this region for most practical situations. The field close to the shadow boundary is also of interest, however, since it reveals the influence of building shape on fields diffracted by successive rooftops in a multiple building situation.

5.3.1: Conducting Half Plane

As previously noted, the simplest canonical structure likely to be of use in representing building diffraction is the half-plane. Here the conducting half-plane is examined using ray theories. It differs from the absorbing half plane examined in Chapter Four in that it supports a reflected field. This field also has associated with it a diffracted field, which influences the field in regions beyond the reflection boundary to a small extent.

Figure 5.8 shows the field scattered by a conducting half-plane according to both the GTD and UTD solutions. Electric polarisation is used and the field point is moved around a circle ten wavelengths in radius, centred on the edge. Marked on the diagrams are the optical boundaries, with the regions as specified in figure 5.4.

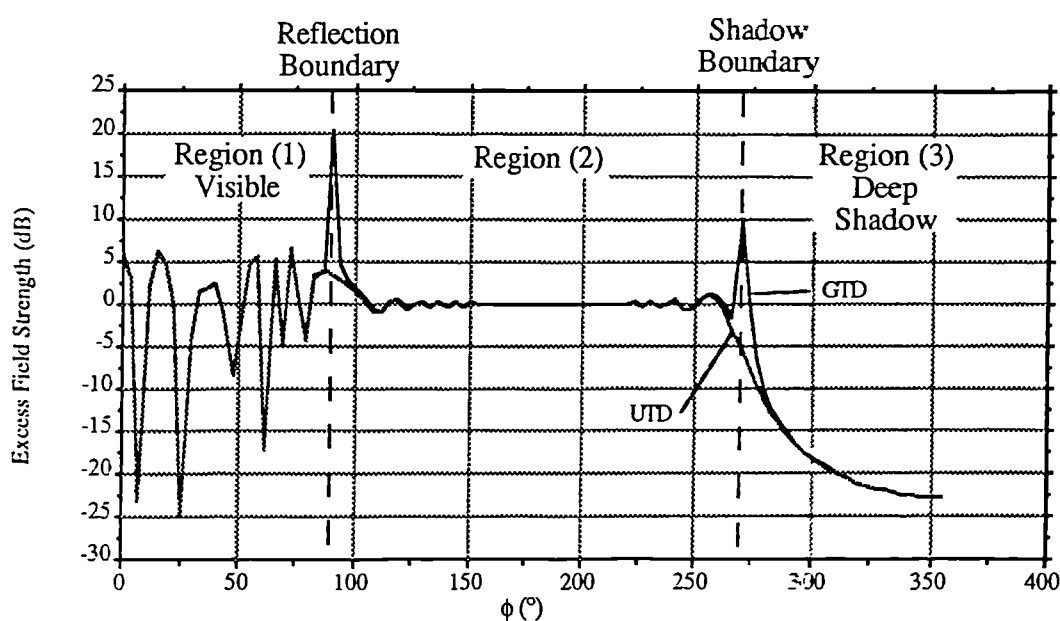


Figure 5.8: Comparison of GTD and UTD solutions for conducting half-plane

In the visible region the interference between the direct and reflected rays is clearly visible. In region (2) the field strength is nearly at its free space value since the diffracted ray is well below the direct ray in amplitude. In the deep shadow region (3) only the diffracted ray is present, so the resulting field decreases very rapidly as the diffraction angle increases. The singularities in the GTD solution at the optical boundaries are visible. In these regions serious errors may result, particularly close to grazing incidence ($\phi = 270^\circ$) where the UTD coefficient is essential. The UTD will therefore be used throughout in the examples which follow. Note that, on the shadow boundary, the field is -6dB, exactly half of the free space field strength, just as for the absorbing half-plane.

Figure 5.9 displays the diffracted field from the half-plane in the deep shadow region as it varies in space as a simple model of a building rooftop. The half-plane is located along the left-hand vertical edge of the diagram and it is assumed that the elevation of the base station antenna from the rooftop is close to zero, which will be the case in most macrocellular applications. Small deviations from this value (within a few degrees) make little difference to single edge diffracted field strengths. It is clear that the field varies more rapidly in the vertical direction than the horizontal direction, implying that building heights are a more significant factor in determining propagation loss than building spacing and mobile positioning, so correspondingly more precision must be applied in determining them.

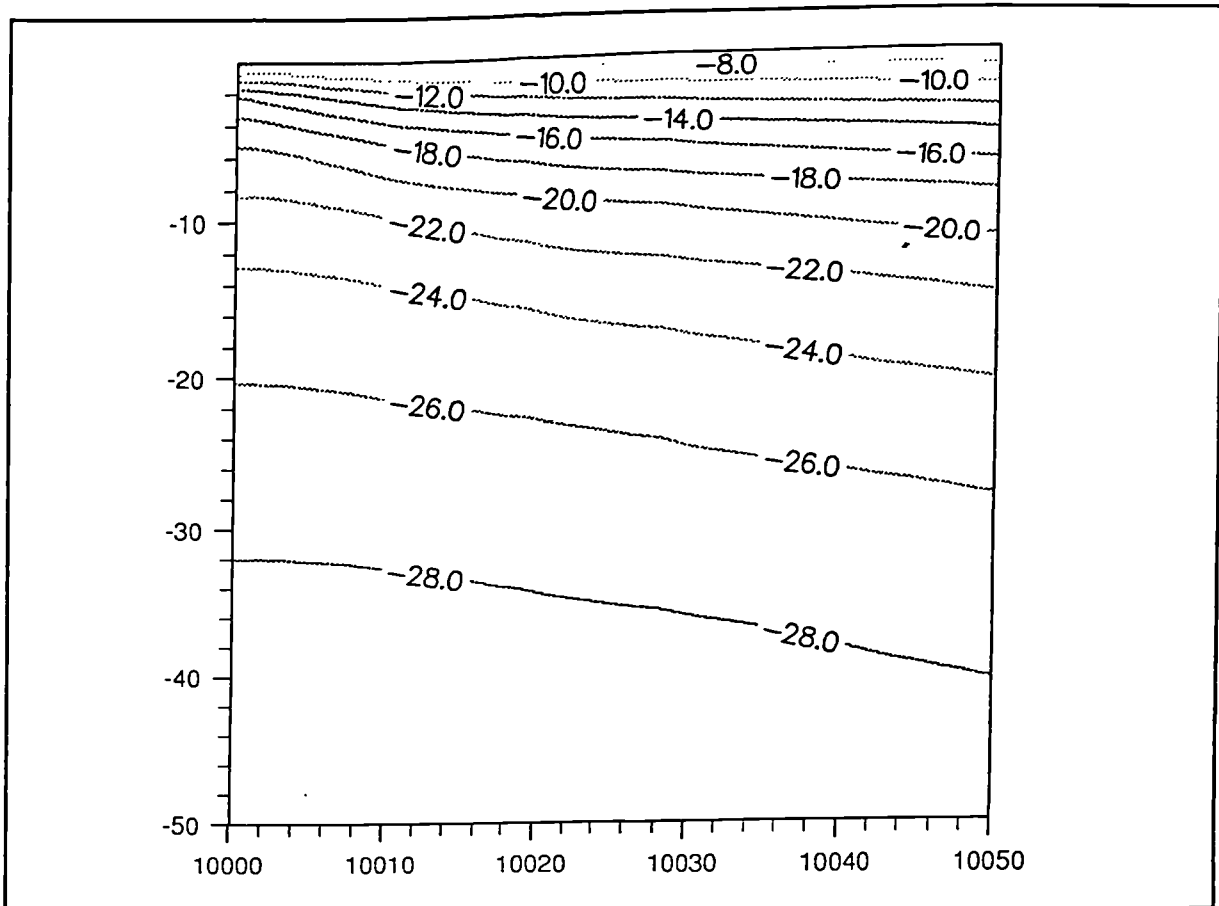


Figure 5.9: *Spatial variation of field strength due to conducting half-plane (in dB)*
(dimensions in wavelengths relative to edge at (10000,0))

In figure 5.10 the effect of polarisation on the single edge field is considered by varying the field point along a vertical line 50 wavelengths from the half-plane. The vertically polarised field shows a considerable gain compared to the opposite polarisation for points deep in the shadow region, but a more modest difference exists close to grazing incidence.

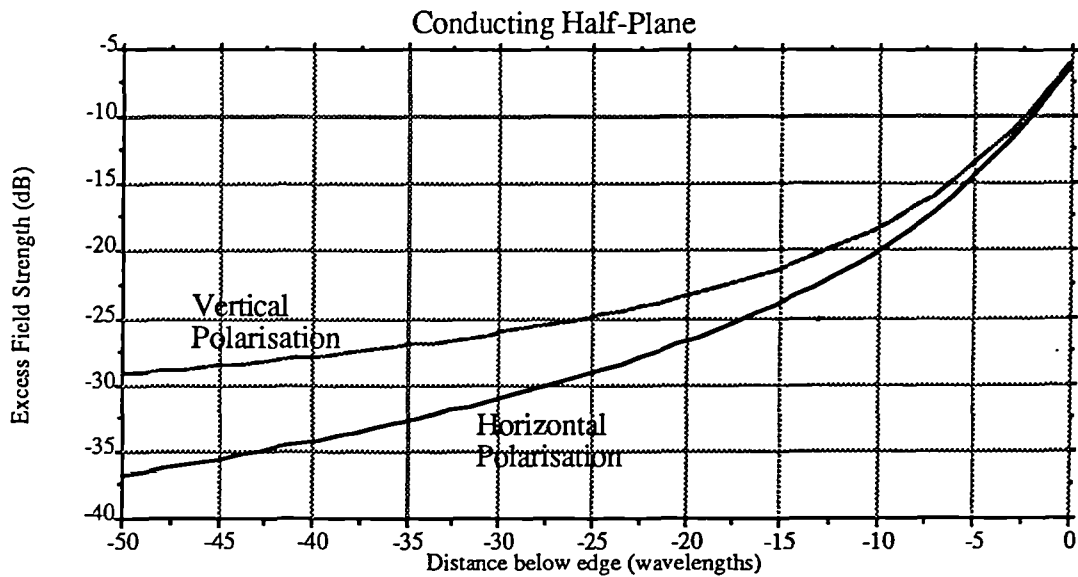
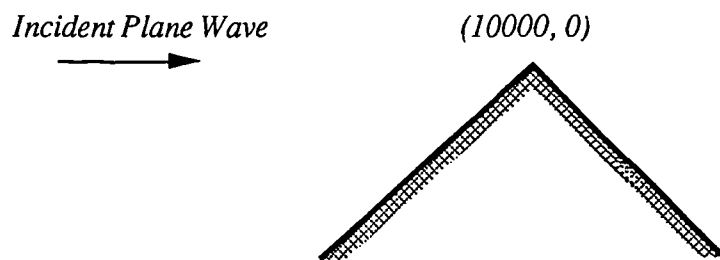


Figure 5.10: Comparison of vertical and horizontally polarised field on half-plane field

5.3.2: Conducting wedge

Whatever the attractions of the simple representation of buildings which may be afforded by the half-plane, the assumption of negligible building thickness must clearly be examined. A canonical wedge structure is more realistic in this respect. Here the UTD is used to examine the effect of a peaked rooftop. Figure 5.11 shows the spatial variation resulting from a 90° conducting wedge used to represent a building.



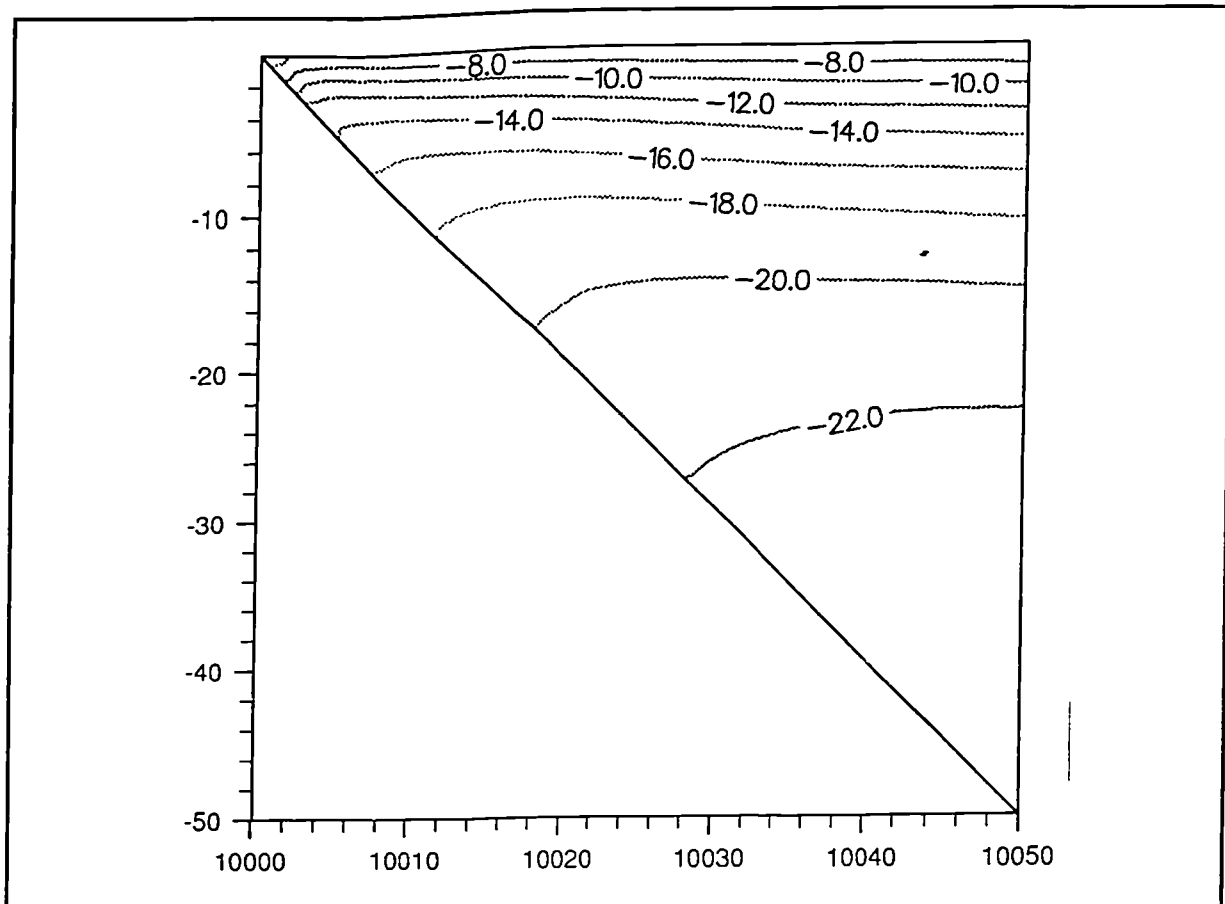


Figure 5.11: *Spatial variation of field strength due to conducting 90° wedge*

Comparison with the half-plane solution in figure 5.9 shows that the field diminishes rather less rapidly deep in the shadow region, but the field is identical on the shadow boundary. It would therefore seem that the shape of the building roof has negligible influence on the field close to grazing incidence, but is significant lower down. The conclusion to be drawn from this is that only the buildings in the immediate vicinity of the mobile need their shapes to be modelled in any detail, while those earlier along the path can be represented by simple half-planes. This saves considerable computational effort and complexity in the modelling process.

Figure 5.12 shows the same comparison between polarisations as for the half-plane case. The results are similar in form, but the vertical polarisation gain is considerably reduced. In both cases the diffracted field is larger than for the half plane.

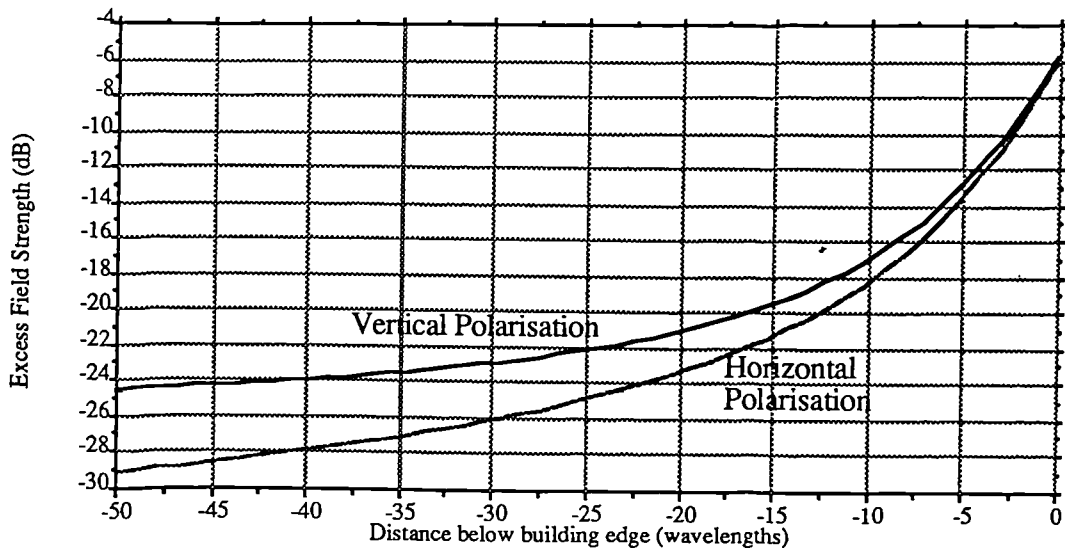


Figure 5.12: Comparison of polarisation for conducting wedge

It is therefore concluded that the half-plane representation is only really adequate for modelling building diffraction when the diffraction angles are small (ie near to grazing) and that building shape may influence the field in the deep shadow region significantly. However, often there will not be sufficient information or computational effort available to justify the use of a more complex scatterer.

5.5.3: Rough Lossy Wedge

In practice, a typical building will not be a particularly good conductor, so it would be helpful to use UTD to analyse the effects of finite conductivity. In addition, the surface of a given building will have some surface roughness. If the roughness at the point of diffraction or reflection is significant then the field will develop phase and amplitude irregularities and the field structure will be altered. Unfortunately, the canonical problems corresponding to these cases have not been solved, so the basic geometrical theories cannot predict these effects. However, this problem has been studied in connection with applying GTD to terrain diffraction by [Luebbers,1984]. Since each of the terms of the UTD diffraction coefficient is associated asymptotically with the direct and reflected parts of the diffracted field separately, the UTD wedge coefficient can be heuristically extended to include finite conductivity by

modifying each of the diffraction terms using the Fresnel reflection coefficient and a term for roughness. One study [Bergljung,1991] has found that inaccuracies do occur for dielectric wedges well away from the shadow boundaries when compared with an exact solution, but for UTD analysis this coefficient is the only option. The coefficient has been found [Luebbers,1984] to give good predictions of field strength in terrain applications and there is every reason to expect similar performance for buildings. It is difficult to obtain appropriate electrical parameters for building materials, but by examining the effect over an appropriately wide range the general effects may be determined. When more particular data are available the model may then be used for actual predictions.

The heuristic diffraction coefficient for rough, lossy wedges, D_{rl} is given as:

$$D_{rl}^{e,m} = \frac{1}{N \sin \theta_o \sqrt{8\pi j k}} \left[\begin{aligned} & \left\{ \cot \left(\frac{\pi + \Phi^i}{2N} \right) F \left[kLa^+ \left(\Phi^i \right) \right] + \cot \left(\frac{\pi - \Phi^i}{2N} \right) F \left[kLa^- \left(\Phi^i \right) \right] \right\} \\ & + \left\{ R_N^{e,m} \cot \left(\frac{\pi + \Phi^r}{2N} \right) F \left[kLa^+ \left(\Phi^r \right) \right] + R_O^{e,m} \cot \left(\frac{\pi - \Phi^r}{2N} \right) F \left[kLa^- \left(\Phi^r \right) \right] \right\} \end{aligned} \right]$$

where the terms are as defined for the perfectly conducting wedge previously. R_N and R_O are the reflection coefficients for plane wave illumination on the N face (away from the source) and the O face respectively. These terms are composed of the Fresnel reflection coefficients multiplied by a factor to account for the effect of roughness, assuming a normal distribution of surface heights whose standard deviation may be specified. The Fresnel coefficients are determined by the relative dielectric constant ϵ_r and the conductivity σ of the wedge material. If R_N and R_O are +1 for electric or -1 for magnetic polarisation then D_{rl} reduces to the perfect conductivity coefficient.

Figure 5.13 shows the result for high conductivity but with a 1 wavelength surface roughness. The attenuation is increased relative to the smooth wedge and the field varies differently close to the wedge surface.

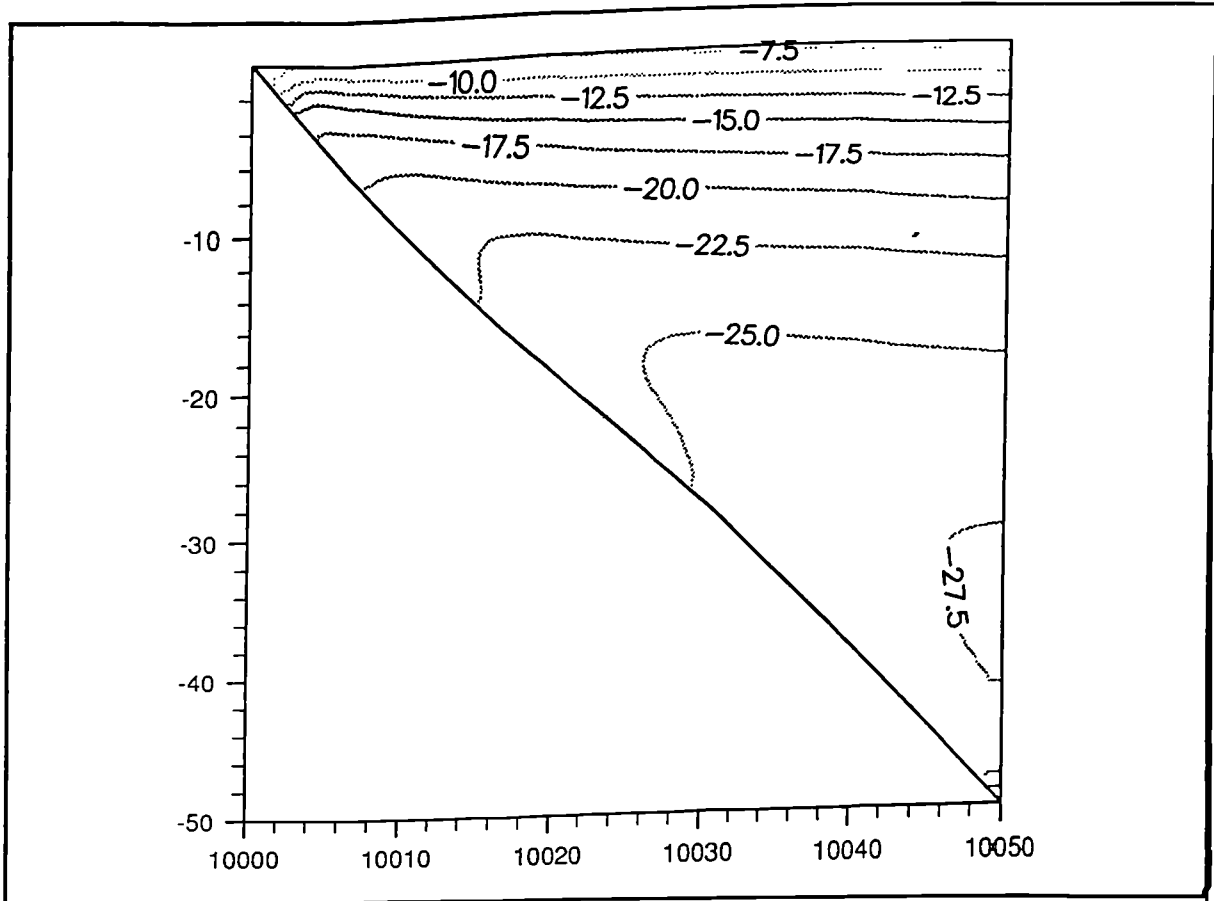


Figure 5.13: Rough wedge

It is interesting to compare the polarisation difference for varying roughness. Figure 5.14 shows the difference between the vertically and horizontally polarised field in various cases. As the roughness is increased the difference between polarisations decreases rapidly, so that with more than one wavelength of surface roughness the polarisation hardly affects the field in most circumstances. This has been confirmed in practice by measurements by [Egli,1957].

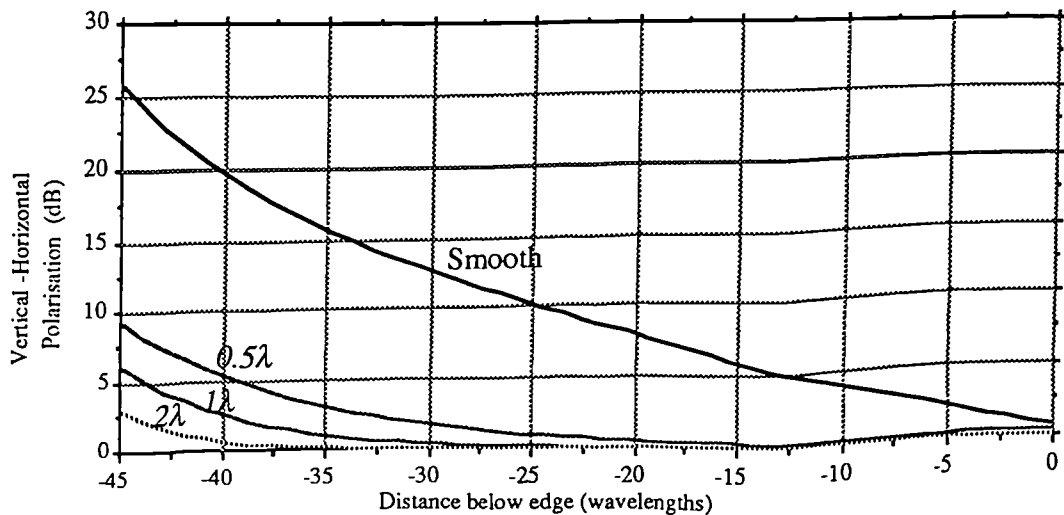


Figure 5.14: Effect of roughness on polarisation gain

Electrical parameters for buildings are difficult to obtain, so for the comparison here an estimate will be adopted. For poor (low conductivity) ground $\epsilon_r = 4$ typically and $\sigma = 0.001$ S/m, while good ground has typically $\epsilon_r = 10$ typically and $\sigma = 0.01$ S/m. For a typical building a reasonable estimate is thus $\epsilon_r = 5$ and $\sigma = 0.005$ S/m. Using these parameters the spatial field variation around the wedge is again plotted in figure 5.15, with no roughness. The difference in attenuation between this and the perfectly conducting wedge is small, so roughness would appear to be the more important factor to model. Plenty of measurement data would however be required to reach firm conclusions here.

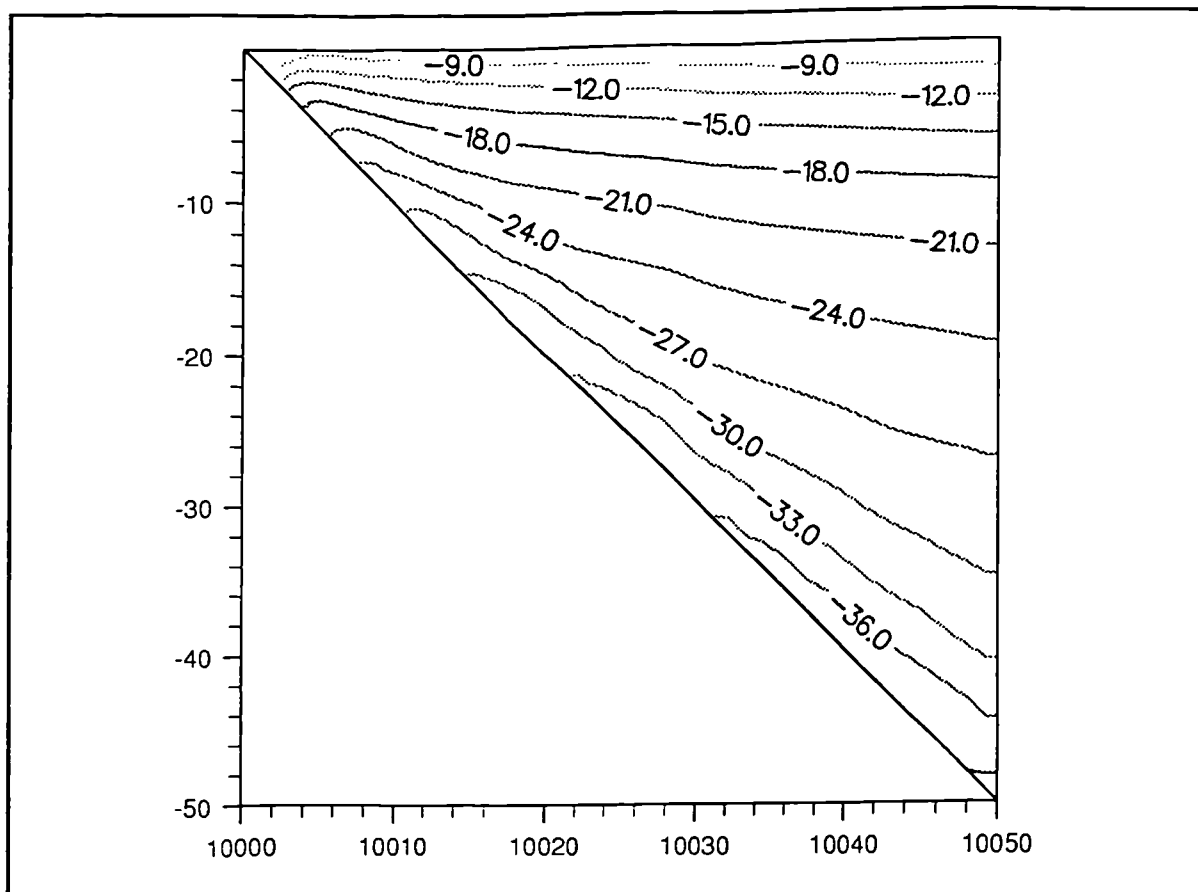


Figure 5.15: *Low conductivity building*

5.3.4: Complex Building Geometries

In principle the methods described here can be extended, subject to the outlined limitations of the theory, to predicting the field scattered by specific buildings. However, no adequate

measurements relating to these problems are currently available, partly due to the difficulties of isolating the effects of individual buildings, with the possible exception of the study described in Chapter Four [Thomas,1990] which examined good conductors only. This makes it difficult to validate the models constructed. However, some directions for future work will be indicated here.

Most buildings encountered in modern towns and cities have two main rooftop shapes: flat and peaked, so it would be useful to develop at least two-dimensional models of these (see figure 5.16).

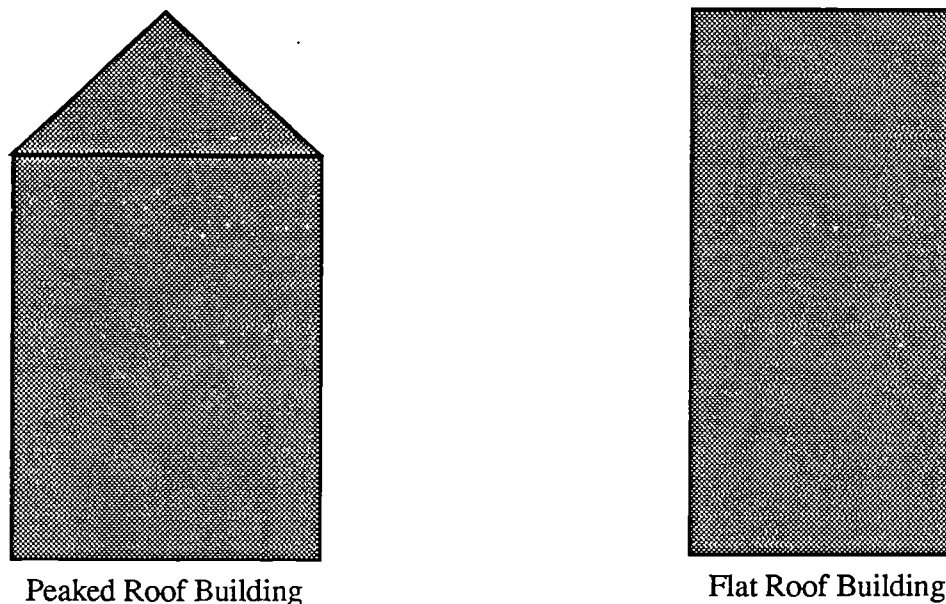


Figure 5.16 : *Two generalised building shapes*

In the peaked roof case, as shown in §5.3.2, the field near to rooftop level can be investigated by modelling the roof as a single wedge. Lower down, however, the field comes under the influence of a second wedge structure as the roof joins the building wall. Since the field incident on this second wedge is the singly diffracted field from the first edge at grazing incidence to the face of the roof, single-term diffraction methods are inadequate for this problem. Slope diffraction techniques such as that described in [Tiberio,1984] are appropriate. The situation is further complicated by another wedge at the leading face of the building. However the field diffracted from this edge is unlikely to be significant on the shadow region field since a triple diffraction process through a large angle is involved. The canonical structure shown in figure 5.17 is therefore proposed.

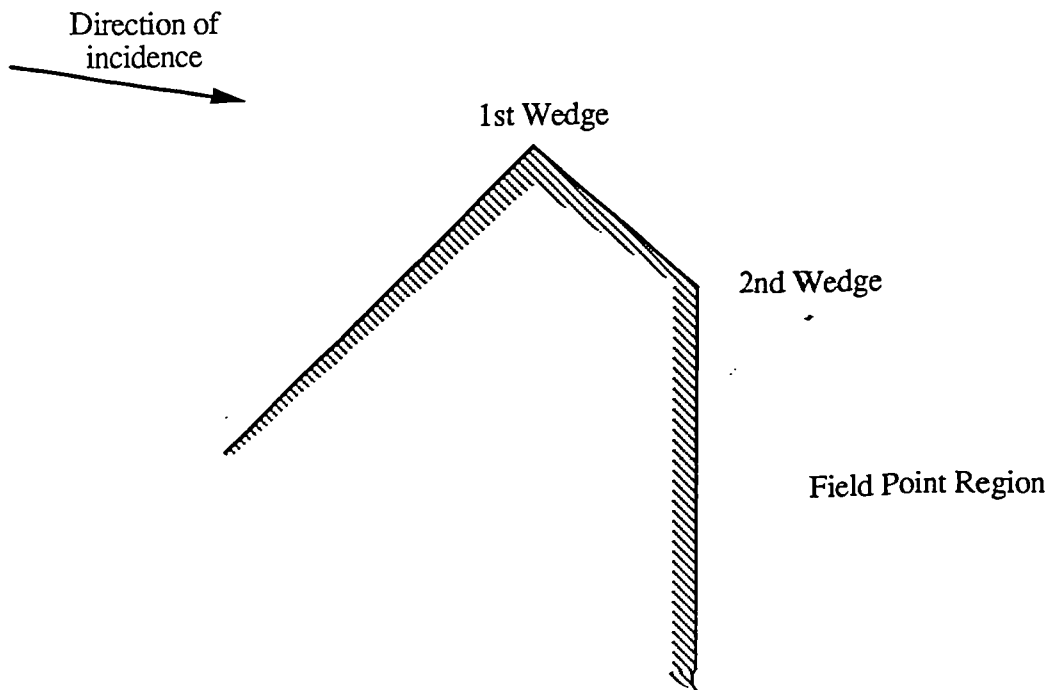


Figure 5.17: *Canonical structure for peaked roof building*

As the calculations in previous sections have shown, it is important to consider the finite conductivity and roughness of buildings. A heuristic UTD slope diffraction coefficient has been developed which would address these needs [Luebbers,1989], but the heuristic nature of the solution implies that careful validation of the model would be required.

The case of the flat-roofed building is simpler since only two significant wedges are involved. Essentially the same technique as for the peaked roof is therefore applicable, with appropriately rearranged edge angles. An appropriate diffraction coefficient for this situation in the perfectly conducting case has been described by [Tiberio,1989] and used successfully in building diffraction calculations by [Lebherz,1991]

More detailed building features could also be studied, but the analysis required is unlikely to be justified by the utility of the results. One useful aspect, however, is to extend the modelling to three dimensions, which cannot be studied using scalar analysis. The next section will commence this process by constructing a UTD model of street orientation, but further studies could particularly consider the effect of diffraction around vertical building edges, which is likely to be of particular importance for short-range propagation.

5.4: Street Orientation Model

5.4.1: Introduction

Here a UTD model of building diffraction is constructed for the prediction of signal variability due to street orientation

Consider a base station placed within a city composed of a large number of streets of differing orientations. As the mobile position is varied around a circle of radius R centred on the base station, the street orientation relative to a radial will vary rapidly, with no preference for any particular orientation. Even in a city planned on a regular grid system, the orientations encountered vary over a wide range. Figure 5.18 illustrates this point and shows the definition of street orientation, θ_s . This angle is defined relative to the great circle path from base to mobile rather than the ray path itself since the two are not in general coincident.

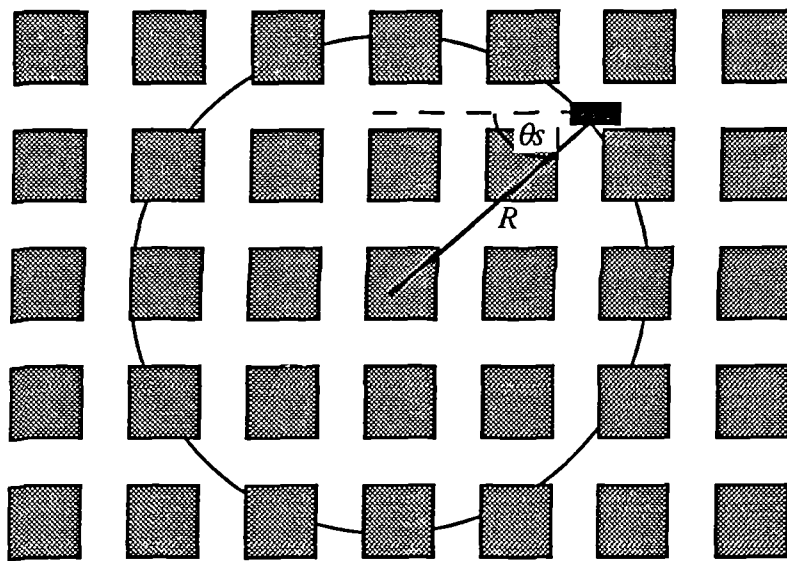


Figure 5.18: *The variation of street orientation as a mobile moves around a city*

It is thus reasonable to assume that θ_s is equally likely to take on any value, so it will be assumed that θ_s is distributed uniformly on $[0, \pi]$. It is not necessary to explicitly consider the interval $[\pi, 2\pi]$ since the results on this interval will be the same on the grounds of symmetry. A two ray model is taken, with a constant reflection coefficient for wall reflection, just as in the oblique incidence scalar model in Chapter Four.

5.4.2: Ray Path Analysis

Direct Ray:

The three dimensional geometry of the situation is shown in figure 5.19. Only the direct ray path is considered first for simplicity. The reflected ray follows in an analogous manner and will be considered later.

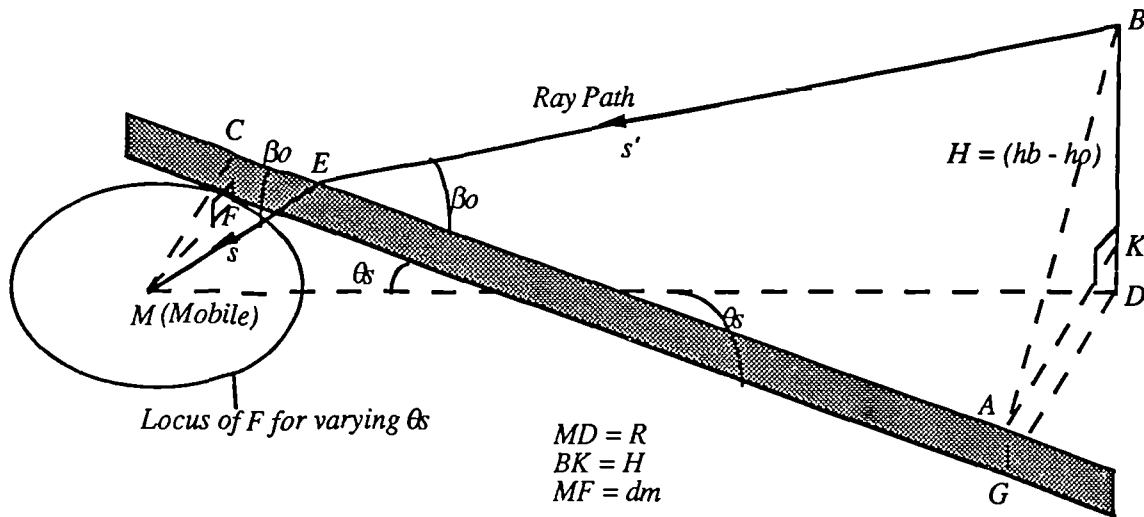


Figure 5.19: Diffraction geometry for oblique incidence on building edge

The building is represented in the diagram as a conducting half-plane. The distance $MF = d_m$ between the building and the mobile is fixed, so F is constrained to rotate about M on the circle shown. When $\theta_s \leq \arcsin(d_m / R)$, the base station is on the same side of the building as the mobile and the model becomes invalid (eg. $\theta_s = 0.75^\circ$ with $d_m = 20\text{m}$ and $R = 1520\text{m}$). For radial streets other models have to be considered, such as [Rustako,1991]. When the direct ray BE impinges on the edge, diffracted rays are produced, emanating as though from a line source coincident with the tangent to the edge at the diffraction point. In accordance with Fermat's principle the total path length ($BE + EM$) is stationary with respect to variations in the diffraction point E . A necessary consequence of this is that the angles made by both the direct and diffracted rays to the edge are equal, so that $BEA = CEM = \beta_0$.

Thus:

$$\tan \beta_o = \frac{CM}{CE} = \frac{\sqrt{d_m^2 + h_o^2}}{CE}$$

Using the similarity of $\triangle CEM$ and $\triangle AEB$:

$$\frac{EC}{CM} = \frac{EA}{AB}$$

Hence $\frac{EC}{CM} = \frac{EA + EC}{CM + AB} = \frac{AC}{CM + AB}$

$$\text{Thus } \tan \beta_o = \frac{CM + AB}{AC} = \frac{\sqrt{d_m^2 + h_o^2} + \sqrt{GD^2 + H^2}}{R \cos \theta_s}$$

where $H = h_b - h_o$

When $\theta_s = \pi/2$, then $\theta_s = \beta_o$.

This expression for the diffraction angle can now be used to determine the parameters for the UTD wedge diffraction coefficient as defined in figure 5.4. The angles of incidence and diffraction are defined in the plane normal to the edge at E .

$$\phi_o = \frac{\pi}{2} + \widehat{BAK}$$

$$\phi = 2\pi + \widehat{MCF}$$

$$\widehat{BAK} = \tan^{-1} \left(\frac{H}{AK} \right) = \tan^{-1} \left(\frac{H}{R \sin \theta_s - d_m} \right)$$

$$\widehat{MCF} = \tan^{-1} \left(\frac{MF}{CF} \right) = \tan^{-1} \left(\frac{d_m}{h_o - h_m} \right)$$

$$s = EM = \frac{CM}{\sin \beta_o} = \frac{\sqrt{(R \sin \theta_s - d_m)^2 + H^2}}{\sin \beta_o}$$

It is also useful to consider the distance that the diffraction point moves along the edge as the orientation is varied away from normal incidence on the edge:

$$\text{Shift of diffraction point} = FX - CE = \frac{d_m}{\tan \theta_s} - \frac{\sqrt{d_m^2 + h_o^2}}{\tan \beta_o}$$

Essentially the analysis for the reflected ray is identical to the direct case, except that the mobile position is replaced by its reflected image, so that d_m becomes $(2W - d_m)$, where W is the street width. When combining the direct and reflected rays, however, it is important to note that the effective street orientation is different in each case, as follows:

Let θ_{sd} be the orientation for the direct ray and θ_{sr} be the corresponding value for the reflected ray. The relationship between these parameters is shown in figure 5.20.

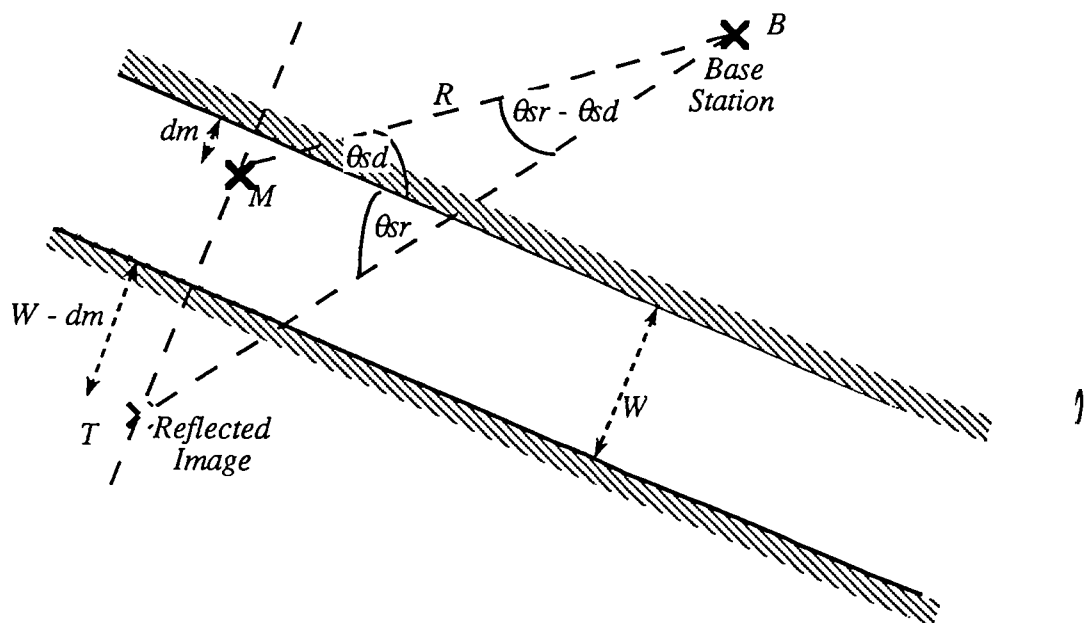


Figure 5.20: Geometry for reflected image of field point

The resulting analysis gives the parameters for the reflected ray:

$$\cos \theta_{sr} = \frac{R \cos \theta_{sd}}{BT}$$

$$\text{where } BT^2 = (R \cos \theta_{sd})^2 + (R \sin \theta_{sd} + 2(W - d_m))^2$$

$$\cos \theta_{sr} = \frac{R \cos \theta_{sd}}{\sqrt{R^2 + 4(W - d_m)^2 + 4R(W - d_m) \sin \theta_{sd}}}$$

In conjunction with the UTD wedge diffraction coefficient given in §5.2.3, the above parameters constitute a complete model of street orientation.

5.4.3: Results

First the model must be verified by comparison to some measured data. Little published work is available to provide this, but some independent confirmation can be given by examining the street orientation results measured by [Loew,1991]. The measurements were compiled from a large number of measurements in Darmstadt in Germany, with varying range and base station antenna height at 945MHz. All of the measurements made in 5° increments of street orientation were grouped together and a mean prediction curve was constructed. Figure 5.21 shows the average building parameters for the area which are used here to obtain simulation results.

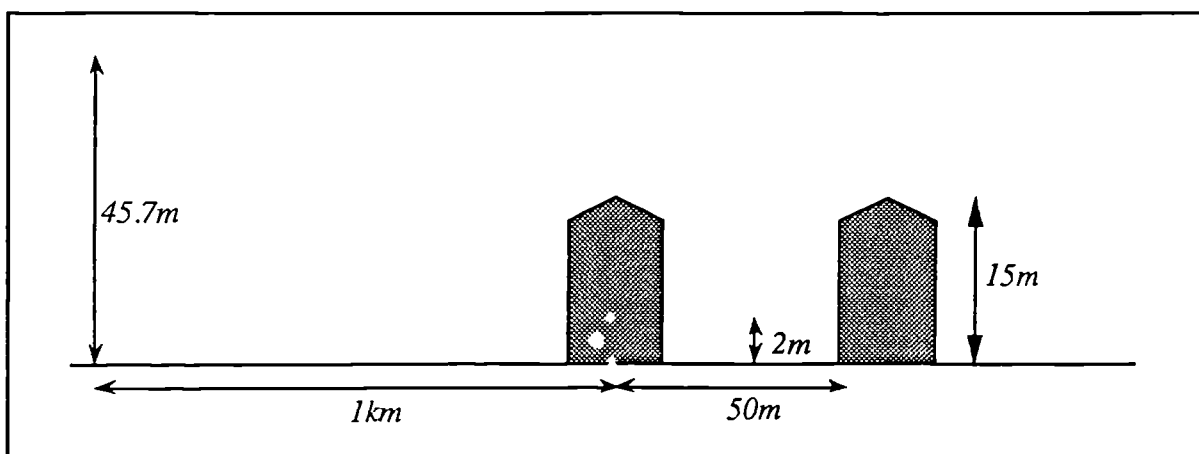


Figure 5.21: System parameters for comparison with measurements

The comparison is shown in figure 5.22. The model performs rather poorly close to 0° as expected. The size of the variation elsewhere is close, confirming use of the model as a

simulation tool. A discrepancy in the absolute level of the prediction could arise from variations in the characteristics of particular buildings, multiple building effects or variation in the transmission range over the complete set of measurements.

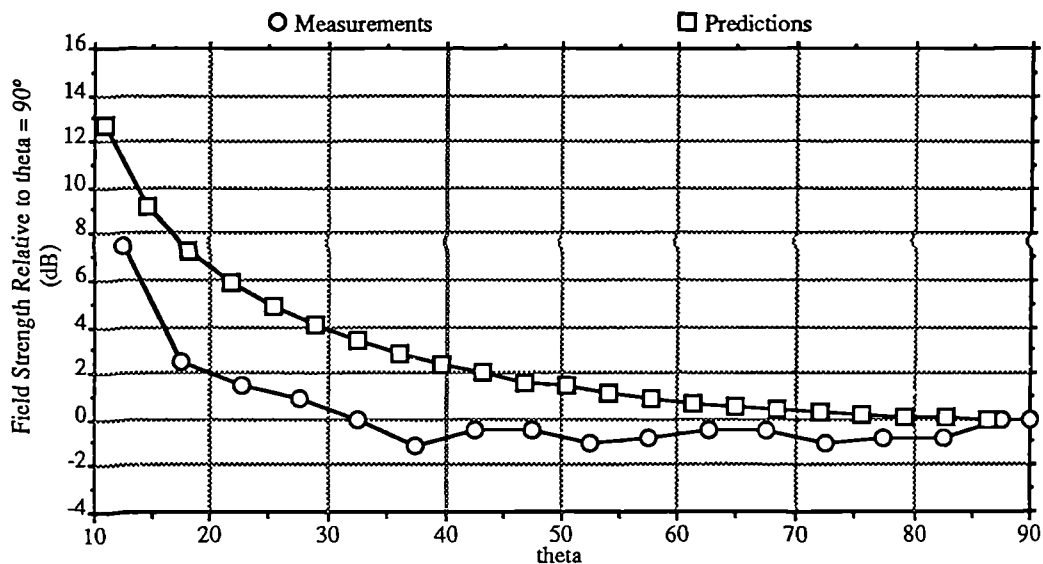


Figure 5.22: Comparison of simulation results and measurements

The remainder of this section is concerned with examining the effect which various system parameters have upon the median field strength using the model. The following parameters are used :

$R = 1.52\text{km}$; $d_m = 20\text{m}$; $(h_o - h_m) = 6.5\text{m}$; $W = 40\text{m}$; $(h_b - h_o) = 10\text{m}$; $\rho = 0.5$. Vertical polarisation is assumed throughout.

Figure 5.23 shows the variation of received field strength due to the direct-diffracted and diffracted reflected ray separately. It is evident that the reflected image is less shadowed, resulting in a larger field. The minimum field strength occurs when the street is oriented tangentially, but changes only slowly close to this orientation. As the street becomes closer to radial variation becomes increasingly rapid. Note that the abscissa here is the *direct* street orientation, so the two curves are slightly shifted with respect to one another. Figure 5.24 shows that the differences are small.

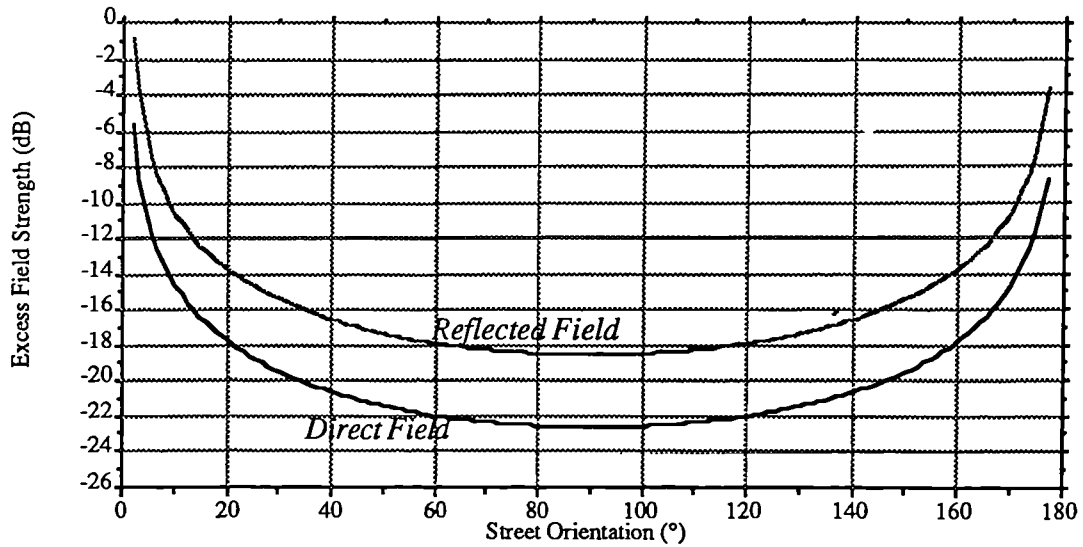


Figure 5.23: Direct and reflected ray field strengths

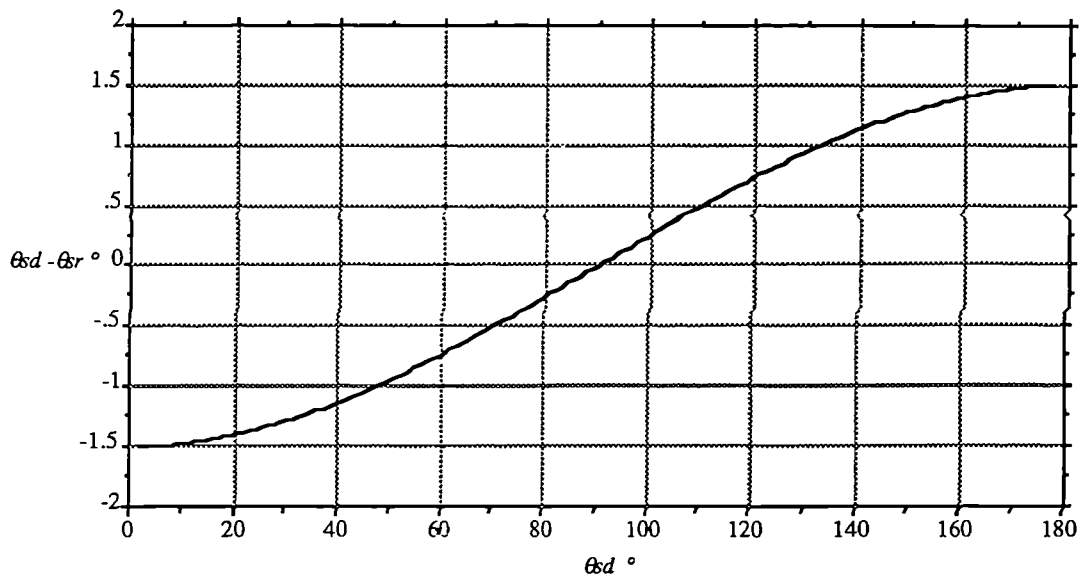


Figure 5.24: Difference in apparent street orientation for each of the main rays

Figure 5.25 illustrates the way in which the diffraction point shifts away from its normal incidence value. This calculation is useful in examining approximations which do not explicitly account for Fermat's edge diffraction principle in calculating the point of diffraction. A variation of some 10m over the range considered is evident. This value will be of use when considering real street geometries in Chapter Eight. It shows that, when streets are close to radial, the diffraction point estimated from the intersection of the edge with the great circle propagation path may be substantially in error.

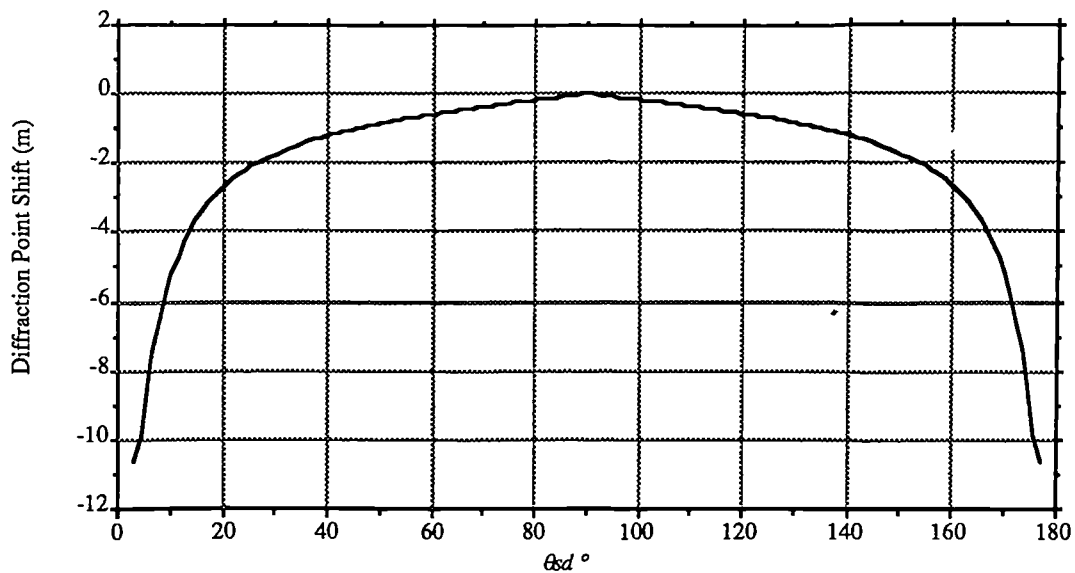


Figure 5.25: Diffraction point shift for oblique incidence

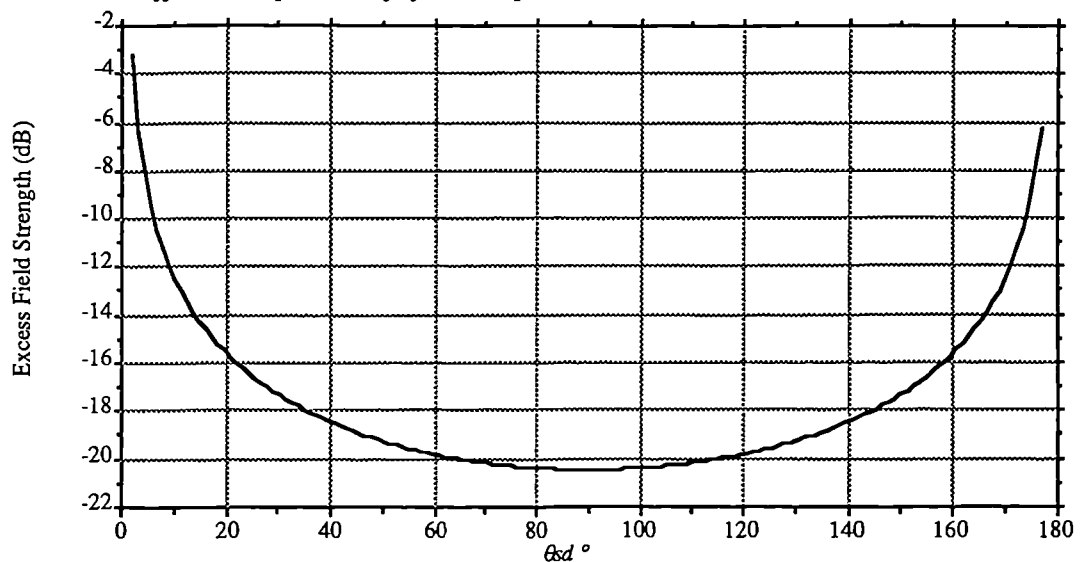


Figure 5.26: Overall sector median field strength versus street orientation

Finally the rays are power summed in figure 5.26 according to the usual modelling paradigm to give an estimate of sector median field strength.

Now the assumption that θ_{sd} is uniformly distributed on $[0, \pi]$ can be used for transforming the results into a cumulative distribution (CDF) of field strengths. Figure 5.27 shows the CDF corresponding to the results of figure 5.26:

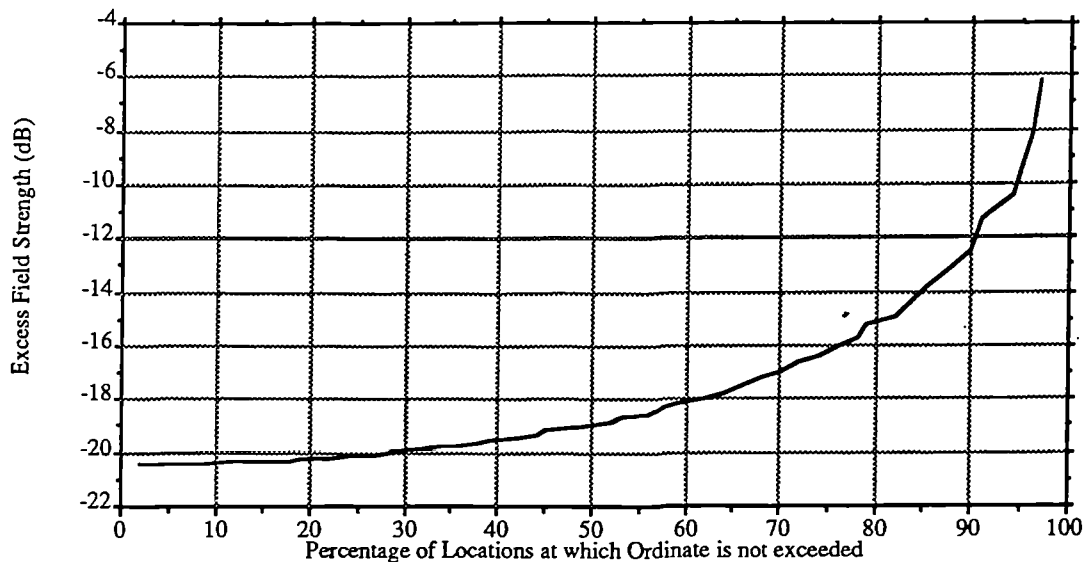


Figure 5.27: Cumulative distribution of field strength variation due to street orientation

Notice from this diagram that the median (50%) value shows only a small uplift from the zero percentage value. Nevertheless it is important to remember that the median corresponds to $\theta_{sd} = 45^\circ$ rather than the tangential value. It may therefore be more sensible to use average street widths corrected to this value when applying prediction models which do not explicitly consider the effects of oblique incidence.

For about 3% of locations data are unavailable since the model is not valid for streets close to radial. This does not affect the CDF outside these limits provided that the relative field strength does not decrease. In particular, the median value is unaffected.

Now it is useful to determine which system parameters significantly affect these statistics. The first of the parameters investigated here is the frequency. Figure 5.28 shows the variation of the CDF with frequency, with the field strength normalised to the 0° value in each case.

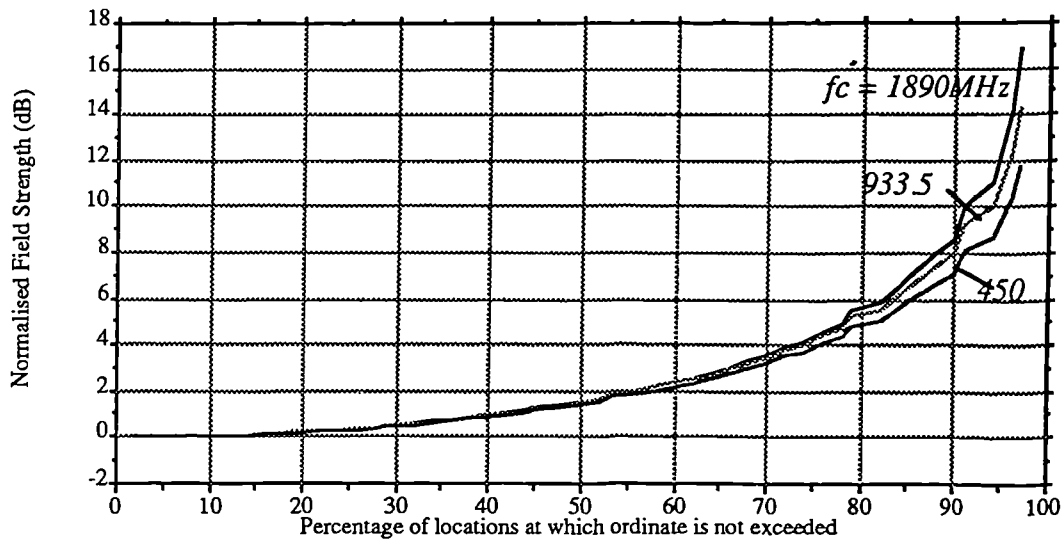


Figure 5.28: Street orientation statistics with varying frequency

The only significant variation is at the high percentile values and even this is small. For area coverage predictions the low percentiles are of most interest and the model is expected to be most valid in this region. It is therefore assumed that the variation with frequency is small enough to be neglected in most situations. A similar assumption is made for the variation with street width, which figure 5.29 shows to be very small.

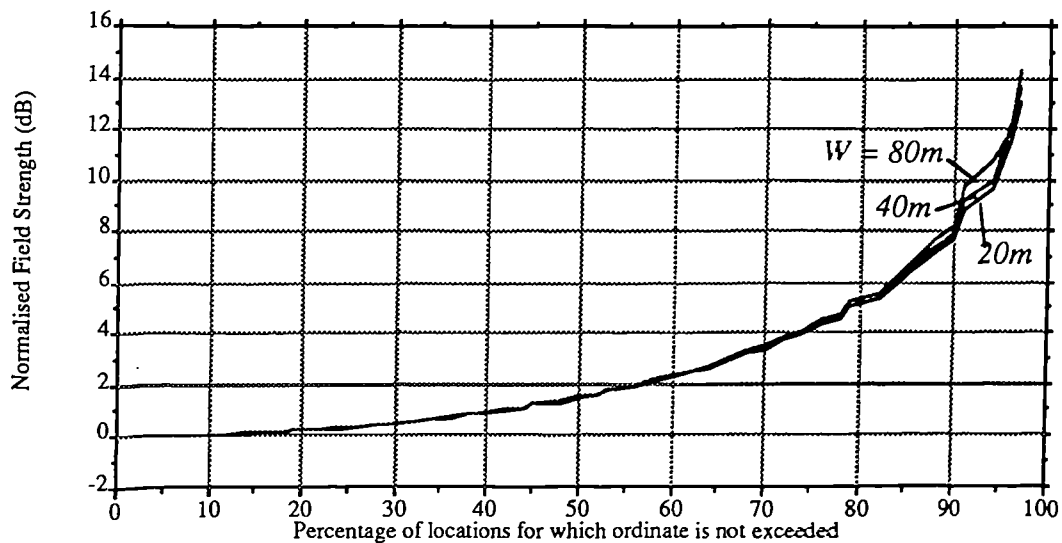


Figure 5.29: Street orientation statistics with varying street width

The variations with $(h_o - h_m)$ and d_m are also negligible, although not shown here. If, however, the overall transmission range is varied, the CDF is markedly affected as shown in figure 5.30.

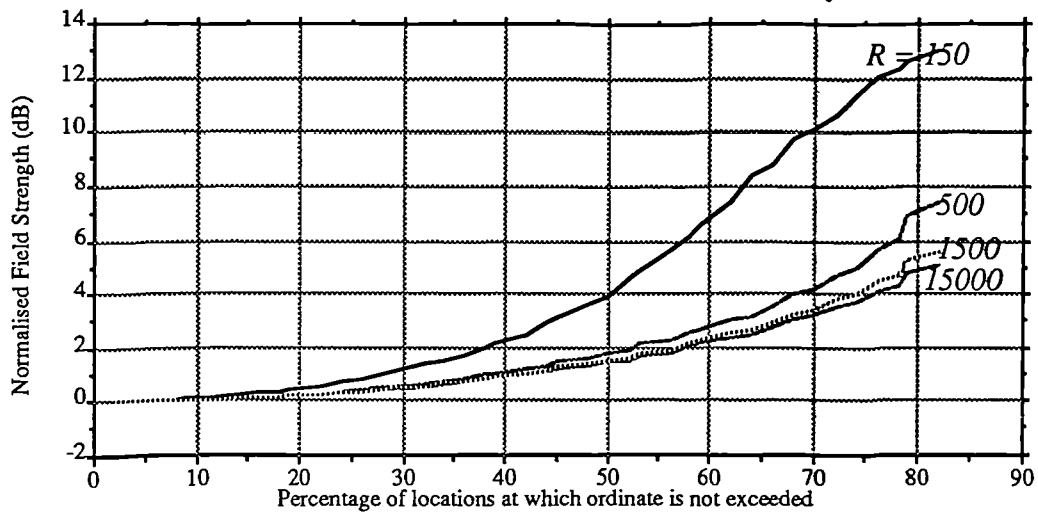


Figure 5.30: Street orientation statistics with varying transmission range

Figure 5.31 uses this fact to provide a prediction curve showing the difference between the median (45°) and the oblique (90°) field strength values, plotted against the elevation angle of the base station antenna from the building rooftop, α .

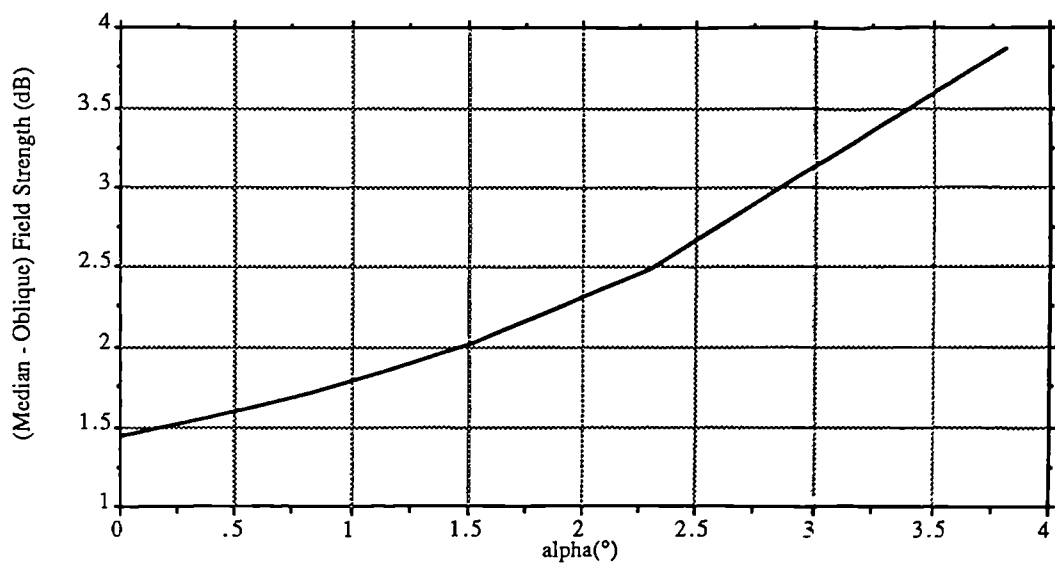


Figure 5.31: Median uplift for street orientation effects

The simulation results indicate overall that the statistics of field strength variation due to street orientation are substantially independent of frequency, street width, relative antenna heights and the mobile's position on the street, but are strongly affected by the range (and base station antenna height), being most variable at short range. This work could form the basis of one factor in a complete theoretical model of slow fading which incorporates physical building parameters.

5.5: Conclusions

The ray methods described in this chapter have been used for modelling various building diffraction geometries in an adaptable and versatile manner. The principal application for the methods is in short-range applications, for determining likely coverage areas and interference levels in cases where considerable geometrical detail is available. In these cases complete deterministic prediction of field strengths may be feasible, although the ultimate prediction accuracy of such an approach is likely to be limited by the extent to which 'weak ray' contributions which cannot be predicted by ray optical methods with the limited amounts of data which are extant. Various limitations of the techniques, however, prevent their use for predicting diffraction effects in situations where many buildings are involved. Other methods for doing this will be sought in the next chapter. Ray methods do nevertheless allow consideration of the effects of final building diffraction by buildings of various shapes, appropriate to the buildings in a particular area whenever this process may be considered separable from the gross characteristics of the rest of the path. Buildings might therefore be classified in terms of the shape of roof they possess and the degree of surface roughness typical of buildings in a given area. Ray methods would provide an appealing method of analysis if such data were available and recent discussions have suggested that aerial photography could provide a reliable means of providing this [Keech,1991].

Chapter Six

Multiple Knife Edge Diffraction

6.0: Introduction

For multiple building problems the building rooftops will often constitute a system of edges illuminated at near grazing incidence, with a large number of buildings involved in the process (see figure 3.3). For an area coverage prediction this diffraction problem may need to be solved a very large number of times, so any method used must be capable of rapid evaluation to be practical, while providing acceptable prediction accuracy. Since Chapter Five showed that ray methods have limitations in the grazing incidence case, alternative methods are needed. Existing solutions to the problem are examined here and found useful in some non-critical cases. A more accurate approach is described and efficient methods of evaluating results using this approach are proposed and compared.

6.1: Approximate Methods

6.1.0: Discussion

A number of approximate methods for calculating multiple edge diffraction have been published and widely used, based upon simple geometrical constructions used to calculate a total diffraction loss in terms of combinations of single edge diffractions between adjacent edges. These were developed primarily for application in terrain diffraction, where the number of edges within low-order Fresnel zones is usually small (less than 5) and the source and field points are frequently in deep shadow. Examples are [Bullington,1977], [Epstein,1953], [Deygout,1966] and [Giovanelli,1984]. As pointed out by Pogorzelski [Pogorzelski,1982], the Deygout method [Deygout,1966] uses appropriate diffraction angles between adjacent edges, while the Epstein approach [Epstein,1953] uses the correct individual diffraction angles

but combines the losses due to individual edges inappropriately. The Giovanelli method [Giovanelli,1984] is probably the best compromise, using the correct diffraction angles and an accurate combining factor. Only this method will be examined in any detail here.

6.1.1: The Giovanelli Method

The geometry for the method is shown in figure 6.1. Only two edges are shown here, but the method is straightforward to extend to multiple edges. The solution involves the single edge result given previously (§4.4.5), which will be denoted here by $A_S(d_1, d_2, h)$ where d_1 and d_2 are the distances between the source and field points and the edge, and h is the height of the edge above the straight line joining the source and field points.

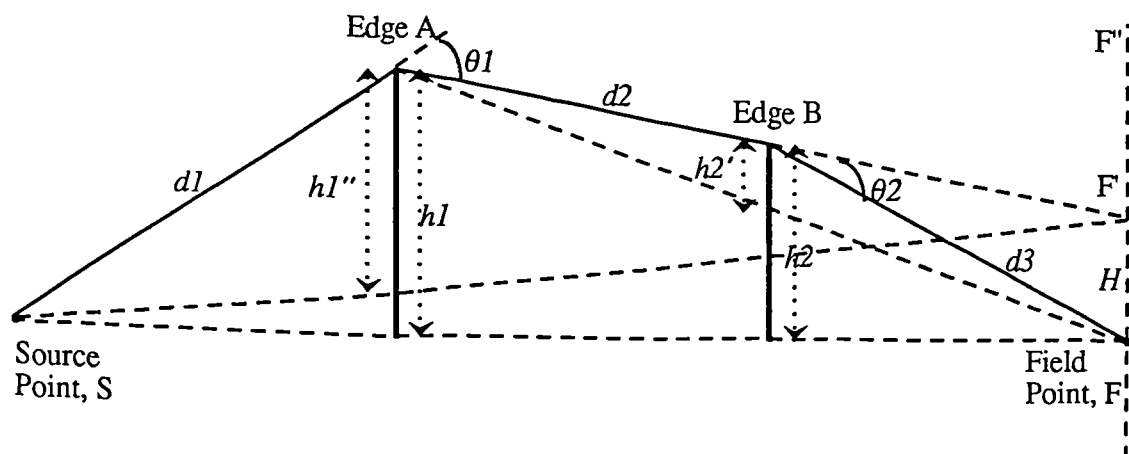


Figure 6.1: Geometry for Giovanelli method

First the **main edge** is identified. This is the edge having the smallest clearance relative to the Fresnel zone radius. Assume edge A to be the main edge in this case. Then a reference field point F' is found by projecting AB onto $F F'$. An effective height for edge A, h_1'' is defined by:

$$h_1'' = h_1 - \frac{d_1 H}{d_1 + d_2 + d_3} \quad (6.1)$$

where $H = h_2 + m d_3$ and $m = (h_2 - h_1) / d_2$. The effective height for the secondary

obstacle B is then given by :

$$h_2' = h_2 - \frac{d_3 h_1}{d_2 + d_3} \quad (6.2)$$

The diffracted field strength is now given by the following expression:

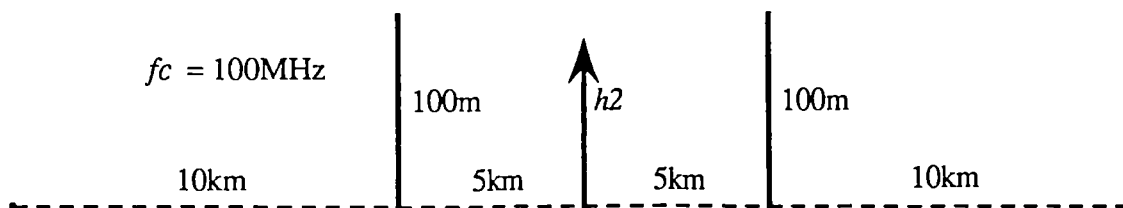
$$A_T = A_s \left(d_1, d_2 + d_3, h_1' \right) \times A_s \left(d_2, d_3, h_2' \right) \quad (6.3)$$

The results are not unconditionally reciprocal (that is, swapping source and field points may give slightly different results.) The method is conveniently extended to more than two edges by recursively applying the above described procedure. Some particular cases of results obtained from this method are now examined to determine its usefulness in multiple building configurations.

Giovanelli Comparisons

The three sets of calculations presented are compared with an evaluation of the multiple edge integral solution (§6.2), which may be regarded as exact in this context. The comparisons were calculated using successive applications of equation (6.3), implemented as a PASCAL program running on a SUN workstation.

The first situation (figure 6.2) shows a three edge arrangement which might be encountered in a terrain diffraction calculation. The edges obstruct the line-of-sight path, and grazing incidence occurs when $h_2 = 100\text{m}$ and when $h_2 = 150\text{m}$.



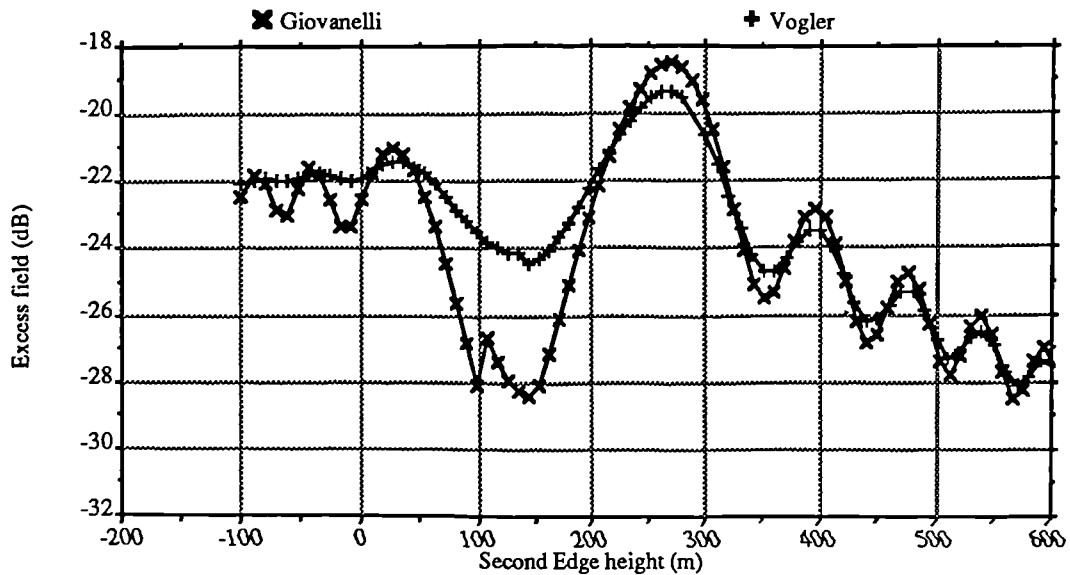


Figure 6.2 : *Giovanelli comparison (1)*

The results show good agreement with the exact solution, with the positioning of all maxima and minima predicted correctly. The absolute accuracy of the predictions is also reasonable, particularly when only one edge dominates the process (h_2 large), as would be expected. The propagation loss is however overestimated when the edges are almost in line and there is a considerable discontinuity at $h_2 = 100\text{m}$.

The next situation (figure 6.3) is more severe. Three edges and the field point are colinear, which would be an unusual situation in terrain diffraction situations, but is important for building diffraction since many adjacent houses may be of the same height. Figure 6.4 shows the way in which the predicted field strength varies with source height.

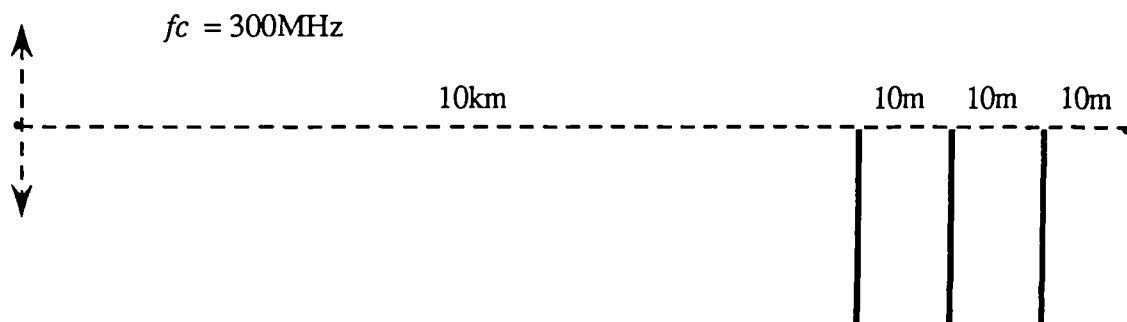


Figure 6.3: *Giovanelli comparison (2)*

The Giovanelli method considerably overestimates the propagation loss in this case, although

the rate of change of field strength with source height is accurate.

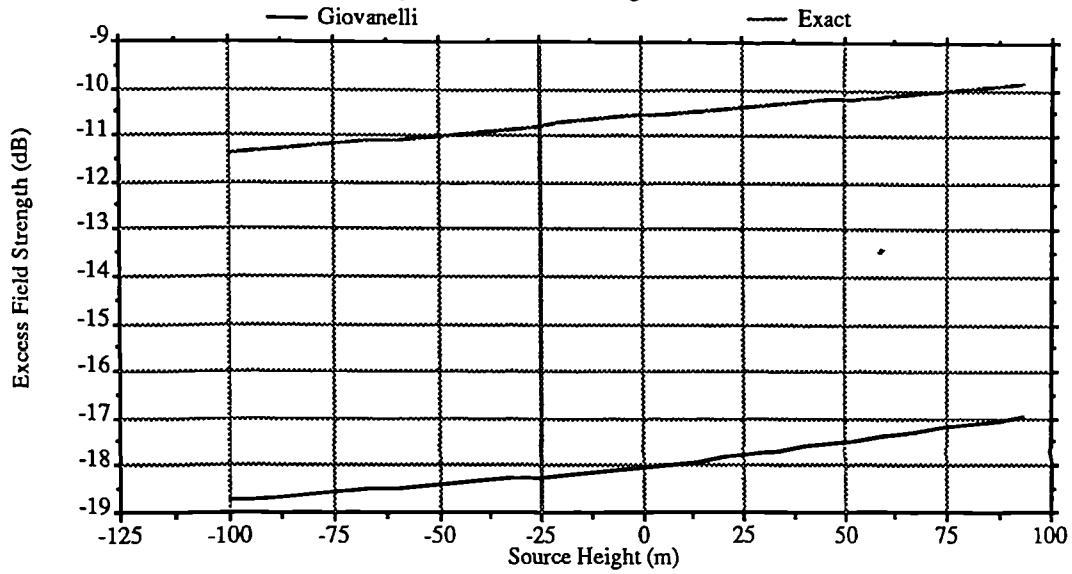


Figure 6.4: Giovanelli predictions for three edge grazing incidence problem (2)

To examine this effect in more detail, the next comparison (figure 6.5) examines the grazing incidence case as the number of edges, n , is varied.

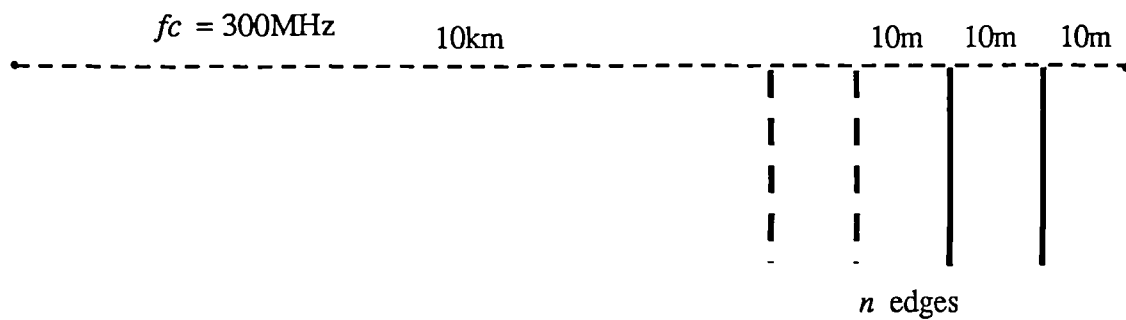


Figure 6.5: Giovanelli comparison (3)

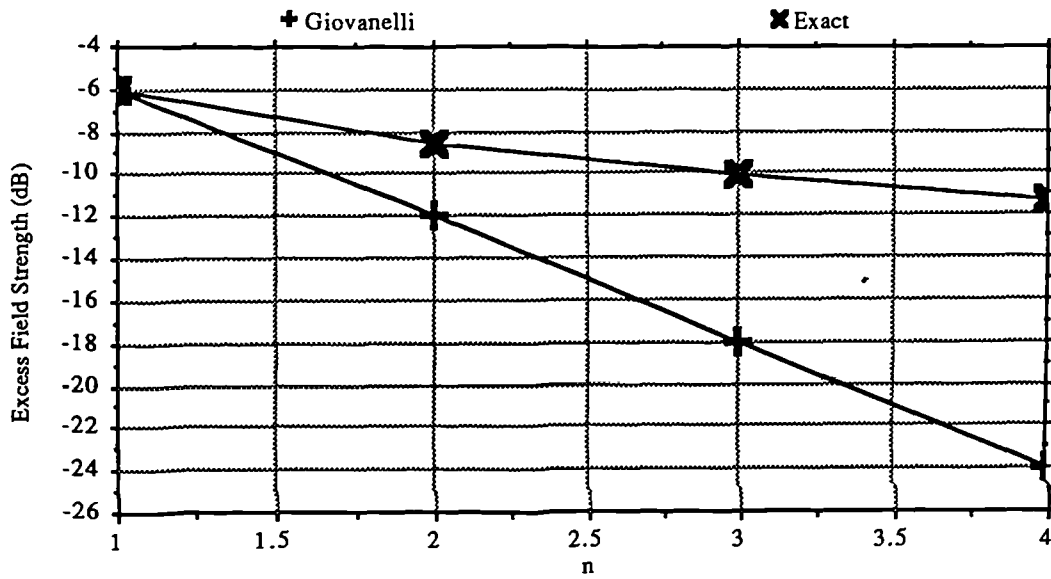


Figure 6.6: Giovanelli predictions for varying number of edges at grazing incidence

Here the Giovanelli approach predicts 6dB loss per edge, resulting in a serious overestimate of loss for $n > 1$ (figure 6.6). It is concluded that the method is inadequate for situations involving large numbers of edges, particularly when a series of edges is colinear although the ease of implementation and speed of calculation make it attractive for terrain diffraction. Alternative methods are now sought.

6.1.2: The Near Field Method

The near-field method for calculating multiple edge diffraction [Whitaker,1984] is unusual since it is an asymptotic ray technique, like GTD, but it uses a scalar description of the field. It is specifically designed to overcome some of GTD's limitations in dealing with transition region fields, whilst retaining some of GTD's intuitive appeal. The method will be described in general terms here and some numerical calculations performed. Considerable effort was devoted to producing a reliable implementation of this method and to extending the method to overcome some of its limitations, since it held considerable promise initially for making rapid calculations with large numbers of edges. Ultimately, however, the method was found to be fundamentally limited.

The near-field method assumes that every edge in a system of multiple edges is illuminated by an astigmatic pencil of rays as in §5.1. Since all of the edges are assumed parallel, with oblique ray incidence throughout, it is considered that the centre of wavefront curvature in the horizontal plane passes through the source point, while in the vertical plane the focus is a line parallel to the edges, at a position dependent on the observation point. In the special case of the first edge, both focal lines are coincident and point source illumination is assumed.

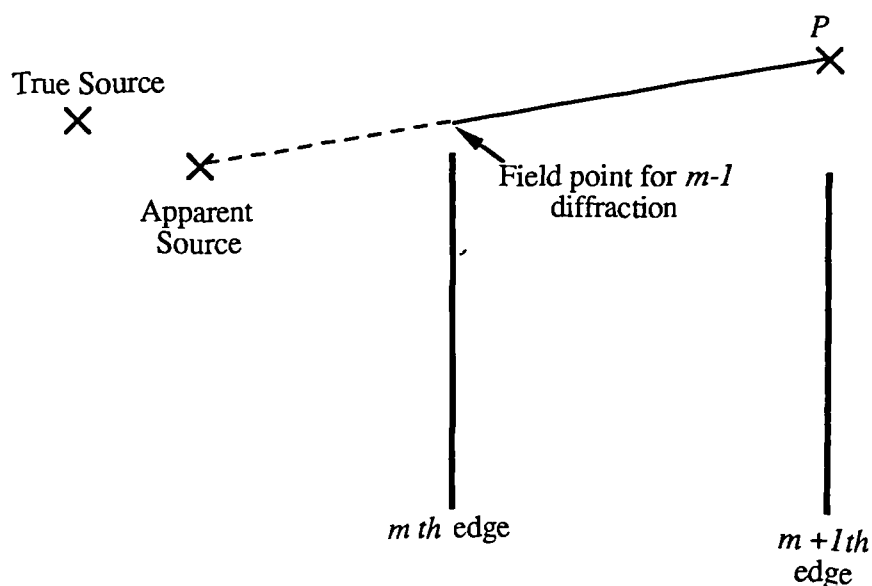


Figure 6.7: Geometry for near-field calculations

Figure 6.7 shows the general case: edge m is illuminated from the left by a point source and the resulting diffracted field is observed at a point P in the plane of the $m+1$ edge. If P is in the deep shadow region then wavefronts have a caustic at the edge, so illumination is assumed to emanate from a focal line at the edge, just as in GTD. When P is very high, the centre of curvature is at the real source and diffraction is negligible. In between these extremes is the near-field region associated with edge m . This corresponds to the transition region in GTD. In this region the focal line is allowed to shift upwards and to recede from P as the height of P is increased, following the centre of curvature calculated from Fresnel-Kirchhoff theory (see figure 6.8). This variation is the key to the technique's improvement over GTD. Having determined the position of the new focal line, this is used to represent the illumination on the $m+1$ edge and so on. The field point for observing diffraction over the $(m-1)$ edge is determined from the line joining the $(m+1)$ field point and the source as it intersects the plane of the m th edge.

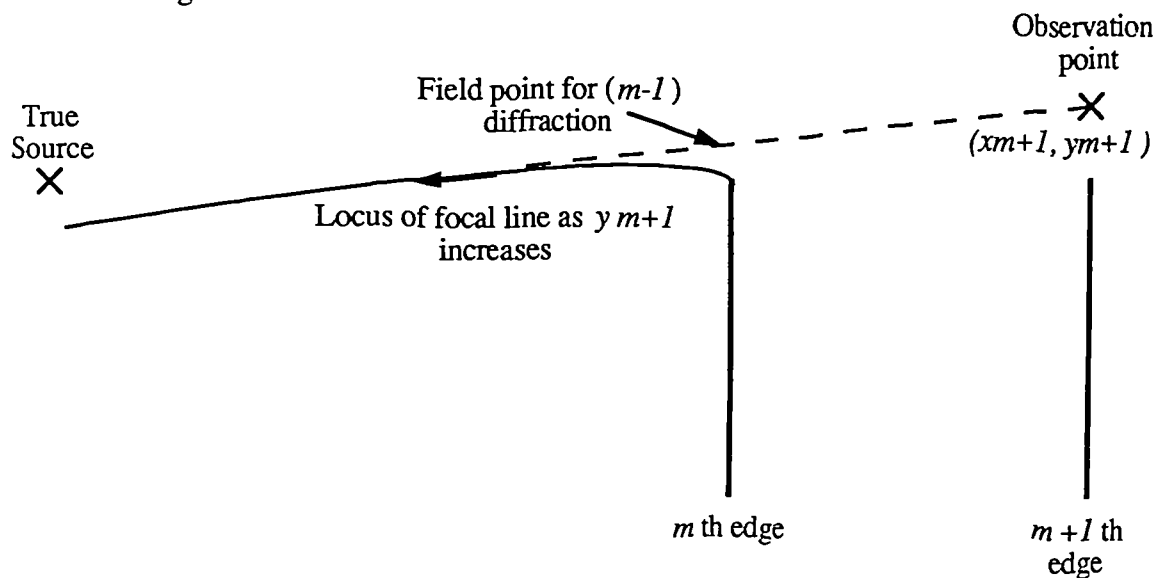


Figure 6.8: Variation of apparent source point

The first step in any analysis using the method is to determine the focal lines and field points which constitute the ray trajectory over the edges. Since only the final field point and the first source point are fixed, the focal lines are initially assumed to be coincident with the edges and iterated calculations across all the edges are made until the ray path settles. A typical path is

shown in figure 6.9. Note that the field point above each edge lies on the direct line from the previous focal line to the following field point. The ray path calculation is thus best performed by starting from the field point and working backwards towards the source. In principle the result of starting at either end should be the same according to the reciprocity theorem, but faster convergence of the path is obtained using backwards iterations.

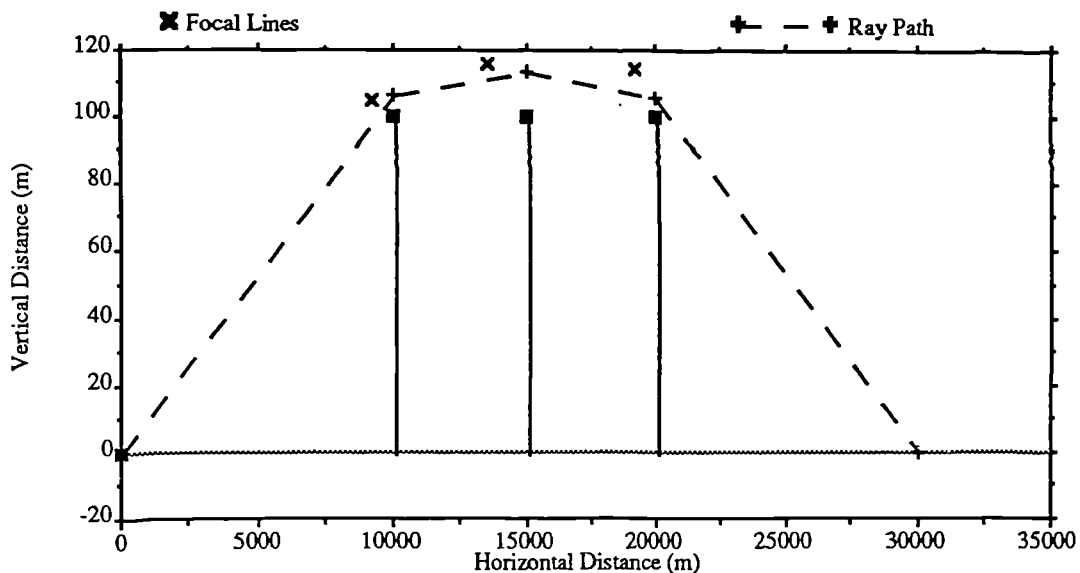


Figure 6.9: Ray path positioning in near-field method

Once the path has been determined, the Fresnel diffraction parameter for each edge is calculated relative to the ray path and repeated applications of the two-dimensional Fresnel-Kirchoff integral yield an overall path loss prediction.

Low edges

The procedure described usually works well if all of the edges are reasonably high relative to the line joining the preceding and succeeding points on the ray path. When, however, the edge is low, the wavefront is highly corrugated and a single ray is a poor description of the field. This difficulty is partially overcome by plotting a new ray path which corresponds to replacing the low edge first with a complementary edge occupying $y > y_m$ and then removing it entirely and applying Babinet's principle [Born,1980,p.381]. A 'low' edge is defined in terms of a threshold value of the Fresnel diffraction parameter. In principle this increases complexity dramatically, since new ray paths should be calculated for all combinations of complementary edges and absent edges, but Whittaker makes the approximation that of any two adjacent low

edges, the lower of the two may be removed entirely. The ray path is also assumed to be unaffected by a complementary edge for more than two edges in either direction. This prevents calculation time from rising exponentially with the number of edges, but limits the accuracy available. Trials were performed where all complementary ray paths were calculated. The prediction accuracy improved in some cases, but generally the improvement is not justified by the increase in computation time.

A further limitation to the method exists. In regions where the radius of curvature varies rapidly small errors in the field point positioning can cause large errors in the ray path calculation and hence large prediction errors. An heuristic extension to the theory is therefore suggested by Whittaker : over a certain range of the diffraction parameter, the wavefront curvature is calculated as an average over approximately the effective aperture. This extension to the theory does improve the calculated results in many cases (see comparisons below), but the improvement is strongly dependent upon the particular situation under analysis. In some cases the results may be highly unreliable. Although various remedies were attempted to improve this situation, it was eventually concluded that the rapidity of spatial variation of the field in many multiple edge cases is simply too great to be approximated by a method based fundamentally upon the properties of single edge diffraction.

Calculations

Here the variants of the near-field method are applied to the same situations as used in §6.1.1 for comparison purposes. Figure 6.10 shows that the method provides considerably better prediction accuracy than Giovanelli in the first situation, particularly around $h_2 = 100\text{m}$ (compare with figure 6.2). Some errors are evident for large h_2 in the basic method, which are mitigated to a large extent by the use of the heuristic extension. At some isolated points, however, the ray path calculation in the extended case fails and large errors result. This is due to an abrupt change in the calculated edge types resulting in errors in the ray path calculation. A different definition of a low edge will change the points at which this occurs, but no consistently better definition was found.

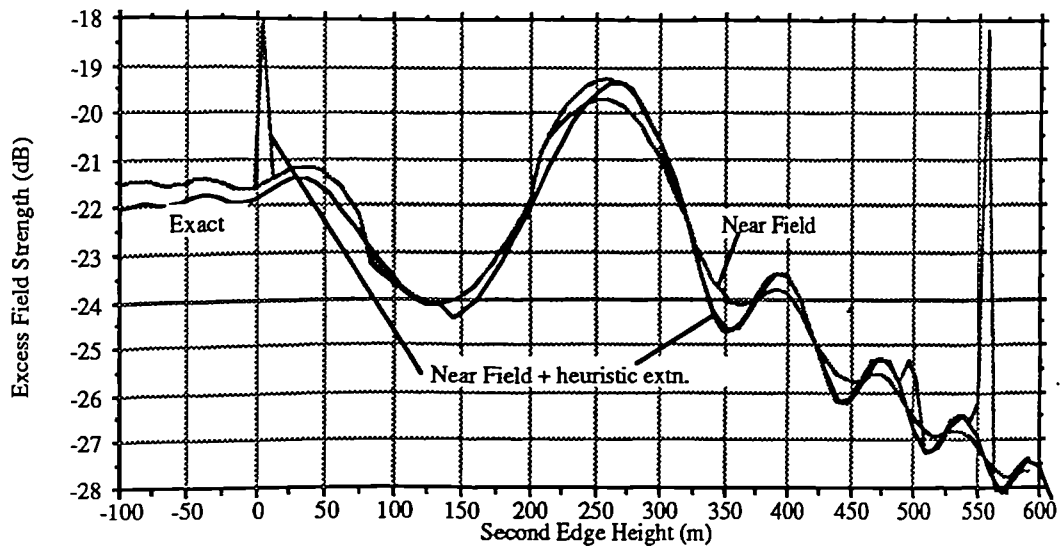


Figure 6.10: *Near Field evaluation (1)*

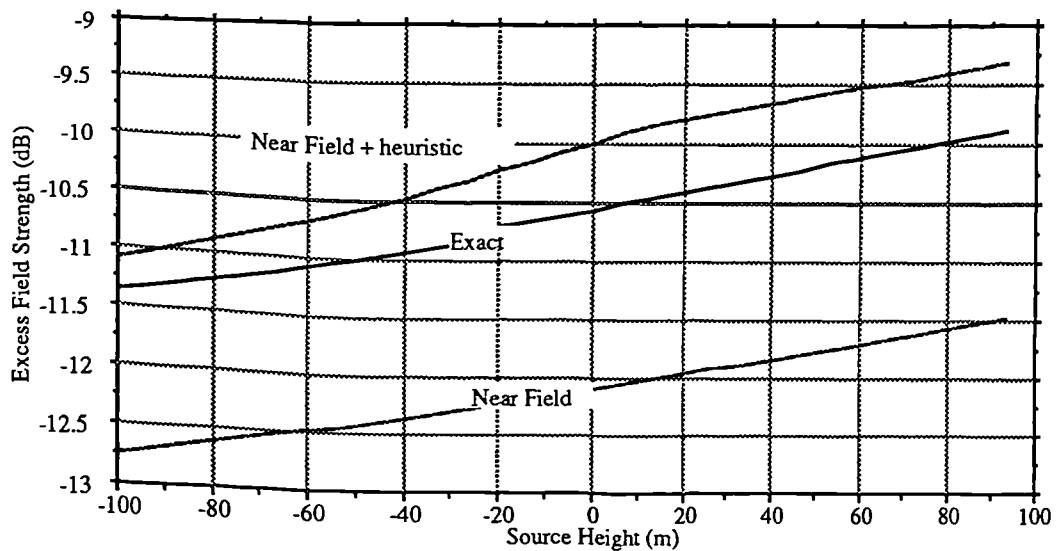


Figure 6.11: *Near Field evaluation (2)*

Results for the three edge grazing problem (figure 6.11) show a still greater improvement over the Giovanelli geometrical approximation, with the improvement produced by the heuristic extension being particularly marked in this case.

Finally, figure 6.12 shows that the heuristic extension allows the near-field method to be used for up to five edges at grazing incidence. Beyond this value, however, the results are unreliable.

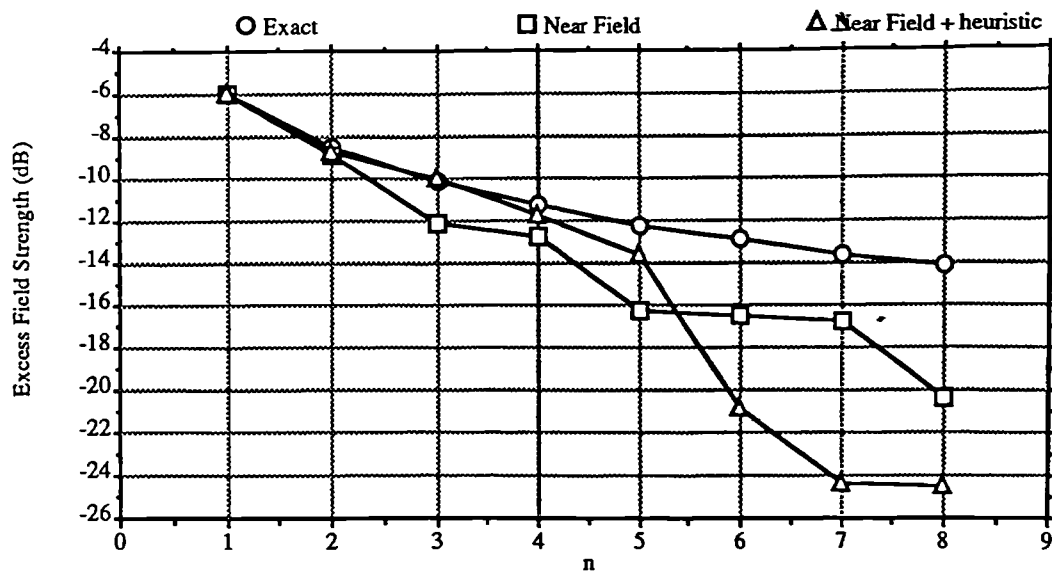


Figure 6.12: *Near Field evaluation (3)*

In conclusion, the near field method is an interesting and unusual approach to calculating multiple edge effects. Its principal appeal is in the extension of a ray method to overcome the usual difficulties of GTD within transition regions, thus retaining a physical description of the propagation process. The method is reasonably rapid to compute and is capable of acceptable accuracy within certain limits. However, since the method lacks the analytical rigour of GTD, its results are frequently unpredictable : it should thus be used with care in any cases where accurate results are important. Its main application would probably be in terrain diffraction analysis where the number of edges of importance is usually small.

6.1.3: Double Knife Edge Diffraction

$$a, b, c \gg h_1, h_2, \lambda$$

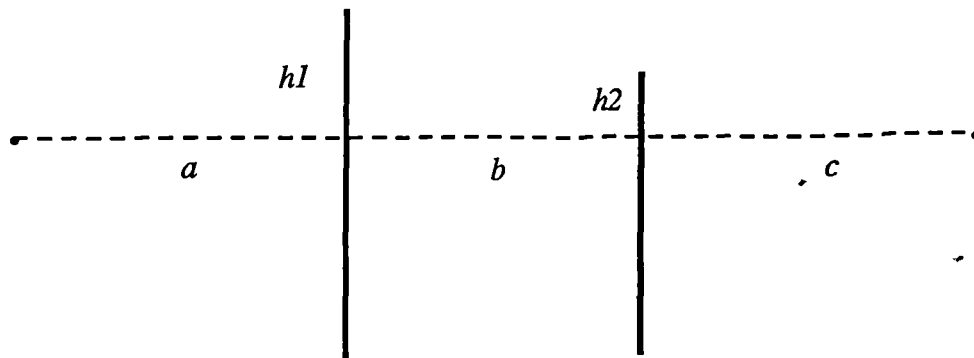


Figure 6.13: Geometry for double knife-edge solution

This problem of two edges with arbitrary positioning (figure 6.13) has been solved analytically by Millington *et al.* [Millington,1962] using Fresnel-Kirchhoff assumptions. The attenuation function A can be expressed in terms of a Fresnel surface integral F_2 as follows:

$$A = -\frac{j}{2} F_2$$

$$\text{where } F_2 = \int_S \exp\left(\frac{j\pi\rho^2}{2}\right) dS$$

is a surface integral taken over the region shown in figure 6.14, where ρ is the distance from the origin to the integration point.

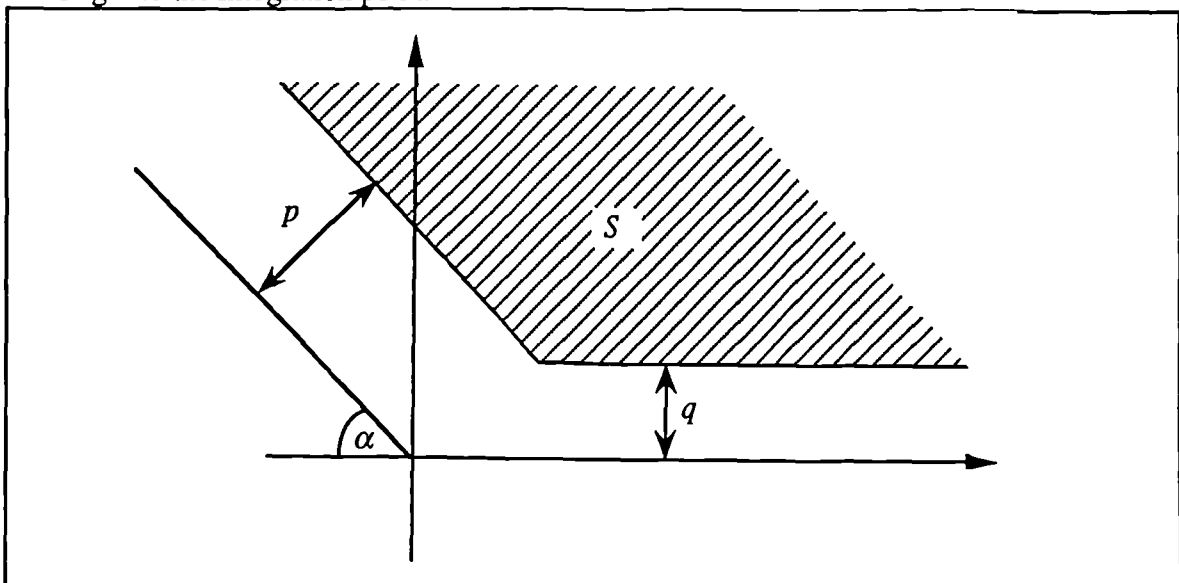


Figure 6.14: Region of integration for double knife-edge problem

The geometry of the region is related to the physical geometry of the problem as follows:

$$\sin \alpha = \sqrt{\frac{b(a+b+c)}{(a+b)(b+c)}}$$

$$p = h_1 \sqrt{\frac{2(a+b+c)}{\lambda a(b+c)}}$$

$$q = h_2 \sqrt{\frac{2(a+b+c)}{\lambda (a+b)c}}$$

Another paper is devoted [Millington,1962b] to methods of evaluating the integral.

Whittaker [Whittaker,1990] has used the method to calculate diffraction over a flat topped reflecting obstacle. Essentially the solution is the same as that for 2 edges, plus a field contribution reflected from the top of the obstacle in the same form as the direct field.

A comparison between measurements and two edge theory for a flat topped building is now given as an example. The geometry of the building is shown in figure 6.15.

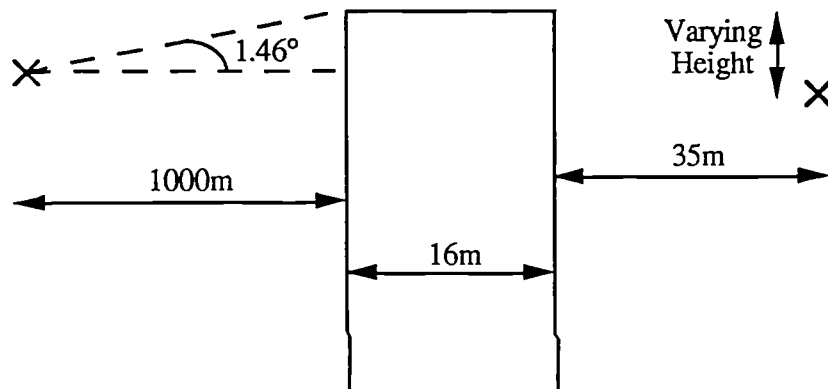


Figure 6.15: Geometry for building measurements

The measurements are taken from [Haslett,1991], and were made at 11.2GHz. Two different approaches to modelling are used : the first is a single knife edge placed at the building face closest to the field point, while the second uses two edges, one for each building face.

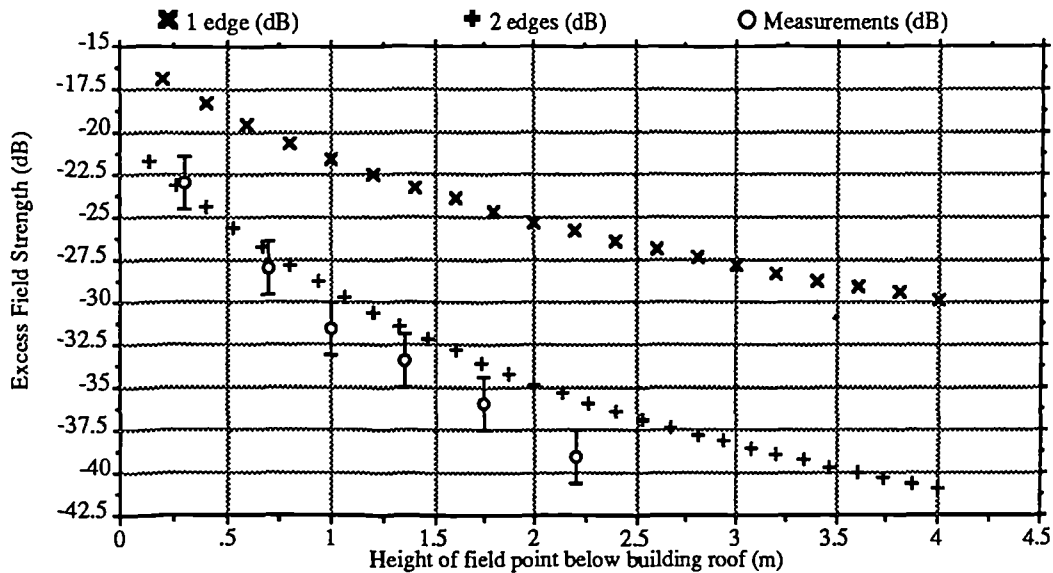


Figure 6.16: Comparison of predictions with measurements for a flat roofed building

The results are shown in figure 6.16: the two edge approach is by far the most successful, showing good agreement with the measurements, although with some tendency to underestimate the loss as the field point is moved into deeper shadow. The single edge representation shows a more serious loss underestimate. Building geometry should thus be taken into account whenever appropriate data exists. A single edge representation is likely to be more acceptable for near-grazing incidence or for buildings with pointed rooves.

The Millington two-edge method has not been widely used in propagation predictions, however, due to the complexities of evaluation and due to the fact that approximate methods are capable of acceptable approximations in the two edge case, but it is useful as a standard of comparison. In principle the method could be directly extended to more than two edges, but the resulting geometry of the integration region becomes impractical to handle. The next section examines a more complete approach to multiple knife edge diffraction.

6.2: The Multiple Edge Diffraction Integral

6.2.1: Development of the Integral

In 1963 Furutsu [Furutsu,1963] published complete expressions for propagation over various configurations of inhomogeneous terrain. One of the cases considered was a two dimensional representation of propagation over multiple cascaded circular cylinders, which includes the multiple knife edge case when the radius of curvature becomes vanishingly small. The results were given in the form of a residue series, which is slow to converge in the knife-edge case. Using a variation on a procedure described by [Bremmer,1949] the series was transformed by Vogler [Vogler,1981] into a multiple integral representation of the attenuation function. Essentially the same representation was derived by [Sharples,1989] using repeated applications of Green's theorem. The same author also showed that the non-zero cylinder radius case may be treated as the superposition of the field due to an array of equivalent knife edges with a perturbation term to describe the effect of the cylinders' non-zero radii and surface impedances. The multiple edge integral is therefore an important result and will be examined in some depth here.

6.2.2: The Multiple Edge Integral

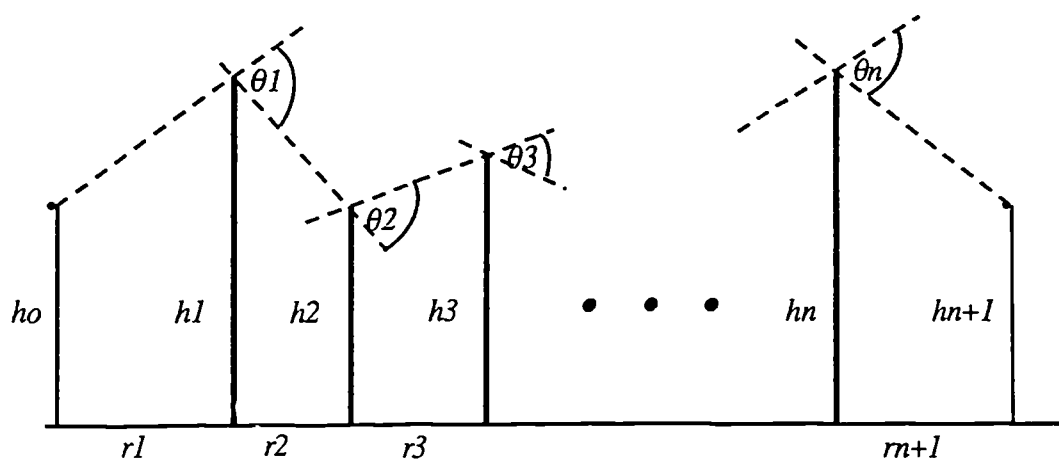


Figure 6.15: Geometry for the multiple edge integral

Vogler [Vogler,1981] expresses the attenuation due to n knife edges as :

$$A_n = C_n \pi^{-n/2} e^{\sigma_n} I_n \quad (6.4)$$

where :

$$I_n = \int_{\beta_n}^{\infty} \dots \int_{\beta_1}^{\infty} \exp \left\{ 2f - \sum_{m=1}^n x_m^2 \right\} dx_1 \dots dx_n \quad (6.5)$$

with

$$f = \sum_{m=1}^{n-1} \alpha_m (x_m - \beta_m)(x_{m+1} - \beta_{m+1}) \quad \text{for } n \geq 2$$

where

$$\alpha_m = \sqrt{\frac{r_m r_{m+2}}{(r_m + r_{m+1})(r_{m+1} + r_{m+2})}} ; m = 1, \dots, (n-1)$$

Note that $0 < \alpha_m < 1$.

$$\beta_m = \theta_m \sqrt{\frac{jk r_m r_{m+1}}{2(r_m + r_{m+1})}} ; m = 1, \dots, n$$

$$\sigma_n = \beta_1^2 + \dots + \beta_n^2$$

$$C_n = \sqrt{\frac{r_2 r_3 \dots r_n r_T}{(r_1 + r_2)(r_2 + r_3) \dots (r_n + r_{n+1})}}$$

$$r_T = r_1 + \dots + r_{n+1}$$

and the geometrical parameters are defined in figure 6.15 (note that θ_1 and θ_3 are positive in this diagram, θ_2 is negative.)

This expression is valid in general, subject only to the usual assumptions of the Kirchhoff-Fresnel theory. It therefore potentially constitutes an extremely powerful tool, provided that efficient methods of evaluation can be found. This problem is non-trivial, since some of the characteristics of the integral present special computational difficulties. Additionally, the high dimensionality of the integral when n is large makes computation slow. These characteristics will now be examined in detail.

6.2.3: Characteristics of The Integral

Here the behaviour of the integrand in particular cases is examined to illustrate the difficulties involved in evaluating the integral. This is most easily done if the integral is expressed in a slightly different form:

The β_m terms can be expressed as :

$$\beta_m = b_m \sqrt{j}$$

where the b_m are entirely real. Now under the transformation $u_m = x_m - \beta_m$ the argument of the exponential may be rearranged as:

$$\begin{aligned} 2f - \sum_{m=1}^{n-1} x_m^2 &= - \left\{ (u_1 + b_1 \sqrt{j})^2 + \dots + (u_n + b_n \sqrt{j})^2 \right\} \\ &\quad + 2 \sum_{m=1}^{n-1} \alpha_m u_m u_{m+1} \\ &= \sum_{m=1}^{n-1} \left\{ 2\alpha_m u_m u_{m+1} - (u_m + b_m \sqrt{j})^2 \right\} - (u_n + b_n \sqrt{j})^2 \\ &= \sum_{m=1}^{n-1} \left\{ 2\alpha_m u_m u_{m+1} - u_m^2 - \sqrt{2} u_m b_m \right\} - u_n^2 - \sqrt{2} u_n b_n - j \sum_{m=1}^n \left(\sqrt{2} u_m b_m + b_m^2 \right) \\ &\equiv A - j B \end{aligned}$$

where:

$$\begin{aligned} A &= \sum_{m=1}^{n-1} \left\{ 2\alpha_m u_m u_{m+1} - u_m^2 - \sqrt{2} u_m b_m \right\} - u_n^2 - \sqrt{2} u_n b_n \\ B &= \sum_{m=1}^n \left(\sqrt{2} u_m b_m + b_m^2 \right) \end{aligned}$$

The term in b_m^2 in the definition of B may be neglected without affecting the magnitude of the

attenuation function, and this convention will be adopted from now on. The integral is now in the following form:

$$I_n = \int_0^\infty du_1 \cdot \dots \cdot \int_0^\infty du_n \left\{ e^A [\cos(B) - j \sin(B)] \right\}$$

The integral may now be separated into its real and imaginary parts, resulting in two real integrals with fixed limits which may be examined directly. Notice firstly that, when all of the edges are at grazing incidence, $b_1, \dots, b_n = 0$, so $B = 0$ and I_n is entirely real.

The b_m parameters can be expressed in terms of the Fresnel zone radius as follows:

$$b_m = \theta_m \sqrt{\pi} \frac{R_1}{\lambda}$$

where R_1 is the radius of the first Fresnel zone about a ray joining the $(m-1)$ and the $(m+1)$ edges. Thus these terms are analogous to the Fresnel integral argument w in the single edge calculation, while the α_m terms express the coupling between adjacent edges. When there is little coupling ($r_{m+1} \gg r_m, r_{m+2}$), the α_m term is negligible so the m and $(m+1)$ integrals may be separated into the product of two independent terms. In such cases approximate methods such as the Giovanelli method may be applicable.

Now consider the e^A factor which appears in both integrands. The factor diminishes as $\exp(-u_m^2 - u_m b_m \sqrt{2})$ along any of the u -axes, but less quickly elsewhere due to the positive exponents of the form: $\exp(2 \alpha_m u_m u_{m+1})$. Resulting from this behaviour the exponential factor reaches a maximum when A is maximised. This occurs when:

$$\frac{\partial A}{\partial u_j} = -2u_j + 2 \alpha_j u_{j-1} + 2 \alpha_{j-1} u_{j-1} - \sqrt{2} b_j = 0; j = 1, \dots, n$$

This maximum does not necessarily occur within the domain of integration. When the b_m are small (near-grazing incidence) the major contribution to the integral will come from a region close to this maximum, so the limits of integration may be truncated for easier evaluation. In physical terms this truncation is equivalent to placing a conceptual inverted half plane in the aperture of the real half-planes, sufficiently high as to make no material difference to the

resulting field.

The integrand is now plotted for some simple two edge configurations. The first case (figure 5.16) produces the smooth, symmetrical and always positive function illustrated in figure 6.17.

In such cases the integral is relatively easy to evaluate.

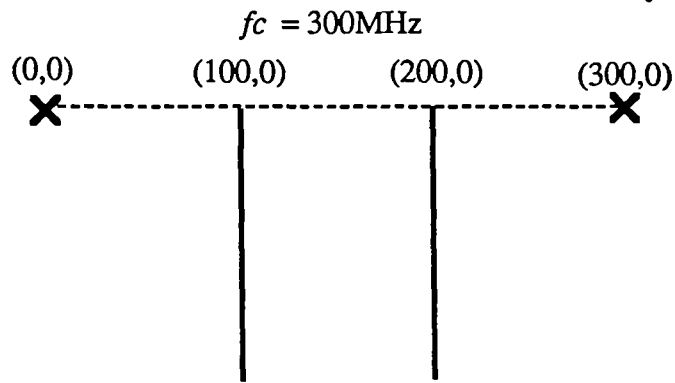


Figure 6.16: First edge geometry for examination of integrand

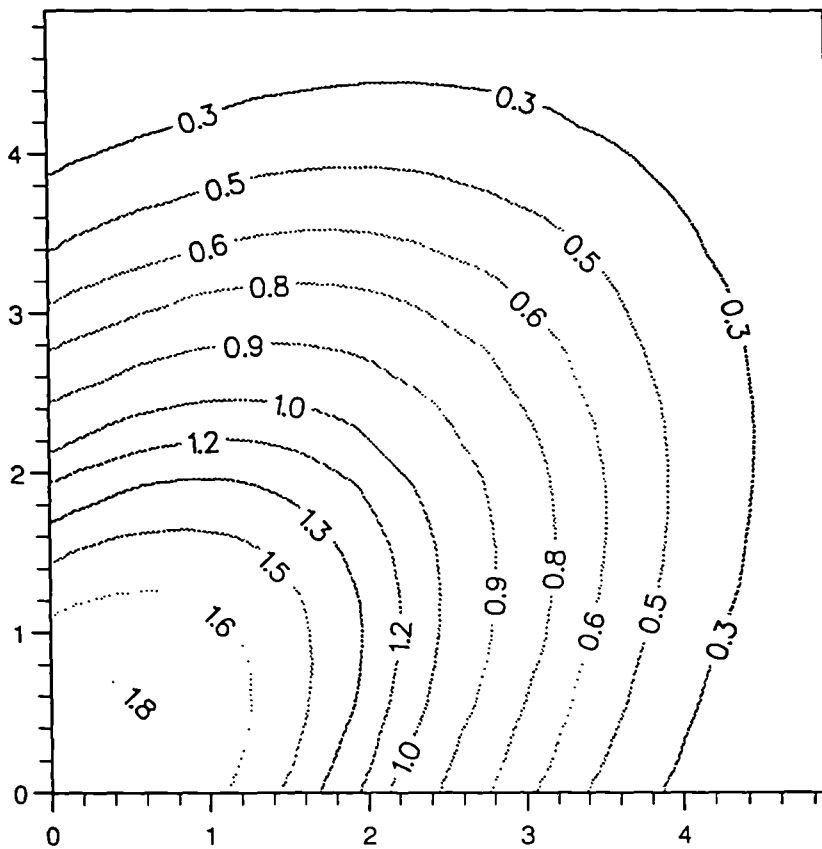


figure 6.17: Integrand in first case

In the second problem, the first edge is allowed to move along the line between the source and the second edge, affecting the coupling between the edges. When the coupling is large the α term is large and the integrand decays only slowly away from the maximum.

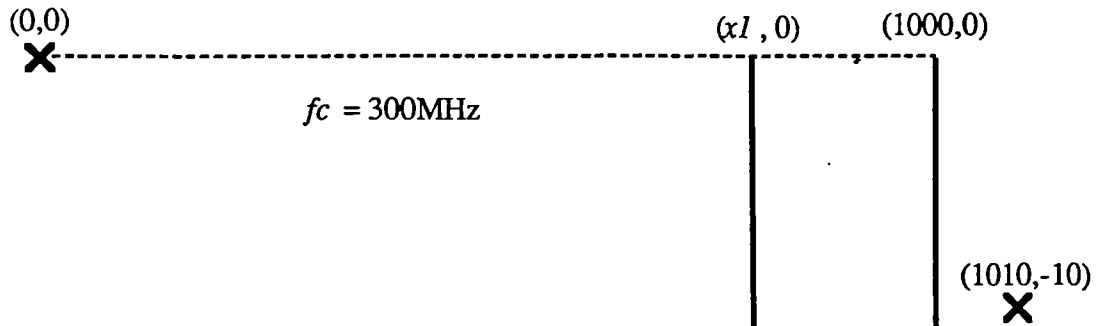


Figure 6.18: First edge geometry for examination of integrand

Figure 6.19 shows the results with relatively little coupling ($\alpha_1 = 0.3, x_1 = 900$), neglecting the oscillatory component in the integrand for the time being. In this case, the major contribution is still close to the origin, but some asymmetry has been introduced, reflecting the asymmetry in the edge arrangement.

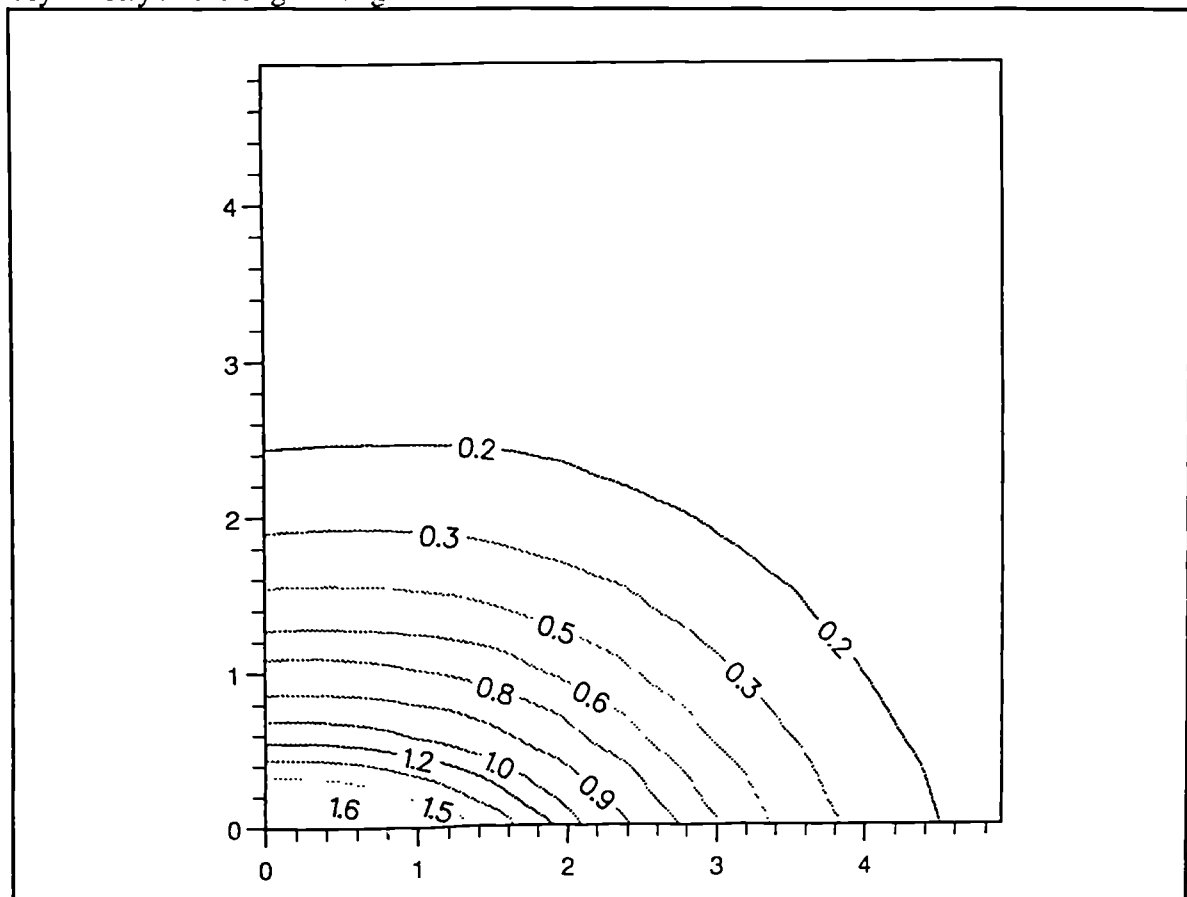


Figure 6.19: Integrand in second case, exponential part only. $x_1 = 900$

In the next case the edges are much closer, ($\alpha_1 = 0.95$, $x_1 = 999$). Now figure 6.20 shows a greater contribution away from the origin, with the integrand diminishing only slowly away from the axes where the term in α has the greatest effect. In a practical evaluation method this would usually require a greater number of integrand evaluations to be made, resulting in a longer evaluation time.

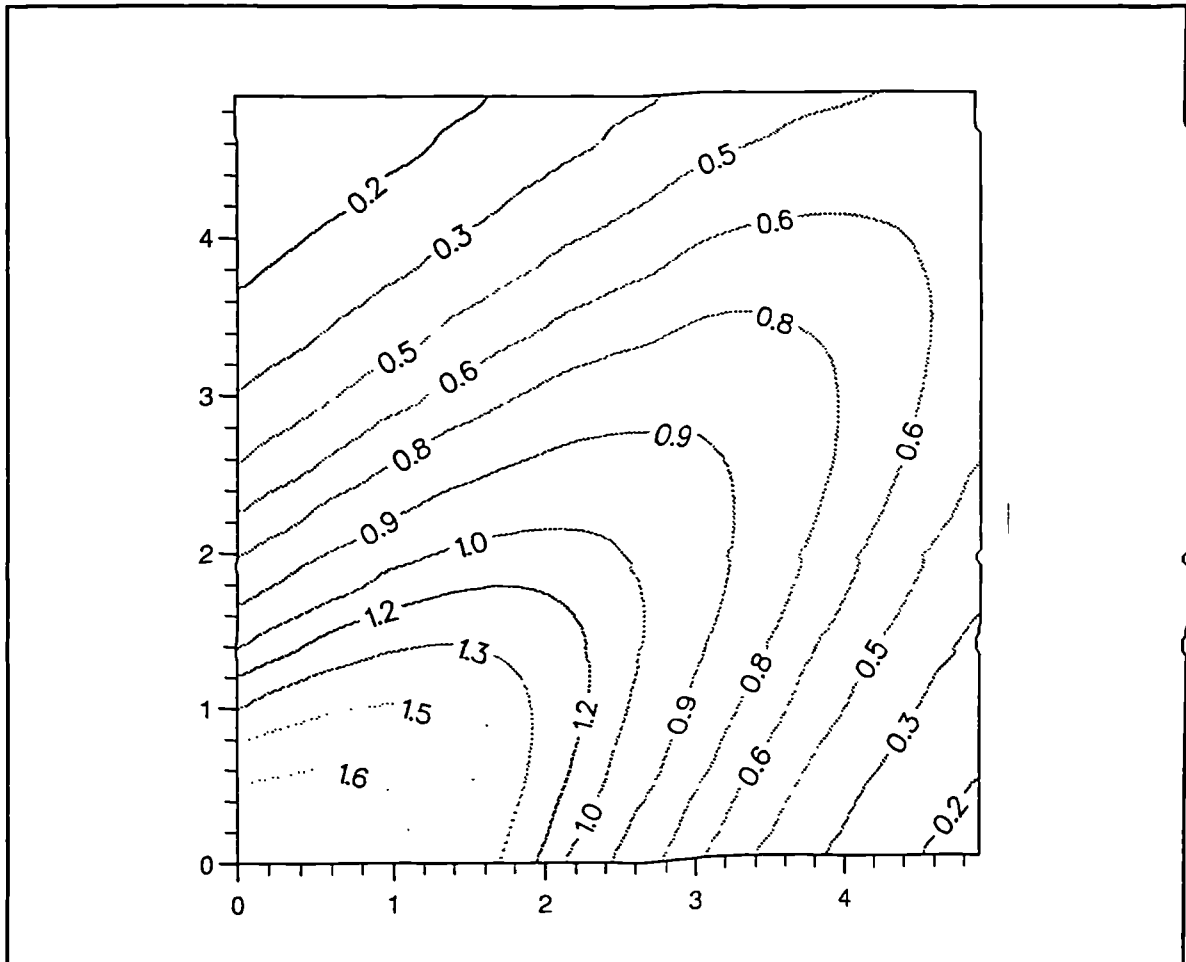


Figure 6.20: *Integrand in second case, exponential part only. $x_1 = 999$*

The cosine and sine terms in the integrands make them oscillatory away from grazing incidence. Positive and negative contributions from adjacent half-cycles tend to cancel, leaving only a small difference which constitutes the complete result. Such processes are very prone to numerical round-off errors. The frequency of oscillations increases with the b_m and hence with the diffraction angles θ_m . In figures 6.21a and 6.21b the real and imaginary parts of the complete integrand is illustrated for the same edge arrangement with $x_2 = 990$.

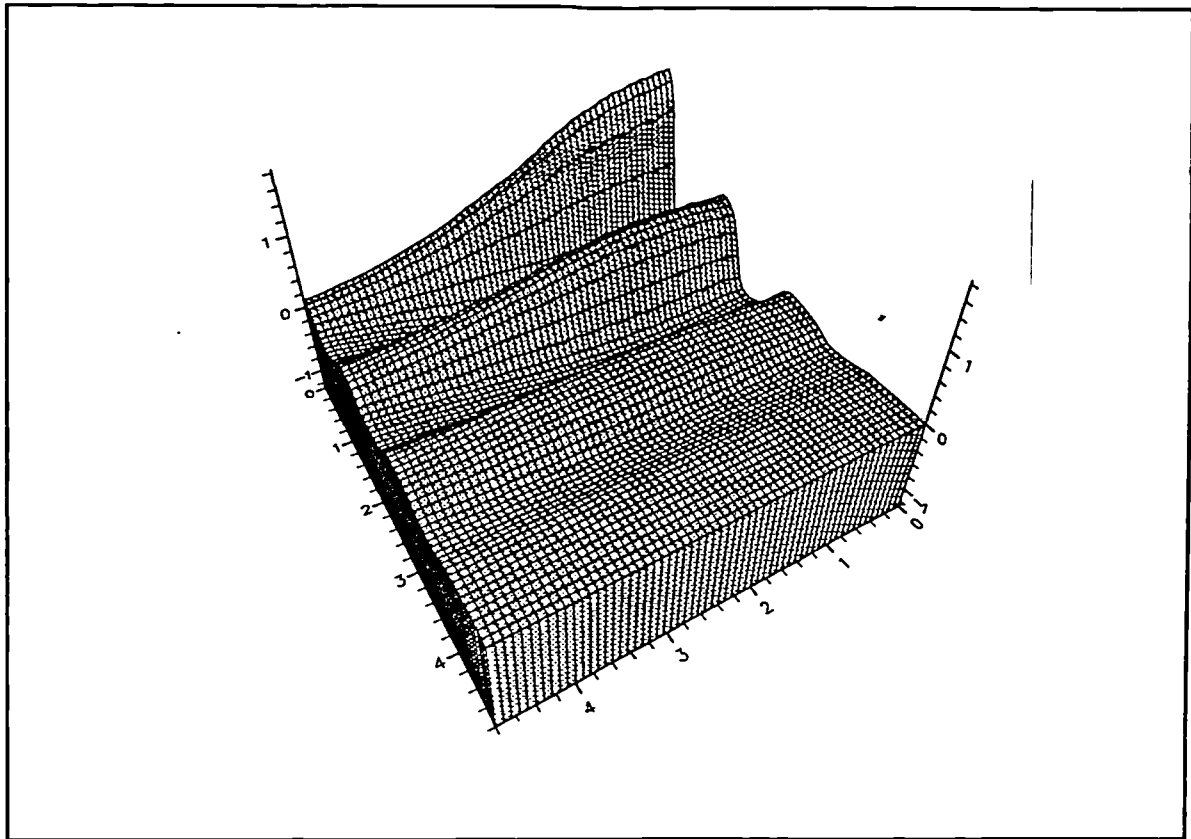


Figure 6.21a: Real part of integrand

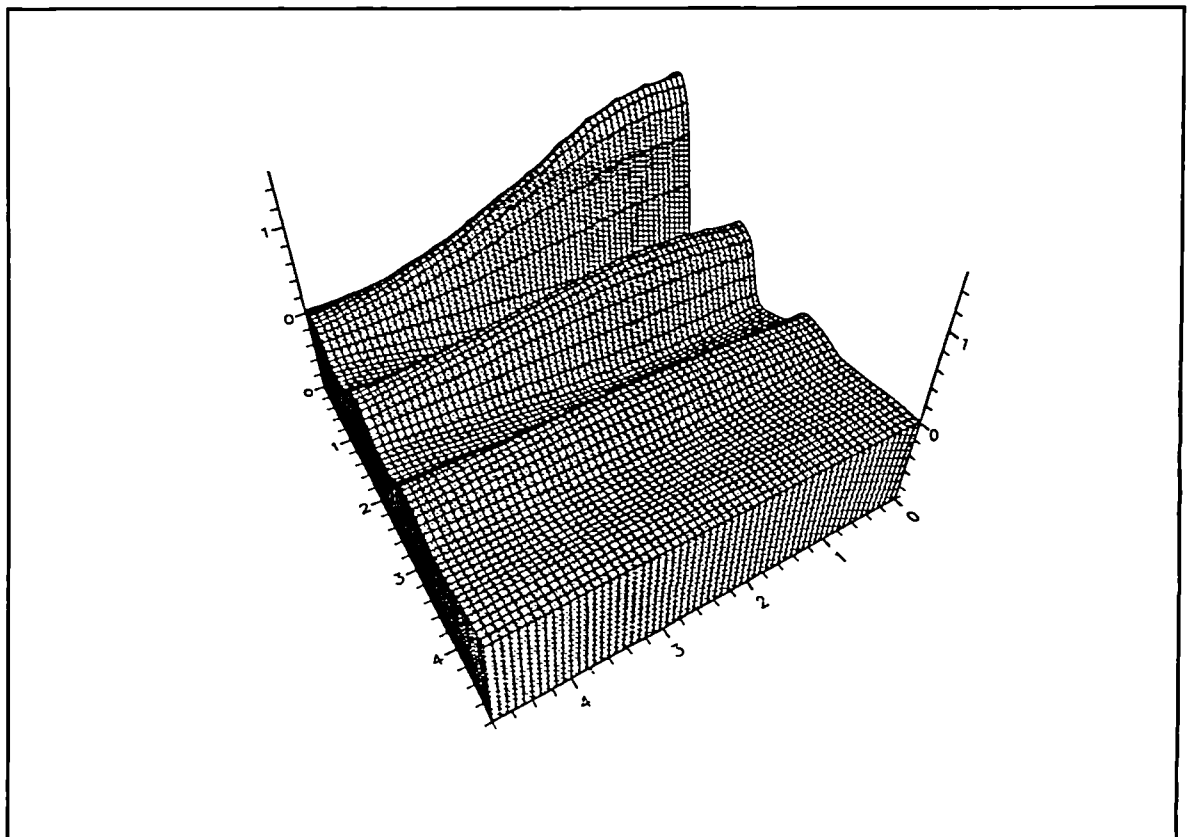


Figure 6.21b: Imaginary part of integrand

Note that there is no oscillatory behaviour along one axis since the source, edge 1 and edge 2 are in line, while the other axis shows variation resulting from a positive diffraction angle θ_2 .

In summary, the principle difficulties in evaluation of the integral come from situations where edges are very close, resulting in high coupling and slow decay of the integrand away from the maximum. Other difficulties occur when edge heights are highly irregular, causing oscillatory behaviour of the integrand, although this problem may be mitigated to some extent by removing edges which are low enough not to substantially affect the field. A procedure for doing this is given in §7.2.

6.3: Closed Form Solutions of Multiple Edge Diffraction

The solutions examined here are essentially complete solutions of the multiple edge integral which apply to a special set of cases. Closed form solutions are to be preferred whenever possible since they allow very rapid evaluation compared to numerical evaluation of the general problem. They also provide insight into the nature of the solution via examination of their form. The limitations are that such solutions exist only for a very limited set of edge arrangements, and their initial formulation requires a large amount of analytic effort. All previously published solutions have been for grazing incidence situations only, although a more general solution will be presented in Chapter Seven.

When all of the edges and the source and field points are colinear (figure 6.22), the multiple edge integral is equivalent to a formulation derived by Lee [Lee,1978] using a method of path integrals. This formulation is solved by Lee for certain special cases. These solutions are presented here since they are useful results in themselves and because they were used extensively in developing the more general evaluation methods described next.

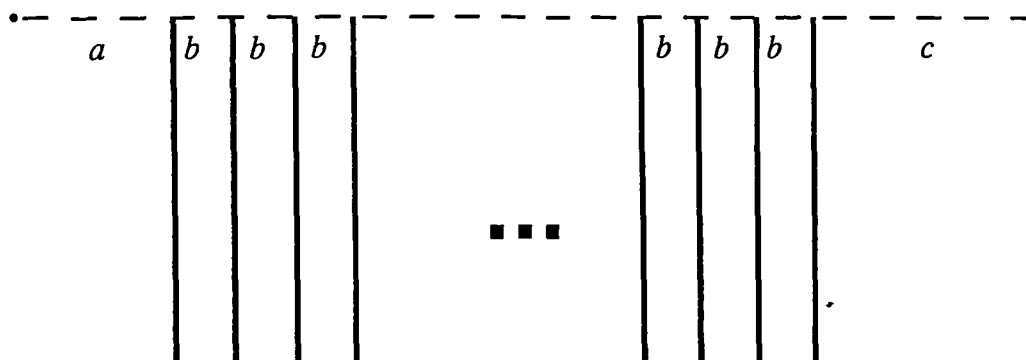


Figure 6.22: Colinear edge arrangement

If $a \rightarrow \infty$ and $c \rightarrow \infty$ then the attenuation function takes on the following form:

$$A_n = \frac{1}{2}$$

This implies that, when the spacing between the edges is small compared with their distances from the source and field points, a system of edges may be replaced by a single equivalent edge.

If $a \rightarrow \infty$ and $c = 0$, or $c \rightarrow \infty$ and $a = 0$ then:

$$A_n = \frac{\Gamma\left(n - \frac{1}{2}\right)}{2(n-1)! \Gamma\left(\frac{1}{2}\right)}$$

If $a = b$ and $c = 0$, or $a = 0$ and $c = b$ then:

$$A_n = \frac{1}{2n}$$

If $a = 0$ and $c = 0$, then:

$$A_n = \frac{1}{4(n-1)}$$

If $a = b = c$ then :

$$A_n = \frac{1}{(n+1)}$$

This case is very useful for testing evaluation schemes of the more general multiple edge problem since, in this case, all of the α_m and b_m parameters are equal.

If $a \rightarrow \infty$ and $c = b$, or $c \rightarrow \infty$ and $a = b$ then:

$$A_n = \frac{\Gamma\left(n + \frac{1}{2}\right)}{n! \Gamma\left(\frac{1}{2}\right)}$$

This is an important practical case for determining the effect of plane wave incidence onto a

series of rooftops as received at a point on the final rooftop. The result is plotted in figure 6.23: it is clear that every additional edge reduces the field strength, although the effect per edge decreases as n is increased.

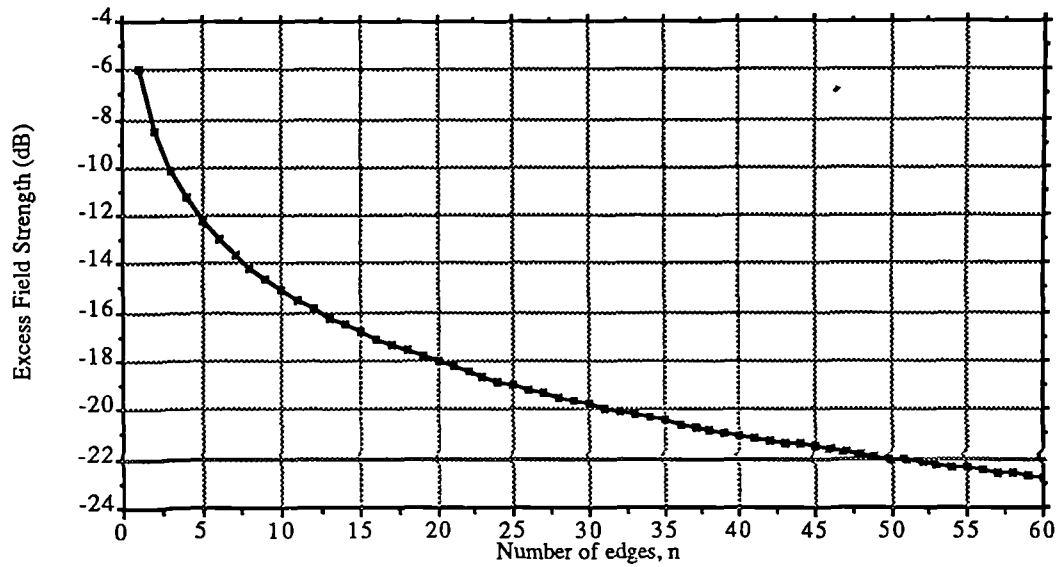


Figure 6.23: *Plane wave incidence on multiple edges at grazing incidence*

The task of §7.1 will be to extend this result to include arbitrary angles of incidence.

6.4: Methods of Evaluating the Multiple Edge Integral

6.4.0: Introduction

This section examines a number of methods of evaluating the multiple edge integral discussed in §6.2 in the general case, where edges may be at arbitrary positions and heights. Some of the methods will be more suited to evaluation of particular sets of edge configuration, so the methods will be examined according to their suitability for the multiple building case, where edges are usually illuminated from above. The important criteria for determining a method's usefulness are as follows:

- i) Speed: This is the most significant factor. Many calculations may be needed in a short time, particularly for area coverage applications, so even small speed improvements may be important.
- ii) Accuracy: In all of the methods presented here, essentially arbitrary accuracy may be obtained if sufficient time is available (subject to numerical limitations). It is important, however, that a method provides an appropriate measure of accuracy to determine how long to allow the evaluation process to continue, or else that the accuracy may be reasonably well estimated in advance.
- iii) Computing resources : In addition to processing time, some methods use large quantities of storage space, which may be limited in some cases.

6.4.1: The Vogler Evaluation

The overall method proposed in [Vogler,1981] is as follows:

$$A = \frac{C_n e^{\sigma_n}}{2^n} \sum_{m=0}^{\infty} I_m$$

$$\text{where } I_m = 2^m \sum_{m_1=0}^m \alpha_1^{m-m_1} I(m-m_1, \beta_1) C(2, m_1, m)$$

The function $C(\cdot)$ is defined by the recursive relationship

$$C(n-L, j, k) = \sum_{i=0}^j \frac{\binom{k-i}{j-i}}{\binom{k-i}{j-i}} \alpha_{n-L}^{j-i} I(k-i, \beta_{n-L}) C(n-L+1, i, j)$$

and the terminating value :

$$C(n-1, p, q) = m_{n-3}! \alpha_{n-1}^p I(q, \beta_{n-1}) I(p, \beta_n)$$

The method was derived by expanding the exponential in the integrand into a power series, which is then integrated term by term resulting in an expression involving the function $I(n, \beta)$ (the repeated integrals of the complementary error function) which is defined by:

$$n! I(n, \beta) = \sqrt{\frac{2}{\pi}} \int_{\beta}^{\infty} (x - \beta)^n \exp(-x^2) dx$$

This function is tabulated in a number of standard texts eg [Abramowitz, 1970] and several algorithms are available for its calculation eg [Gautschi, 1961]. Most of these methods involve calculating successive terms in a power series until a given accuracy criterion is met. It has been found that many terms are required when n is large or when β is large and negative, which occurs when an edge is illuminated by a highly elevated source. The method outlined above for evaluation has been implemented in PASCAL for two different computer systems (SUN and PYRAMID) and tested extensively. The calculation of $I(n, \beta)$ requires careful programming according to the particular computer system used to avoid errors due to lack of precision in the representations used. In practice the series for A is terminated at an upper value of m appropriate to the accuracy required, which depends upon the precise arrangement of edges. In propagation applications the significant accuracy is the relative rather than absolute accuracy, so additional terms are calculated until the last term obeys the following accuracy criterion:

$$20 \log \left(1 + \frac{\text{Last Term}}{A_{sub}} \right) \leq \epsilon,$$

where ϵ_r is the required accuracy in decibels.

When the edge illumination is from above, the series requires many terms to converge and a large amount of computer storage space is occupied. Note also that the method requires the use of complex arithmetic, which is inherently slower than purely real calculations.

In order to ease the storage requirement and to make the use of the multiple edge integral more practical in the case of an elevated source and large n , alternative methods of evaluation are sought.

The first method adopted was a modification of the Vogler approach. The recursive structure

of the basic method, although elegant and simple to program, is very slow and inefficient, since the program compiler must ultimately translate the algorithm into an iterative sequence of low-level instructions. The structure of the algorithm was therefore amended to remove recursion, as follows:

- 1) Set m to 0.
- 2) Find $I(i, \beta)$ for i varying from 0 to m and for every value of β . Store the results.
- 3) Set l to $n - 1$.
- 4) Calculate $C(l, i, m)$ for i varying from 0 to m using stored values of $C(n-l+1, i, m)$ and store the result.
- 5) If $l > 2$ then decrement l and go to (4).
- 6) Use stored values of $C(2, \dots)$ to find I_m . Add this to the running total.
- 7) If I_m does not obey the accuracy criterion then increment m and go to (2).

No recursion is required now, since the modified algorithm uses only previously calculated and stored values of $C()$ at any stage. Also it avoids the recalculation of previously calculated values of $C()$. The penalty for this improvement is that greater storage space is required for the values of $I()$ and $C()$. To examine the performance of this method and those to be described subsequently, the problem illustrated in figure 6.24 is used.

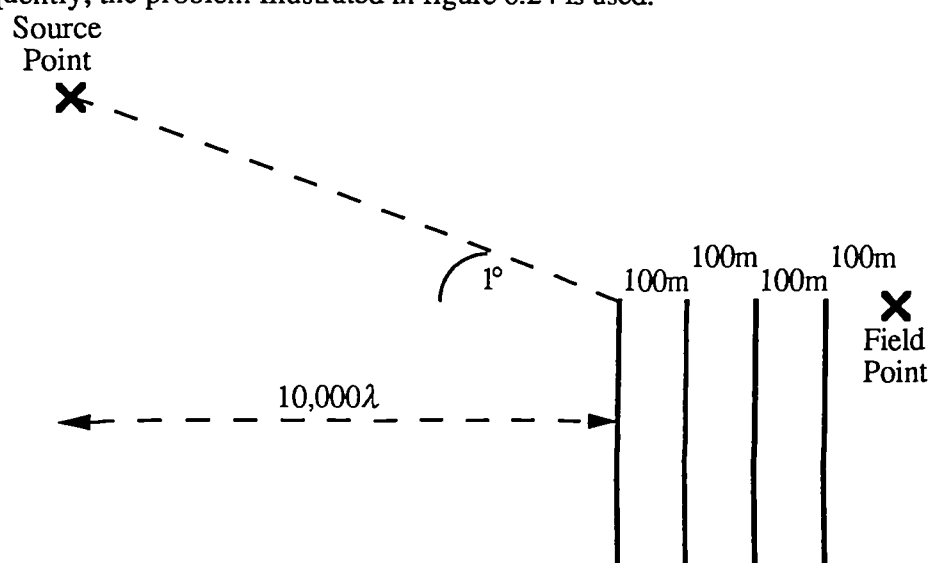


Figure 6.24: Edge configuration for comparison of evaluation methods

This problem is chosen for two reasons : first the problem is an important configuration for multiple building problems and secondly the method derived in §7.1 allows exact values for this problem to be found so that errors can be properly calculated.

Figure 6.25 compares the evaluation times required for the straightforward recursive method and for the modified iterative method as the number of edges is varied, with the accuracy set at 1dB. In both cases the times shown are user cpu times for a PYRAMID mainframe.

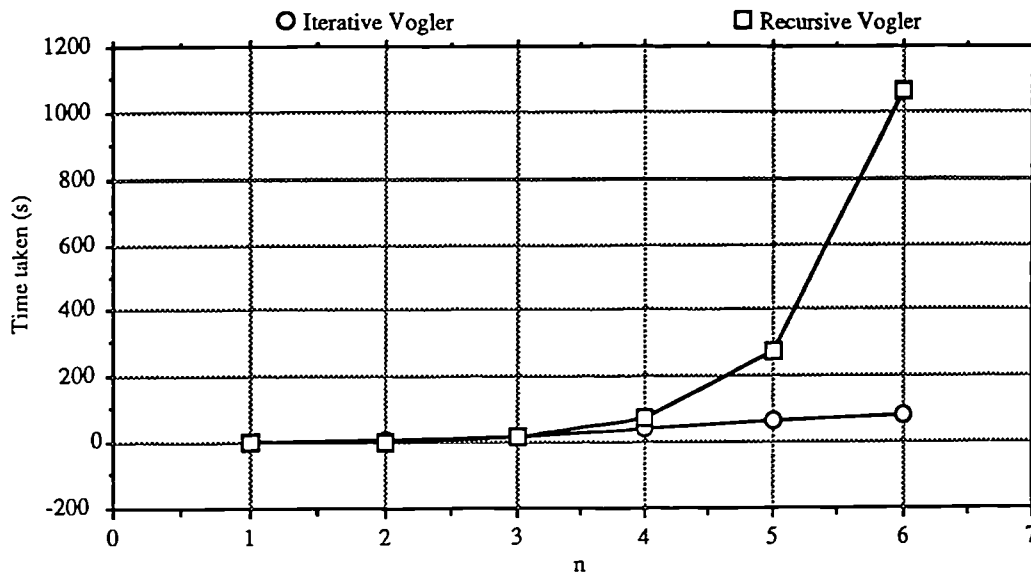


Figure 6.25: Timing for Vogler evaluation

It is clear that the iterative method is a considerable improvement over the recursive approach. The execution time does, however, rise rapidly with n in both cases due to the increased number of terms required for a given accuracy for large n . Also the execution time is strongly dependent upon the particular problem due to the time required to calculate $I(n, \beta)$. The time taken is particularly large in large n cases where β is large and negative. Other methods were therefore examined.

6.4.2: Quadrature Methods

Most conventional formulæ for the numerical evaluation of multiple integrals are of the following form:

$$\int_{R_n} dx_1 \dots dx_n w(x_1, \dots, x_n) f(x_1, \dots, x_n) \approx \sum_{i=1}^P C_i f(v_{i,1}, \dots, v_{i,n})$$

where the B_i are the **coefficients** and the v_i are the **abscissæ** of the formula, all of which are chosen to make the approximation a good one for the smallest possible P , the number of points in the formula [Stroud,1971]. The $w(x)$ is a weighting function. The theory of such formulæ for univariate integration is well established, but the multivariate case presents a number of extra difficulties. Firstly, the construction of integration formulæ depends closely on the theory of orthogonal polynomials, which is well known and complete for one variable, but is only known for special cases when $n > 1$. Next, functions of several variables usually take considerably longer to evaluate than one dimensional functions. Finally, more points are required to obtain acceptable accuracy with a multiple integral, causing computation times to be long.

If a formula has *degree of exactness*, d , then it produces exact results (within machine accuracy) for all $f(x)$ which are polynomials of degree $\leq d$, and there exists at least one polynomial of degree $(d+1)$ for which it is not exact. In the case of primitive formulæ such as Simpson's rule, $d = N$, where N is the number of points used in each dimension. Using the theory of orthogonal polynomials, **Gaussian** formulæ may be constructed having $d = 2N - 1$, which is the highest possible using only N points. Gaussian formulæ therefore represent an optimum in some sense. The success of such formulæ then depends upon how closely the integrand resembles a polynomial of degree $\leq d$.

For the multiple edge integral the polynomial behaviour is improved by separating out the major part of the decay term in the multiple edge integral as follows:

$$A_n = \int_0^\infty dx_1 \dots \int_0^\infty dx_n \exp(-x_1^2 - \dots - x_n^2) f(x_1, \dots, x_n)$$

This suggests the use of a weight function $w(x)$ with:

$$w(x) = \exp(-x_1^2 - \dots - x_n^2)$$

A standard univariate Gaussian rule for $w(x) = \exp(-x^2)$ is available, based upon the zeros of the Hermite polynomials [Davis,1975], p34, but these are defined relative to $[-\infty, \infty]$. It is possible to simply define the integrand as zero on $[-\infty, 0]$, but this is an inefficient approach. A search of the literature reveals a Gaussian formula for the evaluation of:

$$\int_0^b \exp(-x^2) f(x) dx \text{ and } \int_0^\infty \exp(-x^2) f(x) dx$$

This is referred to as the Gauss-Steen quadrature henceforth [Steen,1969]. The paper supplies weights and abscissæ for $N = 2, (1), 10, (15dp)$ when $b = 1$ and for $N = 2, (1), 15, (15dp)$ in the semi-infinite case. The semi-infinite integral is particularly useful since it avoids any need for truncation. It also avoids the need to perform any algebraic transformations on the coefficients and abscissæ when $b \neq 1$.

To extend the univariate formula to the multiple edge integral, use can be made of a **product region**. Assuming $f(x)$ is of polynomial form, the integral may be expressed as a linear combination of integrals of the form:

$$\int_0^\infty dx_1 \dots \int_0^\infty dx_n \exp(-x_1^2 - \dots - x_n^2) x_1^{c_1} \dots x_n^{c_n}$$

where the $c_1 \dots c_n$ are appropriate exponents. This can now be separated into a product of n one-dimensional integrals:

$$\prod_{i=1}^n \int_0^\infty \exp(-x_i^2) x_i^{c_i} dx_i$$

Each of these can be evaluated using an N -point univariate formula:

$$A_n \approx \sum_{k=1}^N \left\{ C_i C_{i_2} \dots C_i f(v_{i,1}, \dots, v_{i,n}) \right\}$$

If the one dimensional formula is exact to degree d , then the n -dimensional formula using $P = N^n$ points also has degree d . In the case of the Gauss-Steen formula, $d = 2N - 1$.

The major disadvantage with such an approach is that the number of functional evaluations rises very rapidly with n . To some extent this can be eased by choosing the number of

abscissae differently in each dimension according to the amount of variation in the integrand in that direction. This corresponds essentially to the magnitude of the b parameter for that dimension and some success has been obtained in estimating the number of points required according to this criterion. A reliable automatic strategy for doing this remains to be found, however, so the results shown here were obtained using the same number of points in every dimension. The number of evaluations and hence the total evaluation time therefore rises approximately as N^n .

In order to minimise the evaluation time required an efficient scheme was devised which takes advantage of the properties of the integrand to enable each integrand evaluation to be as rapid as possible. The portion of the integrand which must be calculated may be expressed as:

$$f(u_1, \dots, u_n) = \exp \left\{ \sum_{m=1}^{n-1} (2 \alpha_m u_m u_{m+1}) - B_n \right\} \{ \cos(B_n) + j \sin(B_n) \}$$

$$\text{where } B_n = \sum_{m=1}^n \sqrt{2} u_m b_m$$

The terms $(\sqrt{2} u_m b_m)$ in B_n need only be calculated once for each of the abscissæ. Similarly the expression $(2 \alpha_m u_m)$ may be calculated outside the main summation and stored for later use. Multiplication of the weights may be avoided by precalculating the natural logarithms of each of the weights and simply adding the transformed values to the exponent, which is far more rapid. Real arithmetic may then be used throughout until the final step of including the phase term.

This procedure may be summarised as follows:

- 1) For each abscissa, calculate $(\sqrt{2} u_m b_m)$ and $(2 \alpha_m u_m)$ and store these values.
- 2) For each integrand evaluation :
 - 2.1) Sum the appropriate transformed weights.
 - 2.2) Add to them the appropriate set of $(2 \alpha_m u_m u_{m+1})$ values.
 - 2.3) Calculate and store B_n , subtracting it from the sum from 2.2.
 - 2.4) Raise e to the power of the results at 2.3.

2.5) Multiply by the phase term, $\{\cos B_n + j \sin B_n\}$

2.6) Add the result to the integral approximation.

This approach has been found to be far more rapid than a straightforward evaluation of the integrand in its standard form.

In the comparisons which follow, GSk means an application of the Gauss-Stein formula with k points in each dimension. Figure 6.26 shows the times taken, which, as expected, rise very rapidly with n although the times are moderate for $n \leq 5$. The execution times are independent of the particular problem under evaluation, although the corresponding errors will vary as shown in figure 6.27.

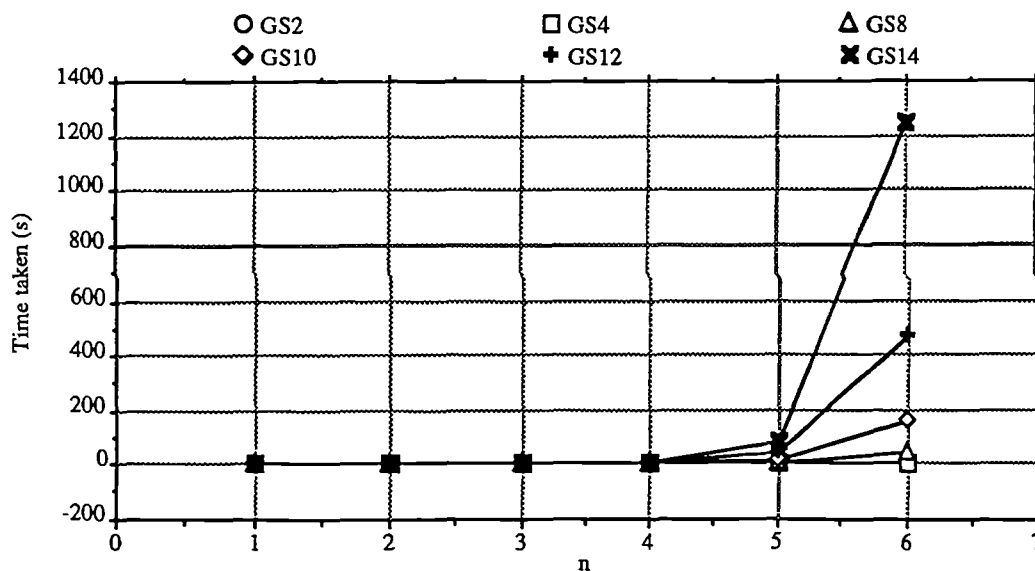


Figure 6.26: Gauss-Stein execution times

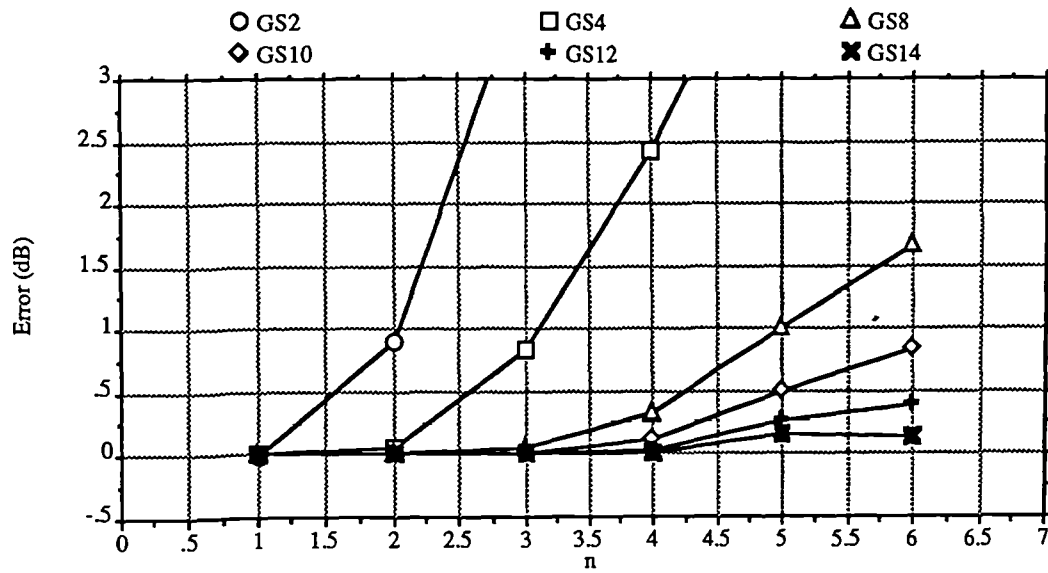


Figure 6.27: Gauss-Stein errors.

It is clear that the method consistently underestimates the field strength and does so in a smooth, well-behaved manner. The errors reduce rapidly as the number of integration points is increased. This method is therefore probably useful in all cases of up to 5 edges.

6.4.3: Monte Carlo Evaluation

This section describes an original approach to evaluating the multiple edge integral using a class of methods which has some special merits in multiple integral calculations. Monte Carlo methods are based upon the assumption that a given integral can be regarded as the expected value of a certain stochastic process. For instance, given:

$$I = \int_a^b f(x) dx$$

then the mean value of $f(x)$ is $I/(b-a)$. If a sample average is constructed:

$$\widehat{f}_N = \frac{1}{N} \sum_{i=1}^N f(x_i)$$

by randomly selecting N abscissæ on $[a, b]$, then

$$I = \int_a^b f(x) dx \approx \frac{b-a}{N} \sum_{i=1}^N f(x_i)$$

where the approximation may be expected to improve as N increases. When the x_i are distributed uniformly on $[a, b]$, statistical considerations suggest that the absolute error decreases as $1/\sqrt{N}$ for a fixed level of confidence [Davis, 1975]p290. Although this rate of convergence is relatively slow, the rate is essentially independent of the dimension, which is the Monte Carlo method's principal advantage.

In practice, **number-theoretic** methods are more often used. Their abscissæ are not strictly random but are chosen using a pseudo-random technique whose numeric properties produce more rapid convergence. The method used here is that of Korobov [Korobov, 1957]. The resulting formula is:

$$\int_0^1 dx_1 \dots \int_0^1 dx_n g(x_1, \dots, x_n) \approx \frac{1}{p} \sum_{i=1}^p g\left(\left\{\frac{ia_1}{p}\right\}, \dots, \left\{\frac{ia_n}{p}\right\}\right)$$

where $\{x\}$ denotes the fractional part of x and the a_i are the Korobov optimal coefficients, given in terms of a parameter a as:

$$a_1 = 1; a_i = a^{i-1} \pmod{p}$$

and a procedure for calculating a is given. The number of points, p must be relatively prime to all the a_i .

This method has been found useful for evaluating the multiple edge integral using a standard numerical algorithm [NAG, d01gcf]. Since the basic method is intended for real integrals only,

the Monte-Carlo method has been applied to the real and complex parts of the integral independently, separated as described in §6.2.3.

The method does not allow for an error estimate as standard, but by calculating the variance in the integrand at a number of random vectors an error may be estimated. This approach has been adopted in the routine implemented in [NAG,d01gcf], but increases the execution times appreciably, with the time becoming greater as the reliability of the estimation improves.

In the comparisons below the key corresponds to the following numbers of points used:

Key	Number of Points
M1	2129
M2	5003
M3	10007
M4	20011
M5	40009
M6	80021

Thus the number of points approximately doubles in each case, so the evaluation time is expected to rise in the same way. Figure 6.28 confirms this behaviour, where the comparisons presented have been performed with no error estimation. The increase in time taken with the number of edges is approximately linear, reflecting the increased time taken in each evaluation of the integrand.

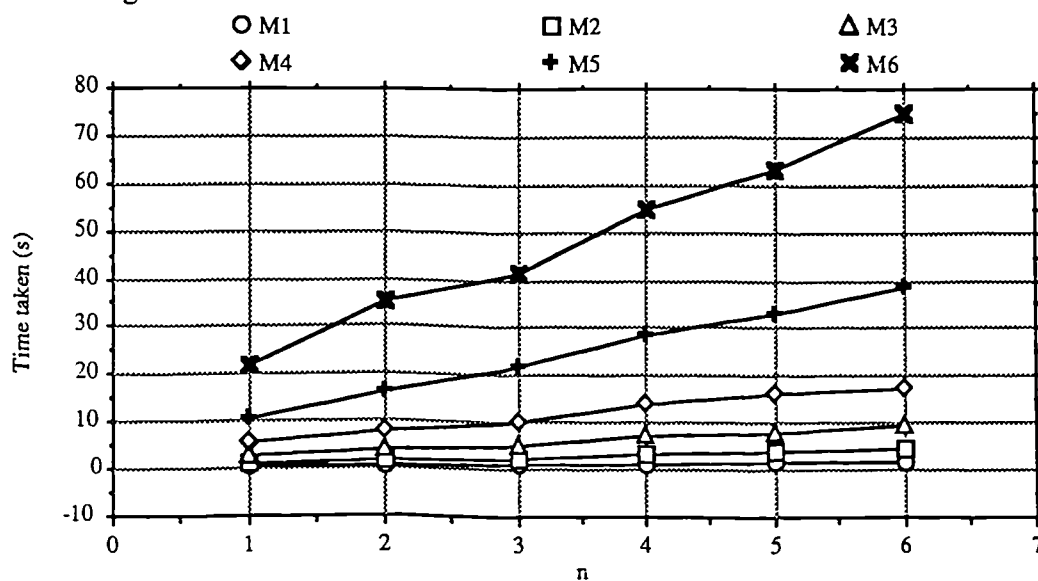


Figure 6.28: Evaluation time for Monte Carlo method

The consequent errors are shown in figure 6.29. It is clear that the errors are very low in most cases, but when the method fails the errors are unpredictable and erratic

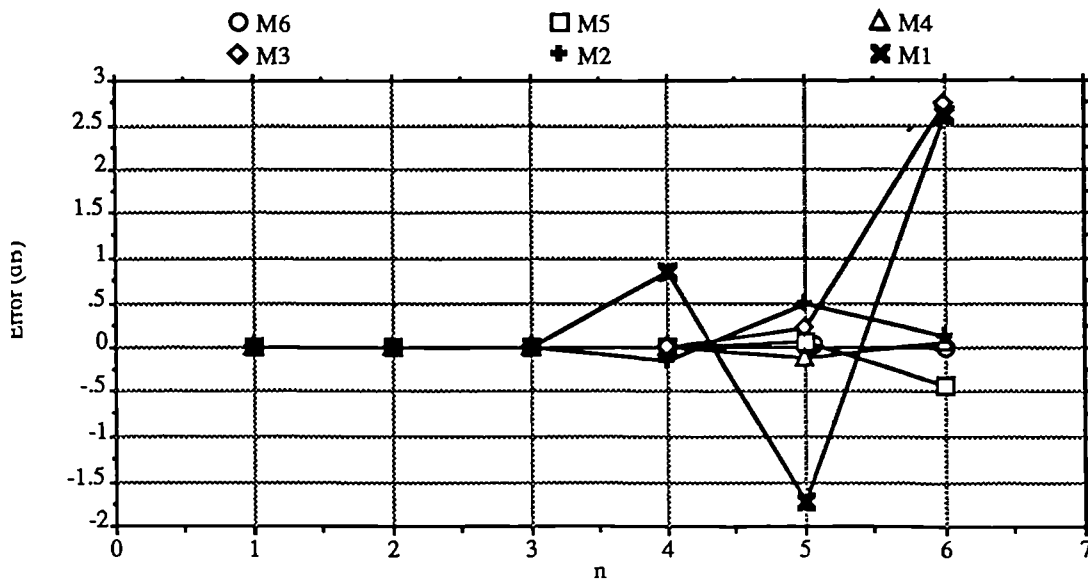


Figure 6.29: Monte Carlo errors

The speed of the method for high dimensionality thus makes it useful for large numbers of edges, but it should be ensured that the number of evaluation points is sufficient for reliable results. Alternatively, some speed may be sacrificed for a degree of error estimation.

6.4.4: Comparison of Methods

To facilitate easy comparisons between the methods, a figure of merit is defined as execution time in seconds, multiplied by the magnitude of the error in decibels. The figure of merit should be as low as possible for a good method over as wide a range of numbers of edges and problem types as possible. Figure 6.30 compares the figure of merit for all three of the methods discussed here. The enhanced Vogler evaluation performs consistently well, but its figure of merit increases steadily with n . The method's major advantage is in allowing the error to be pre-specified, but the resulting evaluation time may be long. Implementation of the method is highly machine dependent for good results and the memory required is large.

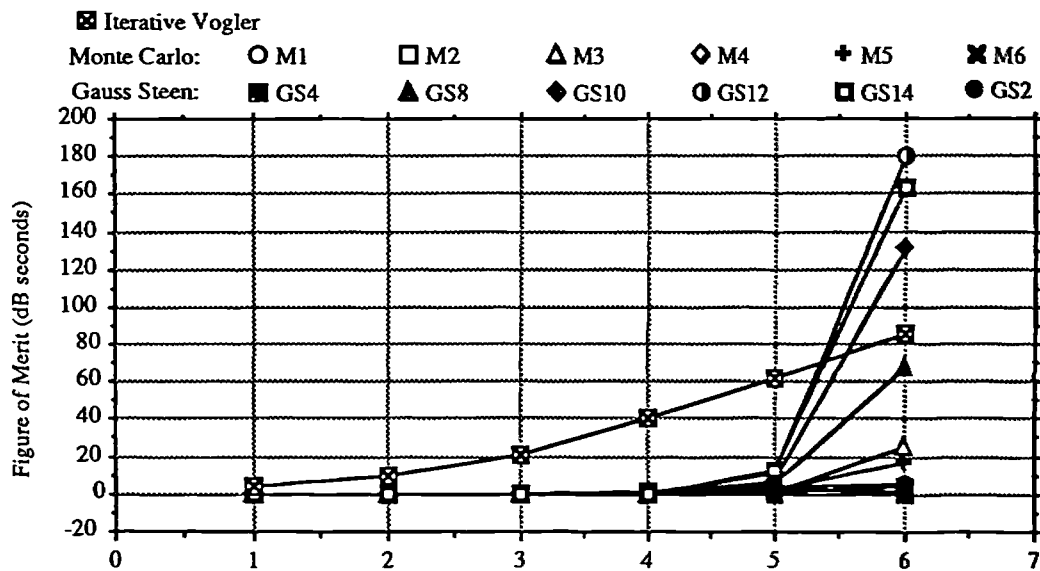


Figure 6.30: Figure of merit comparisons

The Gauss-Stein method's f.o.m. rises rapidly with n resulting from the way its evaluation time rises. Although it takes a long time to evaluate for large numbers of edges, its error performance is reliable and the method is straightforward to program, needing little memory and only simple arithmetic operations. Such an approach makes the approximate geometrical constructions of the methods described in §6.1 redundant, making Gauss-Stein ideal for most terrain diffraction applications.

Finally, in the range presented here, the figure of merit for the Monte-Carlo approach is essentially zero, making it a very useful approach, particularly when the number of edges is

apt to be large. Its major disadvantage is in its error performance when operating with inappropriately large n . In the calculations presented in later sections and chapters, the Monte-Carlo method was used together with an error estimation. When the error occasionally exceeded a predefined maximum, the calculation was simply repeated with more functional evaluations. This was found to be a highly reliable approach.

6.5: Summary

This chapter has examined methods of calculating multiple edge diffraction, resulting in at least one highly efficient approach which overcomes the limitations of conventional approximate methods in this application. If the propagation mechanism proposed by [Walfisch,1988] is valid then multiple diffraction is an essential component of any successful theoretical model of propagation in built-up areas. The next chapter will extend the methods developed here to construct complete models of propagation, capable of application to real-world situations.

Chapter Seven

New Propagation Models

7.0: Introduction

Although the techniques presented in Chapter Six are capable of utilising highly detailed building position and height data, such data are difficult to obtain at present. There are also cases in which such a level of detail is not useful since only average propagation characteristics are required. A model of multiple building diffraction for such cases is derived and examined here. This method is then extended to incorporate the variable building position techniques from Chapter Six, producing a complete model which can incorporate whatever level of detail is available.

7.1: The Flat Edge Model

7.1.0: Introduction

This section establishes a novel closed form solution to the multiple edge integral for the case when all the edges are of the same height and spacing, but the source and field points are at arbitrary heights. This is essentially the same problem treated by [Walfisch,1988] in numerical simulations, but the solution presented here allows much more rapid evaluation and is applicable to any source height or number of edges. The problem is important in building diffraction since it describes the characteristics of areas of reasonably uniform building cover in terms of the building packing density, a relatively easily obtained physical quantity. The solution to be described has been described in [Saunders,1991c]

7.1.1: Flat Edge Solution

A reduced problem is first solved, which has an arbitrary source height, but the field point is fixed at the same height as the edges. Later the solution is extended to allow arbitrary

positioning of the field point.

The geometry for the flat edge problem is illustrated in figure 7.1. The separation between all of the n adjacent edges and between the last edge and the field point is w . The source is distant from the edges and has an elevation θ from the first edge, where θ is negative as illustrated.

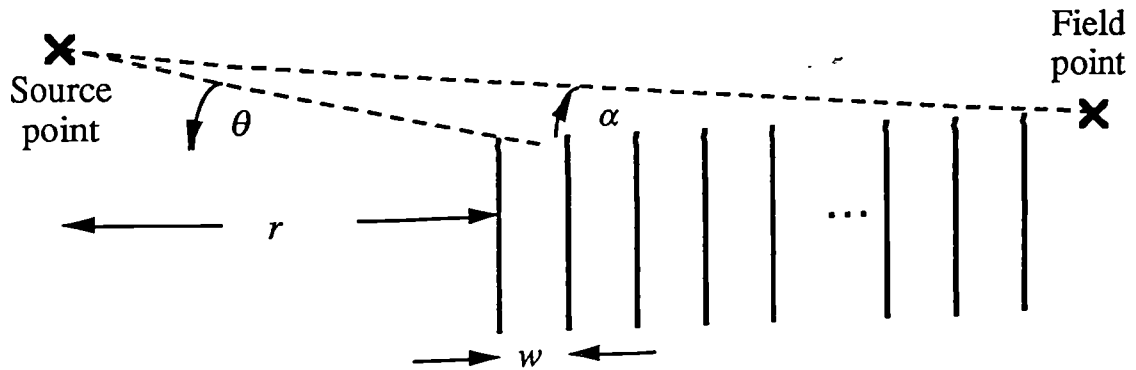


Figure 7.1: Geometry for flat edge problem

First the attenuation function for this situation is expressed using equation (6.4) :

$$A_n = \frac{C_n e^{\sigma_n}}{\pi^{n/2}} I_n$$

$$\text{with } \sigma_n = j t^2 ; t = \theta \sqrt{\frac{k r w}{2(r+w)}}$$

$$C_n = \sqrt{\frac{w^{n-1} (r+nw)}{(r+w) (2w)^{n-1}}} = \sqrt{\frac{(r+nw)}{(r+w) 2^{n-1}}}$$

(7.1)

Since all of the edges are colinear and equally spaced, $\theta_2 = \theta_3 = \dots = \theta_n = 0$ and $\alpha_2 = \alpha_3 = \dots = \alpha_{n-1} = 0.5$ so that, from eqn (6.5):

$$I_n = \int_0^\infty du_1 \dots \int_0^\infty du_n \exp \left[2\alpha_1 u_1 u_2 + \sum_{m=1}^{n-1} u_m u_{m+1} - \sum_{m=1}^n u_m^2 - \sqrt{2} t u_1 (1+j) \right]$$

(7.2)

Now assume that $r \gg nw$. This is equivalent to assuming plane-wave incidence on the first edge. Then $\alpha_1 = 1/\sqrt{2}$, and use of the simple substitution $u_2, \dots, u_n = x_2 \sqrt{2}, \dots, x_n \sqrt{2}$, and $u_1 = x_1$ results in an integral of the form:

$$I_n = (\sqrt{2})^{n-1} \int_0^\infty dx_1 \dots \int_0^\infty dx_n \exp \left[2 \sum_{m=2}^{n-1} x_m x_{m+1} - x_1^2 - 2 \sum_{m=2}^n x_m^2 - 2 t x_1 e^{\frac{j\pi}{4}} \right] \quad (7.3)$$

Now define a new function as follows :

$$S_n = \frac{1}{(\sqrt{\pi})^n} \int_0^\infty dx_1 \dots \int_0^\infty dx_n \exp \left[-2 t x_1 e^{\frac{j\pi}{4}} - x_1^2 - 2 \sum_{m=2}^n x_m^2 + 2 \sum_{m=2}^{n-1} x_m x_{m+1} \right] \quad (7.4)$$

and recall that $r \gg nw$, then the attenuation function can be expressed in the convenient form:

$$A_n(t) = e^{jt^2} S_n(t) ; t = \theta \sqrt{\frac{kw}{2}} = \theta \sqrt{\frac{\pi w}{\lambda}} \quad (7.5)$$

The evaluation of $S_n(t)$ now proceeds according to a general method proposed by [Boersma,1978]. The method involves reducing the problem to an integral equation which is solved using the Wiener-Hopf factorisation and a method of successive approximations [Moiseiwitsch,1977]. The procedure is lengthy, but essentially follows Boersma's evaluation of $T_n(t)$.

The eventual result is that $S_n(t)$ is given by the starting value $S_0(t) \equiv 1$ and the relation :

$$S_n(t) = \frac{1}{n} \sum_{m=0}^{n-1} S_m(t) F_s(-j t \sqrt{n-m}) ; n \geq 1$$

$$\text{where } F_s(t) = \frac{e^{jt^2}}{\sqrt{j\pi}} \int_{-\infty}^t e^{jp^2} dp \quad (7.6)$$

$F_s(t)$ is a definition of the complex Fresnel integral. It may be evaluated in terms of our previous definitions of the Fresnel sine and cosine integrals (§4.4.4) as follows:

$$F_s(j t) = \frac{e^{-j t^2}}{\sqrt{2j}} \left\{ \left[S \left(t \sqrt{\frac{2}{\pi}} \right) + \frac{1}{2} \right] + j \left[C \left(t \sqrt{\frac{2}{\pi}} \right) + \frac{1}{2} \right] \right\} \quad (7.7)$$

The final result (7.6) has apparently not been reported elsewhere, and certainly not in this context. The result performs all that Walfisch's approximate calculations did, but with the following advantages:

- **Speed:** Walfisch reported that calculation of the field at given values of α and w took several hours on a VAX computer for n varying from 1 to 100. On a similar system the same calculation using a FORTRAN implementation of (7.6) required only 0.09 seconds.
- **Flexibility:** This speed advantage allows the method to be used for any n , whether the field has settled or not. This is important in practical cases, where the number of buildings along a given path will often be considerably less than the number required for settling.
- **Uniformity:** The result in (7.6) is valid for θ positive as well as negative. This case (source antenna below building heights) may be important for interference calculations and for prediction of site shielding effects, especially in micro-cellular applications.

The Flat Edge model may be calculated either directly from (7.6), or the results may be estimated from the prediction curves in figures 7.2 (elevated base antenna) or 7.3 (antenna below building rooftops) by first calculating the value of the characteristic parameter t .

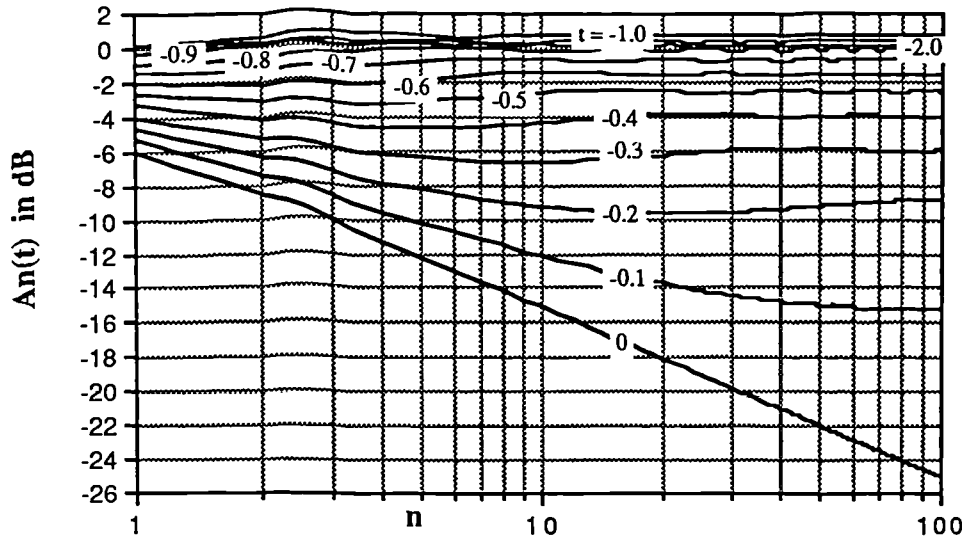


Figure 7.2: Flat Edge prediction curves; elevated base antenna

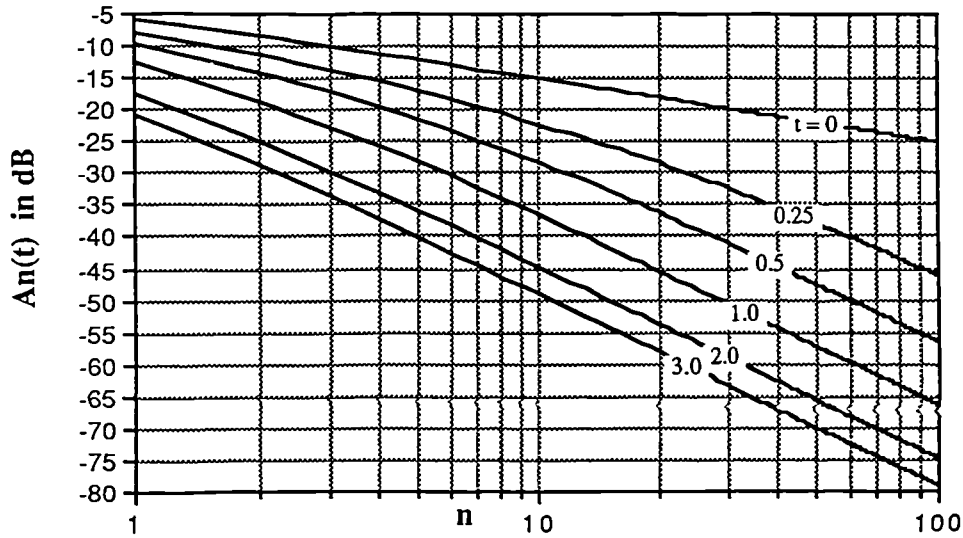


Figure 7.3: Flat Edge prediction curves; low base antenna

7.1.2: Example Calculations

The graph below (figure 7.4) illustrates the behaviour of the function for varying α at $w = 150\lambda$. It is evident that the excess field strength settles to a constant value for n large and α positive. Note also that large differences between the settled field and the small n value are apparent, particularly when α is very small.

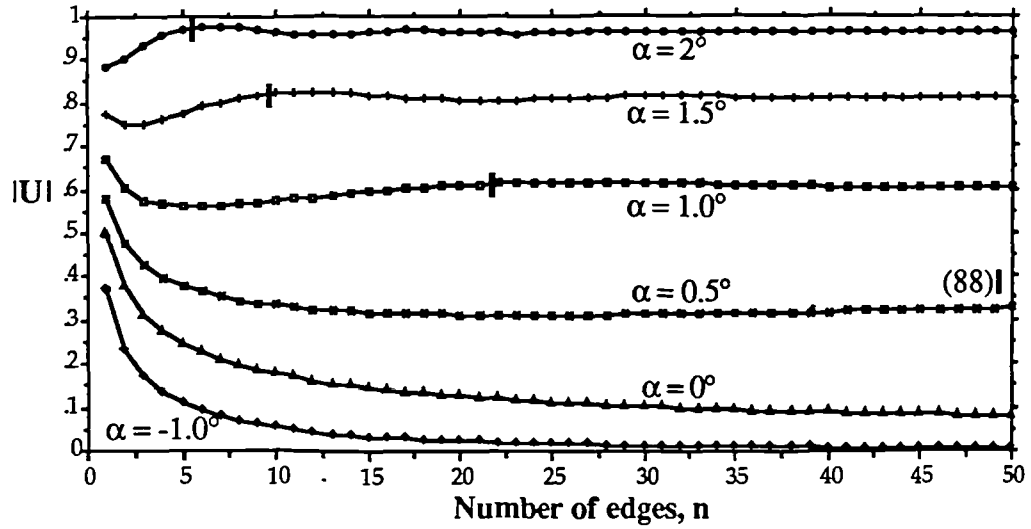


Figure 7.4: Behaviour of flat edge model

Marked on the curves is the number of edges, n_s which just fill the first Fresnel zone about the ray from source to field points, showing that the field may be considered settled once this value has been reached. For a plane-wave source, the first Fresnel zone radius R_1 is given by

$$R_1 = \sqrt{\lambda s}, \text{ where } s \text{ is the distance along the ray from the field point.}$$

$$\text{Hence, for } \alpha \text{ small, } \alpha = \tan^{-1}\left(\frac{R_1}{n_s w}\right) \approx \frac{\sqrt{\lambda n_s w}}{n_s w}$$

$$\text{So } n_s \approx \frac{\lambda}{\alpha^2 w}$$

(7.8)

Note that the number of edges required for settling rises very rapidly with decreasing α . Whenever $\alpha \leq 0$ the field does not settle at all, but decreases monotonically for all n .

7.1.3: Normalising Properties

It is useful to express this solution in terms of the wavelength, λ with $r \gg nw$ so that

$$\theta = -\alpha :$$

$$A_n(\theta) = e^{jt^2} S_n \left(\theta \sqrt{\frac{\pi w}{\lambda}} \right) \approx e^{jt^2} S_n \left(-\alpha \sqrt{\frac{\pi w}{\lambda}} \right)$$

(7.9)

This formally confirms Walfisch's observation that his calculations appeared independent of

the quantity $\alpha \sqrt{(w / \lambda)}$.

7.1.4: Grazing Incidence

A special case occurs when $\theta = 0^\circ$, the grazing incidence case. Lee [Lee,1978] gives the following attenuation function for this case:

$$L_n = \frac{\Gamma\left(n + \frac{1}{2}\right)}{n! \Gamma\left(\frac{1}{2}\right)} \quad (7.10)$$

This may be expressed as:

$$L_n = \frac{1.3.5\dots(2n-1)}{2^n n!}$$

Hence:

$$L_{n+1} = \frac{1.3.5\dots(2n+1)}{2^{n+1} (n+1)!} = L_n \frac{2n+1}{2(n+1)} \quad (7.11)$$

In terms of the flat edge solution in (7.6):

$$A_n(0) = S_n(0) = \frac{1}{n} \sum_{m=0}^{n-1} S_m(0) F_s(0) \quad (7.12)$$

and

$$F_s(0) = \frac{1}{\sqrt{2j}} \left\{ \left[S(0) + \frac{1}{2} \right] + j \left[C(0) + \frac{1}{2} \right] \right\} \\ = \frac{1}{2}$$

$$\therefore A_n(0) = S_n(0) = \frac{1}{2n} \sum_{m=0}^{n-1} S_m(0)$$

$$\begin{aligned} \text{Hence } A_{n+1}(0) &= S_{n+1}(0) = \frac{1}{2(n+1)} \sum_{m=0}^n S_m(0) \\ &= \frac{1}{2(n+1)} \left(\sum_{m=0}^{n-1} S_m(0) + S_n(0) \right) \\ &= \frac{1}{2(n+1)} (2n S_n(0) + S_n(0)) \\ &= S_n(0) \frac{2n+1}{2(n+1)} \end{aligned}$$

(7.13)

Now, since $L_I = 1/2 = A_I(0)$, then $A_n(0) = L_n$ for all $n \geq 1$.

This proof by induction is a validation of the function $S_n(t)$ since Lee's result was obtained by different means.

7.1.5: Inclusion of Final Building Diffraction

In a typical mobile radio situation the field point will actually be considerably below the last edge rather than at the same level as in the flat edge problem (figure 7.5). In this section the flat edge function is heuristically extended to include this process, thereby providing a complete propagation prediction tool.

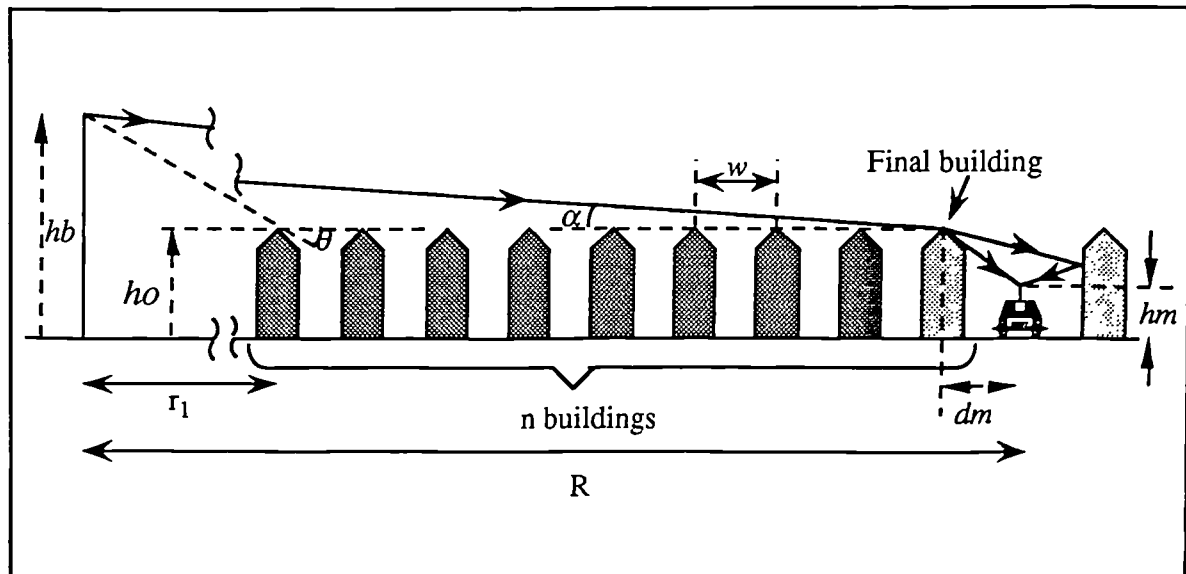


Figure 7.5: Complete geometry for flat edge model

The full solution to diffraction by a conducting half plane reveals that the diffracted field on the optical boundaries has plane wave characteristics [James p119], with a slow transition to cylindrical wave behaviour outside the transition regions (defined in Chapter Five). If the angle α is small, then wave incidence upon the final building is very close to grazing and is certainly well within the transition region. It is therefore reasonable to assume that the incident field has plane wave characteristics. This allows the final diffraction process to be separated from the multiple edge process as follows: If the total number of edges involved is n , then the overall field is given by $A_{flat} = A_{n-1} D_{fb}$, where D_{fb} accounts for the final building and A_{n-1} is found from equation (7.5). If it is assumed that the final building may also be modelled as a simple absorbing half-plane, then the calculations of §4.5 are relevant. The result used is therefore :

$$D_{fb} = \sqrt{A_d^2 + (\rho A_r)^2} \quad (7.14)$$

where

$$A_{d,r} = \frac{F(w_{d,r}) \exp\left(-\frac{j\pi}{4}\right)}{\sqrt{2}} + \frac{1}{2}$$

The Fresnel diffraction parameter is given by:

$$\text{Direct ray: } w_d = - \left[\frac{\pi}{2} - \tan^{-1} \left(\frac{d_m}{h_o - h_m} \right) - \alpha \right] \sqrt{\frac{2 d_m}{\lambda}}$$

$$\text{Reflected ray: } w_r = \left[\frac{\pi}{2} - \tan^{-1} \left(\frac{2w - d_m}{h_o - h_m} \right) - \alpha \right] \sqrt{\frac{2(2w - d_m)}{\lambda}}$$

This approach should be applied whenever no better information on the final building is available. However, the shape and electrical characteristics of the final building are likely to be relatively influential on the street-level field due to the large diffraction angle. If better information is available, then D_{fb} may be found using the methods of Chapter Five.

7.1.6: Characteristics of the Flat Edge Model

Figure 7.6 shows the variation of A_n with α for varying n , with $w = 100\lambda$, showing that the rate of change increases with n . This suggests that increasing building density increases the range dependence of the field, which is consistent with measured effects in built-up areas such as [Ibrahim,1983].

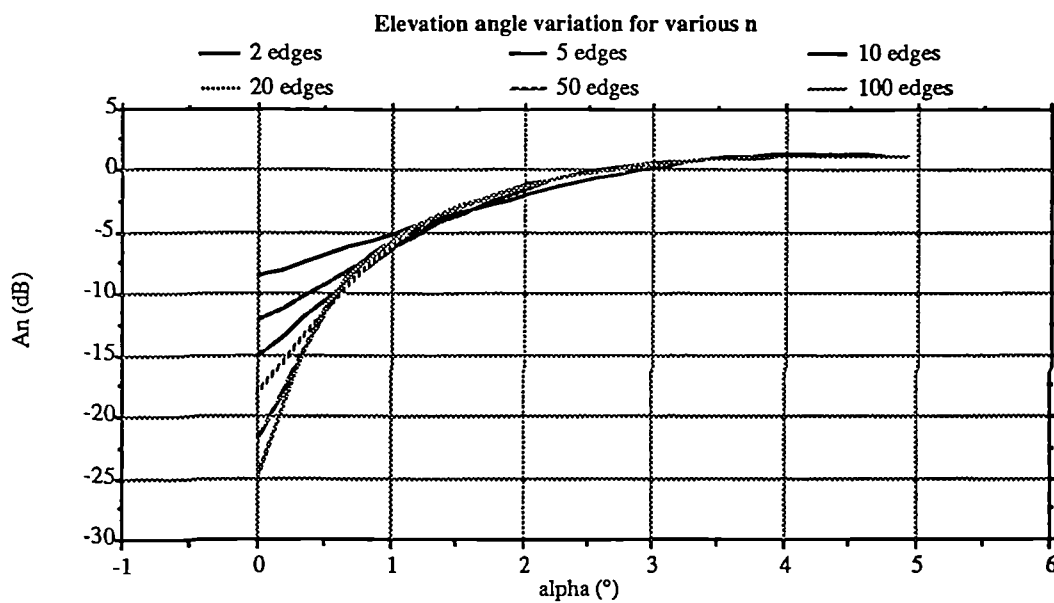


Figure 7.6: Elevation angle variation

Figure 7.7 compares the $n = 100$ curve with the Walfisch approximation to the settled field, given by :

$$A_{settled} \approx 0.1 \left(\frac{\alpha \sqrt{\frac{w}{\lambda}}}{0.03} \right)^{0.9} = \left(2.58 \alpha \sqrt{\frac{w}{\lambda}} \right)^{0.9}$$

This results in -38dB/decade of range when taken together with the free space variation, and assuming that α is proportional to $1/R$, which is valid for small α . Such variation is comparable with the results of many measurements, but more rapid than most.

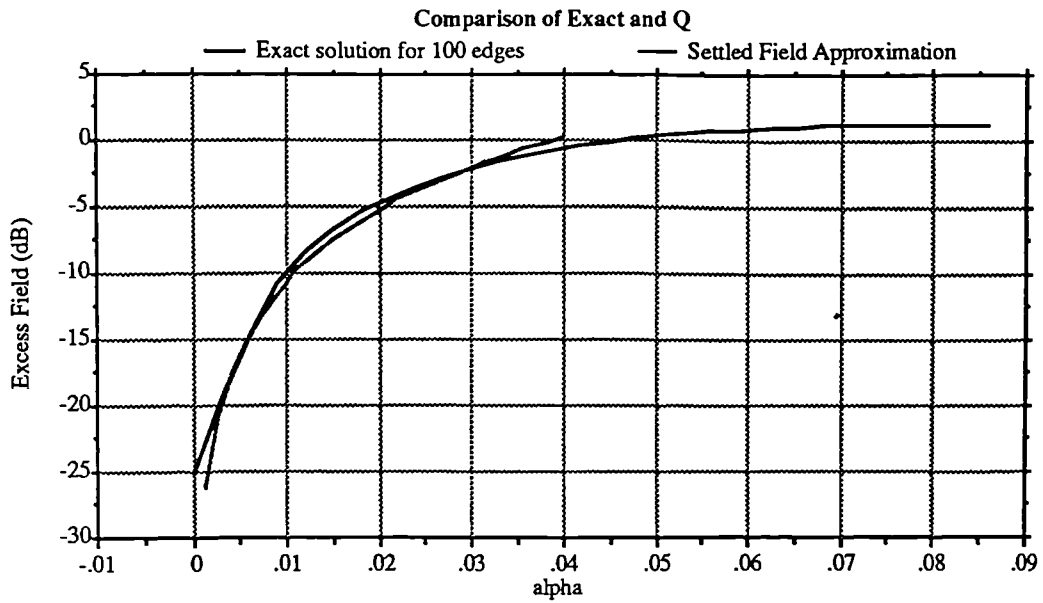


Figure 7.7: Power law approximation to settled field

To examine the effect of small n , a function of the same general form is fitted to the results for small α . Parameters c and p are found according to the following definition:

$$A_n \approx \left(c \alpha \sqrt{\frac{w}{\lambda}} \right)^p$$

The results are shown below:

n	p	c
2	0.126	0.02
5	0.225	0.10
10	0.335	0.29
25	0.54	0.93
50	0.742	1.83
100	0.946	2.90

The path loss law thus varies from -22.5dB/decade to -39dB/decade over the range examined. This covers the range of variation encountered in measurement programmes.

Figure 7.8 shows the variation with inter-edge spacing w , with $\alpha = 0.3^\circ$. The variation is relatively insensitive to w , but increases slowly with n .

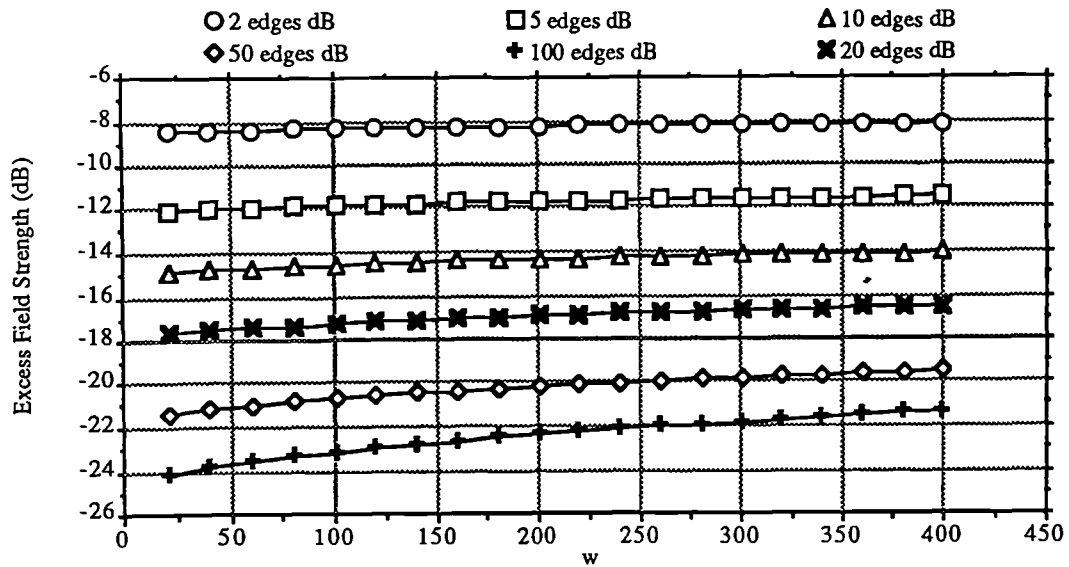


Figure 7.8: Variation with building spacing

Finally the complete model is used to show the effect of building height variation for constant base and mobile antenna heights (figure 7.9). This results from a compound variation of α in A_n and θ_d in D . Here $(h_b - h_o) = 100\text{m}$, $R = 10\text{km}$, $d_m = 40\text{m}$ and $w = 20\text{m}$. The results suggest that, although the overall field strength depends on the number of buildings, the variation with building height is almost constant.

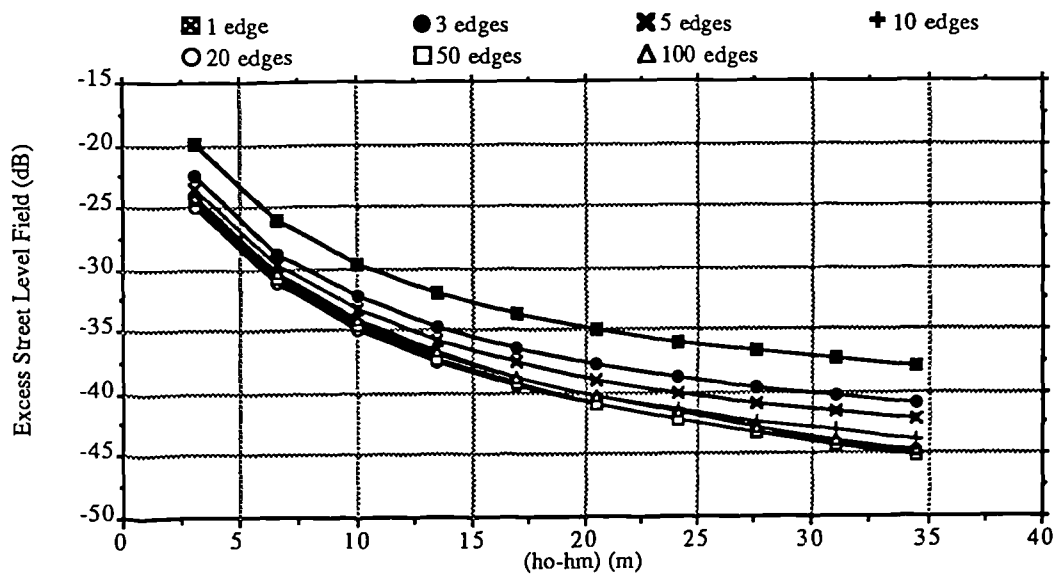


Figure 7.9: The effect of building heights.

7.1.7: Frequency Variation

It has previously been noted (§ 3.3.4) that the settled field does not account properly for observed variations of field strength with frequency since the rooftop field actually increases with frequency, resulting in a street-level field which decreases only slowly as frequency is increased. Measurements suggest that the overall field strength is proportional to f_c^{-r} where r is between approximately 1.5 and 1.3 depending upon building density. This corresponds to a variation in excess loss of between 6 and 8dB per decade of frequency. Figure 7.10 shows the corresponding variation of street-level field predicted by the flat-edge model with $w = 40\text{m}$, $d_m = 20\text{m}$, $(h_b - h_o) = 100\text{m}$ and $R = 10\text{km}$ for various values of n (where n does not include the final building). It is clear that the frequency variation is consistent with measurements when n is small, but too small for large n . This is evidence that relatively small numbers of buildings are involved in diffraction in most practical cases and that the flat-edge mode provides a distinct improvement over the settled field approach.

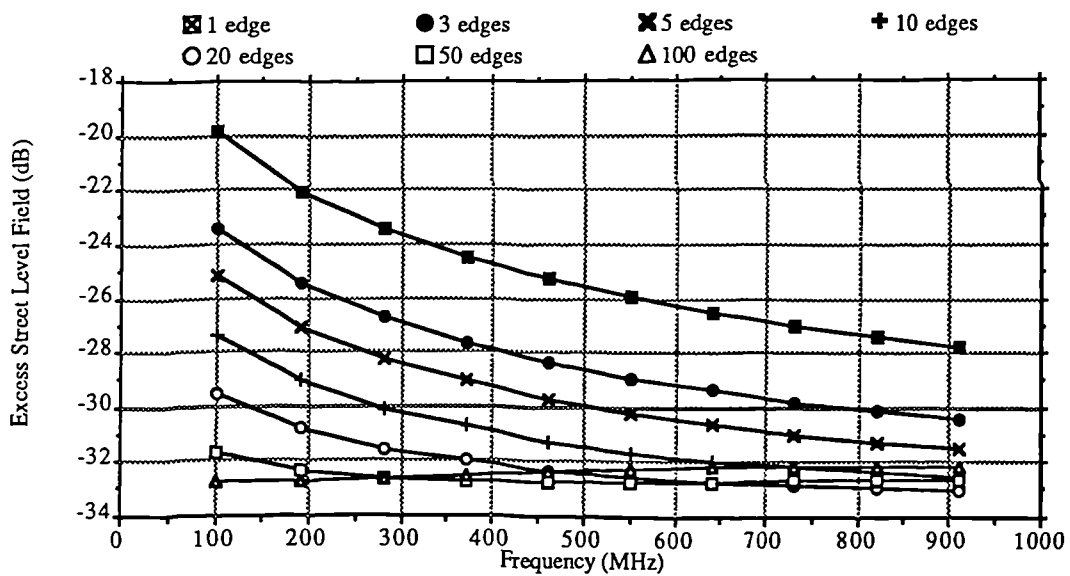


Figure 7.10: Field strength versus frequency for varying building numbers

It is necessary to confirm, however, that the field for small n still retains sensible variation with range. Figure 7.11 illustrates this point using the same edge geometry as previously with $f_c = 900\text{MHz}$. The range variation increases rapidly with n , so that sensible predictions result even for moderate numbers of buildings.

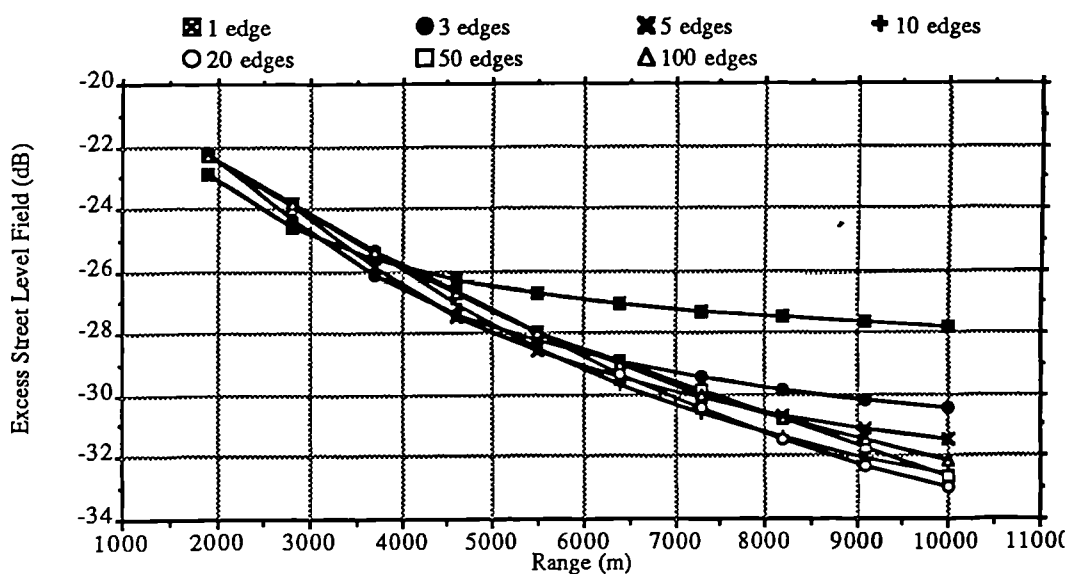


Figure 7.11: Field strength versus range for varying building numbers

7.1.8: Remote Base Station Model

Here a model for the situation of a base station in an open area some distance from the start of the built-up area is proposed. This occurs often in practice.

The validity of the Flat Edge model for any n is particularly important here. In figure 7.12, the base station is shown at a perpendicular distance r_o from a series of parallel building rows with a spacing w . The path BM makes an angle γ with this perpendicular.

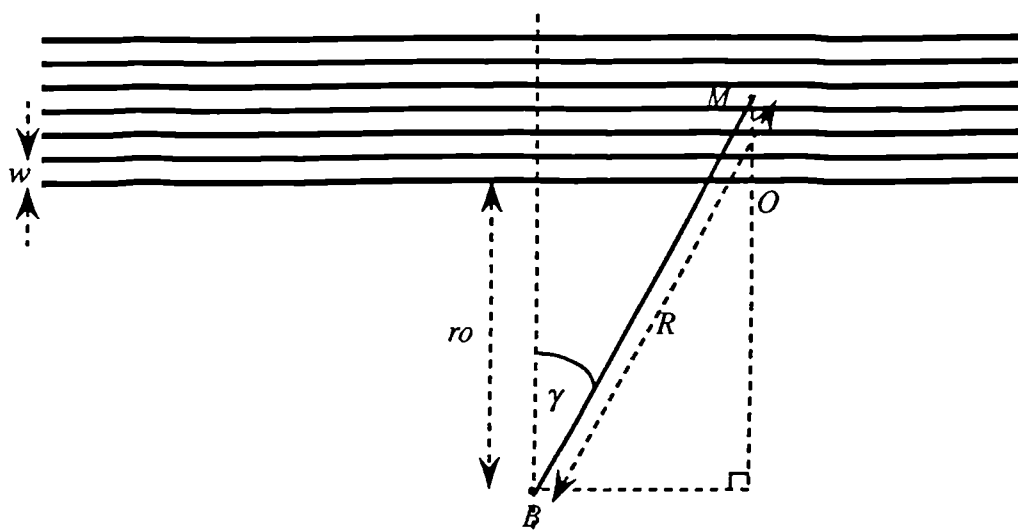


Figure 7.12: Geometry for remote base station effect.

In this case:

$$n = \left[\frac{MO}{w} \right] = \left[\frac{R \cos \gamma - r_o}{w} \right]$$

where $[.]$ denotes the integer less than or equal to the quantity in brackets, subject to the restriction that $n \geq 0$ always. When $n = 0$ then propagation is essentially the same as in free space. The edge spacing in the flat edge model must be replaced by w' , the row spacing measured along BM , given by :

$$w' = \frac{w}{\cos \gamma}$$

The contour plot in figure 7.13 shows the rooftop field calculated using this model, with $f_c = 933\text{MHz}$, $w = 40\text{m}$, $(h_b - h_o) = 17\text{m}$ and $r_o = 500\text{m}$.

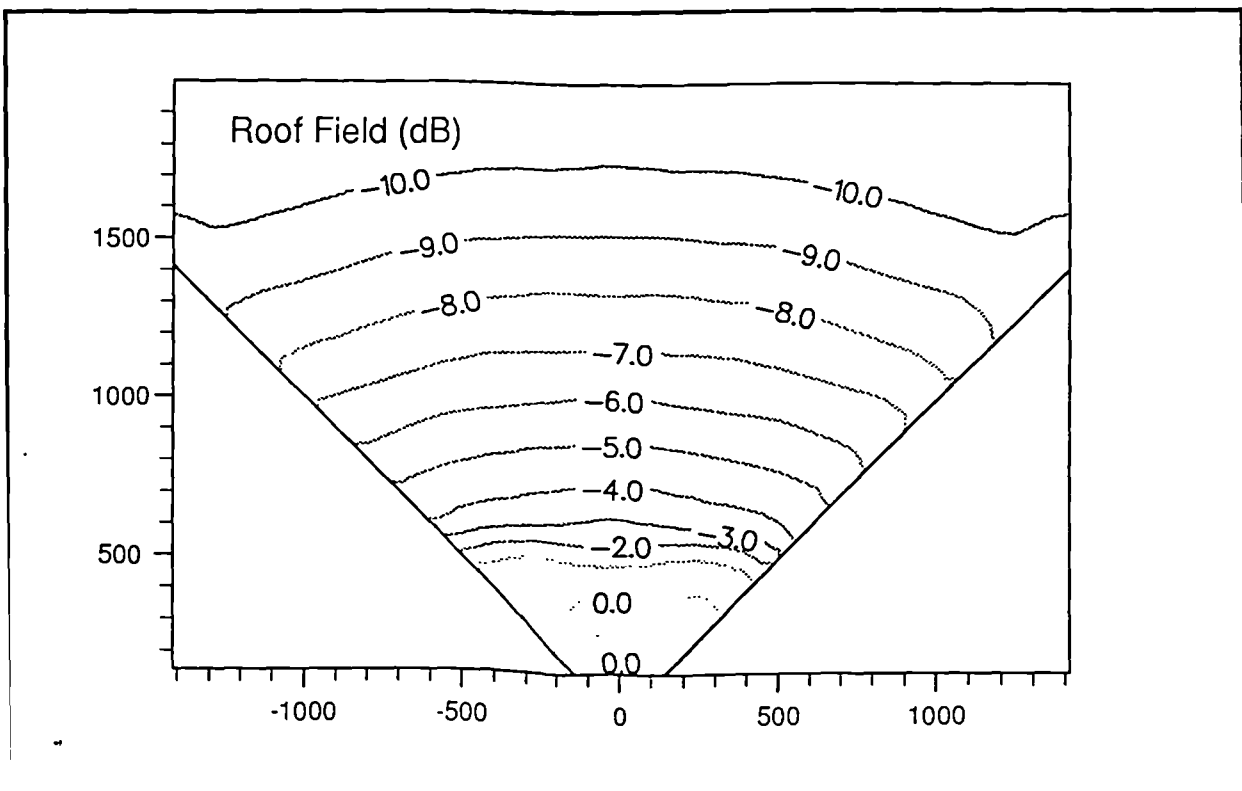


Figure 7.13: Contour plot for remote base station model

The contours are flatter than a circular arc centred on the base station would be. Thus they tend to run along lines of constant n (streets), emphasising that variation with number of

edges is rather more significant than the variation with street width.

In practice, both w and the street orientation are likely to remain constant over only small ranges of γ , so the contour plot indicates the gross variations only.

7.1.9: Conclusions

The Flat Edge model establishes a physical mechanism which accounts for measured path loss characteristics. This applies to both the variation with distance and the base station antenna height. The simplicity of the formulation allows base station antenna heights to be carefully planned for both optimum coverage and interference predictions. Since the formulation is valid for any number of buildings, it is useful in cases where the base station is situated outside of the built-up area or in a region of open space within such an area, a common situation in practice. The validity of the formulation for antennas below the building roof level makes it applicable to prediction of site shielding effects for microcells. Although the model does not account for irregular building heights, in many situations only an estimate of average building heights will be available. In such cases the Flat Edge model represents an optimum use of available physical data. The remaining sections in this chapter will address the issues of applying this model and that from the previous chapter to real-world cases.

7.2: Edge Reduction Technique

When applying a model to practical predictions it is essential that the model may be evaluated in as short a time as possible. The most direct method of reducing the evaluation time is to reduce the number of edges required in the evaluation by eliminating edges which do not appreciably affect the diffracted field. This occurs when an edge is much lower than its nearest neighbours. This can be done using the concept of the Fresnel zone radius, introduced in §4.4.6.

The asymptotic expression for the complex Fresnel integral for large positive arguments which was given in §4.4.4 is used:

$$F(w) \sim \sqrt{\frac{j}{2}} - \frac{j \exp\left(\frac{j\pi w^2}{2}\right)}{\pi w}$$

where the \sim sign indicates the asymptotic nature of this expression. This is now inserted into the expression for scalar single edge diffraction :

$$\begin{aligned} A &= \frac{F(w)}{\sqrt{2j}} + \frac{1}{2} \\ &\sim \frac{1}{\sqrt{2j}} \left\{ \sqrt{\frac{j}{2}} - \frac{j \exp\left(\frac{j\pi w^2}{2}\right)}{\pi w} \right\} + \frac{1}{2} \\ &\sim 1 - \frac{\exp\left(\frac{j\pi w^2}{2}\right)}{\pi w} \sqrt{\frac{j}{2}} \end{aligned}$$

Hence :

$$|A| \sim \left(1 + \frac{1}{2\pi w^2} - \frac{\sqrt{2} \cos \pi \left(w^2 + \frac{1}{4} \right)}{\pi w} \right)^{\frac{1}{2}}$$

In this problem it is the bounds of the deviation of the field from its unobstructed value which are of concern, so consider only the situation when the cosine term is ± 1 . Then:

$$|A|_{peaks} \sim \left(1 + \frac{1}{2\pi w^2} \pm \frac{\sqrt{2}}{\pi w} \right)^{\frac{1}{2}}$$

(7.16)

This result is compared with the complete solution in figure 7.14:

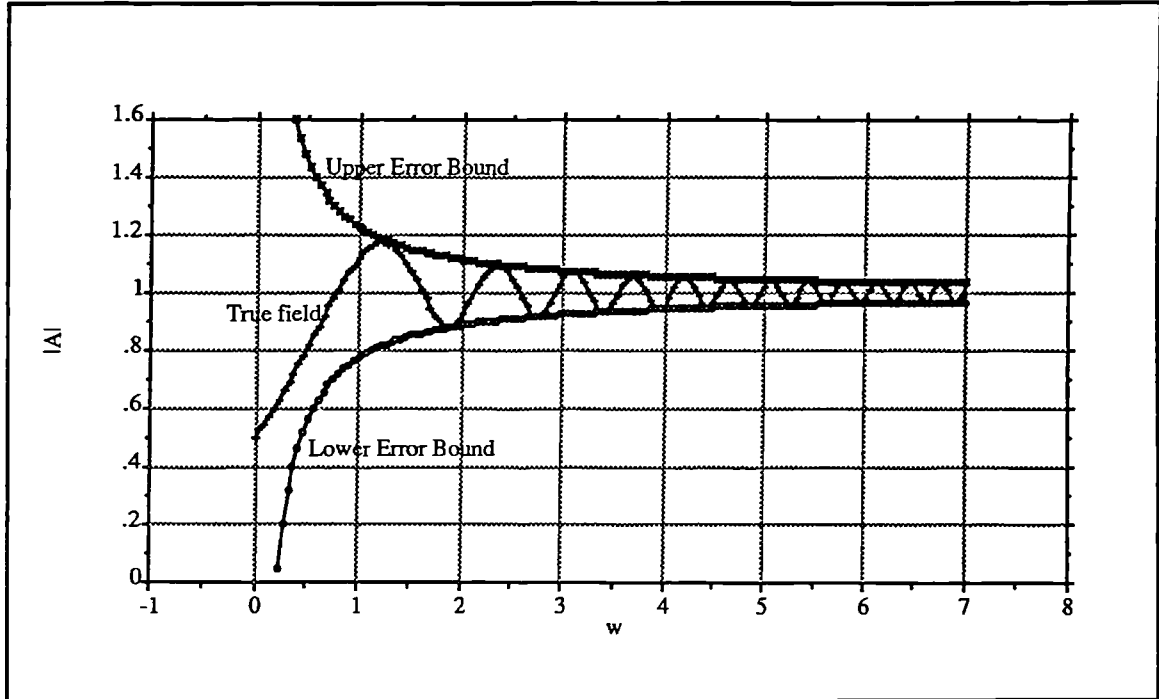


Figure 7.14: The effect of ray path disturbance

If the above expression is now expanded using the binomial theorem, the result is:

$$|A|_{peaks} = 1 \pm \frac{1}{\pi w \sqrt{2}} + O\left(\frac{1}{w^2}\right)$$

Now define a fractional error ϵ , where $\epsilon \ll 1$, as:

$$\epsilon = \frac{|A|_{actual} - |A|_{undisturbed}}{|A|_{undisturbed}} = |A|_{actual} - 1$$

An upper bound for this error is therefore given by:

$$|\epsilon| = \frac{1}{\pi w \sqrt{2}}$$

(7.17)

This expresses how close a neglected obstacle can be to the ray path without causing a prediction error greater than ϵ . If it is now assumed that the field between edges in a multiple edge diffraction problem can be considered ray-like, then this error may now be expressed in

terms of the β_m or b_m parameters for a given edge:

$$b_m = \frac{1}{2\sqrt{\pi}|\epsilon_m|}$$

Vogler [Vogler,1981] suggests that edges may be neglected to a high degree of accuracy if $\text{Re}(\beta_m) < -3$. This corresponds to $|\epsilon_m| = 0.066$, (0.6dB) or to $b_m \approx -4.3$.

To apply this approach to reducing a system of multiple edges it is necessary to confirm that the field is perturbed in a similar way when the perturbing edge is part of a system of more than one edge. To this end the situation illustrated in figure 7.15 is investigated. The edge closest to the field point might represent the final building in a mobile radio problem, while the previous edge may need to be included in the diffraction calculation if it perturbs the field excessively.

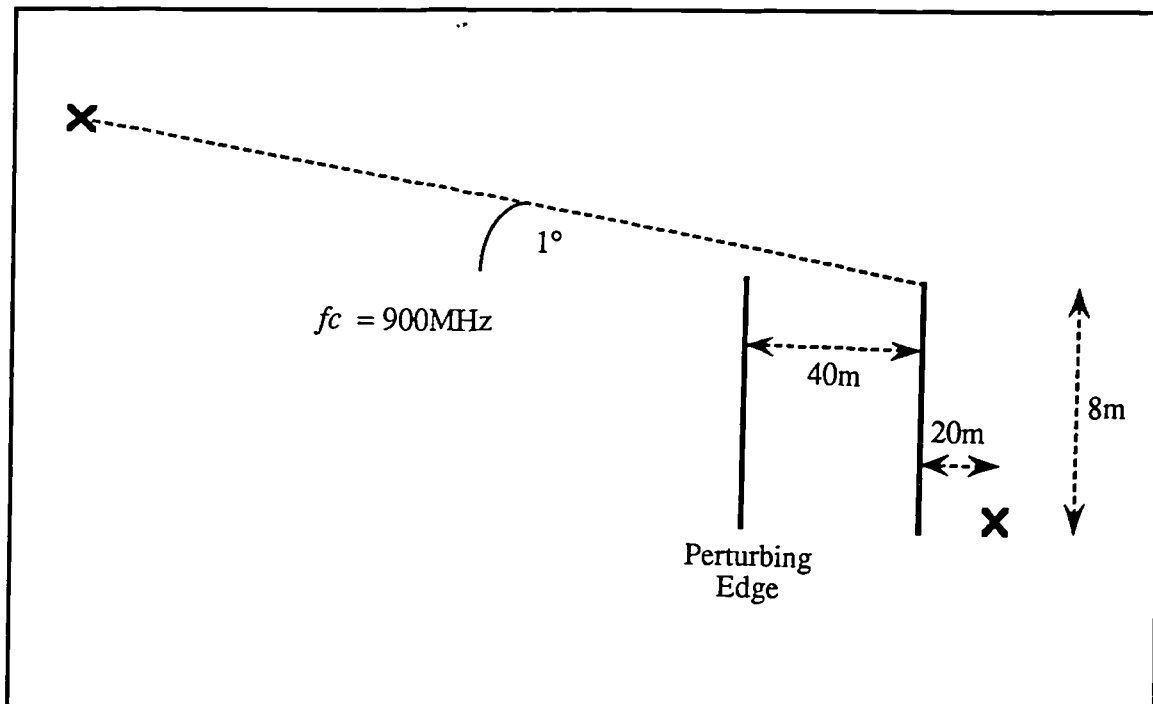


Figure 7.15: Geometry for perturbation of multiple edge fields

The calculated excess attenuation in the absence of the perturbing edge is 24.9dB. Varying the height of the other edge changes the parameter b_1 while maintaining α constant. The result is shown in figure 7.16, plotted together with the error bounds calculated from equation (7.17), where the error is now relative to the unperturbed field rather than unity. It is clear that this approach still predicts sensible error bounds, allowing unnecessary edges to be eliminated from calculations once a lower limit, b_{min} , is set, appropriate to the desired calculation accuracy.

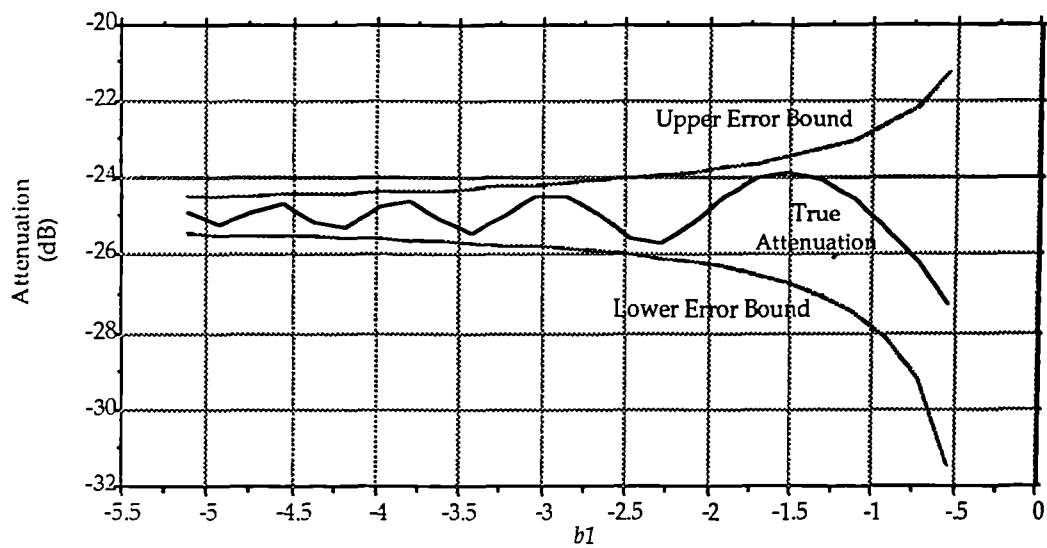


Figure 7.16: Multiple edge field perturbation

To summarise, edges may be removed from a calculation if their b parameters are less than prescribed minimum. The parameters for the other edges are then recalculated and the process repeated until all edges are judged significant. This approach is applied as part of a complete prediction model in the next section.

7.3: Hybrid Prediction Model

7.3.0: Introduction

The Monte-Carlo and Gauss Steen methods together provide a reliable means of evaluating the multiple edge integral for moderate numbers of edges. However, real building profiles over reasonable distances often involve 20 or more buildings. Some of these buildings may be neglected if their diffraction parameters are sufficiently small, but the remaining number may still be too large to be predicted using the full method, particularly when the building heights are relatively uniform. In this case it is necessary to propose an approximate method which makes good use of the available physical data, while remaining within the limitations of the diffraction calculations available. To this end a hybrid model is now proposed which uses elements of both the Flat Edge model and the full diffraction integral.

7.3.1: Description of Model

Consider a real building profile which comprises a large number of building edges (figure 7.17).

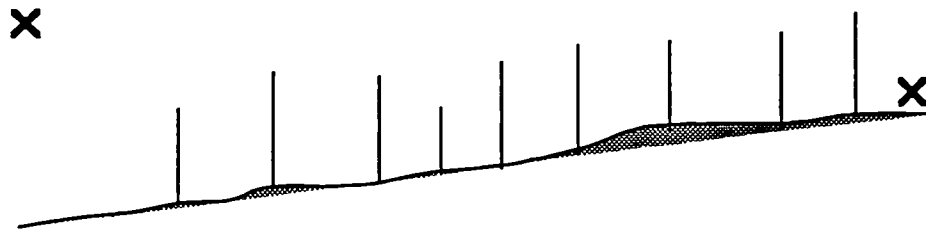


Figure 7.17: Complete building profile

First any edges with diffraction parameters less than a threshold value are eliminated from the calculation. The value used here is $b_m = -2.5$. The next step is to approximate the street level field using the flat edge model in conjunction with single edge down diffraction as described in §7.1.5. The effective base station elevation angle is found by calculating a linear regression through the edges. The average building spacing is calculated and used in the Flat Edge model with the actual final building position in the down diffraction calculation and with n set to the actual number of significant buildings. Let the resulting field strength be E_I . This represents

the gross characteristics of the buildings (figure 7.18).

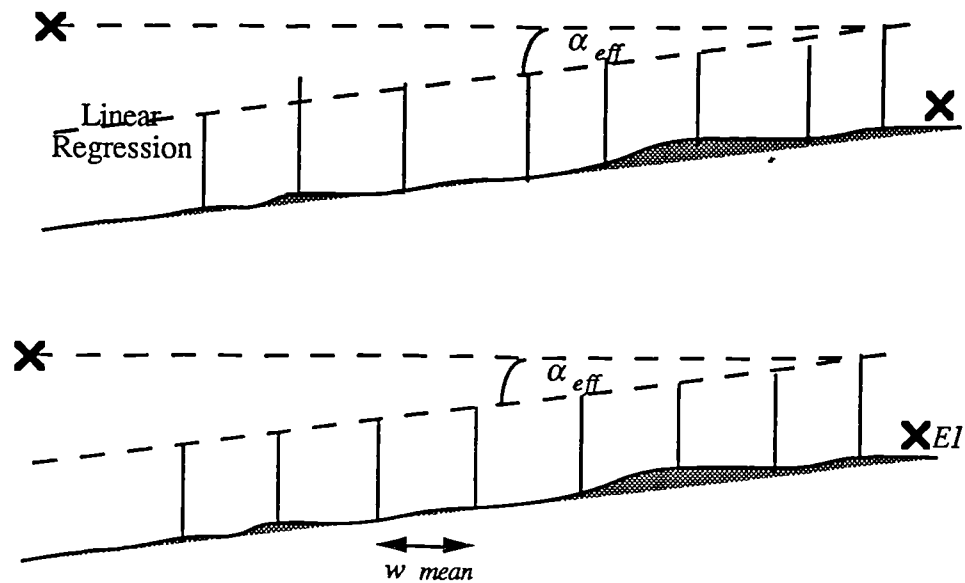


Figure 7.18: Parameters for overall flat edge calculation

Now the full diffraction integral is used to calculate the effect of deviations from the Flat Edge case for the most important edges. In this case assume that the number of edges which may reliably be handled is 5. Then the 5 edges having the most positive b parameters are identified. This is done by finding the edge with the most negative parameter, removing it and recalculating the diffraction parameters for the other edges. This process is repeated until only 5 edges remain. In cases where the edges are of virtually constant height and the source is elevated the important edges will be those nearest the mobile, but using the diffraction parameters in this way enables unusual cases to be handled. For instance, an unusually tall building distant from the mobile will then be sensibly taken into account. The field strength resulting from the full calculation on these 5 edges is $E2$ (figure 7.19).

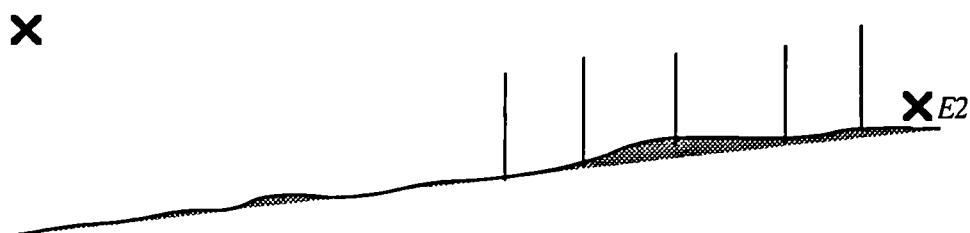


Figure 7.19: Calculating deviations from flat edge behaviour

Now the two calculations must be combined in a sensible manner. This is done using the Flat Edge calculation for 5 edges of the same average spacing and source elevation as used in calculating E_1 . This is shown in figure 7.20.

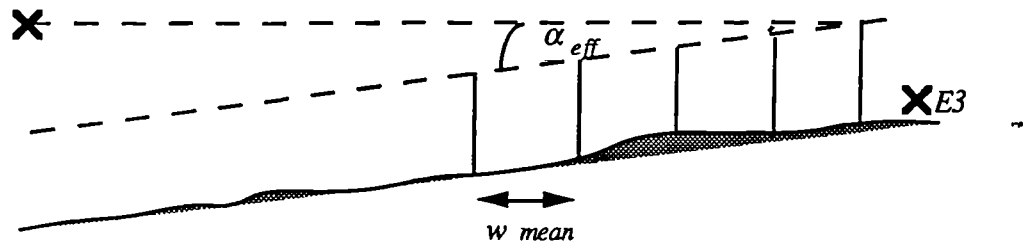


Figure 7.20: Normalising using flat edge for small number of edges

The resulting field strength, E_3 is used to normalise E_2 . Finally the overall field strength, E_d is found as the product of this normalised field and the complete flat edge calculation :

$$E_d = E_1 \frac{E_2}{E_3}$$

The whole process can then be repeated, when appropriate, with the field point replaced by it reflected image to find E_r . The two rays are combined in the usual way to predict the median field strength, E_T

$$E_T = \sqrt{E_d^2 + (\rho E_r)^2}$$

If the most important edges are essentially of uniform height and equal spacing then the field strength will correctly be predicted as the flat edge value. If, conversely, the number of edges is small enough to be handled using the full diffraction integral, then E_1 and E_3 will be equal and the proper field strength results. The method can thus be fully automated, with no need for any judgement of the type of edge arrangement by the engineer. The method forms an integrated model, providing a broad framework for including as much or as little physical data as is available, from an estimate of building density and height through to a detailed description of individual building heights and positions. The method will be applied in real cases in Chapter Eight.

7.4: Location Variability

7.4.0: Introduction

This section examines the contribution which building variations make to location variability. The essence of the method adopted is to simulate differing building arrangements using assumed statistical distributions of building parameters. This is equivalent to varying the mobile position in a given area at constant range, thus simulating the conditions under which measured values of location variability are calculated. Only the effect of building heights are examined here but the same methods could in principle also be applied to other parameters. The statistics of the resulting field strength predictions can then be calculated and compared with expectations from measurements. It is difficult here to provide direct comparison with measurements, since it is impossible to separate these variations in real situations. It should be expected, however, that the distribution of the resulting variability is correct and changes with parameters such as frequency and building density in a manner consistent with the measurements.

It is important here to be aware that building position is only one contribution to location variability. Other important factors are the presence of trees; variations in building shape construction and orientation; and gross terrain variations (small scale terrain variation is accounted for by considering building height effects).

7.4.1 : Fundamentals

Here some important statistical results are reviewed briefly. If excess propagation loss (in decibels) due to two different causes is represented by the random variables X and Y . The total excess loss, L_e is then given by :

$$L_e = X + Y$$

The location variance, σ_L^2 is then given in terms of the individual variances of X and Y as [Winkler,1975] p.188 :

$$\sigma_L^2 = \sigma_X^2 + \sigma_Y^2 + 2\rho_{XY}\sigma_X\sigma_Y$$

where ρ_{XY} is the correlation coefficient of X with Y , given by:

$$\rho_{XY} = \frac{\text{cov}(X, Y)}{\sigma_X \sigma_Y} = \frac{E(X, Y) - E(X)E(Y)}{\sigma_X \sigma_Y}$$

where $\text{cov}()$ indicates covariance, and $E(.)$ denotes the expectation of the quantity in brackets.

If X and Y are uncorrelated (independent) then the result is particularly simple:

$$\sigma_L^2 = \sigma_X^2 + \sigma_Y^2$$

It will be assumed in this section that the factors examined are substantially independent of all others.

In practice, the location variability will be measured via a finite number of measurements, so the measured variability will not be the same as that of the underlying distribution. The same is true of the simulations which are presented in this chapter. The more measurements or simulations that are performed, the greater will be the confidence that the true value lies within specified limits around the sampled value. This confidence may be calculated using the chi-square distribution [Chatfield,1983],p.116.

7.4.2: Previous Work

Very little work on this subject has previously been attempted. There is, however, one paper by [Chrysanthou,1991] which examines the effect of building height variation. The method of diffraction calculation is the multiple edge model from [Walfisch,1988] which is only valid for finding fields at rooftop level, so the final field at street level is calculated using a single edge approximation. Although this is valid in the constant height case, it has been found using the multiple edge integral that this approach may lead to large errors when building heights are not equal. Additionally the paper treats the diffracted-reflected ray by assuming it to be of the same amplitude as the direct-diffracted ray, which may also lead to errors. For a number of configurations of building heights and antenna heights the statistics of the street level field are determined when the building heights are uniformly distributed on $[h_{om} - \Delta h_o / 2, h_{om} + \Delta h_o / 2]$, where h_{om} is the mean building height. The distribution is arbitrary, since no real building heights are surveyed. The simulation results suggest that building height variation tends to reduce the average signal by comparison with the constant height settled field case by approximately $(-0.43 \Delta h_o)$ dB over the range considered, almost independent of h_{om} . This is

significant in using the Flat Edge model, since it implies that the model is likely to underestimate loss values in areas with large deviations of building heights from the mean. The resulting distribution of field strengths is approximately uniform. Its variance increases strongly with h_{om} and decreases slightly with base station rooftop elevation angle. The calculated variability is small by comparison with measurements of overall location variability, strongly suggesting that other factors are involved. A uniform distribution on $[-6.5\text{dB}, 6.5\text{dB}]$ is therefore combined independently with the height simulations to account for the combined effect of building shape, construction and foliage attenuation. The resulting field strength distribution is approximately lognormal with a standard deviation of 4.9dB.

7.4.3 : Building Height Distributions

Here the real distribution of building heights in a particular case is considered. Building heights over a large area are difficult to obtain directly, but it has been pointed out [Ibrahim,1983] that some data are available from planning authorities.

The data used and maintained by most planning authorities in England are divided into **plans**, or 500m \times 500m squares aligned with the Ordnance Survey grid system. For each plan, large cities have available the number of buildings having a given number of stories, plus the total ground floor area occupied by the corresponding buildings. From this statistics such as the percentage of land covered by buildings and the average height of a given building may be derived. In the first instance the distribution of heights according to the total area each building occupies is calculated. Data was obtained for the whole of the area covered by the City of Westminster [Westminster,1990], a total area of nearly 29.5 km², of which 21.5% is occupied by buildings. The area is urban, but there are relatively few very high rise buildings, some residential regions and some large areas of parkland. Figure 7.21 shows the overall distribution of building stories, which has a mean of 4.3 stories. The distribution is asymmetric, with a positive skew.

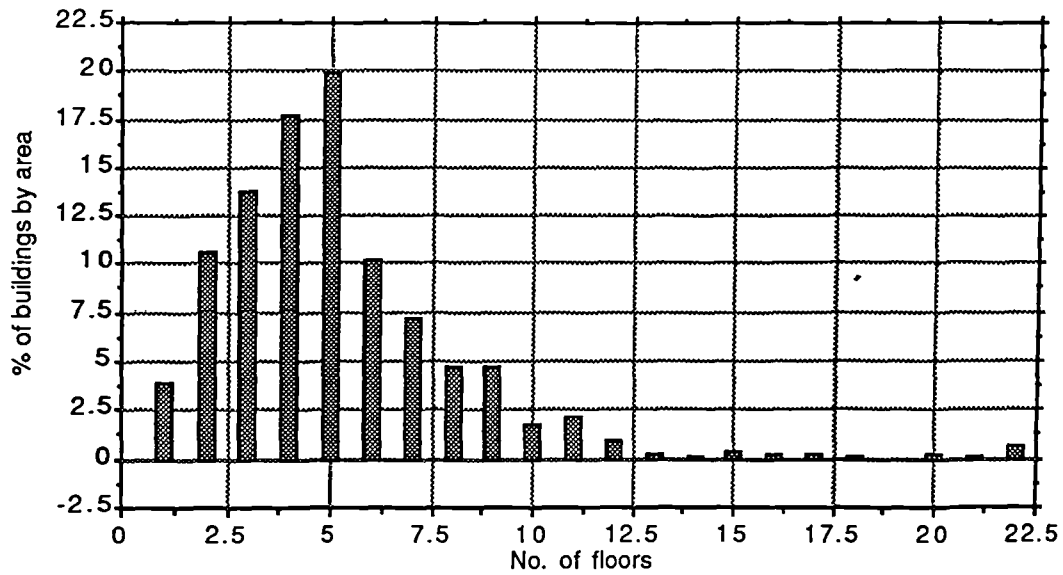


Figure 7.21: *Building stories distribution for the City of Westminster*

It is reasonable to assume that a linear relationship exists between the number of stories and the actual building height, assuming level terrain. For instance, [Loew,1991] has proposed a value of 3.7m per floor for a modern urban building, although some offset to account for the building roof may be considered necessary. In either case, figure 7.21 suggests a general form for a building height distribution in simulations. An asymmetric distribution such as the Rice or Rayleigh distribution would provide a good fit to the data, allowing the distribution to be described by a small number of characteristic parameters. More data needs to be collected to reach firm conclusions here. For the simulations made in the next sections a normal distribution will be used.

7.4.4: Single Building Height Variation

In the case of variation in height for a single half-plane, Appendix A shows that an asymptotic approximation may be made which enables the distribution of field strengths resulting from a given height distribution to be calculated directly. This avoids the need to carry out large numbers of trials in constructing the distribution. The geometry for the calculation is shown in figure 7.22.

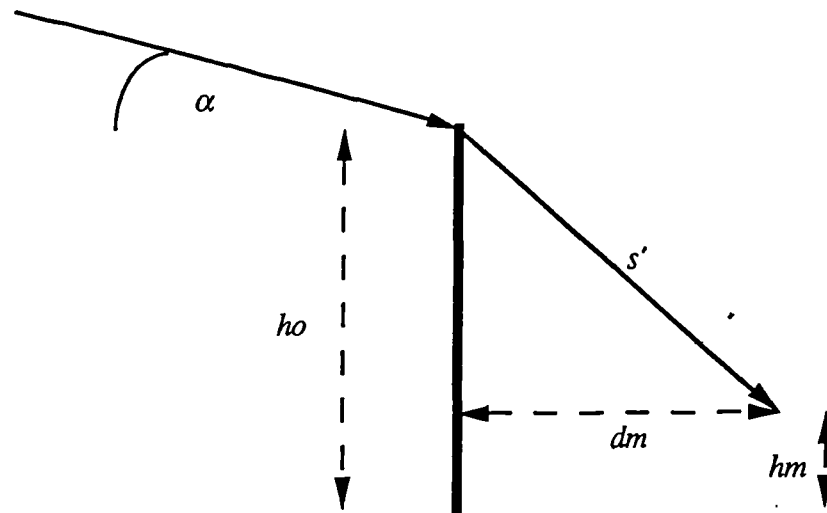


Figure 7.22: Single edge arrangement

Results are given in figure 7.23, using $h_m = 2\lambda$ and $d_m = 75\lambda$. Two different distributions for h_o are examined, a normal distribution with mean 10λ and standard deviation 1λ , and a distribution uniform on $[9\lambda, 11\lambda]$.

In the first case, α is set to 2° . When the building height is uniformly distributed, the mean value of L is 11.75dB, or 11.62dB in the normally distributed case. It is interesting to note that the mean loss is actually smaller than in the constant height case, contrary to the results of [Chrysanthou,1991] for multiple buildings. This strongly suggests that this effect arises from the interactions between buildings, again supporting the case for multiple building models in built-up areas. The corresponding standard deviations are 1.02 and 1.33dB respectively. The probability density function, p_L is shown for both cases in figure 7.23. The result from a uniform distribution for p_{h_o} is an almost linear distribution, favouring higher loss values. Similarly the results from a normal height distribution is rather skewed towards higher loss values. These distributions are likely to be substantially altered in the multiple building case, examined next.

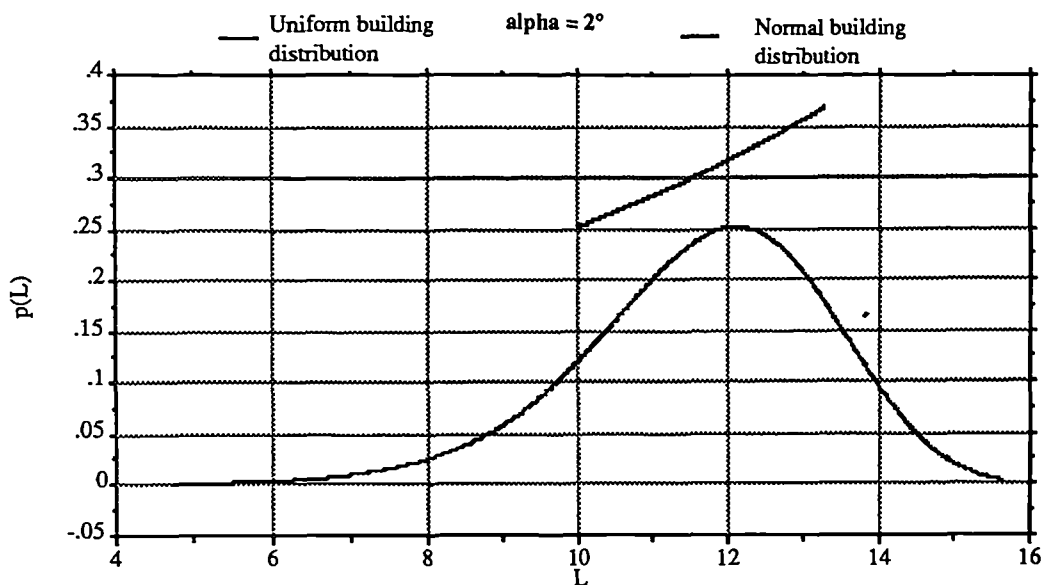


Figure 7.23 : Probability density functions for single building height variations

7.4.5: Multiple Building Height Variations

In the multiple building case, the asymptotic method adopted in §7.4.4 has not been solved, although it is believed that such an approach is possible. In this case the Monte-Carlo multiple edge calculation is used directly in the full model from §7.3. Building heights for the last few buildings along the path (5 in this case) are drawn from a normal distribution and a large number of trials (200) are used to find the distribution of the field strengths and the resulting location variability. Figure 7.24 shows the default parameters used.

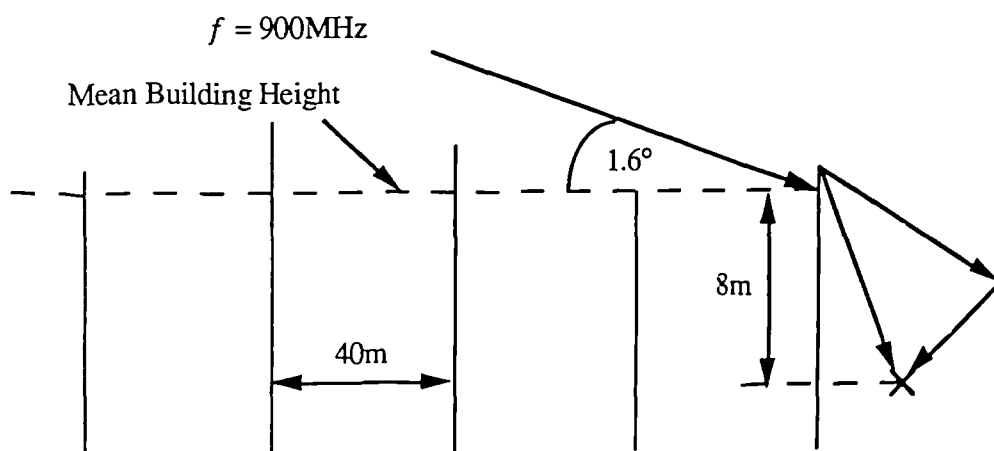


Figure 7.24: Parameters used for multiple building variations

Both direct and reflected rays are calculated independently, using the usual paradigm.

In figure 7.25 the distribution of transmission loss is shown for the case where the standard

deviation of the building heights is 1m. The distribution is approximately symmetrical and a chisquare goodness-of-fit test shows that the distribution of field strengths may be assumed lognormal with a confidence of 97.0%, a very good fit. This agrees with the findings of many measurements and shows that the variation of building heights is alone enough to account for such a distribution. Inclusion of other factors affecting propagation is likely to make the fit to a normal distribution still better, in accordance with central limit theory.

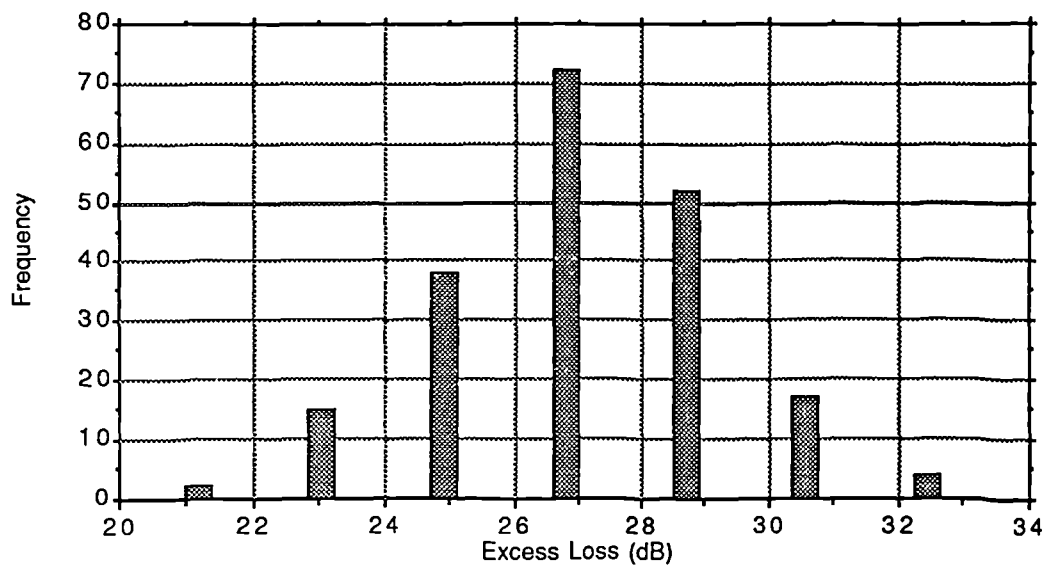


Figure 7.25: *Distribution of transmission loss for multiple building variations*

The loss in the constant height case is 26.1dB, compared with a sample mean of 26.9 in the varying height case, confirming the findings from [Chrysanthou,1991]. The calculated location variability is 2.2dB. Using a Chi-Square distribution, the 95% confidence interval for this variability is [2.0,2.4], indicating that 200 trials are sufficient for a reliable prediction of location variability, given that the assumptions of the model are met. This prediction of location variability is rather low by comparison with most measurements in urban areas which are usually in excess of 5dB although only a small height variability has been assumed. This variability is a highly significant factor, with the field strength variability increasing to 3.8dB for a variability of 2m in heights. If the frequency in the simulations is increased to 1800MHz, the predicted variability increases to 3.5dB, supporting the findings of [Okumura,1968] and others that location variability increases with frequency. Similarly, the results at 450MHz give

$\sigma_L = 1.3\text{dB}$. Measurements have also indicated that location variability is substantially independent of range [Jakes,1974] p.123. This is essentially equivalent in the multiple edge model to varying the base station antenna elevation angle. It is found from the simulations that even bringing the antenna down to the mean level of the buildings (equivalent to a very long transmission range) only increases σ_L slightly compared with the default case from 2.2 to 2.3dB.

7.4.6 : Summary

Simulation of propagation in built-up areas using the building diffraction models of this chapter produces results which are phenomenologically in agreement with the results of measurement programmes, suggesting the results of such models may be useful in estimating the relative significance of various factors on slow fading. Using more extensive simulations combined with more physical building data and measurements it may be possible to separate the causes of long-term signal fluctuations to the extent that models could include correction factors which take as input parameters such as the mean and standard deviations of building heights. This could be regarded as a second-order stochastic model, compared with the first-order approach of the Flat Edge model. Subject to the availability of data, such a model could yield a corresponding increase in prediction accuracy.

7.5: Conclusions

In this chapter, two models have been constructed: the Flat Edge model, which may be regarded as a method of characterising an area according to mean parameters. The method is therefore stochastic, since it does not attempt to predict field strength at any specific point, but in terms of gross characteristics over an area. The Full model, which combines the Flat Edge approach with a rapid multiple edge calculation, is deterministic in that it uses as input a path profile specific to a particular pair of base station/mobile locations. This model has also been found useful in investigating location variability caused by building height variations.

Together these models allow a wide range of available input data to be used for predictions. It remains for the next chapter to validate the models by comparison with measurements.

Chapter Eight

Measurement Programmes

8.0: Introduction

The ultimate test of any propagation model is its ability to accurately predict a set of measurements. Two measurement programmes are used for this in the current chapter. The first was undertaken especially for this work, involving a small set of measurements in an area where the detailed characteristics of the environment were known, enabling both of the models proposed in Chapter Seven to be tested. The second set came from a larger programme of measurements in which only average characteristics were available, allowing the Flat Edge model to be tested more rigorously.

8.1: Description of First Programme

The philosophy behind the design of the first programme was to make in-depth measurements over a relatively small area, whose characteristics could be determined in detail. All of the measurements were made in the King's Hedges / Arbury / Chesterton area to the north of Cambridge. This is a mostly residential area consisting principally of two storey terraced houses with gardens. Some taller buildings are present, together with some light industrial buildings. In many places there are trees as tall as or rather taller than the buildings, together with several open spaces such as parks and playing fields. The terrain in the area is relatively flat, with the base station in a slight dip.

The base station site was chosen to be the Philips building which lies to the south east of the measurement area. Thirty measurement sites were chosen as follows : Five radials were drawn from the base station out across the measurement area with equal angular spacing. Six arcs were then drawn centred at the base station with radii at 1/3 km intervals. Receiver sites were chosen close to the intersections between the arcs and the radials, with the restriction that sites

must fall in accessible streets.

The measurement locations are marked on the map in figure 8.1. The building positions and density can be more clearly seen in the aerial photograph of part of the measurement area reproduced in figure 8.2. Figure 8.3 is the view from the roof of the base station building: the dense tree cover is clearly visible. Measurements are shown in progress at location F in figure 8.4. The receiver antenna is mounted on a trolley on the pavement on the left side of the picture.

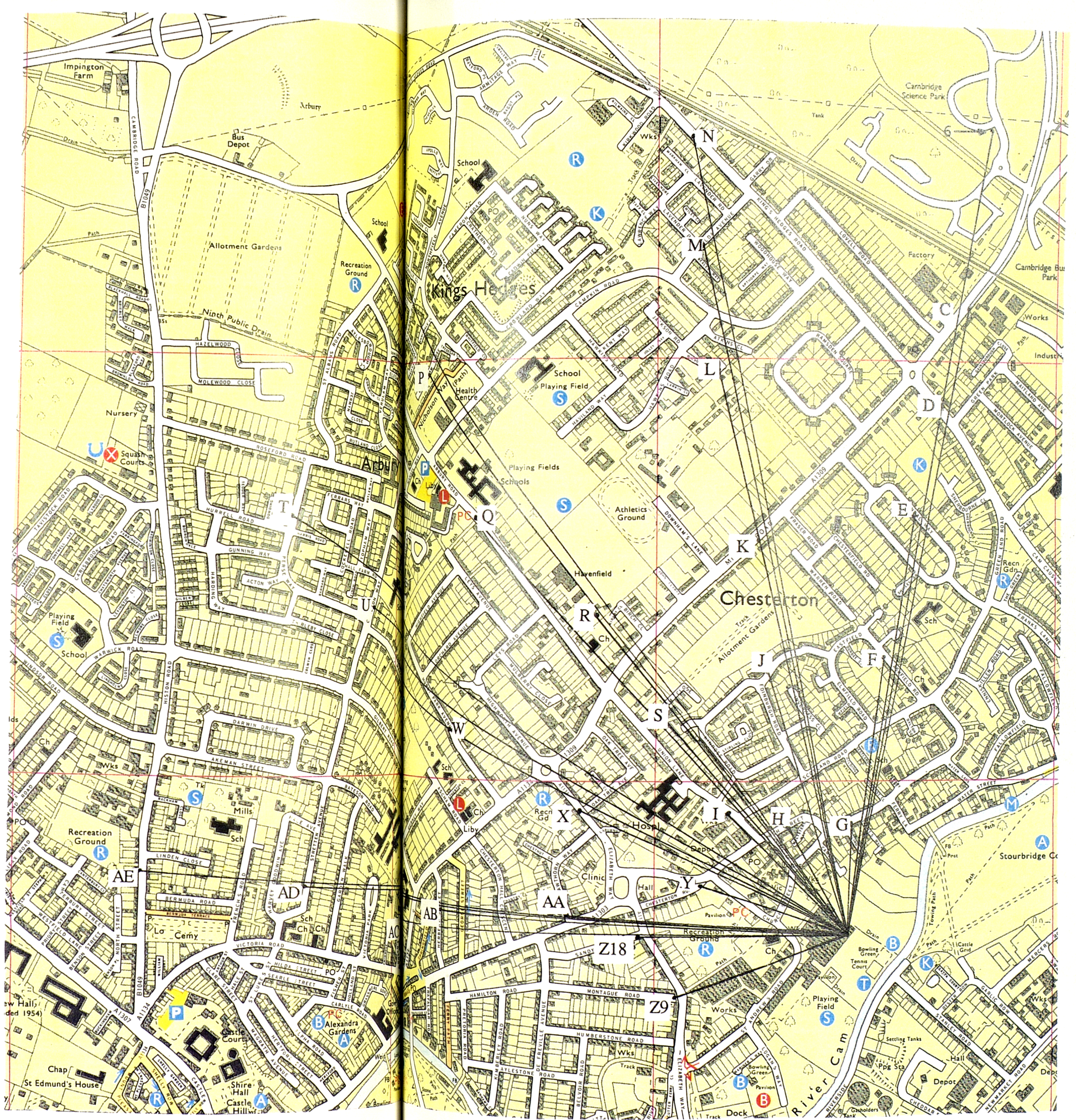


Figure 8.1: Map of measurement area (scale 1:10 000)

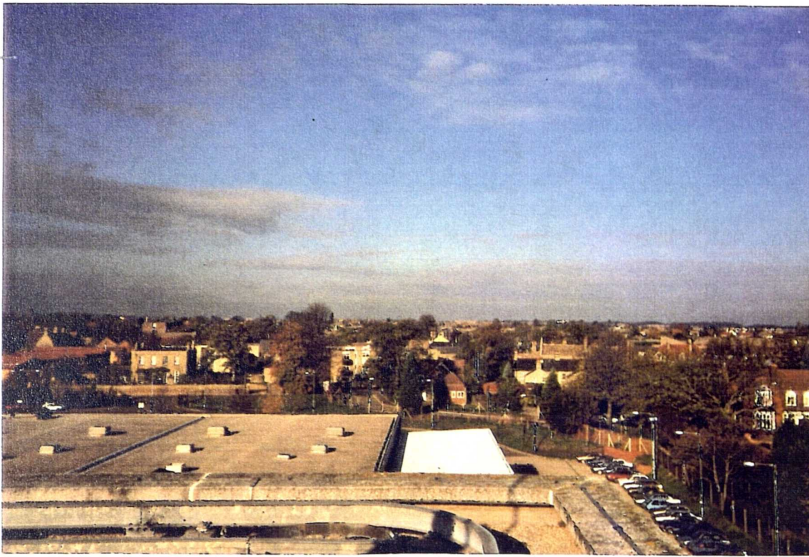


Figure 8.3: View north-westwards from the base station



Figure 8.4: Measurements in progress at location F



Figure 8.2: Aerial photograph (scale 1:10 000 approx.)
Base station appears halfway up right margin

Figure 8.5 gives the positions of the measurement sites, together with their distances from the base station, located at national grid reference TL 46465 59635.

Radial Number	Location Identifier	National Grid Reference (TL...)	Range(m)	Median Path Loss (dBi)	
				933.5 MHz	1890 MHz
1	B	46825 61555	1953	119.4	138.5
	C	46775 61115	1512	123.9	143.3
	D	46705 60885	1273	114.3	135.4
	E	46630 60620	999	118.2	137.1
	F	46555 60285	656	117.2	131.6
	G	46475 59910	275	104.4	121.2
	2	N	46080 61515	1919	124.8
M		46110 61275	1688	128.7	146.6
L		46145 60980	1383	120.2	139.0
K		46245 60600	990	109.7	125.2
J		46270 60270	664	101.5	121.4
H		46320 59890	293	103.1	124.4
3	O	45270 61230	1993	126.0	146.2
	P	45415 60975	1702	128.4	148.2
	Q	45565 60585	1309	111.9	139.8
	R	45855 60395	975	115.1	136.7
	S	46005 60155	694	110.8	131.0
	I	46180 59930	410	93.5	119.6
4	T	44670 60640	2057	129.6	-
	U	44905 60405	1740	120.1	138.4
	V	45240 60405	1447	131.8	143.1
	W	45490 60145	1100	116.8	136.9
	X	45855 59935	680	112.4	132.9
	Y	46110 59700	376	104.7	121.4
5	AE	44310 59780	2160	134.8	-
	AD	44700 59740	1768	127.9	148.3
	AC	45050 59650	1415	125.0	140.8
	AB	45450 59690	1016	123.1	141.9
	AA	45795 59695	673	115.9	138.5
	Z9	46050 59490	440	96.2	-
	Z18	45960 59630	505	-	117.7

Notes: i) Insufficient dynamic range was available to measure the loss at AE and T.
ii) Locations Z9 and Z18 are not coincident.

Figure 8.5 : Measurement locations and median field strengths

Two frequencies were used : 933.5 and 1890 MHz. The 900MHz band is well established for macrocellular services, while around 1.8GHz new short range services are being devised and used (see §2.1). Time and resources did not allow more frequencies to be used to enable greater examination of frequency dependent effects.

8.2 : Measurement System

The measurement system is shown in block form in figure 8.6.

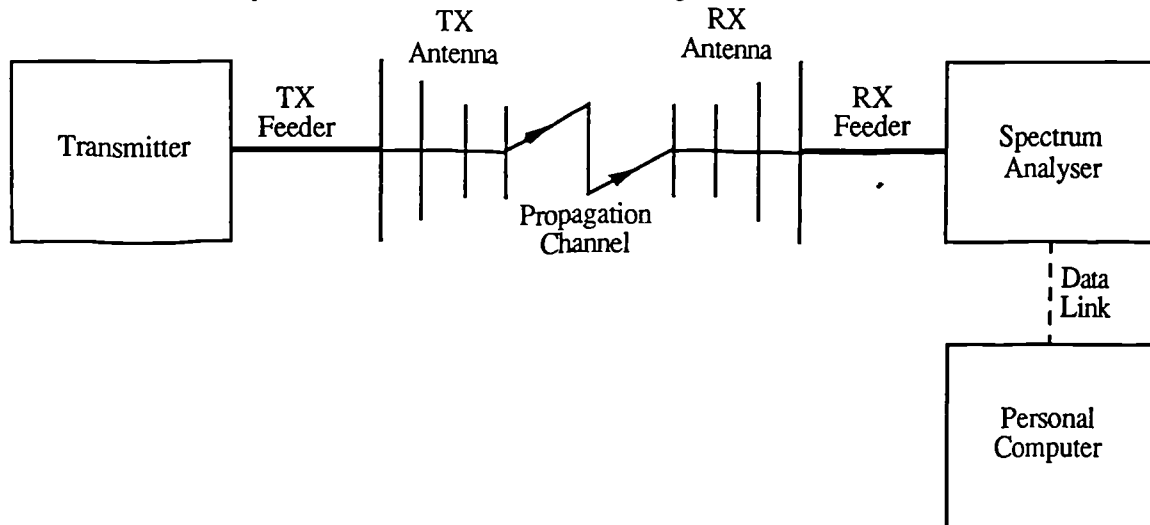


Figure 8.6: Measurement system block diagram.

At both frequencies the signal transmitted from the base station was an unmodulated carrier produced directly from a signal generator and fed to a rooftop antenna, with an additional linear power amplifier in the 900MHz case. An omni-directional antenna mounted 27.4m above local ground level was used at 900MHz, while at 1800MHz insufficient power was available to adequately cover the measurement area. A Yagi array was instead used, having 17 dBi gain, mounted at 21.8m agl. This had to be reorientated for each radial, but the 26° horizontal 3dB beamwidth made exact positioning uncritical. Vertical polarisation was used throughout, just as in most common mobile radio systems.

The mobile antenna was mounted on a surveyors' distance measuring trolley. This allowed position measurement with a reliable resolution of around 5cm to be made. This corresponds to 0.16λ at 933.5MHz and 0.32λ at 1890MHz. This should be sufficient to allow the effects of fast fading to be eliminated. At 933.5MHz a calibrated half wave dipole was used (0dBd), while at 1890MHz a 3dBd whip antenna was employed. Both were mounted 1.5m above the ground.

The receiver used was a digital spectrum analyser with a marker tuned to the carrier frequency allowing the signal level to be logged on a Personal Computer via a digital interface. After each

sweep of the spectrum analyser an audible signal was output by the PC, signifying that the trolley could be moved to the next position. The spectrum analyser and the PC were van mounted and powered from a portable generator. The antenna was fed via a coaxial feeder long enough to allow the effects of the van to be minimised. At each location 200 measurements at 5cm intervals along a 10m track were made and stored on floppy disks for later analysis. A number of measurements were also made with the trolley stationary to ensure that time related effects were not unduly affecting the results. With the exception of occasional signal depression and enhancement in the presence of heavy passing traffic, the median values were considered reliable. Figure 8.5 shows the measured median path loss values.

8.3 : Link Budget

Figure 8.7 shows the system parameters used for calculating the overall path loss. The sector median path loss is given from the received signal power as follows:

$$\text{Path Loss (dB)} = \text{Link Budget Constant (dBi)} - \text{Received signal power (dBm)}$$

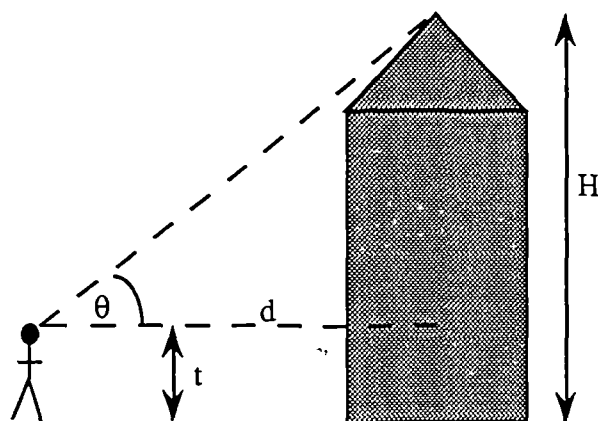
Link Budget Calculation		
Frequency (MHz)	933.5	1890.0
TX Power (dBm)	29.3 / 13.0	13.0
Tx Feeder Loss (dB)	(2.5)	(4.0)
TX Antenna Gain (dBi)	8.15	17.0
RX Antenna Gain (dBi)	2.15	5.1
RX Feeder Loss (dB)	(3.5)	(6)
Tuning Correction (dB)	(0.0)	(2.0 / 0.0)
Net Link Budget Constant (dBi)	33.6 / 17.3	23.1 / 25.1

The second set of figures in the 933.5 MHz column result from an equipment failure. They apply to locations Z9, AA, AB, AC, AD and AE. The first set in the 1890 MHz column compensate for a small tuning error, and apply to all locations except AB, AC and AD.

Figure 8.7 : Link Budget calculation.

8.4: Collection of Building Data

At each measurement site a survey was conducted to gather building information. The perpendicular distances to the buildings on both sides of the street was measured directly. A clinometer was used to measure the elevation angle of the highest visible edge in the direction of the base station. This in turn is used as a measure of the edge height (see figure 8.8).



The edge height H is given by $H = t + d \tan \theta$, with $t = 1.7\text{m}$

Figure 8.8: Clinometer usage.

Finally photographs showing the position of the mobile antenna relative to the adjacent buildings were taken to enable more detailed building features to be determined later.

The profile data was obtained mainly from a set of aerial photographs covering the measurement area [Cambridge,1991]. Locations of buildings along the straight line path from the base station to each measurement location in turn were recorded using a digitising tablet. Some approximation is involved here due to parallax effects on the photographs, but this was considered negligible. In fact, this effect can be used to determine building heights using stereoscopic techniques since overlapping photographs were available. However, the relatively uniform nature of the buildings in this area made it more straightforward to assume a standard building height for all the two storey houses and to take direct measurements of other buildings using the clinometer.

8.5: Construction of Building Profiles

The geometry of the building measurements taken is shown in figure 8.9. In general, the incident wavefronts arrive at an oblique angle to the diffracting edge, so a two dimensional representation is inadequate. It is assumed further that building edge diffraction is independent of edge orientation, so that in effect all edges are replaced by a canonical knife edge transverse to the propagation path. The reflection point no longer lies in the plane containing the point of diffraction, so in principle a different profile should be constructed for the reflected ray. If, however, the street orientation θ does not lie close to 0° or 180° , then the profile encountered will be very similar to that for the direct ray.

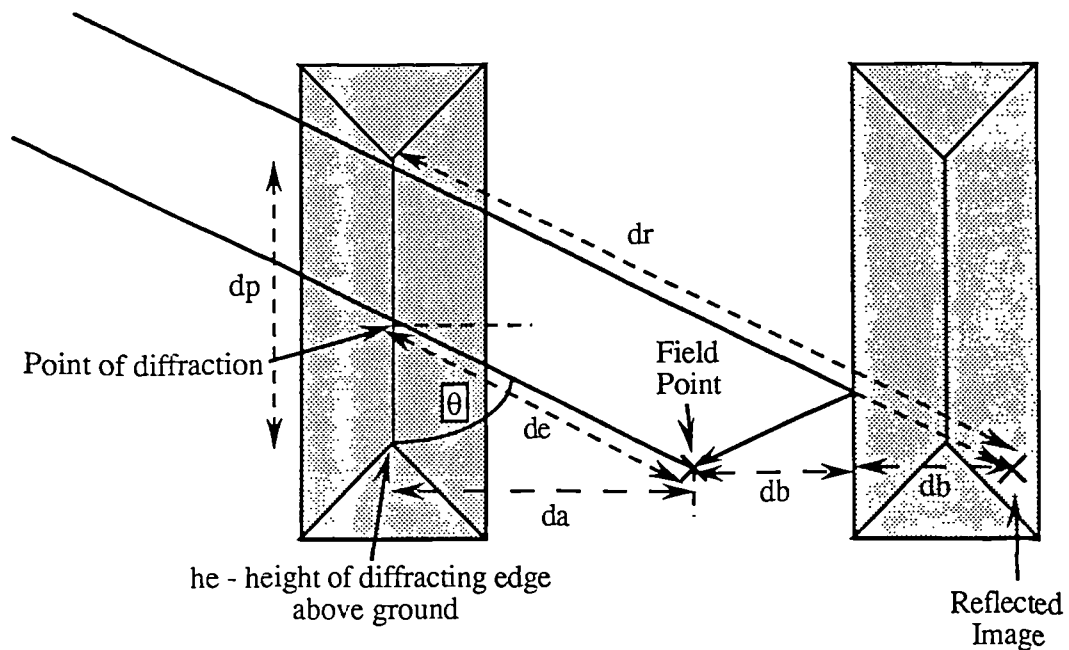


Figure 8.9: Relationship between building measurements and ray parameters.

The parameters given in figure 8.10 are calculated from the measurements of d_a and d_b as follows. The parameters of the reflected ray are calculated using the method of images. The street orientation was measured from the aerial photographs.

Horizontal distance between diffracting edge and field point:

$$de = \frac{da}{\sin \theta}$$

Horizontal distance between diffracting edge and reflected image of field point :

$$dr = \frac{da + 2 db}{\sin \theta}$$

Horizontal distance between field point and diffraction point for reflected ray, measured along the street:

$$dp = (da + 2 db) \cos \theta$$

This parameter indicates the error incurred in using the same building profile for both the direct ray and the reflected ray. It is always less than 50m. For streets close to radial, the two ray representation will be a poor model in any case (eg point Q).

Location	da (m)	db (m)	de (m)	θ (°)	he (m)	dr (m)	dp (m)
B	7.3	-	7.3	60	8.5	-	-
C	40.0	-	40.0	30	8.5	-	-
D	27.9	12.6	35.4	128	8.2	67.4	32.7
E	13.0	23.5	15.9	125	8.3	73.3	34.4
F	10.2	24.9	12.9	128	8.1	76.1	36.9
G	8.1	17.9	9.4	60	7.8	50.7	22.0
H	10.6	25	10.6	95	7.8	60.8	5.3
I	100.0	-	100.0	90	8.0	-	-
J	20.9	14.2	20.9	90	8.0	49.3	0.0
K	28.3	14.3	32.7	60	7.5	65.7	28.5
L	28.7	16.3	373.0	125	7.5	74.8	35.2
M	16.4	17.15	31.8	146	7.5	93.2	43.2
N	17.8	13.6	20.0	55	8.0	53.2	25.0
O	20.0	15.0	40.0	150	8.0	100.0	43.3
P	21.7	22.0	21.8	85	15.0	65.0	5.7
Q	Radial	-	-	0	8.0	-	-
R	24.4	7.5	24.4	90	8.0	39.4	0.0
S	15.0	7.7	15.1	85	7.5	30.5	2.7
T	7.0	17.9	7.4	70	8.0	45.6	14.6
U	26.1	16.8	26.5	80	7.5	60.6	10.4
V	26.5	14.7	27.4	75	8.5	57.9	14.5
W	16.3	16.4	47.7	20	9.5	143.6	46.1
X	64.4	15.6	70.0	113	15.0	45.7	16.5
Y	3.7	-	7.4	150	2.3	-	-
Z9	150.0	-	180.0	90	10.0	-	-
Z18	30.0	3.0	30.0	90	8.0	36.0	0.0
AA	13.8	16.6	15.6	62	9.1	53.2	22.1
AB	5.0	8.5	5.0	90	5.8	22.0	0.0
AC	3.0	30	3.0	90	2.15	63.0	0.0
AD	17.5	3.8	17.6	96	7.5	25.2	2.6
AE	10.5	25	10.5	90	8.5	60.5	0.0

Figure 8.10 : Close-in building parameters

These parameters were used to correct the digitised building profiles appropriately. Examples of the resulting profiles are given in figures 8.11 and 8.12.

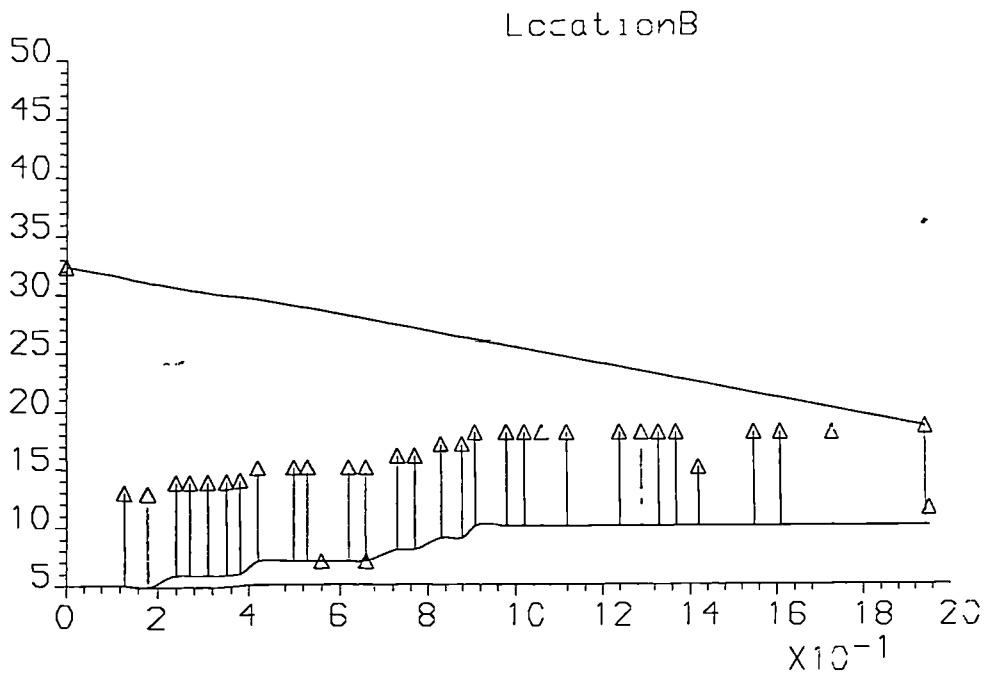


Figure 8.11: Example of reconstructed path profile (location B)

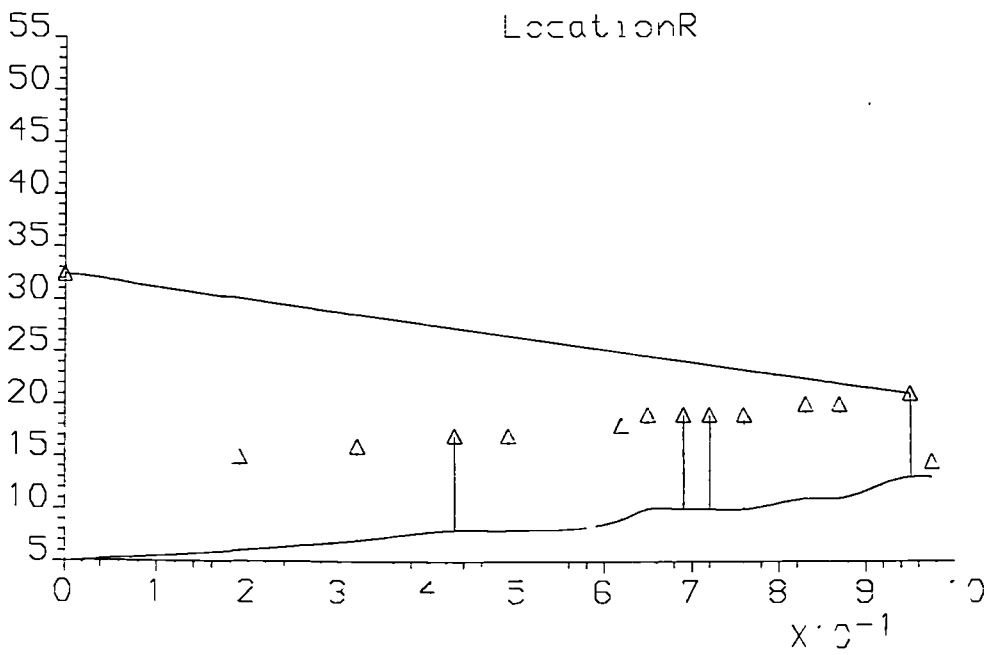


Figure 8.12: Example of reconstructed path profile (location R)

8.6: Results

Figure 8.13 shows the median path loss measurements at 933MHz plotted versus range. Also shown are the results of a least-squares regression analysis.

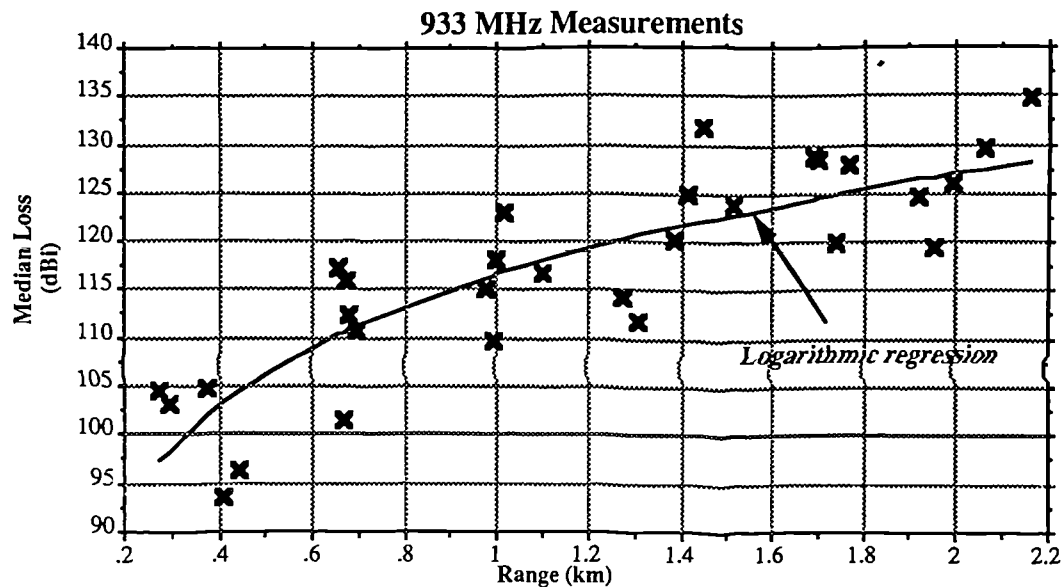


Figure 8.13: Measured path loss versus range (933MHz)

At 933.5 MHz the regression analysis indicates a total median path loss characteristic given by:

$$\text{Total median path loss, } L_T \text{ (dBi)} = 34.5 \log_{10} R + 116.7$$

Subtracting free space loss at this frequency yields :

$$\text{Excess path loss, } L_E \text{ (dB)} = 14.5 \log_{10} R + 24.9$$

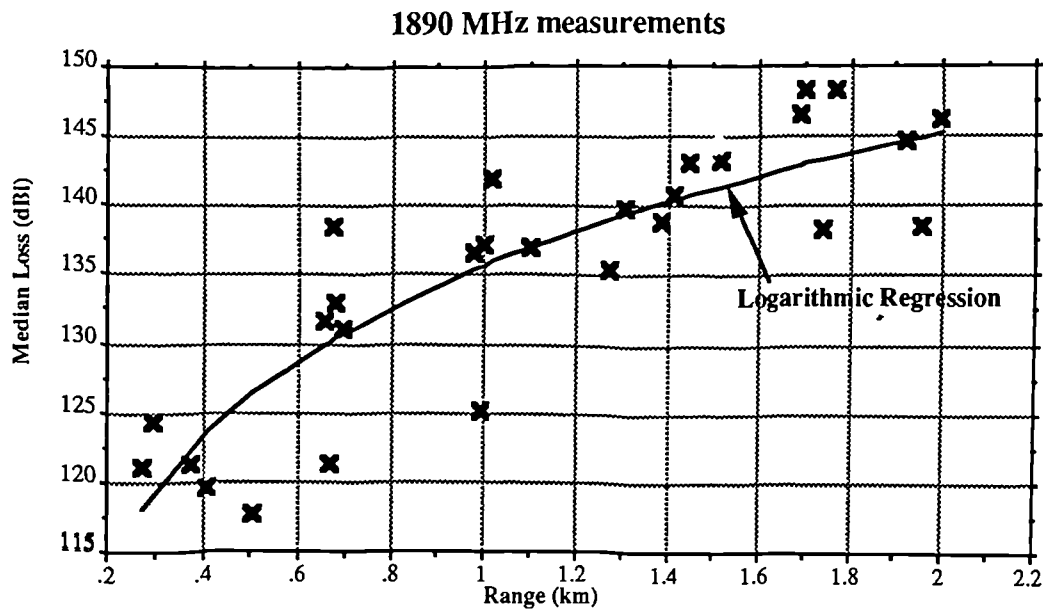


Figure 8.14: Measured path loss versus range (1890 MHz)

At 1890 MHz (figure 8.14) the corresponding parameters are :

$$L_T \text{ (dBi)} = 31.5 \log_{10} R + 135.8$$

Subtracting free space loss at this frequency yields :

$$\text{Excess path loss, } L_E \text{ (dB)} = 11.5 \log_{10} R + 37.8$$

The range dependence characteristic is relatively low in both cases. Many more points would be required to establish the underlying rate of decay, indicating the difficulties of using purely empirical models to predict individual cases.

Figure 8.15 compares the measurements at the two frequencies. Although considerable correlation is to be expected (and is displayed) there is no reason to expect a simple relationship between the two cases, since the frequency characteristics depend upon the precise geometry of the path profile compared to a wavelength. Some errors may have been introduced by incorrect repositioning of the receiver antenna or by changes in the propagation conditions between measurements. Ideally all measurements at a given location should be

performed at the same time.

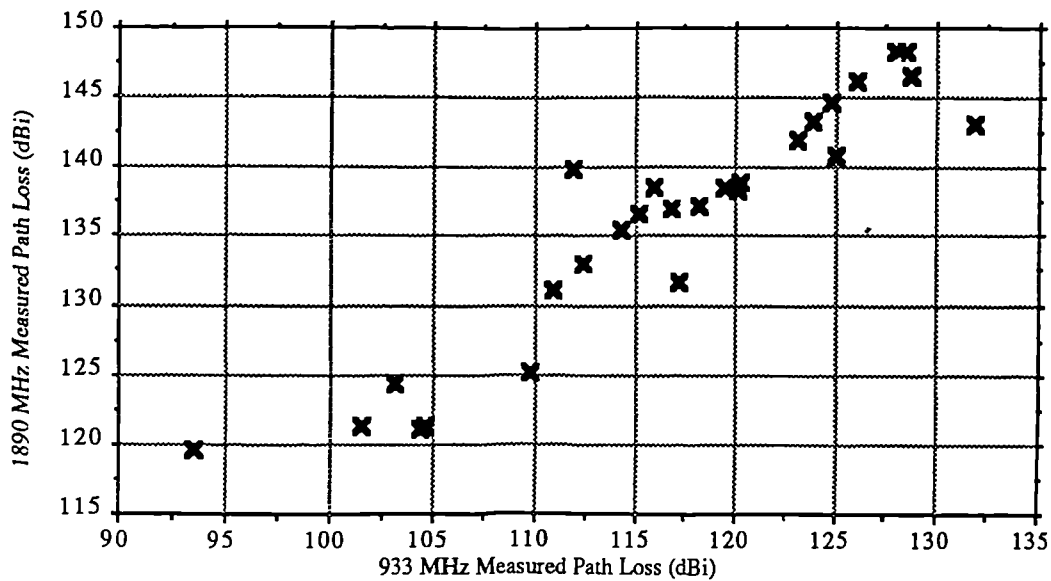


Figure 8.15: Correlation between measurements at 1890 and 933MHz

8.7: Predictions

In this section actual comparisons are made between the measurements and predictions made by the models proposed in Chapter Seven. These are the Flat Edge model (§7.1) and the full hybrid model (§7.3). As a standard of comparison predictions are also made using the Hata [Hata,1980] empirical prediction model. In each case, predictions of total path loss are plotted against the respective measured value. The line $y = x$ is plotted, along which all of the predictions should ideally lie. As a measure of deviation from this ideal, a prediction error is defined as:

$$\text{Prediction Error, } \varepsilon = \text{Measured } L_T - \text{Predicted } L_T$$

The mean of ε thus indicates how close the predicted values are to the measurements on average. However, a zero mean could arise from widely scattered points which are equally spaced about the ideal line. This possibility is avoided by also calculating the standard deviation of the error which reflects how widely scattered the points are, independently of the mean. The standard deviation therefore provides an indication of how well the prediction model follows changes in the measured signal, and thus how accurately the underlying

propagation mechanisms are being modelled.

8.7.1: 933MHz Comparisons

Figure 8.16 shows the Hata suburban predictions of total loss plotted against the measured values at 933MHz. A low prediction mean of 0.28 dB is obtained, which is small enough for most system design applications, so the model is well suited to comparisons in this particular environment. However, considerable scattering of points about the mean is evident, resulting in an error standard deviation of 5.42dB. It is important to recall at this stage that the Hata model will always predict the same loss at a given range in a particular environment, giving no estimate of location variability at constant range.

Figure 8.17 gives the results of applying the Flat Edge model. In accordance with §7.3.1 building parameters appropriate to each individual path are used here, reflecting variations from location to location better than mean parameters representing the whole area would. The mean propagation loss is underestimated by 4.21 dB, indicating that loss is being caused in practice by factors other than the constant height buildings accounted for by the model. This level of error is still acceptable however and shows that a purely theoretical model is capable of accounting for measured field strengths with prediction accuracy at least comparable to that of empirical models. Moreover, the standard deviation of the error (4.43dB) actually shows an improvement over the Hata model, indicating that building geometry is being accounted for with good accuracy even when only average building heights are used.

Examination of the predictions of the full multiple edge model (figure 8.18) shows that still better predictions may be made when complete building position data is considered. The mean prediction error is very small in this case (2.45dB), indicating that varying building positions may be considered as a factor which causes additional loss relative to the flat edge case. The standard deviation is smaller still in this case (4.40dB), again indicating that propagation mechanisms are being correctly modelled. At particular locations the transmission loss is predicted very accurately, frequently to within 1dB, while the error is larger (up to 9dB) in

other cases. This may result from errors in the digitised path profiles or from factors affecting propagation besides those modelled. The improvement may nevertheless be considered rather small when the extra prediction effort and data required is considered. In an area where the building height distribution is rather less narrow, however, it may be expected that greater improvement over the Flat Edge model would be obtained.

933 MHz Comparisons

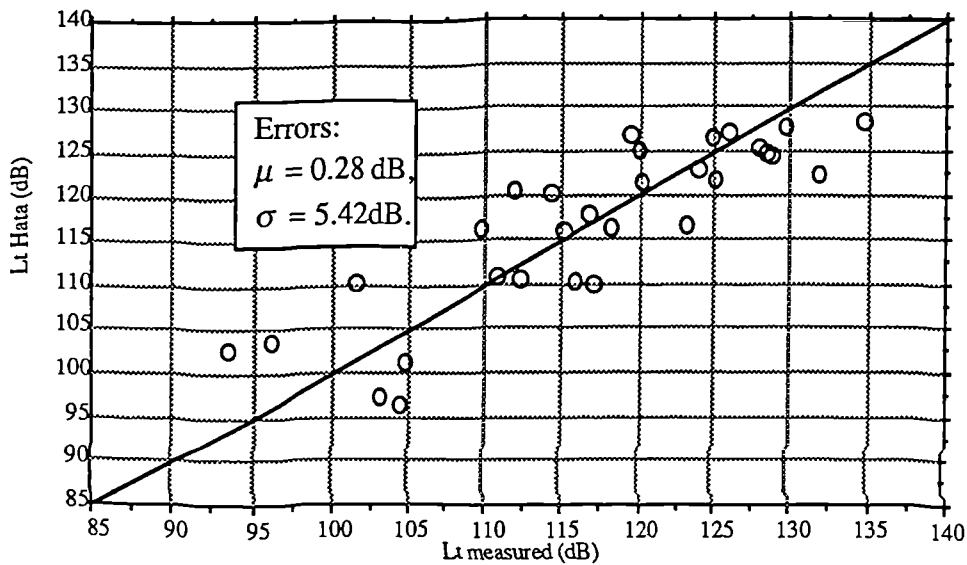


Figure 8.16: Comparison of Hata prediction with measurements at 933MHz.

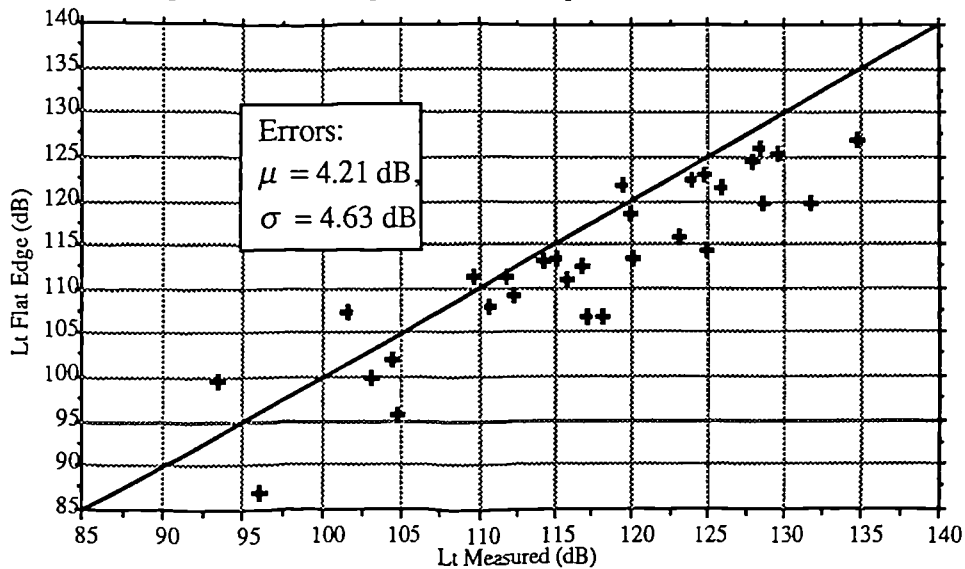


Figure 8.17: Comparison of Flat Edge prediction with measurements at 933MHz.

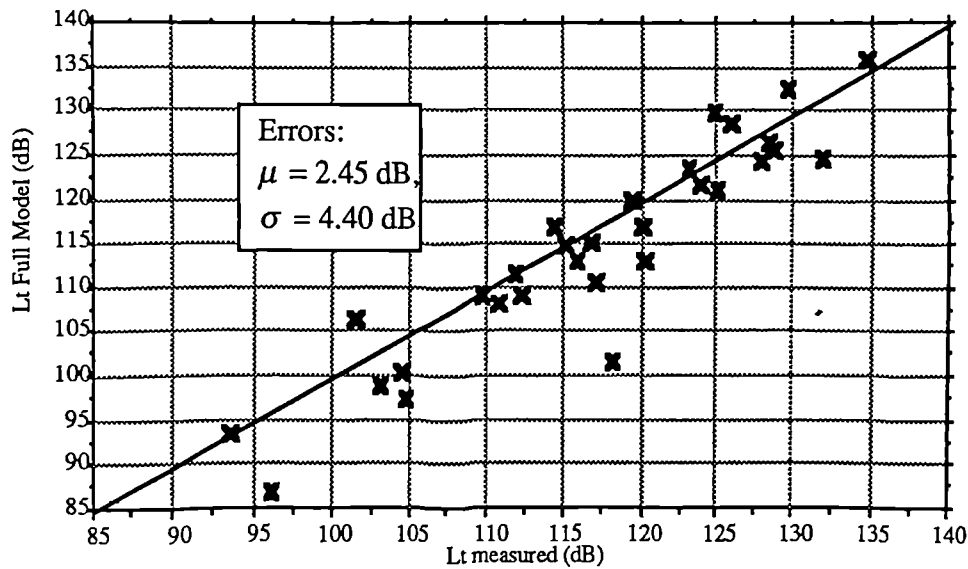


Figure 8.18: Comparison of Full prediction with measurements at 933MHz.

8.7.2: 1890 MHz Comparisons

At the higher frequency, all of the models substantially underestimate propagation loss although the error deviations are similar to the values at 933MHz (Figures 8.19, 8.20 and 8.21). On a point by point comparison the errors are considerably greater than at 933MHz (up to 15dB).

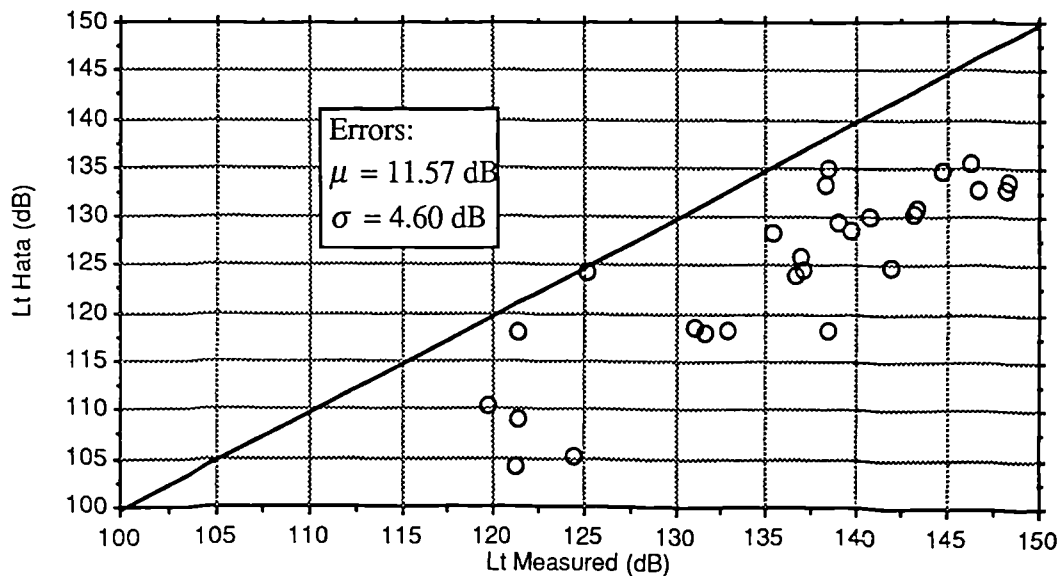


Figure 8.19: Comparison of Hata predictions with measurements at 1890MHz

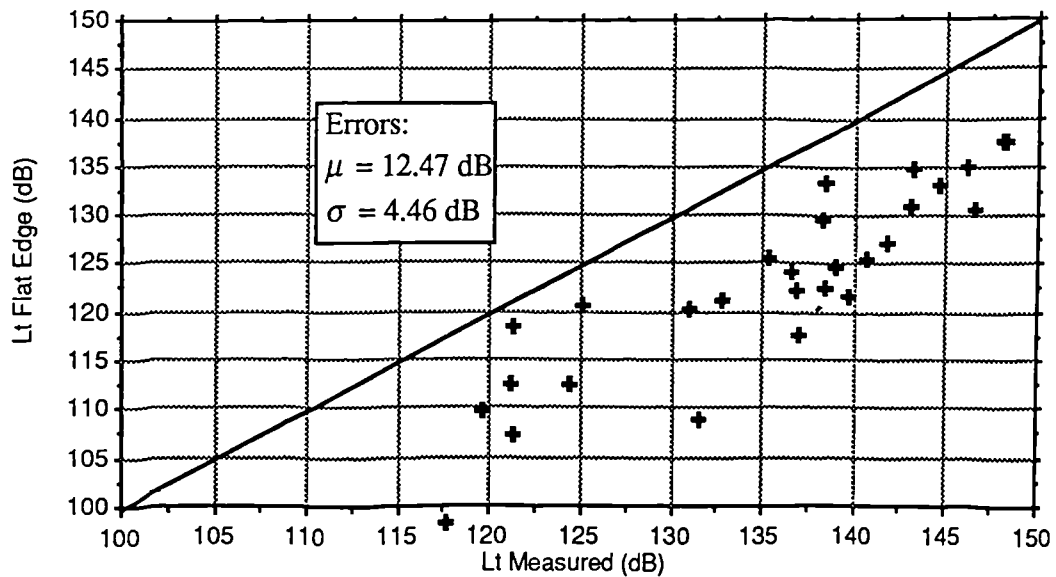


Figure 8.20: Comparison of Flat Edge predictions with measurements at 1890MHz

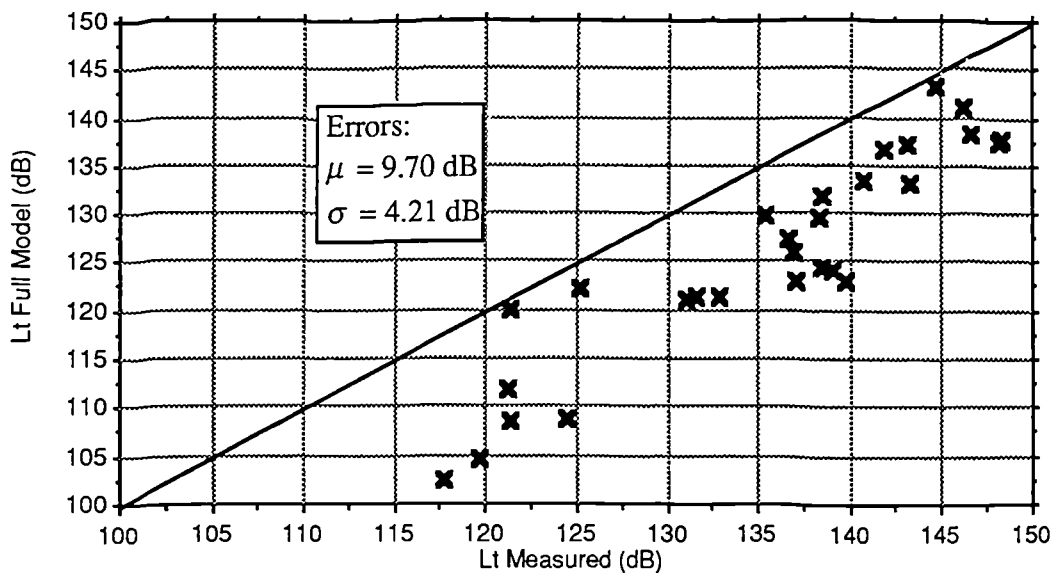


Figure 8.21: Comparison of Full predictions with measurements at 1890MHz

The increase in the errors at the higher frequency may result from:

- i) Any errors in measuring the heights and positions of the buildings increase in significance by comparison to a wavelength at higher frequencies. Thus a given level of prediction accuracy demands an increasing quality of data as frequency increases.
- ii) The influence of actual building shapes and their electrical characteristics relative to the canonical knife edge is likely to be more pronounced at high frequencies.

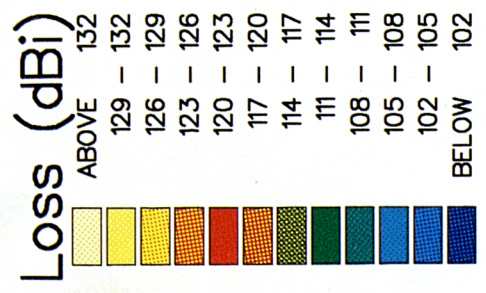
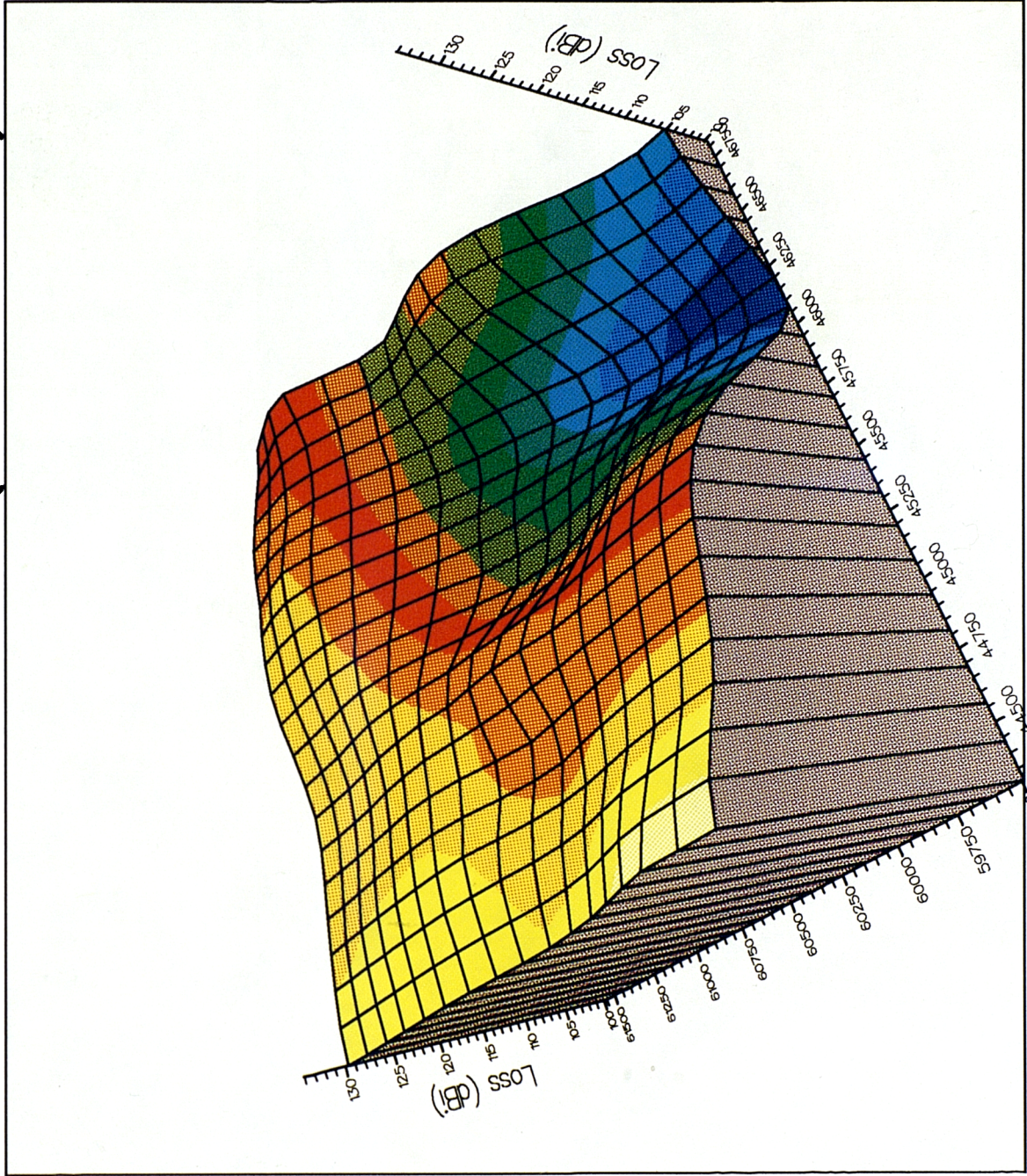
iii) Other scatterers such as trees become more opaque at high frequencies, so that their importance as diffracting obstacles (and hence interference with the building diffraction model) increases.

This last factor is also likely to be the cause of the loss underestimates. As was previously noted, the measurement area included large numbers of tall trees. The majority of the wave energy therefore had to penetrate relatively large foliage depths between the building rows. An extra loss factor should ideally be included to account for this effect, but previous studies of tree attenuation have concentrated on either dense forest areas (eg[CCIR,236-6,1986]), or single avenues of trees at very high elevation angles (eg[Vogel,1986]), neither of which are appropriate here. Further work should examine this effect, particularly in terms of the interaction between the absorption and diffraction mechanisms. Additional evidence that foliage is the cause of the extra measured attenuation is provided in an independent study [Morgensen,1991], which compared measurements at 900 and 1800 MHz. The area had very little tree cover, and the results showed that the path loss at 1800MHz was fairly consistently 10dB greater than the corresponding value at 900MHz. This corresponds well with the predictions of the theoretical models shown here.

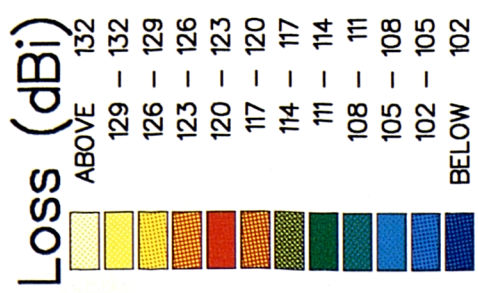
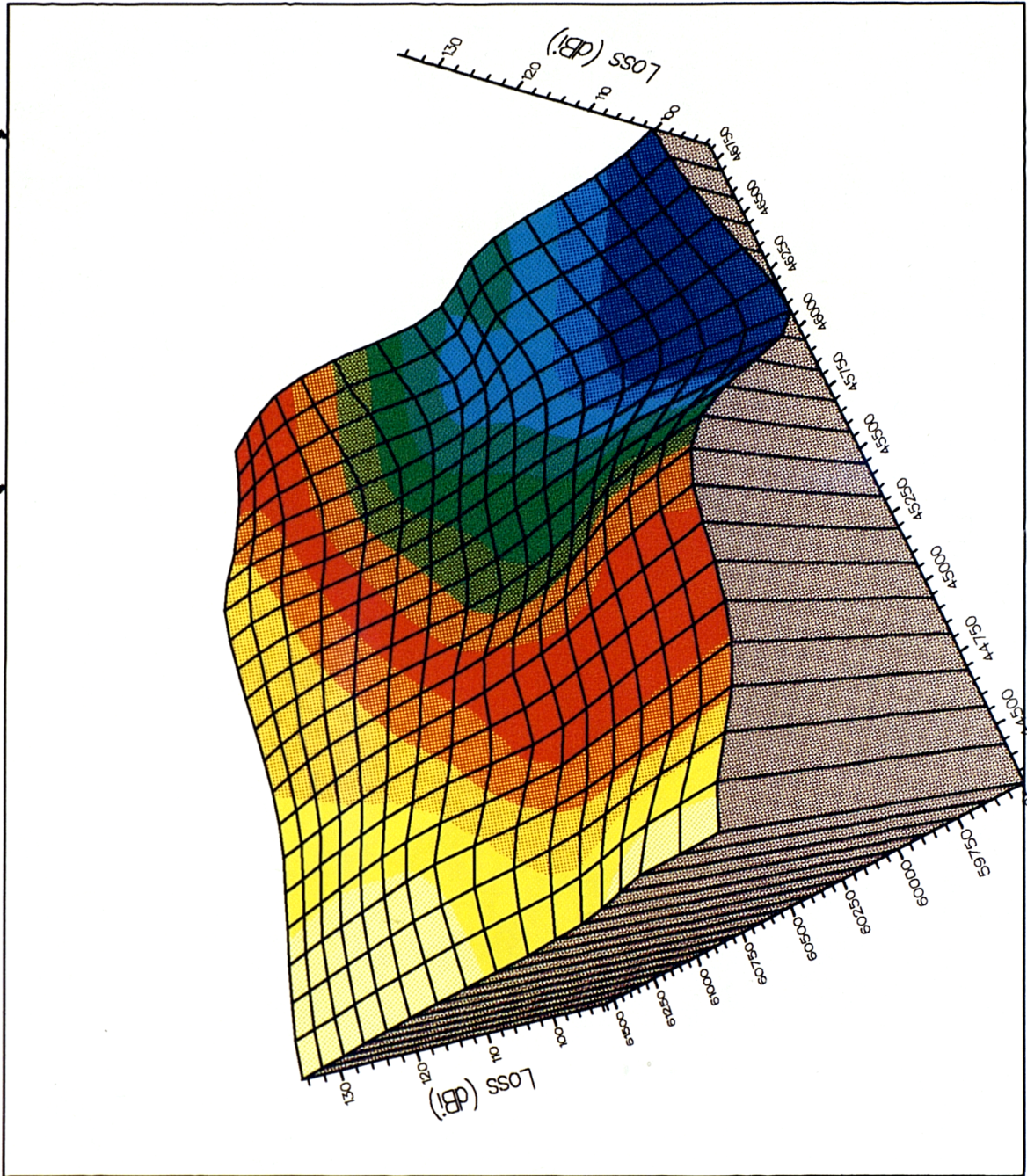
Another method of presenting the data shows further advantages of the theoretical methods over empirical ones. Figure 8.22 is a plot of the measured data, interpolated across the whole area where the data was gathered. Increasing height on the plot indicates increasing loss. The axes are national grid references in square TL. In the case of the Hata model, the corresponding prediction contours would be a series of concentric circles, indicating no variation with azimuthal angle from the base station.

Contrast this behaviour with the predictions of the full model at 933.5MHz, shown in figure 8.23. The model successfully predicts the overall structure of the spatial variation of the field, making it a useful tool for identifying potential trouble spots and allowing appropriate countermeasures to be taken. Note particularly the more rapid increase moving west from the base station than to the north, where street widths are larger and buildings are lower.

Measured Loss (933.5MHz)



Predicted Loss (933.5MHz)



8.8: Second Measurement Programme

8.8.1: Description

In order to further verify the Flat Edge model a second set of measurements was obtained. These were made simultaneously at 955 and 1845 MHz in the Danish cities of Aalborg and Copenhagen as part of the COST231 initiative, which has been investigating propagation issues for the GSM and DCS-1800 systems (see §2.1). The measurement system is described in detail in [Morgensen,1991]. Sector medians were calculated from samples measured over a 10 meter sector length. Short ranges were in use (50-1000m) with low base station antenna heights, often below the average building height, making prediction challenging for existing empirical methods designed for longer ranges and higher antennas. Although detailed building data was unavailable, mean street widths and building heights were supplied. Maps of Aalborg and Copenhagen are shown in figures 8.24 and 8.25 respectively. Four different base stations were in use in Aalborg: the measurement routes are indicated by dotted lines.

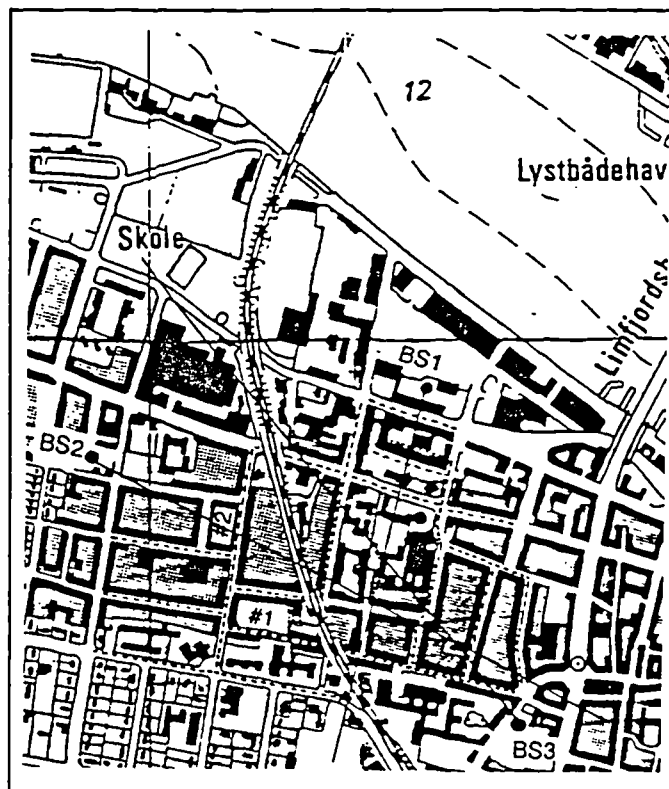


Figure 8.24: Map of measurement area in Aalborg.

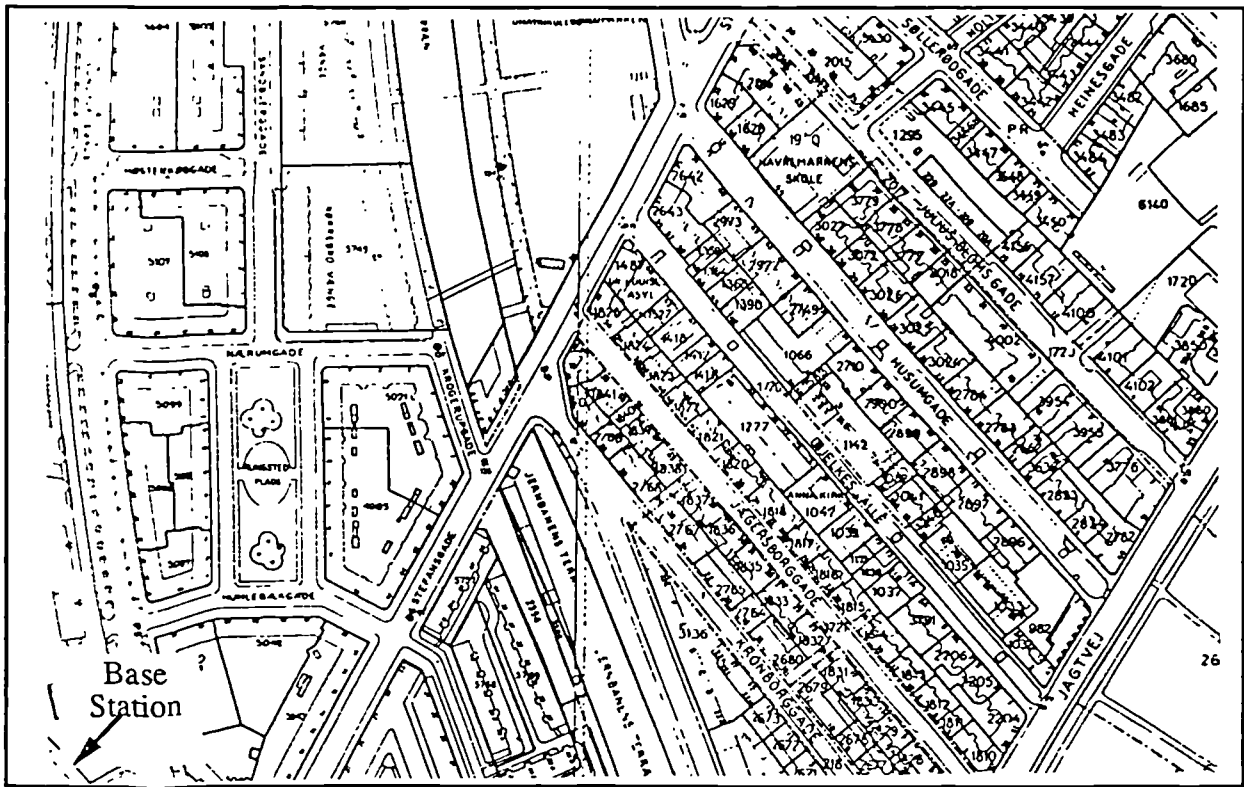


Figure 8.25: Map of measurement area in Copenhagen.

The Flat Edge model was applied exactly as described in §7.3 , except that an estimate of the number of buildings along a given propagation path had to be made. This was done in accordance with the following expression:

$$n = \left\lceil \frac{R - r - d_m}{w} \right\rceil + 1$$

where the quantities are defined in figure 8.26.

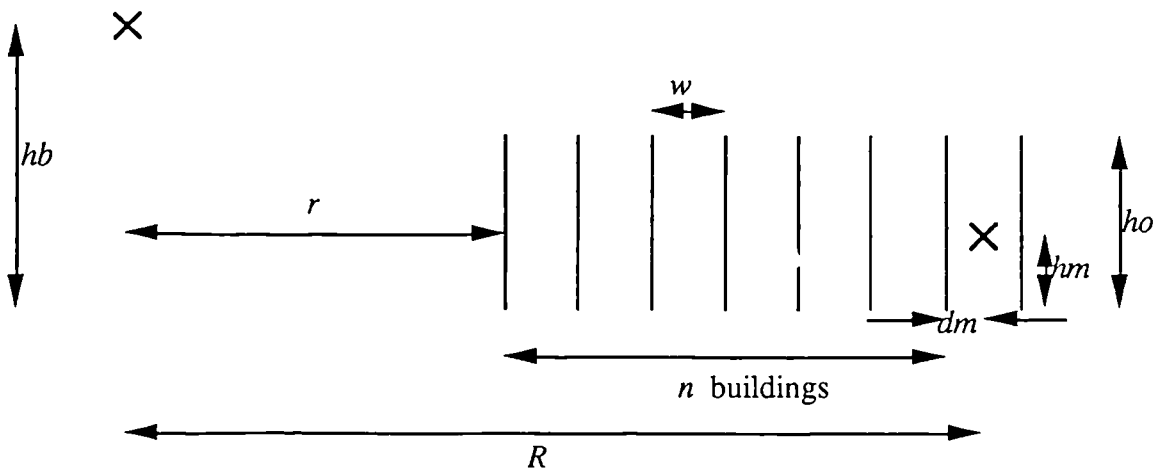


Figure 8.26: Geometry for Flat Edge model

The building spacing w was set to $w_s \sqrt{2}$, where w_s is the mean street width, in accordance with the arguments of §5.4 which suggest that median predictions of field strength will be obtained with an assumed street orientation of $\theta_s = 45^\circ$.

For comparison purposes predictions were also made using the Hata urban model [Hata,1980] and the settled field approximation [Walfisch,1988], which was applied with the same two ray final diffraction calculation as for the Flat Edge case (§7.1.5). The settled model is entirely inapplicable for base station antennas below the building heights, however, since no settling behaviour occurs.

8.8.2: Results

Some example results are now presented. As well as displaying the behaviour of the measurements and predictions as a function of range, the error statistics of each model will be shown, with the error again defined as (measured loss) - (predicted loss). The following symbols are used:

μ_f, σ_f Mean, standard deviation of error for Flat Edge model.

μ_h, σ_h Mean, standard deviation of error for Hata urban model.

μ_s, σ_s Mean, standard deviation of error for settled field model.

Figure 8.27 shows some Aalborg data at 955MHz with $h_b = 14.35\text{m}$ and $h_o = 14.4\text{m}$. The Flat Edge model performs well with $\mu_f = 4.3$, $\sigma_f = 6.9$ while agreement with the Hata model is less good: $\mu_h = 10.9$, $\sigma_h = 6.5$. The Flat Edge model displays discontinuities at each increasing value of n which is not a feature of conventional methods, but is entirely consistent with the measurements which show a large variation in field strength from street to street. There is some increase in the measured loss relative to the model at large ranges in this example. This is probably due to some taller buildings on this particular section of the measurement run.

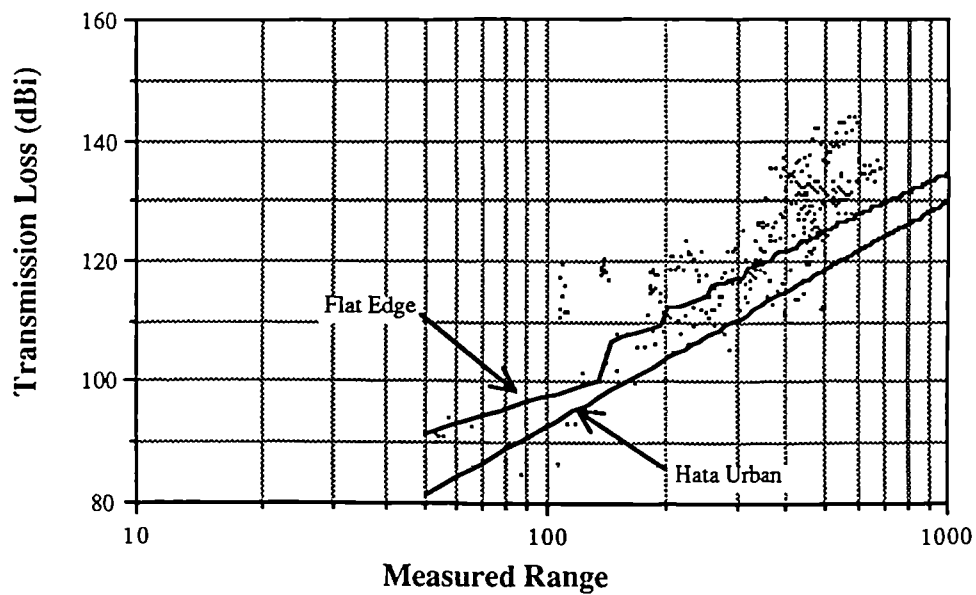


Figure 8.27: Comparisons for run A at 955MHz.

The corresponding results at 1845MHz (figure 8.28) show excellent correlation with the 955MHz measurements and similar prediction results with $\mu_f = 4.6$, $\sigma_f = 8.0$, $\mu_h = 12.4$ and $\sigma_h = 7.6$. The underestimate of loss which was observed in the Cambridge data at 1.8GHz is not apparent here, further supporting the suggestion that this was due to particular characteristics of the Cambridge measurement area.

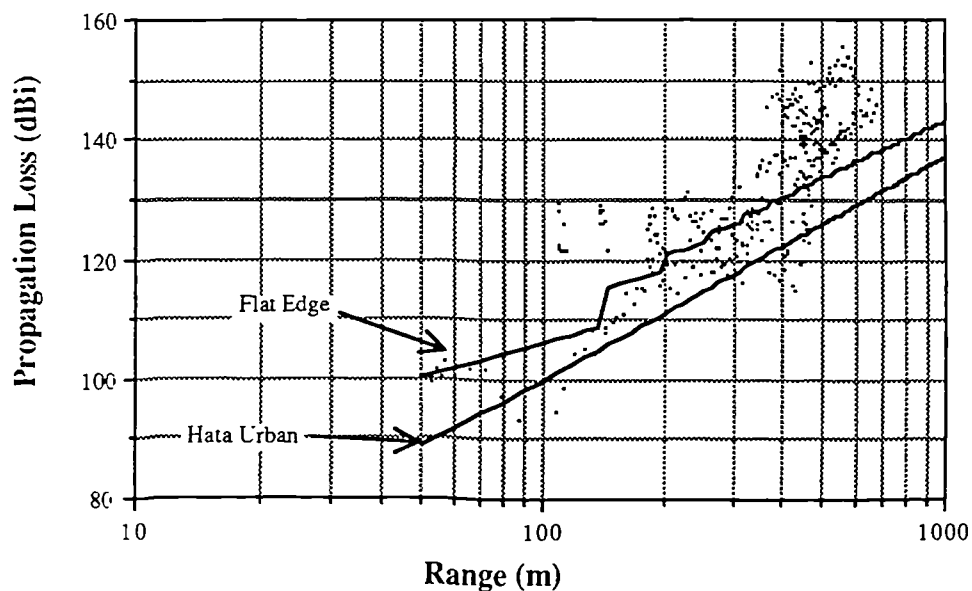


Figure 8.28: Comparisons for run A at 1845MHz.

The next pair of results show that such results may be consistently obtained. In figure 8.29 at 955MHz with $h_b = 11.55\text{m}$ and $h_o = 15\text{m}$ the error statistics are $\mu_f = -0.6$, $\sigma_f = 5.6$,

$\mu_h = 9.7, \sigma_h = 5.5$. The model follows the measurements throughout the range considered this time, suggesting more homogeneous building cover.

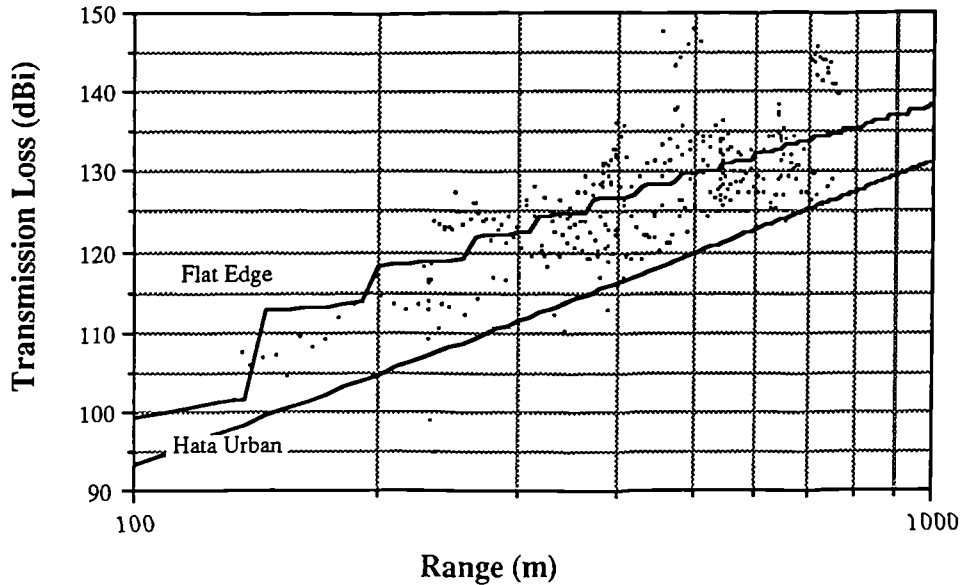


Figure 8.29: Comparisons for run B at 955MHz.

At 1845MHz the corresponding results (figure 8.30) are $\mu_f = -0.6, \sigma_f = 6.1, \mu_h = 12.5, \sigma_h = 6.1$ which is again very similar to the results at the lower frequency.

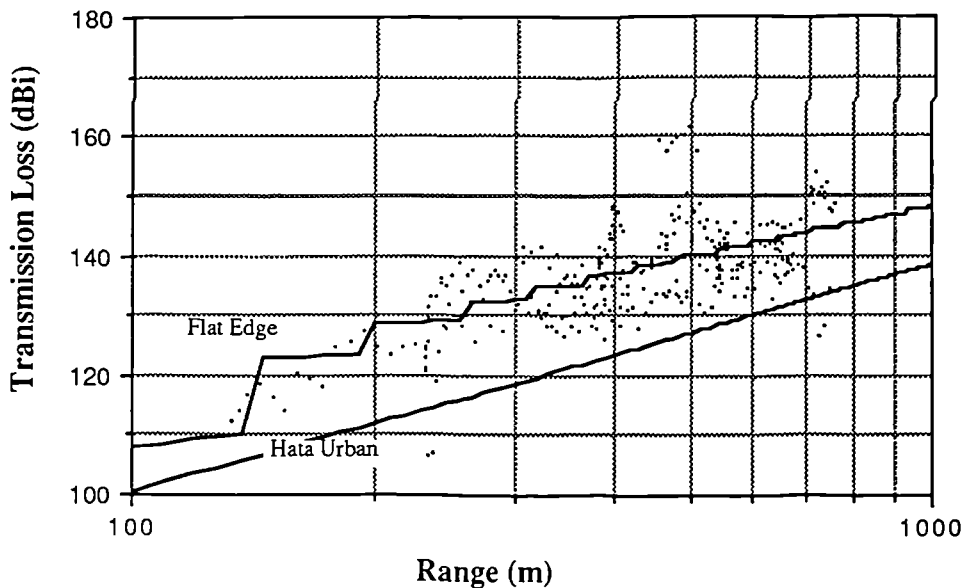


Figure 8.30: Comparisons for run B at 1845MHz.

Figure 8.31 shows the performance of the Flat-Edge model with a very low base station antenna at 1845MHz with $h_b = 8.5\text{m}$ and $h_o = 15\text{m}$. The error statistics are $\mu_f = -0.3, \sigma_f = 5.0, \mu_h = 15.8, \sigma_h = 6.1$. The Hata model performs poorly, but the Flat Edge model is entirely applicable here.

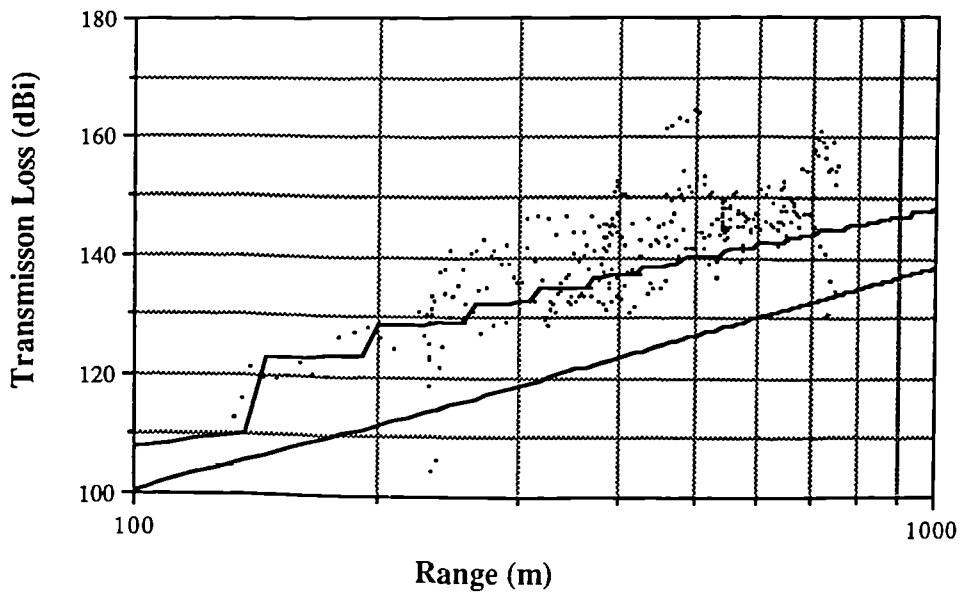


Figure 8.31: Comparisons for run D at 1845MHz.

Figure 8.32 shows some Copenhagen data with the base station antenna slightly above the rooftop, allowing comparison with the settled field approach. The Hata model still shows relatively poor performance with a mean error of 6.1 dB, while both the Flat Edge and settled field models display high accuracy with -1.0 and -4.0 dB mean errors respectively. The discrepancies between the two models increase with range indicating the inaccuracies in the settled field approximation [Walfisch,1988] when the elevation angle of the base station antenna is low.

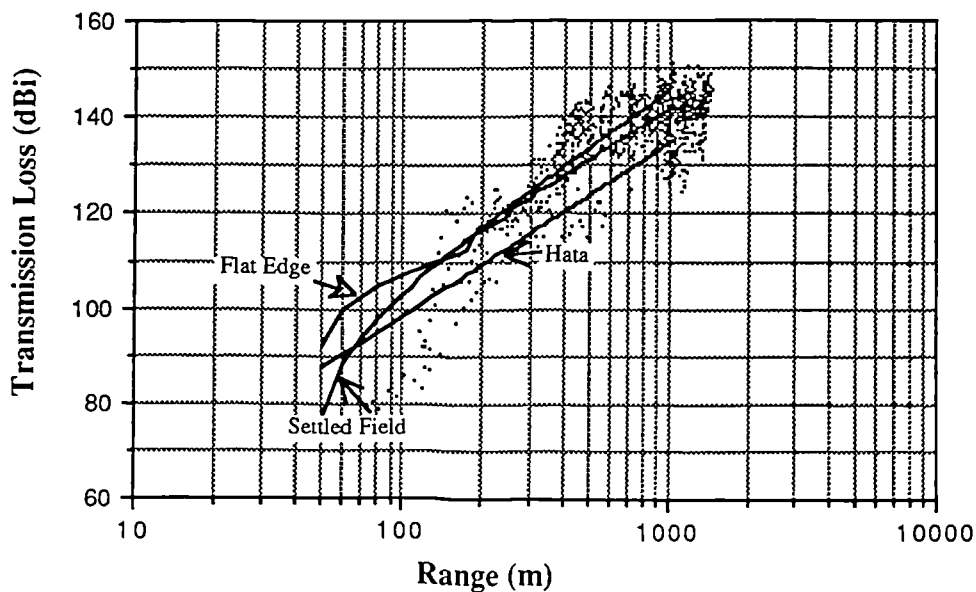


Figure 8.32: Comparisons for run N at 1845MHz.

The tables in figures 8.33 and 8.34 show the results from all of the measurement runs considered at both frequencies. Base stations with the prefix 'A' are in Aalborg, while those with a 'C' prefix are in Copenhagen. The parameters used in each prediction are displayed in figure 8.35 together with the number of measured sector medians in each run. In all cases r was set equal to w due to lack of better information. If the open ground close to the base station in Copenhagen was considered then the fit at short ranges in cases such as figure 8.32 would improve.

Run	Flat Edge		Settled Field		Hata Urban		Base Station
	Mean μ_f	SD σ_f	Mean μ_s	SD σ_s	Mean μ_h	SD σ_h	
A	4.3	6.9	•	•	10.9	6.5	A1
B	-0.6	5.6	•	•	9.7	5.5	A2
C	6	9.1	•	•	15.1	8.5	A1
D	-0.4	6.1	•	•	12.0	5.7	A2
E	5.6	10.4	•	•	16.9	9.6	A1
F	3.5	10.9	•	•	16.0	9.8	A1
G	5.1	9.4	-2.3	9.6	8.0	9.4	A3
H	-0.3	8.2	-13.3	10.1	5.6	8.1	A4
I	9.2	9.6	•	•	13.9	9.6	A3
J	-1.6	10.3	•	•	7.1	9.8	A4
K	10.1	9.9	•	•	17.3	9.8	A3
L	-1.9	12.9	•	•	9.1	12.6	A4
M	-3.8	6.3	-3.7	6.4	-0.2	6.3	C1
N	-2.3	6.8	-7.2	6.9	4.1	6.8	C1
O	1.8	7.7	•	•	11.3	7.9	C1
P	3.6	8.8	•	•	15.6	9	C1

Figure 8.33: Error statistics at 955MHz

Run	Flat Edge		Settled Field		Hata Urban		Base Station
	Mean μ_f	SD σ_f	Mean μ_s	SD σ_s	Mean μ_h	SD σ_h	
A	4.6	8.0	•	•	12.4	7.6	A1
B	-0.6	6.1	•	•	12.5	6.1	A2
C	6.4	9.6	•	•	18.0	9	A1
D	0.5	6.4	•	•	15.8	6.1	A2
E	4.1	10.5	•	•	19.0	9.5	A1
F	2.2	11.2	•	•	18.7	9.9	A1
G	5.2	10.0	0.0	10	8.9	9.9	A3
H	2.5	10.0	-8.0	11.5	9.4	9.9	A4
I	9.0	11.1	•	•	15.5	11	A3
J	2.4	13.8	•	•	13.4	13.6	A4
K	8.2	10.8	•	•	18.4	10.7	A3
L	0.5	15.4	•	•	14.7	15.7	A4
M	-0.3	6.8	0.5	6.6	2.6	6.6	C1
N	-1.0	6.9	-4.0	6.9	6.1	6.9	C1
O	3.1	8.1	•	•	14.6	8.3	C1
P	4.6	8.7	•	•	24.0	9.2	C1

Figure 8.34: Error statistics at 1845MHz

Run	hb	ho	w	Points
A	14.35	14.4	56.6	514
B	11.55	15	56.6	320
C	11.55	14.4	56.6	327
D	8.5	15	56.6	312
E	8.5	14.4	56.6	323
F	5.25	14.4	56.6	325
G	13	12	56.6	319
H	14.35	14	56.6	81
I	11.05	12	56.6	320
J	11.55	14	56.6	81
K	7.9	12	56.6	324
L	8.5	14	86.6	79
M	26	20	70.7	1000
N	22	20	70.7	967
O	18	20	70.7	940
P	14	20	70.7	940

Figure 8.35: Parameters used in prediction model

The errors in the Hata model increase with frequency, while there is no significant increase in the Flat Edge mean error, suggesting that frequency variation is being correctly modelled. The mean errors are summarised in figure 8.36 for all three models at both frequencies, together with one standard deviation error bars. At both frequencies the Flat Edge model outperforms the others, both in terms of the mean error and the variability, suggesting that a degree of

consistency has been achieved. Recall that the settled field approach is only valid in a small number of the cases presented here. The settled field method consistently overestimates the field, confirming the suggestion that it is unnecessarily predicting diffraction over non-existent edges. The Hata model is clearly not applicable in low base station antenna cases. Although a new empirical model could in principle be constructed based on the measurements used here, the Flat Edge model would appear to offer a more consistent and reliable approach for all base station heights and differing building densities.

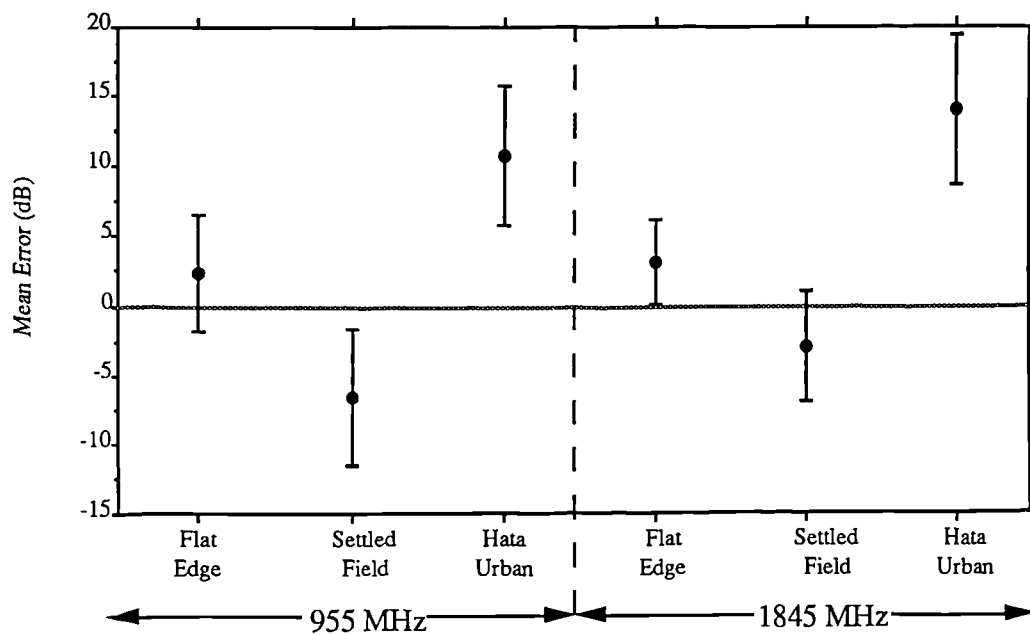


Figure 8.36: Mean error statistics for all measurement runs

There is some tendency for the Flat Edge model to underestimate loss, confirming that other factors besides 'mean height' building diffraction are significant, such as variable building heights (§7.4), foliage attenuation and street orientation (§5.4). Further development of the model could address these issues by including appropriate corrections. The penalty would be a need for extra data supplied on a point-by-point basis. It should be remembered that the Flat Edge model is not truly deterministic, since only mean building parameters are used. On particular measurement routes the characteristics of particular buildings will affect the accuracy of the predictions, but as a mean characterisation across an area the Flat Edge model appears to perform well.

8.8.3: Discussion

The Flat Edge model has shown that remarkably good performance is possible from a purely theoretical model which requires no adjustments derived from measured data. This performance is achieved using only two more parameters than would be required in an empirical model (building height and spacing) and dispensing entirely with any qualitative classification of the environment. Further improvements could be made by including a factor to account for variability in building heights and spacings, possibly derived from simulations such as those shown in Chapter Seven. It would also be useful to use more measurements to indicate the limits of applicability of the model, since it may be anticipated that the multiple half-plane assumptions are not valid in very dense urban situations or at very short ranges (less than 50-100m or within the line-of-sight of the base station).

8.9: Conclusion

This chapter has shown that the theoretical models developed offer real promise as useful and reliable prediction models. The prediction errors are in general low suggesting that the mechanisms of propagation across buildings have been well modelled, although factors other than buildings require consideration to produce small overall errors in some cases. More extensive measurements need to be performed in order to truly determine the range and limits of applicability of the models.

Chapter Nine

Conclusions and Further Work

9.1: Summary of Achievements

Chapter Two showed that, of the major propagation mechanisms which affect the sector median mobile radio signal, diffraction is dominant for the ranges commonly encountered in macrocellular systems.

The need for an improved model of propagation which accounts explicitly for diffraction effects was expounded in Chapter Three. Most existing models do not account specifically for building heights or positions which can cause large errors in some cases. Those theoretical models which do exist were shown to have certain limitations in real situations due to inadequate assumptions regarding multiple rooftop diffraction.

In Chapter Four the feasibility of modelling the diffraction characteristics of buildings using simple structures was examined. The structure of measured field pattern was seen to have sufficient regularity to allow sector median values to be predicted with good accuracy using discrete wave representations. Mobile antenna height gain was seen to be accounted for using a simple knife edge model.

The analysis of more complex shapes and arrangements of buildings using ray methods such as the Geometrical Theory of Diffraction was explained in Chapter Five. These techniques allow great flexibility and ease of calculation in many cases, although they are limited to small numbers of buildings. Differing representations of rooftop structure were found to significantly affect the field in the deep shadow region, but close to grazing a knife edge representation is adequate. A model of the contribution of street orientation to location

variability using ray techniques was derived, showing that median fields appear to be affected principally by the transmission range.

For modelling the effect of multiple buildings a number of techniques for calculating multiple knife edge diffraction were compared in Chapter Six. Approximate geometrical methods were found inadequate in this application and a more exact method required lengthy computations. More efficient evaluation techniques were proposed and found to have good performance for large numbers of edges close to grazing incidence.

In Chapter Seven a new closed-form solution to the problem of multiple buildings of the same height and spacing was described. This allowed rapid calculation of average propagation characteristics in area where only limited building data is available. An heuristic extension to the model allowed more complete building representations to be used, representing real-world situations rather better and allowing slow fading effects to be examined.

Finally, Chapter Eight verified the models by comparing the predictions with a set of measurements in a suburban area with extensive building data available and in two cities with only average data. Good agreement was found in both cases, although the extended method yielded only modest performance improvements since the suburban area was relatively homogeneous.

9.2: Further Work

Arising from the work presented here there are a number of suggestions for future work which should be performed to extend and complement the achievements to date. These are divided into three areas : collection of building data , modelling and measurements.

9.2.1: Collection of Building Data

The major limitation to extending the use of theoretical models is the lack of availability of adequate physical building data. More work must be done in this area, particularly since the development of new models is to some extent influenced by the nature of the data available. Sources of data which could usefully be investigated are as follows:

- **Existing Planning Data**

For general characterisation of an area data such as that described in §7.4.3 can be used. This has the advantage of being cheap and relatively simple to process, but it provides only coarse resolution, with no information regarding particular buildings. The data also varies in availability and format from city to city.

- **Aerial Photography**

Using combinations of photographs such as that reproduced in figure 8.2 building positions and heights can be determined, subject to practical limitations in the areas which can be covered by the aircraft's flight path. Manual extraction of this data is laborious, so automatic methods are needed. Advanced pattern recognition and image processing techniques offer considerable potential, but are unlikely to be particularly reliable for extracting parameters for individual buildings. It is more likely that these approaches will be able to provide measures of mean building density in particular regions.

- **Remote Sensing**

Developments in satellite remote sensing technology offer the potential to collect data over very wide areas. The same limitations of data extraction and processing apply as with the aerial

photography case and this is compounded by poorer available resolution. The increasing commercial availability of satellite data is nevertheless likely to increase the importance of this source of data in the future.

These sources need to be critically examined for their usefulness in driving the models and their quality and ease of availability.

9.2.2: Modelling

As a more direct continuation of the work contained here, the following points should be developed:

- A model of propagation along streets close to radial is needed to complement the model of street orientation derived in Chapter Five. This could take the form of a multiple ray model as in [Rustako,1991] or a more complete full field solution. The latter has advantages in describing the situation when the radial street is illuminated by diffraction over (or around) a previous building, a situation which often occurs.
- The ray tracing algorithm mentioned in Chapter Five needs to be extended to incorporate three dimensional building arrangements. This is important for modelling microcellular propagation.
- Using this algorithm some conclusions need to be reached regarding propagation in cases where exact building data is unavailable and to make general recommendations for the type of systems best suited to covering such areas.
- The asymptotic technique introduced in §7.4.4 and Appendix A can probably be extended to multiple buildings using the multiple edge integral. This would allow direct evaluation of the effects of varying building arrangements on location variability. The technique also has the potential for extremely rapid multiple edge diffraction evaluation by calculating field perturbations from a known situation such as the flat edge arrangement. This would avoid the

need to make heuristic assumptions such as those used in §7.3 in constructing the full deterministic model.

- More extensive simulation using either repeated applications of the full multiple edge integral or using the technique suggested above could be used to derive correction factors for the Flat Edge model to account for building height, spacing and orientation variability. This could be done using either directly collected building distributions or assumed arrangements such as regular grid structures.

9.2.3: Measurements

Ultimately, even theoretical propagation models can only be verified by direct comparison with measurements. The following investigations would be of particular interest:

- Measurements of propagation around particular buildings should be made to permit isolation of the effects of particular building types. The buildings should be chosen to encompass a range of different construction materials and shapes and should preferably be as distant from other scattering features as possible. This will enable the best choice of canonical scatterer to be chosen for particular situations.
- Since it may be difficult to find appropriately isolated buildings, scaled down measurements made on an appropriate test range may be necessary. This approach also allows more careful control over the shape of the building and separation of the effects of the building from terrain and other effects. Similar multiple building measurements could be made to determine the effects of deviations in shape from ideal half-plane structures.
- Laboratory measurements of the high frequency electrical parameters of various common building materials would be helpful in supporting modelling of buildings as dielectric scatterers.

- Most importantly, there is a great need for propagation measurements performed over extensive areas in situations where precise building positions and shapes are known. These would follow the approach of the first programme described in Chapter Eight, but using a far larger data set and variety of environments.

9.2.4: Overall

This work has focused on the techniques and methods used in constructing theoretical models for a wide variety of cases. Greater experience of applying these models in specific cases of interest is needed to make future progress.

9.3: Conclusions

In the wake of knowledge comes understanding. Insight into the nature of measurements has allowed theoretical models to describe and account for observed effects, yielding more consistent predictions applicable in a wider range of situations. Developing these models in the future to take account of the the availability of data and the use to which predictions will be put has the potential to produce increasingly efficient systems, tailored to the environment in which they will be used. It is hoped that this work has made some contribution to this process and that this contribution will be developed and extended in the future.

Appendix A

Single Edge Height Statistics

This appendix derives the statistical distribution of propagation loss due to a single knife edge given the distribution of the height of the edge. Firstly, using the asymptotic approximation to the Fresnel integral previously given (§4.4.4), the field after single edge diffraction deep into the shadow zone is derived:

$$\begin{aligned}
 A &= \frac{F(w)}{\sqrt{2j}} + \frac{1}{2} \\
 &\sim \frac{1}{\sqrt{2j}} \left(-\sqrt{\frac{j}{2}} - \frac{j \exp\left(\frac{j\pi w^2}{2}\right)}{\pi w} \right) + \frac{1}{2} \\
 &\sim -\frac{\exp\left(\frac{j\pi w^2}{2}\right)}{\pi w} \sqrt{\frac{j}{2}} \\
 \text{Hence } |A| &\sim \frac{1}{\pi |w| \sqrt{2}}
 \end{aligned}$$

In figure A.1 the behaviour of this expression is compared with the complete solution. The accuracy of the approximation improves as the field point moves deeper into the shadow region.

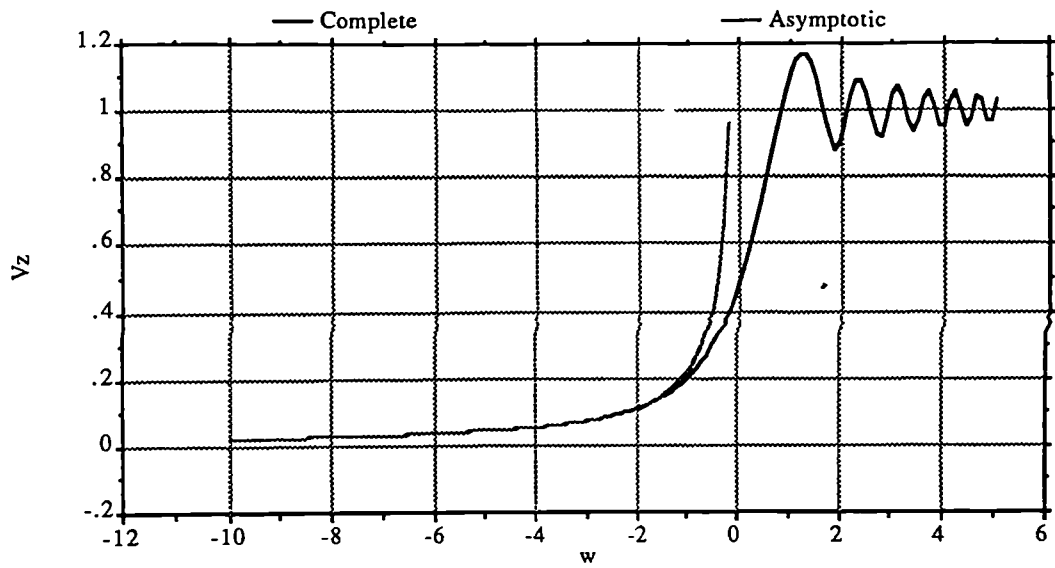


Figure A.1: *Asymptotic half plane diffraction in deep shadow region.*

Now assuming that the source is very distant, this may be expressed in terms of the geometry of the situation illustrated in figure A.2:

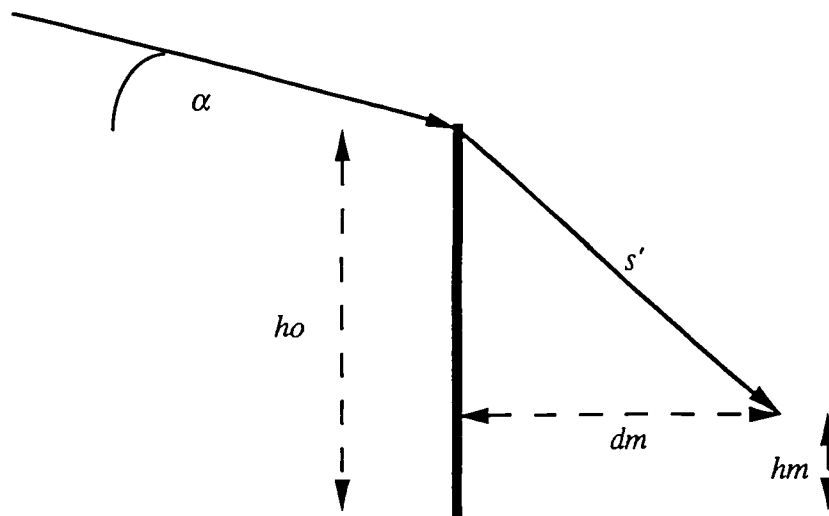


Figure A.2: *Single edge arrangement*

Under these assumptions:

$$w = \theta \sqrt{\frac{2s'}{\lambda}}$$

From which : $|A| \sim \frac{\sqrt{\lambda}}{2\pi \left[\tan^{-1} \left(\frac{h_o - h_m}{d_m} \right) - \alpha \right] \left[d_m^2 + (h_o - h_m)^2 \right]^{1/4}}$

Using this expression it is desired to find the distribution of the propagation loss, L , where

$$L = -20 \log_{10} A$$

given the distribution of h_o . This is achieved using the following relation, which follows from elementary statistical considerations:

$$p_L(L) = p_h(h_o) \left| \frac{dh_o}{dL} \right|$$

where the $p()$ are the probability density functions of $|A|$ and h_o . The differential required is easily found and will not be explicitly stated here. It is assumed that α is independent of variations in h_o , so that the problem is essentially concerned with plane wave incidence.

The mean μ_A and standard deviation σ_A of $|A|$ are found using the following expressions:

$$\mu_L = \int_{-\infty}^{\infty} L p_L(L) dL; \sigma_L^2 = \int_{-\infty}^{\infty} L^2 p_L(L) dL - \mu_L^2$$

and the integrations are performed using a standard numerical algorithm.

References

- [Abramowitz,1970] Abramowitz, M. and Stegun, I.A., "Handbook of mathematical functions", Dover publications, New York, 1970.
- [Allsebrook,1977] Allsebrook, K. and J.D. Parsons, "Mobile radio propagation in British cities at frequencies in the VHF and UHF bands," *IEEE Trans. Veh. Tech.*, vol. VT 26, no. 4, pp. 95 - 102, 1977.
- [Barnett,1972] Barnett, W.T., "Multipath propagation at 4, 6 and 11 GHz," *Bel Sys. Tech. J.*, vol. 51, no. 2, pp. 321-361, Feb. 1972.
- [Beckman,1963] Beckman, P. and Spizzichino, A., "The scattering of electromagnetic waves from rough surfaces", Macmillan, New York, p.246, 1963.
- [Bergljung,1991] Bergljung, C., "A comparison of solutions to the problem of diffraction of a plane wave by a dielectric wedge", COST 231 TD(91)81, Leidschendam Sep.1991.
- [Black,1972] Black, D.M. and Reudink, D.O., "Some characteristics of mobile radio propagation at 836MHz in the Philadelphia area", *IEEE Trans. Veh. Tech.*, vol. VT-21, no. 2, pp.45-51, 1972.
- [Blomquist,1974] Blomquist, A. and L. Ladell, "Prediction and calculation of transmission loss in different types of terrain," *NATO-AGARD Conf. Publ.*, vol. CP 144, pp. 32/1 - 32/17, 1974.
- [Boersma,1978] Boersma, J., "On certain multiple integrals occurring in a waveguide scattering problem", *SIAM J. Math Anal.*, vol.9, no.2, pp.377-393, 1978.
- [Born,1980] Born, M. and Wolf, E., "Principles of optics", sixth edition Pergamon press, Oxford, 1980.
- [Bramley,1973] Bramley, E.N. and Cherry, S.M., "Investigation of microwave scattering by tall buildings", *Proc. IEE.*, vol.120, no.8, pp.833-843. 1973.

-
- [Bremmer,1949] Bremmer, H., "Terrestrial radio waves", Elsevier Publ. co., Amsterdam, 1949.
- [Bullington,1977] Bullington, K., "Radio propagation for vehicular communications," *IEEE Trans. Veh. Tech.*, vol. VT-26, no. 4, pp. 295 - 308, 1977.
- [Cambridge,1991] University of Cambridge collection of air photographs, Free School Lane, Cambridge.
- [CCIR,370_1,721_2] *Recommendations and reports of the CCIR, XVIth plenary assembly*, vol. V, "Propagation in non-ionized media", Dubrovnik, 1986.
- [Chatfield,1983] Chatfield, C., "Statistics for technology", 3rd ed., Chapman and Hall, London, 1983.
- [Chrysanthou,1991] Chrysanthou, C. and Bertoni, H.L., "Variability of sector averaged signals for UHF propagation in cities", *IEEE Trans. Veh. Tech.*, vol.VT-39, no.4, pp.352-358, 1990.
- [COST207,1989] Final report of the COST-207 management committee, "Digital land mobile radio communications", *Commission of the European Communities*, L-2920 Luxembourg, 1989.
- [Davis,1975] Davis, P.J. and Rabinowitz, P., "Methods of numerical integration", Academic Press, New York, 1975.
- [Deschamps,1972] Deschamps, G.A., "Ray techniques in electromagnetics", *Proc. IEEE.*, vol. 60, no.9, 1972. pp. 1022-1035.
- [Delisle,1985] Delisle, G.Y., J. Lefevre, M. Lecours, and J. Chouinard, "Propagation loss prediction : a comparative study with application to the mobile radio channel," *IEEE Trans. Veh. Tech.*, vol. VT-26, no. 4, pp. 295 - 308, 1985.
- [Deygout,1966] Deygout, J., "Multiple knife edge diffraction of microwaves," *IEEE Trans. Antenn. & Prop.*, vol. AP-14, no. 4, pp. 480 - 489, 1966.
- [Edwards,1969] Edwards, R. and J. Durkin, "Computer prediction of service areas for VHF mobile radio networks," *Proc. IEE*, vol. 116, no. 9, pp. 1493 - 1500, 1969.

-
- [Eggers,1990] Eggers, P., "Preliminary suggestions for COST231 urban path loss model", COST231 TD 90 (107), Darmstadt, 1990.
- [Egli,1957] Egli, J.J., "Radio Propagation above 40MC over irregular terrain," *Proc. IRE*, pp. 1383 - 1391, 1957.
- [Epstein,1953] Epstein, J. and D.W. Peterson, "An experimental study of wave propagation at 850 MC," *Proc. IRE*, pp. 595 - 611, 1953.
- [Furutsu,1963] Furutsu, K., "On the theory of radio wave propagation over inhomogeneous earth", *J. Res. NBS*, vol.67D, no.1, pp.39-62, 1963.
- [Gans,1972] Gans, M.J., "A power spectral theory of propagation in the mobile radio environment," *IEEE Trans. Veh. Tech.*, vol. VT-21, no. 1, pp. 27 - 38, Feb. 1972.
- [Gautschi,1961] Gautschi, W., "Recursive computation of the repeated integrals of the error function", *Math. Comp.*, vol.15, pp.227-232.
- [Giovannelli,1984] Giovannelli, C.L., "An analysis of simplified solutions for multiple knife-edge diffraction", *IEEE Trans. Ant. & Prop.*, vol. AP-32, no.3, pp.297-30 March,1984.
- [Gong,1990] Gong, J. and MacLean TSM, "Propagation over finite width knife edge at arbitrary angle to direction of propagation", *IEE colloquium digest*, no.1990/143, pp.2/1-2/4, 1990.
- [Groves,1990] Groves, I.S., "Personal mobile communications - a vision of the future", *British Telecom Technology Journal*, vol.8, no.1, pp.7-11,1990.
- [Hacking,1968] Hacking, K., "Propagation over rounded hills," *BBC research report*, no. RA - 21, July 1968.
- [Hansen,1977] Hansen, F. and F.I. Meno, "Mobile fading - Rayleigh and lognormal superimposed," *IEEE Trans. Veh. Tech.*, vol. VT-26, no. 4, pp. 332 - 335, Nov. 1977.
- [Haslett,1991] Haslett, CJ and Al-Nuaimi, M., "Prediction of diffracted field strength in the shadow of a flat-roofed building", *Electronics Letters*, vol.27, no.11, pp.950-951.
- [Hata,1980] M.Hata., "Empirical formula for propagation loss in land mobile radio services," *IEEE Trans. Veh. Tech.*, vol. VT-29, pp. 317 - 325, 1980.

-
- [Holbeche,1985] Holbeche, RJ, ed., "Land mobile radio systems", Peregrinus, London, 1985.
- [Hufford,1987] Hufford, G., "A general model for signal level variability," *IEEE J. Sel. Areas in Comms.*, vol. SAC-5, no. 2, pp. 299 - 301, Feb. 1987.
- [Ibrahim,1983] Ibrahim, M.F. and J.D. Parsons, "Signal strength prediction in built-up areas," *Proc. IEE*, part F, vol. 130, no. 5, pp. 377 - 384, 1983.
- [Ikegami,1980] Ikegami, F. and Yoshida, S., "Analysis of multipath propagation structure in urban mobile radio environments", *IEEE Trans. Antenn. and Prop.*, vol. AP28, no.4, pp.531-537, 1980.
- [Ikegami,1983] F.Ikegami, and S. Yoshida, "Feasibility of predicting mean field strength for urban mobile radio by aid of building databases," *Conf. rec. IEEE int. conf. commun. (ICC '83)*, vol. A2.6, pp. 68 - 76, 1983.
- [Ikegami,1984] F.Ikegami,, T. Takeuchi, and M. Umehira, "Propagation factors controlling mean field strength on urban streets," *IEEE Trans. Ant. & Prop.*, vol. AP-32, no. 8, pp. 822 - 829, Aug.1984.
- [Ikegami,1991] Ikegami, F., Takeuchi, T. and Yoshida, S., "Theoretical prediction of mean field strength for urban mobile radio", *IEEE Trans, Ant. & Prop.*, vol. AP-39, no. 3, pp.299-302.
- [Jakes,1974] Jakes, W.C., "Microwave mobile communications", publ. John Wiley, New York, 1974.
- [James,1980] James, G.L., "Geometrical theory of diffraction for electromagnetic waves",book, publ. Peter Peregrinus, 1980.
- [Kafaru,1989] Kafaru, O.O., "An environment-dependent approach to wideband modelling and computer simulation of UHF mobile radio propagation in built-up areas ", PhD Thesis, Department of Electrical Engineering and Electronics, Liverpool University, February 1989.
- [Keech,1991] Keech, M.A.. "UK land cover database for radio systems planning". presented at the Radiocommunications agency, 26th March, 1991.

-
- [Keller,1962] Keller, J.B., "Geometrical theory of diffraction", *J. Opt. Soc. Am.*, vol. 52, no.2, pp.116-130, 1962.
- [Korobov,1957] Korobov, N.M., "Approximate calculation of multiple integrals", *Dokl. Acad., Nauk., SSSR.*, vol.115., pp. 1062-1065, 1957. (In Russian)
- [Kouyoumjian ,1974] Kouyoumjian, R.G. and P.H. Pathak, "A uniform geometrical theory of diffraction for an edge in a perfectly conducting surface," *Proc. IEEE*, vol. 62, pp. 1448 - 1461, Nov. 1974.
- [Kouyoumjian ,1975] Kouyoumjian, R.G.in R.Mitra ed., "Numerical and asymptotic techniques in electromagnetics", Springer-Verlag, Berlin, 1975.
- [Kozono,1977] Kozono, S. and Watanabe, K., "Influence of environmental building on UHF land mobile radio propagation", *IEEE Trans., Comm.*, vol. COM-25, no.10 pp.1133-1143, 1977.
- [Lebherz,1991] Lebherz M., Wiesbeck W., "Features of 3D VHF/UHF propagation channel modelling", 7th International Conference on Antennas and Propagation, York University, 15th-18th April 1991, IEE Conf. Publ. no.333, pp.2-976 to 2-979.
- [Lebherz,1991b] Lebherz M., Kurner T., "A UTD wave propagation model for microcell planning purposes", 21st European microwaves conference, vol. 1, pp.379-384, 1991.
- [Lee,1978] Lee, S.W., "Path integrals for solving some electromagnetic edge diffraction problems", *J. Math. Phys.*, vol.19, no.6, pp.1414-1422, 1978.
- [Lee,1982] Lee, W.C.Y. "Mobile communications engineering", publ.McGraw-Hill, New York, 1982.
- [Longley,1968] Longley, A.G. and P.L. Rice, "Prediction of tropospheric radio transmission loss over irregular terrain - a computer method," *ESSA Tech. Rep.*, vol. ERL 79 - ITS 67, 1968.
- [Longley,1978] Longley, A.G., "Radio Propagation in urban areas," *Institute for Telecommunication Sciences*, pp. 503 - 511, 1978.

-
- [Loew,1991] Loew, K., "A comparison of CW measurements performed in Darmstadt with the COST231 Walfisch-Ikegami model", COST231 TD(91)74 ,Leidschendam, 1991.
- [Luebbers,1984] Luebbers, R.J., "Finite conductivity uniform GTD versus knife edge diffraction in prediction of propagation path loss," *IEEE Trans. Ant. & Prop.*, vol. AP-32, no. 1, pp. 70-76, Jan. 1984.
- [Luebbers,1989] Luebbers, R.J., "A heuristic UTD slope diffraction coefficient for rough lossy wedges," *IEEE Trans. Ant. & Prop.*, vol. AP-37, no. 2, pp. 206-211, Feb. 1989.
- [Matthews,1991] Matthews, P.A. and Mohebbi, B., "Direction of arrival and building scatter at UHF", *Seventh International Conference on Antennas and Propagation*, IEE Conf. Pub. no.333, vol.1 pp 1.147-1.150.
- [Mehler,1991] Mehler, M.J., "Ground Cover Databases", document DIF(91)3 of the TWP on diffraction, scattering and terrain effects, June, 1991.
- [Michaeli,1985] Michaeli, A., "A new asymptotic high-frequency analysis of electromagnetic scattering by a pair of parallel wedges: Closed form results," *Radio Science*, vol. 20, no. 6, pp. 1537-1548, Nov. - Dec. 1985.
- [Michaeli,1987] Michaeli, A., "Uniform GTD solution for the far-field scattering by polygonal cylinders and strips," *IEEE Trans. Ant. & Prop.*, vol. AP-35, no. 8, pp. 983-986, Aug. 1987.
- [Millington,1962] Millington G., Hewitt R., Immirzi F. S., "Double knife edge diffraction in field strength predictions". *IEE Monograph*, no. 509E, pp.419-429, 1962.
- [Millington,1962b] Millington G., Hewitt R., Immirzi F. S., "The fresnel surface integral", *IEE Monograph*, no. 508E, pp.430-437, 1962.
- [Mitobe,1974] Mitobe S., and Ito, S., "Measurements of VHF reflection from precast concrete walls", *NHK Tech. Rep.*, 1974.
- [Moiseiwitsch,1977] Moiseiwitsch, B.L., "Integral Equations", London, Longman, 1977.

- [Morgensen,1991] Morgensen P.E., Eggers P., Jensen C., "Urban area radio propagation measurements for GSM / DCS1800 macro and micro cells", *7th International Conference on Antennas and Propagation York University*, 15th-18th April 1991, IEE Conf. Publ. no.333, pp.1-500 to 1-503.
- [NAG,s20acf] "The NAG fortran library manual", Mark II, Numerical Algorithms Group Ltd., Oxford, 1983. Routine s20acf.
- [NAG,d01gcf] "The NAG fortran library manual", Mark II, Numerical Algorithms Group Ltd., Oxford, 1983. Routine d01gcf].
- [Okumura,1968] Okumura, Y., E. Ohmori, T. Kawano, and K. Fukuda, "Field strength and its variability in VHF and UHF land mobile radio service," *Rev. Electr. Commun. Lab.*, vol. 16, pp. 825-873, 1968.
- [Parsons,1983] J.D. Parsons and Ibrahim, M.F., "Signal strength prediction in built-up areas part 2 - signal variability," *Proc. IEE*, part F, vol. 130, no. 5, pp. 385 - 391 1983.
- [Parsons,1989] Parsons, J.D., "Mobile communication systems", publ. Blackie Glasgow, 1989.
- [Parsons,1989b] Parsons, J.D., "Propagation effects on mobile services," in *Radiowave Propagation*, ed. L.W. Barclay, pp. 262 - 278, IEE / Peter Peregrinus,1989.
- [Pogorzelski,1982] Pogorzelski, R.J., "A note on some common diffraction link loss models", *Radio Science*, vol.17, pp.1536-1540, 1982.
- [Ranade,1987] Ranade, A. and Noerpel, A.R., "Microwave energy shows strong dependence on orientation of city blocks", *Electronics Letters.*, vol.23, no.18, pp. 922-924, 1987.
- [Reudink,1974] Reudink, D.O., "Properties of mobile radio propagation above 400MHz", *IEEE Trans. Veh. Tech.*, vol. VT-23, no. 4, pp.143-159,1974.
- [Rustako,1991] Rustako, A.J. Jr., Gans, M.J., Owens, G.J. and Roman R.S, "Radio propagation at microwave frequencies for line-of-sight microcellular mobile and personal communications", *IEEE Trans. Veh. Tech.*, vol. VT-40, no. 1, pp.203 - 210, Nov. 1977.

-
- [Ruthroff,1971] Ruthroff, C.L., "Multiple path fading on line-of-sight microwave radio systems as a function of path length and frequency," *Bell Sys. Tech. J.*, vol. 50, no. 7, pp. 2375 - 2398, Sept.1971.
- [Saunders,1989] Saunders, SR, "Interim Report : Theoretical modelling of mobile radio propagation", Department of Electrical and Electronic Engineering, Brunel University, 1989.
- [Saunders,1990a] Saunders, S.R. and Bonar, F.R., "The feasibility of theoretical models for VHF/UHF mobile radio system design", *Seventh National Radio Science Colloquium*, 23rd/24th April 1990, Rutherford Appleton Laboratories.
- [Saunders,1990b] Saunders, S.R. and Bonar, F.R., "Building diffraction modelling for area coverage predictions in mobile radio propagation", *IEE colloquium on "Diffraction modelling embracing surface feature data"*, Digest no. 1990/157, pp.4/1-4/3, 16th November 1990.
- [Saunders,1991] Saunders, S.R. and Bonar, F.R., "A propagation model for slow fading in urban mobile radio systems", *7th International Conference on Antennas and Propagation*, York University, 15th-18th April 1991, IEE Conf. Publ. no.333, pp.1-160 to 1-163.
- [Saunders,1991b] Saunders, S.R. and Bonar, F.R., "Mobile radio propagation in built-up areas: a numerical model of slow fading", *41st IEEE vehicular technology society conference*, May 1991, pp.295-300.
- [Saunders,1991c] Saunders, S.R. and Bonar, F.R., "Explicit multiple building diffraction attenuation function for mobile radio wave propagation", *Electronics Letters*, vol.27, no.14, pp.1276-1277, July 1991.
- [Saunders,1991d] Saunders, S.R., "The Flat Edge Model", COST231 TD(91)84, Leidschendam, 1984.
- [Sharples,1989] Sharples, P.A. and Mehler, M.J., "Cascaded cylinder model for predicting terrain diffraction loss at microwave frequencies", *Proc. IEE*, vol. 136, Pt.H, no.4, pp.331-337, 1989.
- [Shearman.1989] Shearman, E.D.R. "Electromagnetic wave propagation" in "Radiowave Propagation", eds.Hall M.P.M. and Barclay,L.W.. publ. Peter Peregrinus, London, 1989.

-
- [Stroud,1971] Stroud, A.H., "Approximate calculation of multiple integrals", publ. Prentice-Hall, New Jersey, 1971.
- [Sommerfeld,1911] Sommerfeld, A. and Runge, J., "Anwendung der Vektorrechnung auf die Grundlagen der Geometrischen Optik", *Ann. Phys.*, vol.35, pp.277-298, 1911.
- [Steele,1991] Steele,R., "The importance of propagation phenomena in personal communication networks", *Seventh international conference on antennas and propagation*, pp.1.1-1.5, York, 1991.
- [Steen,1969] Steen, N.M., Byrne, G.D. and Gelbard, E.M., "Gaussian quadratures for the integrals

$$\int_0^{\infty} \exp(-x^2) f(x) dx \text{ and } \int_0^b \exp(-x^2) f(x) dx$$
Math. Comp., vol.23, pp.661-671, 1969.
- [Thomas,1990] Thomas,D. Checketts DG, Edwards JA, Mehler MJ, Bagwell DJ, "Short range VHF/UHF propagation", University of Birmingham report, ref EDH512, January 1990.
- [Tiberio,1979] Tiberio, R. and Kouyoumjian, R.G., " A uniform GTD solution for the diffraction by strips illuminated at grazing incidence", *Radio Science.*, vol. 14, no.6, pp.944-941, 1979.
- [Tiberio,1982] Tiberio, R. and Kouyoumjian, R.G., "An analysis of diffraction at edges illuminated by transition region fields", *Radio Science*, vol.17, no.2, pp.323-336, 1982.
- [Tiberio,1984] Tiberio, R. and R.G. Kouyoumjian, "Calculation of the high-frequency diffraction by two nearby edges illuminated at grazing incidence," *IEEE Trans. Antenn. & Prop.*, vol. AP-32, pp. 1186 - 1196, Nov. 1984.
- [Taylor,1991] Taylor, J.T., Omura, J.K., "Spread spectrum technology: a solution to the personal communications services frequency allocation dilemma", *IEEE Comm.mag.*, vol29, no.2, pp.48-51, 1991.
- [Vogel,1986] Vogel, W.J., and Goldhirsh J., "Tree attenuation at 869MHz derived from remotely piloted aircraft measurements", *IEEE Trans. Antenn. and Prop.*, vol. AP-34, no.12, pp.1460-1464, 1986.

-
- [Vogler,1981] Vogler, L.E., "The attenuation of electromagnetic waves by multiple knife-edge diffraction", *NTIA Rep. 81-86*, 20 pp., Natl. Telecommun. and Inf. Admin., Boulder, Colo., 1981.
- [Vogler,1982] Vogler, L.E., "An attenuation function for multiple knife-edge diffraction", *Radio Science*, vol.17, no. 6, pp. 1541-1546, 1982.
- [Volakis,1986] Volakis, J.L., "A uniform geometrical theory of diffraction for an imperfectly conducting half-plane," *IEEE Trans. Ant. & Prop.*, vol. AP-34, no. 2, pp. 172-180, Feb. 1986.
- [Walfisch,1988] Walfisch, J. and H.L. Bertoni, "A theoretical model of UHF propagation in urban environments," *IEEE Trans. Ant. & Prop.*, vol. AP-36, no. 12, pp. 1788-1796, Dec. 1988.
- [Westminster,1990] Westminster City Council, Dept. of Planning and Transportation
- [Whitaker,1984] Whitaker, JH., "Near-field ray calculation for multiple knife-edge diffraction", *Radio Science*, vol.19, pp.975-986.
- [Whitaker,1990] Whitaker, JH., "Diffraction over a flat-topped terrain obstacle", *Proc. IEE*, vol.137, pt.H, no.2, pp. 113-116, 1990.
- [Winkler,1975] Winkler, RL., "Statistics - probability, inference and decision", New York, Holt, Rinehart and Winston, 1975.